

---

Electronic Thesis and Dissertation Repository

---

8-14-2013 12:00 AM

# The Effect of Stem Surface Treatment and Substrate Material on Joint Replacement Stability: An In-Vitro Investigation into the Stem-Cement Interface Mechanics under Various Loading Modes

Yara K. Hosein  
*The University of Western Ontario*

Supervisor  
Dr. Cynthia E. Dunning  
*The University of Western Ontario*

Graduate Program in Biomedical Engineering  
A thesis submitted in partial fulfillment of the requirements for the degree in Doctor of Philosophy  
© Yara K. Hosein 2013

Follow this and additional works at: <https://ir.lib.uwo.ca/etd>



Part of the [Biomechanics and Biotransport Commons](#)

---

## Recommended Citation

Hosein, Yara K., "The Effect of Stem Surface Treatment and Substrate Material on Joint Replacement Stability: An In-Vitro Investigation into the Stem-Cement Interface Mechanics under Various Loading Modes" (2013). *Electronic Thesis and Dissertation Repository*. 1479.  
<https://ir.lib.uwo.ca/etd/1479>

This Dissertation/Thesis is brought to you for free and open access by Scholarship@Western. It has been accepted for inclusion in Electronic Thesis and Dissertation Repository by an authorized administrator of Scholarship@Western. For more information, please contact [wlsadmin@uwo.ca](mailto:wlsadmin@uwo.ca).

THE EFFECT OF STEM SURFACE TREATMENT AND SUBSTRATE MATERIAL ON JOINT  
REPLACEMENT STABILITY: AN *IN-VITRO* INVESTIGATION INTO THE STEM-CEMENT INTERFACE  
MECHANICS UNDER VARIOUS LOADING MODES

(Thesis format: Integrated Article)

by

Yara Kareen Hosein

Graduate Program in Biomedical Engineering

A thesis submitted in partial fulfillment  
of the requirements for the degree of  
Doctor of Philosophy

The School of Graduate and Postdoctoral Studies  
The University of Western Ontario  
London, Ontario, Canada

© Yara K. Hosein 2013

## ABSTRACT

Mechanical loosening is a common mode of joint replacement failure. For cemented implants, loosening at the implant-cement interface may be affected by stem surface design. Altering the surface topography facilitates the infiltration of bone cement onto the stem, creating a mechanical interlock, improving interface stability. However, few *in-vitro* studies have investigated this. Therefore, the purpose of this thesis was to investigate the effect of stem surface treatments and substrate materials on stem-cement interface stability *in-vitro*.

Four separate studies were performed to assess the stability of various stem surface treatments, with two substrate materials, under three loading modes. Titanium and cobalt chrome implant stems were custom machined and treated with one of four surfaces: smooth, sintered beads, plasma spray, and circumferential grooves. Sintered bead and plasma sprayed stems were tested in independent torsion, compression and bending; circumferential groove designs were compared in torsion and then compression. All stems were potted in aluminum tubes using PMMA, and loaded cyclically using a materials testing machine. A custom optical tracking system (resolution under 5  $\mu\text{m}$ ) was validated for use, and subsequently employed to measure stem-cement interface motion during loading. Overall, results showed surface treatments improved stability, but this was affected by substrate material. Across all loading modes, beaded treatments applied to titanium stems, and plasma spray treatments applied to cobalt chrome stems, improved interface stability and strength when large surface treatment areas were employed. Additionally, the machining of circumferential grooves onto the stem surface improved interface strength in compression, with no influence in torsion.

A final study was performed using  $\mu$ -CT imaging to observe stem and cement motion under bending loads. A custom-built loading device applied static loads to smooth titanium stems, while acquiring CT images of the stem-cement interface. Interface motion was quantified by comparing scans before and after the stem underwent cyclic loading. Results indicated the stem and the surrounding cement had displaced following loading, yet the stems remained relatively stable.

These studies offer valuable information regarding the effect of stem surface treatments on stem-cement interface mechanics under various loading modes and will be used in the development of future implant systems.

**Keywords:** joint replacement system; implant design; stem loosening; stem surface treatment; stem material; bone cement, stem-cement interface; implant stability

## CO-AUTHORSHIP STATEMENT

The *in-vitro* experiments performed in this thesis were multi-disciplinary in nature, with the collaboration of various researchers. The individual contributions are listed below:

**Chapter 1:** Yara K. Hosein—wrote manuscript; Cynthia E. Dunning—reviewed and revised manuscript.

**Chapter 2:** Yara K. Hosein—study design, data collection, data analysis, wrote manuscript; Cynthia E. Dunning—study design, reviewed and revised manuscript.

**Chapter 3:** Yara K. Hosein—study design, data collection, data analysis, wrote manuscript; Graham J.W. King—study design, reviewed and revised manuscript; Cynthia E. Dunning—study design, reviewed and revised manuscript.

**Chapter 4:** Yara K. Hosein—study design, data collection, data analysis, wrote manuscript; Graham J.W. King—study design, reviewed and revised manuscript; Cynthia E. Dunning—study design, reviewed and revised manuscript.

**Chapter 5:** Yara K. Hosein—study design, data collection, data analysis, wrote manuscript; Graham J.W. King—study design, reviewed and revised manuscript; Cynthia E. Dunning—study design, reviewed and revised manuscript.

**Chapter 6:** Yara K. Hosein—study design, data collection, data analysis, wrote manuscript; Meghan P. Clynick—data collection; Cynthia E. Dunning—study design, reviewed and revised manuscript.

**Chapter 7:** Yara K. Hosein—study design, data collection, data analysis, wrote manuscript; Hristo Nikolov—data collection; Matthew Teeter—study design; David Holdsworth—study design; Cynthia E. Dunning—study design, reviewed and revised manuscript.

**Chapter 8:** Yara K. Hosein—wrote manuscript; Cynthia E. Dunning—reviewed and revised manuscript.

## ACKNOWLEDGMENTS

First and foremost, my sincerest gratitude goes to Dr. Cynthia Dunning, who acknowledged my research potential five years ago, and guided me through the most formative years of my research. Dr. Dunning has always been a dedicated, patient and caring supervisor. Her encouraging leadership style, along with her positive and motivational attitude, has made my graduate studies that much more enjoyable. Dr. Dunning—I thank you for the wonderful opportunity to have worked with you. You have instilled in me the qualities and attributes needed to move forward in my research career. I could not have found a better mentor.

Secondly, I would like to acknowledge my advisory committee members. In particular, I would like to thank Dr. Graham King, who provided his wealth of clinical knowledge and research expertise throughout the duration of this thesis. I am extremely grateful for the time he took from his busy schedule to guide me through my study designs and manuscript preparations. I would also like thank Dr. Jim Johnson for his overall support and research advice throughout my graduate studies. I was very fortunate to have worked with the both of you.

To my amazing lab mates at the Jack McBain Biomechanical Testing Lab, thank you for your support and assistance over the years. In particular: Dr. Stew McLachlin and Dr. Tim Burkhart for their abundance of research experience; Jake Reeves for his Solidworks help and cementing support; Mark Neuert for his engineering wisdom; Sayward Fetterly for her countless hours of cementing assistance; Meghan Clynick for her assistance with testing and data collection; and all the past lab members I have had the pleasure to work with. Thank you for making grad school memorable and enjoyable.

I have also had the opportunity to collaborate with numerous people over the duration of my graduate studies. I would especially like to thank Dr. David Holdsworth, Dr. Matthew Teeter and Hristo Nikolov for their contribution to the imaging study within this thesis. In addition, I would like to acknowledge the staff at University Machine Services, specifically Clayton Cook and Chris Vandelaar, for lending their expertise.

I must thank the funding sources that supported me through the duration of my PhD work: The Joint Motion Program (JuMP)—A CIHR training program in Musculoskeletal Health Research and Leadership and The University of Western Ontario. Thank you for contributing to my research.

Finally I would like to say a huge thank you to my family. To my parents—thank you for giving me the opportunity to relocate to Canada to pursue my academic goals, your infinite love and encouragement will never be forgotten. To Charis and Yanis— thank you for your cheering me on through my years of never-ending study, your support meant the world to me.



## DEDICATION

*To Azard and Yasmin Hosein,*

*You have supported me endlessly through all of my dreams and aspirations.*

# TABLE OF CONTENTS

Abstract .....	ii
Co-Authorship Statement.....	iv
Dedication .....	viii
Table of Contents .....	ix
List of Tables .....	xiii
List of Figures .....	xiv
List of Appendices .....	xviii
List of Abbreviations, Symbols and Nomenclature .....	xix
CHAPTER 1: Introduction.....	1
1.1 Joint Replacement Systems.....	1
1.1.1 Implantation Technique .....	3
1.1.2 Implant Loading.....	7
1.2 Stem Loosening .....	11
1.2.1 Stem Design .....	12
1.2.2 Stem Substrate Material.....	18
1.3 Implant Stability.....	21
1.3.1 Implant Stability Measurements <i>in-vitro</i> .....	22
1.4 Optical Systems .....	23
1.4.1 Camera Systems.....	24
1.4.2 Illumination.....	25
1.5 Computed Tomography (CT) Imaging .....	28
1.6 Study Rationale.....	29
1.7 Specific Objectives and Hypotheses.....	32
1.8 Thesis Overview .....	33

1.9 References.....	35
<b>CHAPTER 2: Development And Validation Of A Custom Optical Tracking System To Quantify Stem-Cement Interface Micromotion In Stemmed Implant Components ....</b>	
2.1 Introduction.....	48
2.2 Materials and Methods.....	49
2.3 Results.....	55
2.4 Discussion.....	58
2.5 Conclusion .....	61
2.6 References.....	62
<b>CHAPTER 3: The Effect Of Stem Surface Treatment On The Torsional Stability of Titanium and Cobalt Chrome Cemented Joint Replacement Systems.....</b>	
3.1 Introduction.....	64
3.2 Materials and Methods.....	66
3.3 Results.....	68
3.4 Discussion.....	75
3.5 Conclusion .....	79
3.6 References.....	80
<b>CHAPTER 4: The Effect Of Stem Surface Treatment And Material On Pistoning Of Ulnar Components In Linked Cemented Elbow Prostheses .....</b>	
4.1 Introduction.....	84
4.2 Materials And Methods.....	86
4.3 Results.....	90
4.4 Discussion.....	95
4.5 Conclusion .....	101
4.6 References.....	102
<b>CHAPTER 5: The Effect Of Stem Circumferential Grooves On The Stability At The Implant-Cement Interface .....</b>	
5.1 Introduction.....	104

5.2 Materials And Methods.....	106
5.3 Results.....	107
5.4 Discussion.....	109
5.5 Conclusion .....	117
5.6 References.....	118
<b>CHAPTER 6: The Effect Of Stem Surface Treatment And Material On The Stability Of Joint Replacement Systems Subjected To Bending Loads .....</b>	<b>121</b>
6.1 Introduction.....	121
6.2 Material And Methods .....	123
6.3 Results.....	125
6.4 Discussion.....	129
6.5 Conclusion .....	133
6.6 References.....	134
<b>CHAPTER 7: The Use of Micro-Computed Tomography (<math>\mu</math>-CT) Imaging to Visualize and Quantify Motion at the Stem-Cement Interface with an Applied Bending Moment .....</b>	<b>136</b>
7.1 Introduction.....	136
7.2 Materials and Methods.....	138
7.2.1 Testing Specimens .....	138
7.2.2 Custom-built Loading Device.....	138
7.2.3 Loading and Imaging Protocol.....	139
7.2.4 Data Analysis .....	142
7.3 Results.....	144
7.4 Discussion.....	149
7.5 Conclusion .....	153
7.6 References.....	154
<b>CHAPTER 8: General Discussion and Conclusions.....</b>	<b>156</b>

8.1 Summary .....	156
8.2 Strengths and Limitations .....	160
8.3 Future Directions .....	162
8.4 Significance.....	164
8.5 References.....	166
Appendices.....	167
Curriculum Vitae .....	241

## LIST OF TABLES

Table 2.1: Intra-class correlation coefficients (ICC's) and Standard Errors of Measurement (SEM) for the Vertical and Horizontal Displacement Measurements of the Optical System.	57
Table 7.1: Pre-dynamic Cemented Stem and Bead Motion.....	146
Table 7.2: Post-dynamic Stem and Bead Motion .....	147
Table 7.3: Offset Stem and Bead Motion .....	148
Table F.1: Vertical and Horizontal Pixel Lengths.....	185
Table I.1: Tabulated Data for Titanium Surface Treated Implant Stems in Torsion.....	208
Table I.2: Tabulated Data for Cobalt Chrome Surface Treated Implant Stems in Torsion..	209
Table I.3: Tabulated Data for Titanium Surface Treated Implant Stems under Compression .....	210
Table I.4: Tabulated Data for Cobalt Chrome Surface Treated Implant Stems under Compression .....	211
Table I.5: Tabulated Data for Circumferential Grooved Implant Stems under Compression .....	212
Table I.6: Tabulated Data for Circumferential Grooved Implant Stems in Torsion.....	213
Table I.7: Tabulated Data for Titanium Surface Treated Implant Stems in Bending.....	214
Table I.8: Tabulated Data for Cobalt Chrome Surface Treated Implant Stems in Bending.	215
Table L.1: Bending Modulus of Bone Cement with Various Bead- Cement Ratios.....	223
Table O.1: Deviation in Stem and Bead Surfaces between Scan- Re-scan Tests.....	240

## LIST OF FIGURES

Figure 1.1: Examples of Synovial Joint Types in the Upper and Lower Limb .....	2
Figure 1.2: Joint Replacement System at the Hip.....	4
Figure 1.3: Methods of Implant Fixation at the Elbow Joint.....	8
Figure 1.4: Loading at the Replaced Shoulder Joint.....	9
Figure 1.5: Stem Surface Treatments used in Cemented Elbow Systems .....	16
Figure 1.6: Schematic of the Plasma Spray Process .....	17
Figure 1.7: Schematic of the Sintering Process .....	19
Figure 1.8: Schematic of a Typical Camera System.....	26
Figure 1.9: Schematic of a Conventional Lens versus Telecentric Lens .....	27
Figure 2.1: Hardware of the Optical Tracking System .....	51
Figure 2.2: Calibration Grid used for Pixel to mm Conversion.....	52
Figure 2.3: Optical Tracking Software .....	53
Figure 2.4: Experimental Set-up for Validation of Optical Tracking System .....	54
Figure 2.5: Bland & Altman Plot Comparing Agreement of Measurement Systems.....	56
Figure 3.1: Surface Treated Stems used for Torsional Testing .....	67
Figure 3.2: Experimental Set-up for Torsional Testing of Implant Stems .....	69
Figure 3.3: Stem Rotation for Titanium and Cobalt Chrome Surface Treated Stems .....	70
Figure 3.4: Inspection of Stem Surface Treatments Post-Torsion Tests .....	72
Figure 3.5: Torque at Failure for Surface Treated Stems .....	73

Figure 3.6: Normalized Interface Toggle for Surface Treated Stems in Torsion .....	74
Figure 4.1: Surface Treated Implant Stems used for Compression Testing .....	87
Figure 4.2: Experimental Set-up for Compression Testing of Implant Stems.....	89
Figure 4.3: Inspection of Stem Surface Treatments Post-Compression Tests.....	91
Figure 4.4: Survival Curves for Titanium and Cobalt Chrome Stems.....	92
Figure 4.5: Stem Motion for Titanium and Cobalt Chrome Stems under Compression .....	93
Figure 4.6: Interface Stability Offered by the Surface Treated Stems in Compression .....	94
Figure 4.7: Global Stem Motion of Surface Treated Stems in Compression .....	96
Figure 5.1: Smooth and Circumferential Grooved Surface Designs Tested in Both Compression and Torsion .....	108
Figure 5.2: Stem Motion for Smooth and Circumferential Grooved Stems .....	110
Figure 5.3: Interface Stability for Smooth and Circumferential Grooved Surfaces in Compression .....	111
Figure 5.4: Interface Stability for Smooth and Circumferential Grooved Surfaces in Torsion .....	112
Figure 5.5: Stem Motion with Increased Number of Cycles .....	113
Figure 6.1: Experimental Set-up used for Bending Tests of Implant Stems .....	124
Figure 6.2: Stem Motion of Surface Treated Stems under Bending Loads .....	126
Figure 6.3: Proximal and Distal Views of Stems Post- Bending Tests .....	127
Figure 6.4: Maximum Interface Toggle for Surface Treated Stems in Bending .....	128
Figure 6.5: Offset Motion for Surface Treated Stems in Bending.....	130
Figure 7.1: Custom-Built Loading Device used for Application of Bending Loads .....	140



Figure 7.2: Schematic of Loading and Imaging Protocol used for Static and Dynamic Tests .....	141
Figure 7.3: Surface Deviation Analysis with Geomagic® .....	143
Figure 7.4: Average Stem Motion during Loading for the Pre-and Post-dynamic Scans ...	145
Figure B.1: Specifications for the Basler Pilot AG piA 2400- 12gc Camera.....	172
Figure B.2: Specifications for the Opto Engineering Telecentric Lens.....	173
Figure B.3: Specifications for the Advanced Illumination, Axial Diffuse Illuminator .....	174
Figure C.1: Back Panel of Calibration Program.....	175
Figure C.2: Back Panel of the Optical Tracking Program .....	176
Figure D.1: Bland Altman plots for Region 1-9 of Horizontal Displacement.....	177
Figure D.2: Bland Altman plots for Region 1-9 of Vertical Displacement.....	178
Figure E.1: Line of Best-Fit for Measured against True Displacements.....	181
Figure E.2: Deviation Plot for Optical System Measurements.....	182
Figure F.1: Calibration Grid used for Pixel to mm Conversion.....	184
Figure G.1: Engineering Drawing of Smooth Implant Stem.....	188
Figure G.2: Engineering Drawing of 20 mm Length Plasma Spray Implant Stem .....	189
Figure G.3: Engineering Drawing of 20 mm Length Beaded Implant Stem .....	190
Figure G.4: Engineering Drawing of 10 mm Length Plasma Spray Implant Stem .....	191
Figure G.5: Engineering Drawing of 10 mm length Beaded Implant Stem .....	192
Figure G.6: Engineering Drawing of 0.6 mm Grooved Implant Stem .....	193
Figure G.7: Engineering Drawing of 1.1 mm Grooved Implant Stem .....	194

Figure G.8: Engineering Drawing of Parts for Potting Jig Assembly .....	195
Figure G.9: Engineering Drawing of Delrin® Block used to Centralize Stems for Potting.	196
Figure G.10: Engineering Assembly of Jig used for securing Stem in Torsion and Compression .....	197
Figure G.11: Engineering Drawing of Securing Plates used for Bending Tests .....	198
Figure G.12: Engineering Assembly of Cement Sample Template.....	199
Figure G.13: Engineering Drawing of Parts for the Cement Sample Template .....	200
Figure G.14: Engineering Assembly of Stem Holder used in $\mu$ CT-imaging Bend Tests....	201
Figure G.15: Engineering Drawing of Parts for Stem Holder Assembly used in $\mu$ CT-imaging Bend Tests.....	202
Figure G.16: Engineering Drawing of Back Plate for Stem Holder Assembly used in $\mu$ CT- imaging Bend Tests.....	203
Figure H.1: Potting Jig used for Securing Stems during Cementing.....	205
Figure L.1: Bead Embedded Cement Samples.....	221
Figure L.2: Experimental Set-up for Three-point Bending of Cement Samples.....	222
Figure M.1: Mechanical Parts of Loading Device.....	228
Figure M.2: Custom-Built Loading Device.....	229
Figure N.1: Region of Interest (ROI) used to Create Isosurfaces.....	232
Figure N.2: Geomagic® Surface Deviation Analysis.....	237

## LIST OF APPENDICES

Appendix A:	Thesis Glossary .....	168
Appendix B:	Specifications for Hardware of Optical System .....	172
Appendix C:	LabVIEW® Programs .....	175
Appendix D:	Bland-Altman Plots for Optical System Validation .....	177
Appendix E:	Calculation of Optical System Accuracy .....	179
Appendix F:	Calculation of Optical System Resolution.....	183
Appendix G:	Engineering Drawings and Assemblies.....	188
Appendix H:	Cement Preparation and Potting Technique .....	204
Appendix I:	Tabulated Data .....	208
Appendix J:	Letter of Permission .....	216
Appendix K:	Bead Embedment Procedure .....	218
Appendix L:	Mechanical Testing of Beaded Cement Samples .....	219
Appendix M:	Custom-built Loading Device .....	226
Appendix N:	Surface Deviation Analysis .....	230
Appendix O:	Uncertainty of Stem and Bead Displacements .....	238

## LIST OF ABBREVIATIONS, SYMBOLS AND NOMENCLATURE

$\emptyset$	diameter
$^{\circ}$	degrees
%	percent
$\mu$	micro
$\mu\text{m}$	micrometer
$^{\circ}\text{C}$	degrees Celsius (unit of temperature)
<b>ANOVA</b>	analysis of variance
<b>CCD</b>	charged couple device
<b>CT</b>	computed tomography
<b>DIC</b>	digital image correlation
<b>F</b>	applied force
<b>FOV</b>	field of view
<b><math>F_{res}</math></b>	resultant force
<b><math>F_x</math></b>	component of force in x direction
<b><math>F_y</math></b>	component of force in y direction
<b><math>F_z</math></b>	component of force in z direction
<b>g</b>	grams
<b>GSM</b>	global stem motion
<b>HA</b>	hydroxyapatite

<b>HU</b>	Hounsfield unit
<b>Hz</b>	unit of frequency
<i>i.e.,</i>	‘that is’
<b>ICC</b>	intraclass correlation coefficient
<b>ISO</b>	International Organization for Standardization
<b>IT</b>	interface toggle
<b>mm</b>	millimeters
<b>N</b>	newton (unit of force)
<b>Nm</b>	newton meter (unit of torsional load)
<b>p</b>	probability value
<b>pixel</b>	pixel element
<b>PMMA</b>	polymethymethacrylate
<b>Ra</b>	average roughness value
<b>ROI</b>	region of interest
<b>Rz</b>	mean roughness depth
<b>s</b>	second (unit of time)
<b>SD</b>	standard deviation
<b>voxel</b>	volume element
<b><math>\alpha</math></b>	alpha (significance level of a test)

## CHAPTER 1: INTRODUCTION

**Overview:** *Stemmed joint replacement systems play an important role in the treatment of diseased or damaged joints; however, their success depends on the stability of the system after implantation, and its ability to withstand implant loosening over time. As such, the overall goal of this thesis was to investigate the stability at the implant-cement interface, using mechanical testing and an imaging technique, to determine the contribution of stem surface designs and substrate material in resisting the onset of implant loosening. This chapter introduces stemmed components of joint replacement systems, describes various stem design parameters considered for successful implantation, overviewing techniques used in this thesis for quantifying implant stability, and concludes with the study rationale, objectives and hypotheses.*

### 1.1 JOINT REPLACEMENT SYSTEMS

Joint replacement systems (*i.e.*, implant systems) are used in field of orthopaedic surgery as a treatment option for joints affected by degenerative diseases such as osteoarthritis, osteoporosis or rheumatoid arthritis, where the articular cartilage of the joint is destroyed. The damage imposed by these diseases is generally considered as irreversible. As such, replacement of the damaged joint is required. Similarly, traumatic injury to joints requires removal of the destroyed anatomy, to be replaced with an artificial prosthesis that restores the joint structure and function.

Implant systems are specific to the joint being replaced. In particular, stemmed joint replacement systems are unique to the treatment of synovial joints. These include joints of the lower (*i.e.* hip, knee, and ankle) and upper (*i.e.* shoulder, elbow, and wrist) extremities (Figure 1.1). Compared to the other joints of the body (*i.e.*, cartilaginous and

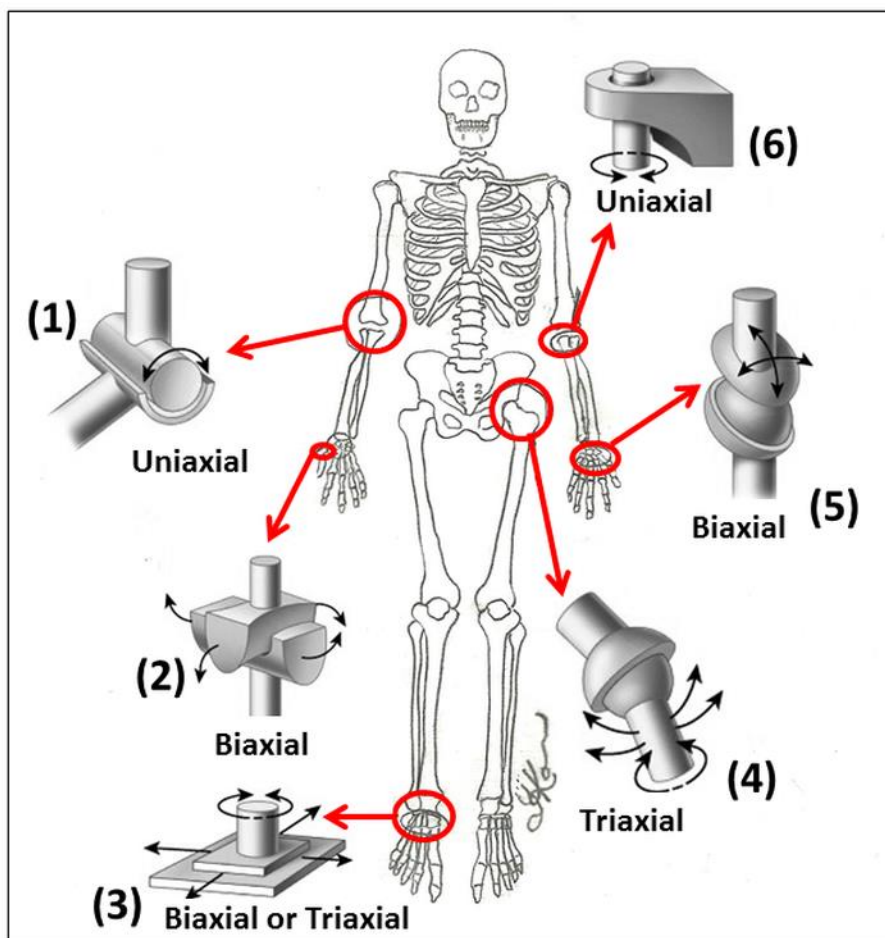


**Figure 1.1: Examples of Synovial Joint Types in the Upper and Lower Limb**

The above schematic shows examples of the synovial joints found in the human body; (1) hinge joint found between the humerus and ulna at the elbow, (2) saddle joint between the thumb and wrist, (3) plane joint found between the bones of the tarsus in the foot, (4) ball-and-socket joint located between the femoral head and acetabulum at the hip, (5) condylloid joint found between the bones at the wrist, and (6) pivot joint found between the head of the radius and radial notch of the ulna at the elbow. (*Joint images modified from Tortora and Nelson, 2009*)

fibrous joints), synovial joints provide a large range of motion (Tortora and Nielsen, 2009).

During the joint replacement procedure, the damaged or diseased joint is removed using established surgical techniques, and the host bone is prepared to accommodate the artificial joint. This is done by resecting the damaged joint head, and creating a canal through the remaining bone. The surgeon then inserts the stem of the artificial joint into host bone canal to allow for implant fixation.

Stemmed replacement systems typically consist of two main parts; the articulating component and intramedullary stem. The articulating region makes up the bearing surface, and depending on the degrees-of-freedom in the joint being replaced, may be classified as; (i) hinge joint, (ii) saddle joint, (iii) plane joint, (iv) ball-and-socket joint, (v) condyloid joint, and (vi) pivot joint (Figure 1.1) (Tortora and Nielsen, 2009). The intramedullary stem does not mimic a particular structure of the natural joint, but instead has a role in implantation of the artificial joint. That is, the stemmed region is inserted into the reamed host bone canal, and allows for fixation and anchoring of the replacement system to the healthy bone, which remains once the damaged articulating portion is removed (Figure 1.2).

The success of these replacement systems to stay implanted over time (*i.e.*, to avoid loosening) depends on the ability of the stemmed component to keep fixated within the host bone canal. Therefore, to improve on the longevity of joint replacement systems, the fixation process of the intramedullary stem needs to be thoroughly explored, with the purpose of ensuring secure anchorage of the implant to the healthy bone.

### 1.1.1 IMPLANTATION TECHNIQUE

There are two methods used to create a mechanical connection at the implant-bone interface; biologic fixation and cemented fixation (Figure 1.3). The choice of



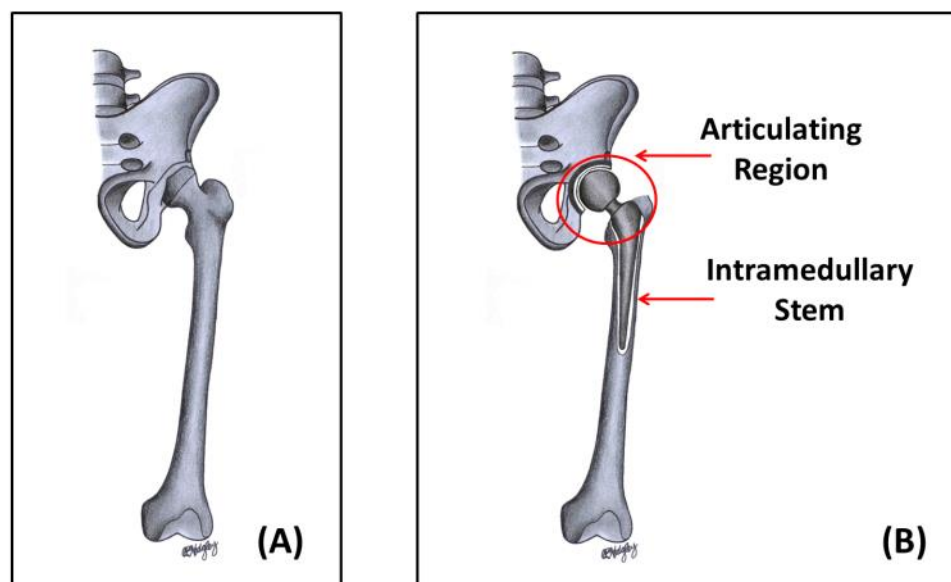


**Figure 1.2: Joint Replacement System at the Hip**

(A) Healthy hip joint, and (B) replaced hip joint. During joint replacement surgery, the damaged or diseased joint is removed and replaced with the artificial joint. The joint replacement consists of the articulation region that replaces the structure and function of the joint. The intramedullary stem is inserted into the canal of the host bone and allows for implant fixation. (*Drawing of hip provided by Dr. Angela Kedgley*)

fixation method may be dependent on implant design, surgeon preference, and patient specificity (Bauer and Schils, 1999; Morshed et al., 2007; Ni et al., 2005; Park, 1992).

#### 1.1.1.1 BIOLOGIC FIXATION

Biologic fixation involves the osseointegration, or direct structural and functional connection of the bone with the implant surface (Brånemark *et al.*, 2001). The success of osseointegration as a method for implant fixation is dependent on the material properties and the design of the implant stem (Bauer and Schils, 1999; Skinner, 2006). In particular, implant stem designs incorporating rough finishes, porous surfaces, and bioactive coatings have been utilized in biologic fixation (Bauer and Schils, 1999).

Rough or porous surfaces are applied to the implant surface to promote bone growth and ensure biological anchoring of the healthy bone to the implant (Incavo *et al.*, 2004; Park, 1992). These surface designs have been explored with regards to optimum surface roughness and pore size needed to optimize bone ingrowth (Bobyne *et al.*, 1980; Engh and Bobyne, 1988).

In addition to roughened surfaces, the application of bioactive coatings has also been used in biologic fixation. Incorporating a bioactive coating such as hydroxyapatite (HA) facilitates stimulation of bone formation on the stem surface (Geesink *et al.*, 1988), and its osteoconductivity is dependent on the coating composition, density, thickness and texture (Bauer and Schils, 1999).

Biologic fixation is typically used in younger patient populations, where the quality of the healthy bone can successfully accommodate ingrowth onto the stem surface. Additionally, depending on the stage of joint replacement surgery (*i.e.*, initial replacement versus revised replacement), along with the joint being replaced (*i.e.*, upper limb versus lower limb), biologic fixation may be preferred.

### 1.1.1.2 CEMENTED FIXATION

Orthopaedic bone cement is another method used for stem fixation. This method involves the incorporation of bone cement into the reamed bone canal, followed by the subsequent insertion of the intramedullary stem of the joint replacement system, ensuring appropriate alignment during implantation. Once inserted, a cement mantle thickness of approximately 2–3 mm (Banaszkiewicz, 2009a) is generated at the fixation interface, matching the surface of the implant to the bone canal. Cemented fixation is typically performed in the older patient population, where compromised bone quality may affect the success of implantation. In addition, a major advantage of using this type of fixation is the shorter recovery time associated with its procedure, allowing almost immediate weight bearing at the replaced joint.

One example of the cement used for fixation is polymethylmethacrylate (PMMA) bone cement, which is a synthetic polymer that works to secure the implant into the bone canal. PMMA bone cement is packaged as a polymethylmethacrylate powder and a monomer methacrylate liquid. When the powder and liquid are mixed together, the monomer is polymerized in a free radical process, to form the viscous paste that hardens over time (Navarro *et al.*, 2008; Serbetci and Hasirci, 2004; Webb and Spencer, 2007). Mixing of bone cement can be done using hand mixing techniques or under vacuum pressure (Dunne *et al.*, 2004; Geiger *et al.*, 2001; Lewis, 1997). After implantation, the PMMA bone cement does not adhere the implant to the bone, but instead enters the space between the bone and implant, providing a mechanical connection between the implant and the bone (Janssen *et al.*, 2008; Scheerlinck and Casteleyn, 2006). As such, when introduced into the bone canal, the cement conforms itself to the shape of the canal as well as the shape of the implant stem, creating a ‘customized’ prosthesis fit (Wroblewski *et al.*, 2008).

There are four main phases that occur during cement preparation and curing. Phase 1, or the mixing phase, begins immediately after the powder and liquid monomer are combined. When the mixture becomes fully integrated and sticky in consistency, the start of Phase 2 begins. When the sticky consistency is lost and the mixture starts to

appear doughy, this signals the start of Phase 3, the duration of which is termed the working time. The final phase occurs when the mixture can no longer be manipulated, but instead begins to harden, signaling Phase 4 (Kuhn, 2009; Serbetci and Hasirci, 2004). Typically the stem is inserted during Phase 3, and the exact time point of the working phase in which the insertion takes place is important to the success of stem implantation (Iesaka *et al.*, 2003; Park, 1992; Smeds *et al.*, 1997). A longer working time, with doughy cement consistency, facilitates better positioning and support of the implant (Smeds *et al.*, 1997); however, a shorter working time, with lower viscosity cement may be useful to allow for better intrusion of the bone cement into interface spaces (Hansen and Jensen, 1990).

In addition to the different phases of cement preparation and curing, the physical properties of the PMMA bone cement during those phases play an important role in implant fixation (Lewis, 1997; Saha and Pal, 1984). Porosity and viscosity are two such properties that can affect the static and dynamic loading response of bone cement (Lewis, 1997; Saha and Pal, 1984; Verdonschot and Huiskes, 1995). These properties have been shown to be affected by the temperature during preparation and handling, as well as mixing method of the cement just prior to implantation (Dall *et al.*, 2007; Hernigou *et al.*, 2009; Macaulay *et al.*, 2002; Smeds *et al.*, 1997). As such, it is important to ensure a controlled environment for the preparation of bone cement during joint replacement implantation.

### 1.1.2 IMPLANT LOADING

Mobility of the replaced joint is facilitated by muscles, tendons and ligaments acting together to both stabilize the joint while still allowing motion. Forces exerted by the individual muscles and ligaments, along with external loads supported by the limb, work collectively to produce resultant forces acting at the replaced joint. These resultant forces generate torsion, tension/compression and bending, which typically occur in a combined state (Figure 1.4). These loads have been shown to be up to three times body

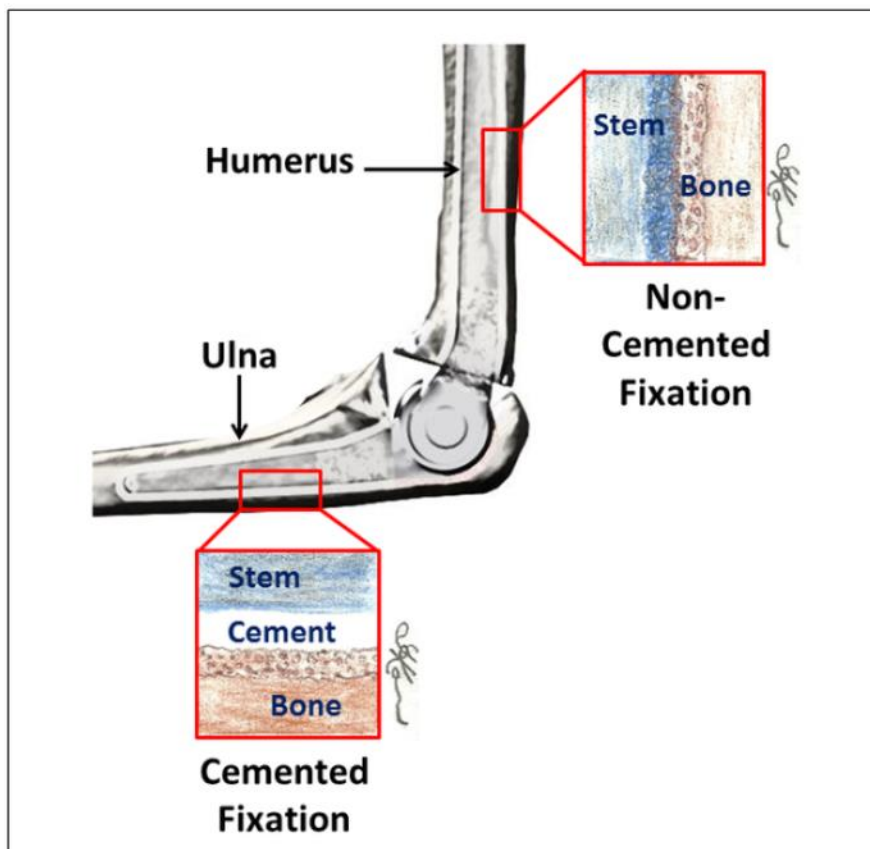


**Figure 1.3: Methods of Implant Fixation at the Elbow Joint**

Shown above are examples of implant fixation at the elbow joint. Non-cemented fixation incorporates a porous coating onto the surface of the implant stem (humerus), allowing ingrowth of the surrounding healthy bone. In comparison, cemented fixation uses orthopaedic bone cement as a filler to match the surfaces of the implant stem (ulna) to that of the healthy bone. (*Image of replaced elbow adapted from [www.orthogate.org](http://www.orthogate.org).*)

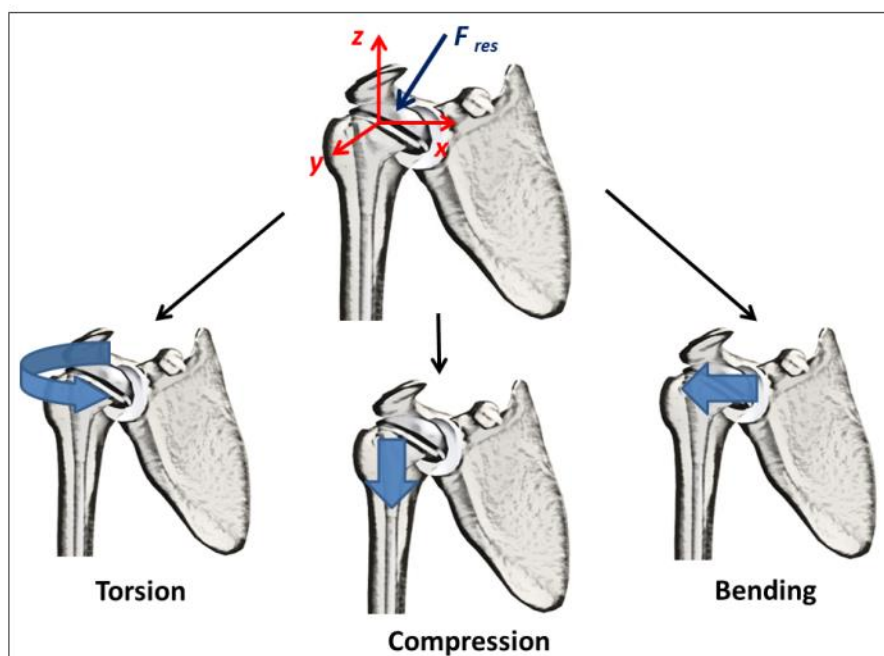


**Figure 1.4: Loading at the Replaced Shoulder Joint**

Resultant forces ( $F_{res}$ ) occur at the joint due to internal muscle and ligamentous forces, and external joint loads. These forces generate torsion, compression and bending, which typically occur in a combined state at the joint. (*Image of replaced shoulder adapted from [www.orthogate.org](http://www.orthogate.org).*)

weight for many joints (*i.e.*, elbow, hip and knee) during daily activities, and even higher for strenuous activities (Amis *et al.*, 1980; Bergmann *et al.*, 2004, 1993; Kutzner *et al.*, 2010).

Torsional loads refer to those that occur around the longitudinal axis of the implanted stem (*i.e.*,  $z$ -axis of Figure 1.4). This type of loading is common at the hip joint, where studies done by Bergmann *et al.*, have shown that torque about an instrumented prosthesis ranged between 5 Nm and 17 Nm for routine daily activities (Bergmann *et al.*, 2001, 1993). Daily activities included walking, sitting and ascending/descending stairs, with the highest torques occurring during stair ascent (Bergmann *et al.*, 2001). At joints such as the knee, shoulder and elbow, these torsional loads are present in lower magnitudes than at the hip (Guerra, 2004; Kutzner *et al.*, 2010; Westerhoff *et al.*, 2009), but can increase during strenuous joint activity.

In addition to torsional loading, all joints are exposed to axial loads (*i.e.*, tensile and compressive forces) which act along the length of the implant stem (Figure 1.4). At the lower limb joints such as the hip and knee, compressive loads are apparent due to the weight bearing nature of the joint. At the hip, these loads can be up to 2000 N during normal gait (Bergmann *et al.*, 2001, 1993), and up to 7000 N during stumbling (Bergmann *et al.*, 2004). At the tibial component of the knee joint, compressive forces of up to 3000 N have been recorded for daily activities (Kutzner *et al.*, 2010). Upper limb joints such as the elbow and shoulder experience similar compressive loads, despite being considered non-weight bearing joints (Amis, 2012; Amis *et al.*, 1980; Bergmann *et al.*, 2007; Johnson and King, 2005). For the shoulder joint, a force of one times body weight is generated across the glenohumeral joint during 90° of shoulder abduction, and up to 2.5 times body weight when lifting a weight of approximately 50 N (Bergmann, 1987). Similarly, during 90° elbow flexion carrying a weight, the compressive force at the ulnohumeral joint can be up to six times the external load at the hand, and even higher during elbow extension (Amis, 2012; Amis *et al.*, 1980). It is important to note that in addition to compressive forces at the replaced ulnohumeral joint, tensile forces may also be apparent. These tensile forces act along the length of the unlar component of linked elbow prostheses during elbow hyperflexion. The effect of these forces may also be

exaggerated when impingement occurs between bony structures or cement, and the anterior flange of the implant, further creating distraction forces along the length of the ulnar component (Cheung and O'Driscoll, 2007).

Bending loads applied to implant occur as a result of forces acting perpendicular to the longitudinal axis of the implant (*i.e.*,  $F_x$ ,  $F_y$  of Figure 1.4). These forces, although smaller than those axially, have been reported to be approximately 0.5 times body weight at the hip and shoulder during routine activities (Bergmann *et al.*, 2007, 2001). At the elbow and knee, these forces were shown to be lower in magnitude (Guerra, 2004; Kutzner *et al.*, 2010).

Taking into consideration the various types and magnitudes of loads that occur at the joint, it is necessary to assess the ability of implanted systems to withstand these loads, in order to determine the overall success of joint replacement systems.

## 1.2 STEM LOOSENING

Although cemented replacement systems have been a successful treatment option, stem loosening is the most common method of implant failure (Australian Orthopaedic Association, 2010; New Zealand Orthopaedic Association, 2010). Stem loosening occurs when there is disruption to the mechanical connection at the stem-cement interface, as a result of continuous loading that occurs at the joint, which is transferred to the fixation interface. There are a variety of factors that can contribute to stem loosening such as patient profile, surgical technique, and implant stem design (Barrack, 2000; Harris and Tarr, 1979; Rodriguez-Gonzalez, 2009). Stem design, in particular, can be explored by biomechanical analysis.



### 1.2.1 STEM DESIGN

Stem design is important for ensuring adequate implant fixation and mechanical stability to the implant system (Barrack, 2000; Mohler *et al.*, 1995; Scheerlinck and Casteleyn, 2006). Since the stem undergoes a mechanical connection with the cement during fixation, altering its design to improve that connection can play a key role in stem stability, and resistance to stem loosening.

#### 1.2.1.1 STEM SHAPE AND LENGTH

Stem shape is one factor of stem design that can contribute to the mechanical stability of the implant system. Over the years, many studies have investigated the role of stem shape on implant stability, and proposed shape designs that are specific to joint type and loading (Einsiedel *et al.*, 2008; Evans *et al.*, 1988; Huiskes *et al.*, 1998; Kedgley *et al.*, 2007; Olofsson *et al.*, 2006; Westphal *et al.*, 2006). Stem cross-sectional shape and curvature are two examples of stem shape that have been proposed to provide implant stability under torsional loading (Berzins *et al.*, 1993; Callaghan *et al.*, 1992; Crowninshield *et al.*, 2006; Hosein *et al.*, 2012; Kedgley *et al.*, 2007). With regards to cross-sectional shape, it has been explained that stems with longer edges provided the greatest stability under torsional loading (Kedgley *et al.*, 2007). Likewise, the longitudinal curvature of stem can work to improve the torsional stability of the implant (Berzins *et al.*, 1993; Callaghan *et al.*, 1992), however, this may be dependent on the degree of stem curvature (Hosein *et al.*, 2012).

Stem length is another factor that is important in the design of implants. The length of the implant stem can influence the load transfer to the cement and bone. A study by Mann *et al.*, demonstrated that shorter stems contributed to higher cement mantle stresses, which can result in cement damage and initiation of implant loosening (Mann *et al.*, 1997). With regards to interface fixation, the length of the stem may also affect implant stability, where a longer stem increases the length of the fixation interface, thereby increasing the stem-cement connect, and improving initial implant stability.

However, this is often at the expense of decreased stresses to bone, which may ultimately lead to bone loss around the implant and subsequent loosening through the process known as stress shielding (Austman *et al.*, 2007).

### 1.2.1.2 STEM SURFACE MODIFICATION

In addition to the stem's shape and length, stem surface modifications such as surface finish and surface treatments can also play a role in stabilization of cemented implant systems. Stem surface finishes have been investigated in cemented implant designs with the premise that a roughened surface would contribute frictional resistance to interface loading (Davies and Harris, 1993; Huiskes *et al.*, 1998; Jamali *et al.*, 2006). Likewise, implant surface treatments are used with some cemented stem designs (Van der Lugt and Rozing, 2004) to accommodate infiltration of bone cement onto the textured stem surface, providing improved fixation and stability (Jeon *et al.*, 2012). Both methods are aimed at providing mechanical resistance to loading at the stem-cement interface.

#### 1.2.1.2.1 STEM SURFACE FINISH

The role of stem surface finishes in implant stability has been described based on their surface characteristics. These characteristics include the stem's average surface roughness ( $R_a$ ), and mean roughness depth ( $R_z$ ). The  $R_a$  value is the arithmetic average of all departures from the center line of the roughness profile, the center line being located where the area of the roughness profiles above and below are equal (Crowninshield, 1998). The  $R_z$  is the mean of the depths (highest peak to lowest valley) of five consecutive sample lengths within the roughness profile.  $R_a$  values are, however, more commonly used to describe implant surfaces. A review by Verdonschot classified implant surfaces based on these values; smooth ( $R_a < 1 \mu\text{m}$ ), matte ( $R_a < 2 \mu\text{m}$ ), and rough surfaces ( $R_a > 2 \mu\text{m}$ ) (Verdonschot, 2005).

Although rougher surface finished implants have been shown to increase interface strength due to their frictional resistance to loading, additional studies have argued that the micro-roughened surfaces of the implant stem also contributed to abrasion and fretting at the stem-cement interface (Beksac *et al.*, 2006; Crowninshield *et al.*, 1998; Hinrichs *et al.*, 2003; Mohler *et al.*, 1995). Interface abrasion would ultimately promote the onset of loosening, in addition to causing concern for the patient as a result of the accumulation of cement and/or metal debris at the replaced joint. As such, there has been mixed reviews regarding the use of surface finished stems in cemented implant systems.

#### 1.2.1.2.2 STEM SURFACE TREATMENT

In comparison to surface finishes, stem surface treatment is the alteration of the surface topography of the implant stem. Surface treatments can involve the addition of material (*i.e.*, plasma spray and sintered beads), or removal of material (*i.e.*, machined surface patterns) from the implant stem surface. Both methods change the surface profile of the stem, accommodating infiltration of bone cement onto the stem surface.

Surface treatments such as plasma spray and sintered beads involve the addition of porous metal coatings onto the implant stem (Bundy and Penn, 1987; Glass and Pierfrancesco, 2011; Ryan *et al.*, 2006). Initially, surface treatments were incorporated into non-cemented implant designs to allow for bony ingrowth, however, within recent years, cemented elbow implant designs have incorporated surface treatments to enhance the mechanical interlock between the stem and cement (Evans *et al.*, 1988; Skytta *et al.*, 2009; van der Lugt and Rozing, 2004) (Figure 1.5). The type of surface treatment, along with its fabrication process, can dictate the porosity of the stem's surface to allow for infiltration of bone cement.

#### 1.2.1.2.2.1 PLASMA SPRAY FABRICATION

Plasma spraying is a surface treatment used to create macro-roughened surface textures on implant stems. The roughness value ( $R_a$ ) associated with plasma spray treatments, however, are greater than those defined by Verdonschot *et al.*, to describe micro-roughened surfaces (Verdonschot, 2005).

During the plasma spraying process, an electric arc is generated by a high voltage discharge, and formed between two water-cooled electrodes (see Davis, 2003). The electric arc heats plasma gas flowing through the electrodes to extreme temperatures, as high as 22000 °C, partially ionizing the gas to form plasma. The powder used for coating the implant surface is introduced into the plasma gas stream using a carrier gas, and the mixture is accelerated at high speeds onto the stem substrate material (Figure 1.6). The degree of roughness of the coating can be varied by adjusting the spraying parameters of the process (Ryan *et al.*, 2006). For application of titanium plasma spray coatings, controlled atmospheric plasma spray (CAPS) or vacuum plasma spray (VPS) are used. Titanium is extremely sensitive to oxidization in high temperature environments, and as such, the CAPS units applies the coating in a positive pressure inert atmosphere, while the VPS unit applies the coating in controlled low vacuum pressure (Glass and Pierfrancesco, 2011). The plasma spray coatings prepared with this method result in irregular pores that facilitate a mechanical connect between the stem surface and bone cement during implant fixation.

#### 1.2.1.2.2.2 SINTERED BEAD FABRICATION

Another method for creating roughened stem surfaces is the attachment of bead particles to the stem surface, thereby creating a porous network through which bone cement can fill the spaces. Sintered bead coatings are applied to implant stem by a process that involves binding and sintering metal beads onto the stem surface (Davis, 2003; Ryan *et al.*, 2006). A binder is first used to attach the metal beads to the stem

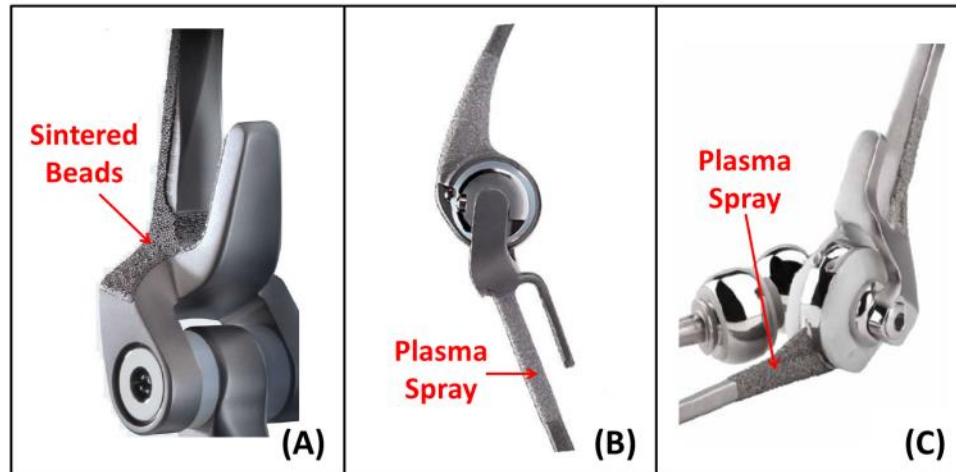


**Figure 1.5: Stem Surface Treatments used in Cemented Elbow Systems**

Three commercially available elbow systems that incorporate stem surface treatments onto their cemented implant designs. (A) Coonrad/Morrey I Total Elbow (Zimmer) with sintered beads on a titanium substrate ([www.zimmer.com](http://www.zimmer.com)), (B) Discovery Elbow System (Biomet) with plasma spray on a titanium substrate ([www.biomet.com](http://www.biomet.com)), and (C) Latitude<sup>®</sup> EV Total Elbow (Tornier) with plasma spray on a cobalt chrome substrate ([www.tornier-us.com](http://www.tornier-us.com)).

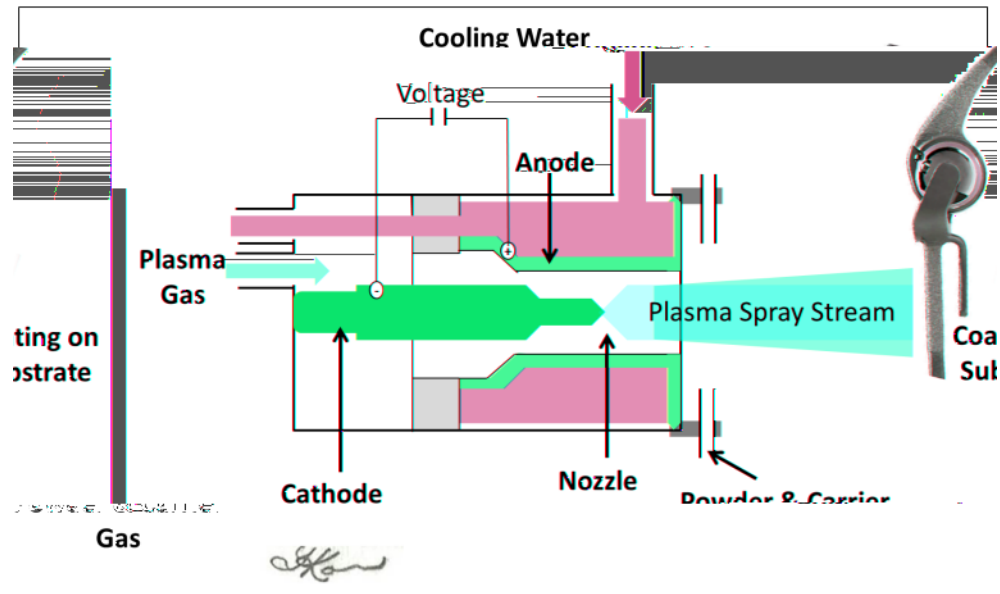


**Figure 1.6: Schematic of the Plasma Spray Process**

An electric arc is generated by a high voltage discharge formed between the cathode and anode within the chamber. This arc heats the plasma gas flowing into the chamber, partially ionizing the gas to form plasma. The titanium powder used for coating the implant is incorporated into the plasma gas stream, and the mixture is accelerated at high speeds onto the stem substrate. (Image of implant: *Discovery Elbow System (Biomet)*; [www.biomet.com](http://www.biomet.com).)

substrate material. The attached beads are then sintered at high temperatures in a high vacuum oven, where the binder is vaporized, and the beads are diffused onto the stem substrate material, as well as with each other. The sintering process generally involves heating the implant stem to one half times the melting point of the metal alloy, to allow for diffusion of the beads to the stem surface and one another (Davis, 2003) (Figure 1.7). Typically, the same stem substrate metal is needed to make the beads that will be sintered to the stem surface (*i.e.*, cobalt chrome beads on cobalt chrome stem, or titanium beads on titanium stems). The volume fraction of sintered bead surfaces can be altered by changing the bead size as well as the number of layers of bead coating on the stem. It can be controlled by variables such as compacted powder density, sintering temperature and time, and alloy additions (Ryan *et al.*, 2006). The pore size, morphology, distribution of the beads, and the inter particle neck size can all have a major impact on the mechanical properties of the resulting coating (Davis, 2003; Ryan *et al.*, 2006).

### 1.2.2 STEM SUBSTRATE MATERIAL

Implant stems utilize metal alloys as their base substrate material (Korkusuz and Korkusuz, 2004; Navarro *et al.*, 2008), with the goal of providing a suitable material replacement for the resected bone. Commonly used metals include iron-based, cobalt-based and titanium-based alloys. These alloys are chosen based on their biocompatibility, strength, wear, and corrosion characteristics. Within recent years, however, the use of iron-based alloys in stem design has been restricted because of inferior mechanical and corrosion properties compared to cobalt-based and titanium-based alloys (Navarro *et al.*, 2008).

Cobalt-based alloys are useful as an orthopaedic implant material due to their high fatigue strength, and high ultimate tensile strength, which make them suitable for their longevity and ability to resist fracture (Buechel *et al.*, 2012; Korkusuz and Korkusuz, 2004; Navarro *et al.*, 2008). With regards to its biocompatibility, the addition of chromium is known to inhibit corrosion (Rodriguez-Gonzalez, 2009), and have also

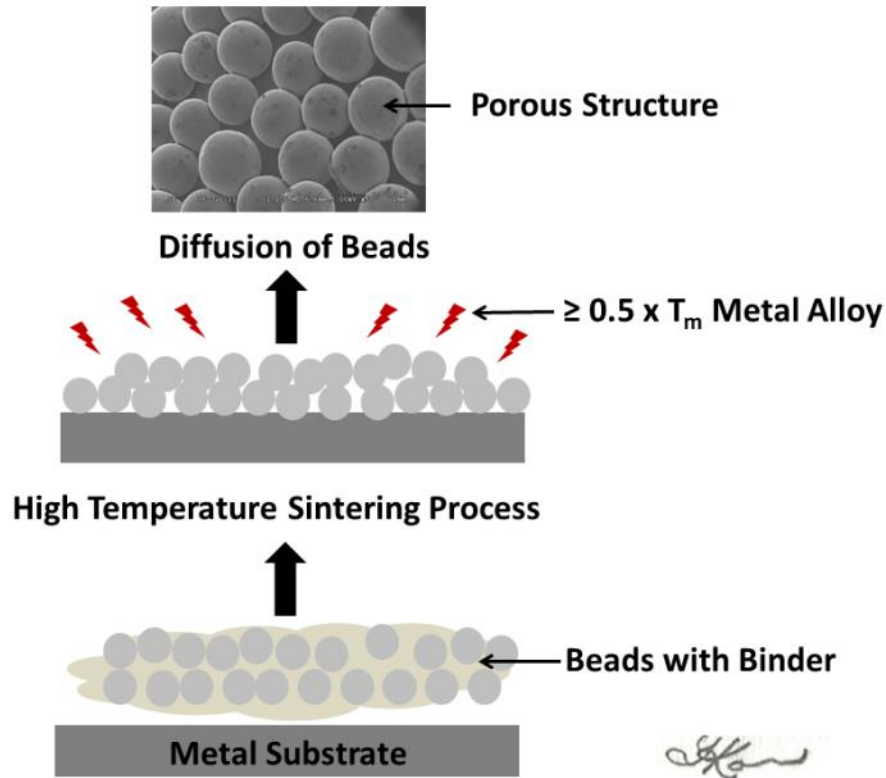


**Figure 1.7: Schematic of the Sintering Process**

Sintered bead coatings are applied to the stem in a process that involves both binding and sintering the metal beads to the stem's surface. A binder is incorporated with the beads to hold the particles together, while high temperatures are used to diffuse the beads onto the stem surface, and with one another. Temperatures used for sintering are at least one half times the melting temperature of the metal alloy. The resultant coating is a porous structure, through which bone and cement can fill the spaces (Note: Picture at the top is from an SEM scan at x50 magnification.)



shown good resistance to wear (Navarro *et al.*, 2008). In addition, the introduction of small quantities of molybdenum and tungsten has also been used to harden the cobalt chrome alloys (Rodriguez-Gonzalez, 2009).

Titanium-based alloys were introduced into stem design because of their low density, moderate elastic modulus, and good corrosion resistance, which made them biocompatible to the surrounding environment (Hallab *et al.*, 2004; Navarro *et al.*, 2008). The corrosion resistant nature of titanium is due to an oxide layer that is formed on the surface, which acts as a protective barrier to corrosion of the material substrate beneath it. Although titanium is known to exhibit poor shear strength and wear resistant properties, the addition of aluminum and vanadium in orthopaedic applications improves the mechanical properties of the metal alloy (Navarro *et al.*, 2008; Rodriguez-Gonzalez, 2009).

However, there has been much debate between the choices of titanium or cobalt chrome stem material. Within recent years, titanium has been a controversial material for use with femoral cemented stem designs, since it has been reported to experience increased rates of loosening, as well as high sensitivity to corrosion (Boyer *et al.*, 2009; Maurer *et al.*, 2001; Thomas *et al.*, 2004; Willert *et al.*, 1996). It is thought that micromotion of the stem within the cement leads to abrasion of the titanium protective oxidized layer, resulting in exposure and gradual corrosion of the base titanium material over time (Hallam *et al.*, 2004). In contrast, non-cemented titanium femoral stems are believed to be less prone to corrosion because oxygen is readily available from the surrounding bone, allowing for a stable oxide-layer to re-accumulate on the surface of the titanium stem (Willert *et al.*, 1996). Despite mixed reviews about the use of cemented titanium in femoral implants, it is still commonly employed in cemented upper-limb implant applications (Van der Lugt and Rozing, 2004).

### 1.3 IMPLANT STABILITY

Implant stability is a term used to describe the ability of a joint replacement system to resist movement and loosening. In the case of cemented implants, stability can be measured (in part) by quantifying the displacement, or micromotion of the implant stem relative to the surrounding cement.

A stable implant system incorporates a stem design that utilizes optimal geometry, surface mechanics, and material properties that facilitate transmission of loads to the surrounding cement and bone, without creating damaging stresses and excessive stem motion (Scheerlinck and Casteleyn, 2006). To achieve stability of implant systems, two methods of implant design are explored to ensure mechanical longevity over repeated loading; force-closed and shape-closed designs (Huiskes *et al.*, 1998).

Force closed systems, such as straight, polished stem designs, are aimed to allow initial stem subsidence during interface loading (Huiskes *et al.*, 1998). Subsidence of the implant stem after interface debonding generates frictional forces at the stem-cement interface, which balances the applied load. This equilibrium of forces at the interface, therefore, creates a stable implant condition. In comparison, shape-closed systems such as longitudinally curved and non-circular cross section stems, as well as modified stem surface designs (*i.e.*, surface treatments and finishes), take into consideration initial stability of the implant system. This is done by ensuring a well fixed stem-cement system during fixation, so that migration of the stem does not occur. This method aims to guarantee no motion at the stem interface, therefore preventing the initiation of loosening (Huiskes *et al.*, 1998). Although some force closed systems have been successful for particular joint replacement designs, this thesis will focus on shape closed systems with a particular interest in surface treatments.

### 1.3.1 IMPLANT STABILITY MEASUREMENTS *IN-VITRO*

Clinically, implant migration is observed from radiographic analysis of the stem-cement interface, particularly regions of radiolucency surrounding the implant stem (Chambers *et al.*, 2001), with regions greater than 1 mm indicative of definite loosening (Banaszkiewicz, 2009b). Experimentally, there are a variety of tools used to measure implant micromotion.

Linear variable differential transducers (LVDT's) are used to measure displacement of the implant stems *in-vitro*. By drilling window holes through the bone and/or cement mantle, the LVDT or pins connected to the LVDT, can be inserted through the holes to be in direct contact with the implant stem (DiSilvestro *et al.*, 2004; Doehring *et al.*, 1999; Engh *et al.*, 1992; Maher *et al.*, 2001). Once there is displacement of the stem, this is recorded by the LVDT as a voltage change and resulting micromotion measurement. This technique has proven useful, however, the method is invasive and LVDT's are specific to measuring linear displacement only, so therefore not very effective when rotational motion is of interest.

Radiostereophotogrammetric analysis is another method used for implant displacement measurement both *in-vivo* and *in-vitro*. Metal bead markers are placed onto the bone, cement and implant during the replacement procedure, and motion at the interfaces can be measured from stereoradiograph images taken before and after loading (Nilsson *et al.*, 1991). Although this method offers information about motion occurring at the interface, it can only measure displacement of the implant once loading is complete. This can be problematic for studies interested in investigating how loading affects micromotion in real time.

Another technique incorporates the use of an optical system with reflective markers to observe motion of the implant relative to the bone (Westphal *et al.*, 2006). Markers are placed on the implant and bone, and cameras are used to track the motion of the markers throughout mechanical tests. The software associated with optical systems can then determine the relative distances of the implant and bone markers, to obtain measurements of implant stability. This method, however, may not be suitable for

measuring motion at the level of the stem cement-cement interface, since optical markers associated with these systems may be limited by the size and volume restrictions at the cemented interface.

More recently, stability studies done by Mann *et al.*, and Race *et al.*, discussed digital image correlation (DIC) as a method for measuring micromotion at the stem-cement and cement-bone interfaces (Mann *et al.*, 2010; Race *et al.*, 2010). This method involved using a camera with telecentric lens, and custom written software to document motion occurring at the stem, cement and bone interfaces during torsional loading of transverse sections of the implanted stem. The optical system (*i.e.*, camera and telecentric lens) recorded video of the interfaces during mechanical loading, and the software program measured relative displacement of sampling locations placed on either side of the interfaces. While this methodology was only useful for detecting interface motion of sectioned implant stems during torsional loading, the optical system served as an imaging modality for observing the interfaces. As such, a similar system could be adapted for use in future interface stability studies with careful selection of the required optical components (see below).

## 1.4 OPTICAL SYSTEMS

As mentioned previously, optical systems can be useful as a tool for measuring interface motion. Depending on the environment of implant testing, as well as the resolution of the intended measurement, the hardware and software components of the optical system can be carefully chosen to ensure best optical system design. While the software components are specific to the optical system, the hardware components are generally standard, and include a camera system (*i.e.*, camera with lens) and source of illumination (Relf, 2004).

### 1.4.1 CAMERA SYSTEMS

Like all digital based cameras, those used in optical systems operate on a principle, where reflected light from the object being imaged enters the camera through the lens, and is focused and transmitted to the camera sensor (Figure 1.8) (Relf, 2004). The camera's sensor is made up of an array of sensors called pixel elements (*i.e.*, pixels), which act as sites for the collection of the transmitted light. One type of sensor used in cameras is known as a charged couple device (CCD), where the collected light photons in each of the sensors are converted to electric charges (Relf, 2004). The produced charge is directly proportional to the number of light photons that hit the sensor. The charge is then converted to voltage that is read by a digital converter as a range of integers, which represents the location and brightness value for each element of the sensor array. These brightness values can range between 0–255 in the red, green and blue channels that make up the image's color (Nakamura, 2005).

The camera system's resolution is the measure of detail that can be discerned in an image (see Relf, 2004) (Figure 1.8). For measurement applications, the resolution of the camera system should be appropriate in order to detect changes in the image. Camera system resolution is influenced by its sensor pixel size, in addition to the characteristics of the lens (Nakamura, 2005). For a good system resolution, the lens must be compatible with the sensor, facilitating optimal diffraction of light relative to the sensor's pixel size. This characteristic of the lens is controlled by its f-number, which is a ratio of the lens focal length to the diameter of its aperture (Relf, 2004).

In addition to the system resolution, the characteristics of the lens also influence the magnification changes with working distance (Figure 1.8). Typical lenses show greater magnification for shorter working distances (*i.e.*, the object is closer to the lens). This is not useful for optical measurement systems, since it gives a false representation of object sizes in the image's field of view. As such, telecentric lens have been introduced to mitigate the dependency of object distance on image magnification, by controlling the path of the rays entering the optical system.

With a telecentric lens, the magnification of the object is independent of working distance, providing the object stays within the lens' depth of field (see Relf, 2004) (Figure 1.8). Telecentric lens are designed with specific features in order to limit the type of rays entering the optical system. Only light rays that are parallel to the main axis, or have a principle angle of zero, are collected by the lens. For a conventional lens, this principle ray angle can be quite large depending on the distance of the object from the lens, resulting in large changes in image magnification (Figure 1.9). However, by limiting the size of the principle angle, the magnification errors can be reduced. In addition to magnification control, high quality telecentric lens show low degrees of image distortion and reduced perspective errors.

#### 1.4.2 ILLUMINATION

The source of illumination is another important hardware component of the optical system. The basis of optical systems depends on the harvesting of light to form images. In particular, the harvesting of light for optical systems used in experimental design needs to be of a controlled nature, to reduce effects of variability in resulting image measurements (Relf, 2004). By determining an appropriate source of illumination for a particular optical system, light rays can be controlled to fall within the image's field of view, reducing the effects of glare.

When choosing an appropriate light source, the type of reflection expected from the object needs to be considered. There are two main types of reflections expected; specular and diffuse (Relf, 2004). Specular reflection is bright, and occurs in a single direction, such as the reflection from smooth, shiny surfaces. This type of reflection is variable because it disappears with change in positioning of the illuminator or object. Specular surfaces are best lit with diffused illumination, which allows optical imaging without bright reflections. In comparison, diffuse reflection is quite faint but not variable, and occurs in many directions. Reflection from rough or textured surfaces is an example of diffuse reflection.

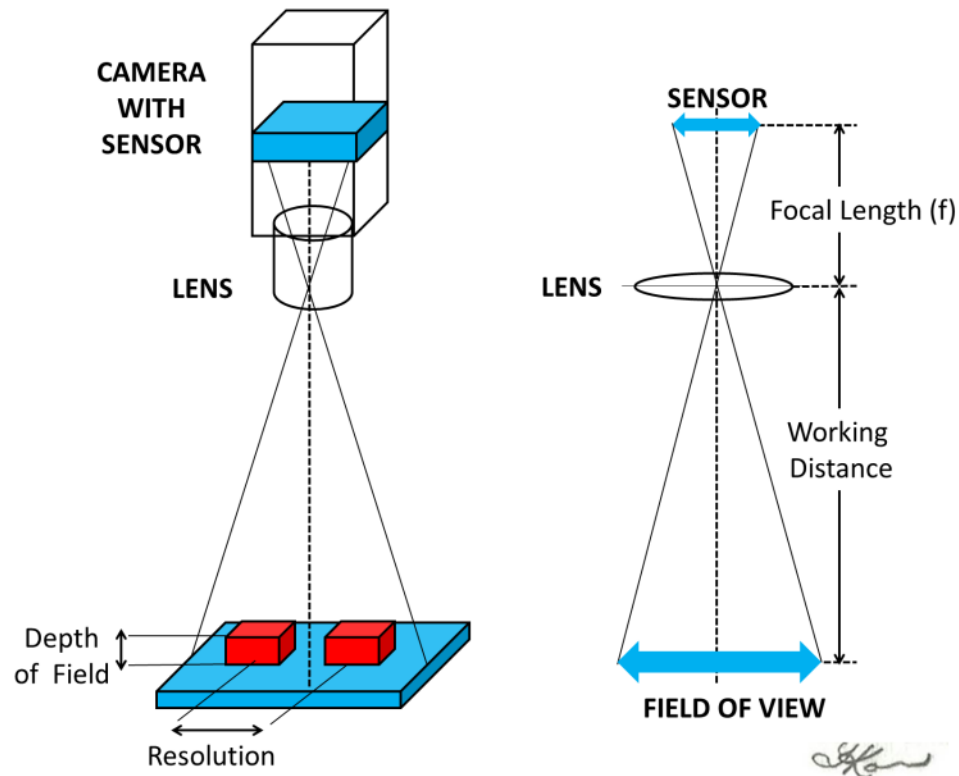


**Figure 1.8: Schematic of a Typical Camera System**

The optical system consists of a lens positioned at a working distance from the object being imaged, through which reflected light is focused onto the camera sensor, and produces a resultant image. The distance between the lens and the camera sensor is a measure of the focal length ( $f$ ). The overall size of object space is known as the Field of View (FOV). For any two objects located within this field of view, the resolution of the camera system dictates how far apart the objects can be, and still be perceived as individual entities. The depth of field represents the range of the working distance in which the objects are in focus.

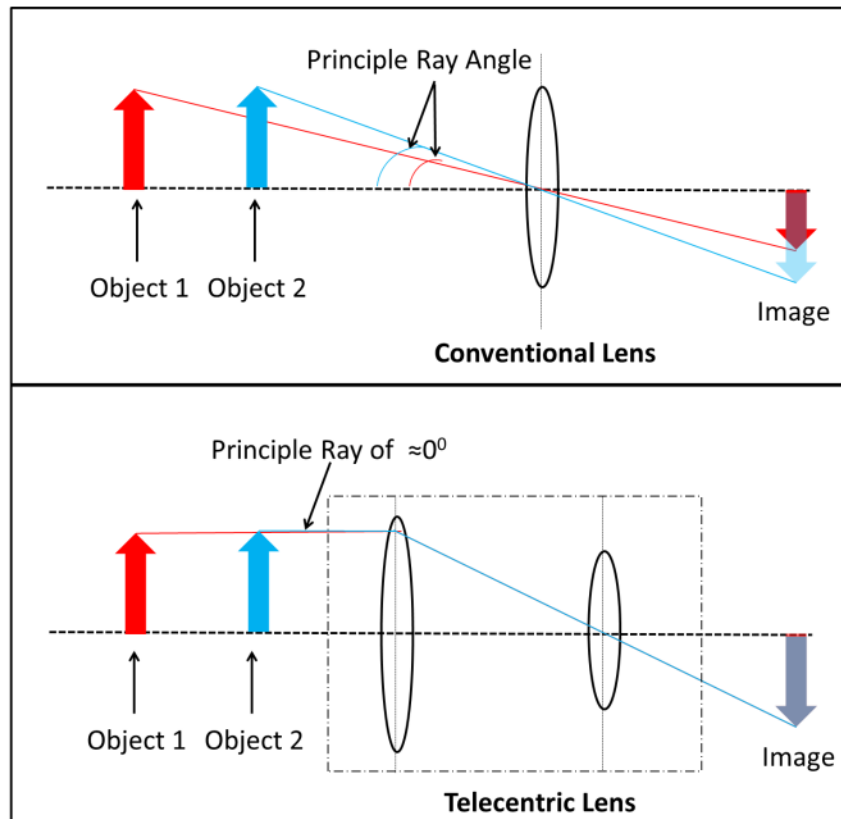


**Figure 1.9: Schematic of a Conventional Lens versus Telecentric Lens**

For a conventional lens, the magnification of the image is dictated by the distance of the object from the lens. An object situated close to the lens would appear larger due to the larger angle of the principle ray entering the lens. In comparison, a telecentric lens limits the type of rays entering the lens, filtering only the light rays that are parallel to the main axis. As a result, the principle rays are maintained at angles close to  $0^\circ$ , producing an image with magnification independent of the objects' distance from the lens.



## 1.5 COMPUTED TOMOGRAPHY (CT) IMAGING

Computed tomography (CT) has been used in the field of orthopaedics as a tool for studying bones and joints in a three-dimensional space. In particular, CT imaging has been used to investigate fracture biomechanics of joints, as well as joint contact mechanics (Greenspan, 2011; Lalone, 2012). With regards to the biomechanics of joint replacement systems, CT analysis has been less popular due to the sensitivity of the system to metal artifacts. Metal artifacts can produce bands or streaks across the image, causing loss of visualization, as well as image data. The effect that metal has on CT images can be explained by the operations of the CT system.

CT systems work on the basis of x-ray imaging, where x-rays emitted from a source interact with an object, and results in absorbance, scatter, and transmission of rays (Stock, 2009). With CT imaging, the source produces a narrow, fan-shaped beam of x-rays which rotate around the object being imaged, and detectors on the exit side of the object receive the transmitted rays. During one rotation of the source, multiple x-rays are transmitted through the object at various angles. Depending on the density value of the object being irradiated, the amount of x-rays absorbed or scattered varies, causing reduced intensity (*i.e.*, attenuation) of the transmitted rays. The attenuation is measured by the ratio of absorbed or scattered rays per unit thickness of the object, and this value is used to determine the corresponding Hounsfield Unit (HU) or CT number of the object. The attenuated rays collected by the detector are represented as individual images at the various angles of x-ray projection, which are stitched together to create a cross-sectional image of the object. When the object is translated through the rotating x-ray source, multiple cross-sectional images are collected along the translational length, and are used to create a three-dimensional model of the object being imaged.

With regards to metals, however, the density values and resulting CT numbers are beyond the normal range that can be handled by the CT software, causing incomplete attenuation profiles and resulting metal artifacts (Barrett and Keat, 2004). Metal artifacts are more prominent in higher atomic number metals such as stainless steel and cobalt alloys, but are less prominent with lower atomic number metals such as titanium (Boas

and Fleischmann, 2012). CT imaging is more likely to be affected by metal artifacts compared to conventional radiographs due to the larger number of detector measurements obtained in a single scan (Barrett and Keat, 2004). However, techniques have been proposed to reduce metal artifacts in CT images (Boas and Fleischmann, 2011; Olsen *et al.*, 2000; Wang *et al.*, 2000).

In addition to artifact limitations of joint replacement systems in CT imaging, resolution of the CT system has not been useful for the study of joint replacement biomechanics. Conventional CT scanners provide a resolution on the order of 1–2 mm (Kalender, 1995), however, instability of implant systems is detected by micromotion occurring at the stem-cement interface. This can potentially be overcome through the use of micro-computed tomography ( $\mu$ CT). As a high resolution CT technology, voxel sizes of  $\mu$ -CT systems can vary between 50–250  $\mu$ m, depending on the manufacturer and specifications (Stock, 2009).  $\mu$ -CT systems differ from conventional systems with regards to their smaller field-of-view, as well as higher resolution detector. These changes allow for more detailed models of micro-architecture. As such,  $\mu$ -CT analysis has been used orthopaedics to quantify implant wear (Bowden *et al.*, 2005; Teeter, 2012), as well as for the analysis of bone micro-architecture (Waarsing *et al.*, 2005). However, its use in joint replacement biomechanics has not been well-established. With new methods being developed to improve on metal artifact limitations,  $\mu$ -CT imaging may prove useful as a tool for assessing implant loosening micromechanics at the stem-cement interface.

## 1.6 STUDY RATIONALE

The prevalence of joint replacement surgeries has increased over the last decade, and numbers are expected to continue to increase as a result of the treatment of musculoskeletal conditions (degenerative joint diseases and joint injury) with the aging of the baby boomer population (Kurtz *et al.*, 2009; Perruccio *et al.*, 2006). Within recent

years, joint replacement surgeries alone accounted for 25% of all orthopedic surgeries in Ontario (Canizares *et al.*, 2009).

This demand for joint replacement surgery, however, is not limited to the older population, with reports showing an increase in total joint replacements performed on younger patients or patients less than 65 years old (Kurtz *et al.*, 2009). In addition, because of increasing rates of obesity, arthritis and expanded clinical criteria for eligibility, the need for joint replacement surgery has become overwhelming (Gelber *et al.*, 1999; Karlson *et al.*, 2003).

The rise in popularity for primary joint replacement surgeries is also expected to trigger the increase in revision joint replacement surgeries. Although joint replacements are successful, failure of the replacement systems can result in revision surgeries (Clohisy *et al.*, 2004). Taking this into consideration, it seems necessary to explore ways of improving the longevity of these implant systems.

This may be realized, in part, through the alteration in the design of implant stems. Stem surface modification is an example of stem design that can contribute to reducing the onset of implant loosening. Stem surface finish has been explored for improving cemented implant stability (Datir *et al.*, 2006; Huiskes *et al.*, 1998; Jamali *et al.*, 2006), however, the use of stem surface treatments with cemented implants is one area of stem design that has not been widely investigated. A clinical study by Jeon *et al.*, addressed the success of surface treated stems (*i.e.*, plasma sprayed and beaded) on the survival rates of cemented elbow systems (Jeon *et al.*, 2012), but there are no known experimental studies that have assessed these surface treatments for improved implant stability. While these treatments are currently only employed with cemented upper limb replacement designs, knowledge regarding their stability response could also be applied to the design of other joint replacement systems.

Titanium and cobalt chrome are two common metals used in implant stem design (Korkusuz and Korkusuz, 2004; Navarro *et al.*, 2008). However, there has been varied clinical success with the use of titanium and cobalt chrome stem substrate materials with surface treated implants, where increased rates of fracture have been reported for sintered

bead treatments on titanium components (Athwal and Morrey, 2006; Jeon *et al.*, 2012). In addition to the variability with surface treated stems, there has also been mixed reviews over the use of cemented titanium stems in lower limb joint. In particular, studies have reported increased rates of loosening, and high sensitivity to corrosion, associated with the femoral component at the hip joint (Hallam *et al.*, 2004; Schweizer *et al.*, 2005). Despite these varied clinical outcomes with titanium stems, they are still commonly used in upper limb joints (Van der Lugt and Rozing, 2004), and as such, are important to consider in stability studies of cemented implant systems.

The stability of implant systems is directly affected by joint loading. Joint loads acting on the implant are transmitted to the stem-cement interface. If the fixation strength at the interface is less than that of the acting loads, the stem can experience debonding and eventual loosening. Therefore, it is necessary to explore the effects of joint loading in implant stability studies.

Taking these factors into consideration, the overall goal of this thesis was to determine the role of stem surface treatment and substrate material on the stem-cement interface stability of implanted stems under various loading modes. Studies presented within this thesis focused on surface treatments used clinically with upper limb replacement systems; however, their role in cemented implant stability was analyzed for generic joint replacement applications, as well as elbow specific components. With the knowledge gained from this research, it is expected that improvements can be made to the surface design of current implant stems. Improved implant stem design will enhance the longevity of implant systems by enhancing the stem's function as an implant stabilizer, thus reducing the implant's rate of loosening. Ultimately, this will improve patient care by decreasing the chances of revision surgery after a joint replacement procedure, and consequently reduce the number of joint replacement surgeries, and subsequent costs to the healthcare system.

## 1.7 SPECIFIC OBJECTIVES AND HYPOTHESES

The specific objectives of this work were as follows, to:

1. develop and validate an optical tracking system to quantify stem-cement interface micromotion in stemmed implant components;
2. experimentally investigate the effect of stem surface treatment on the torsional stability of titanium and cobalt chrome stems;
3. compare the roles of stem surface treatment and substrate material on the stability of implant stem subjected to cyclic compressive loading;
4. determine the contribution of stem circumferential grooves to the stability of cemented stemmed joint replacement systems under compression and torsional loading;
5. compare the stability response of stem surface treatment and substrate material during the application of a bending moment; and
6. use  $\mu$ -CT imaging to visualize the stem-cement interface during bending, and thereby investigate the influence of bending loads on internal stem-cement interface motion.

The corresponding hypotheses were as follows:

1. A custom optical tracking system could be developed to quantify stem-cement interface motion, on the order of 5  $\mu$ m in stemmed implant systems, and this system could be used to non-invasively analyze interface motion.
2. Surface treated implant stems would provide improved torsional stability compared to smooth surfaces, with cobalt chrome stems showing less rotation in torsion than titanium stems, due to its higher shear modulus.

3. Smooth stems would provide the least resistance to cyclic compressive loading compared to the surface treated stems, and there would be no effect of stem material on implant stability under compression.
4. Application of circumferential grooves would not affect torsional stability of cemented stemmed joint replacement systems, but would have a stabilizing influence in compression.
5. Smooth stem surfaces would show greatest instability under bending, with titanium stems experiencing greater interface motion than cobalt chrome stems due to a lower flexural modulus of elasticity.
6. Micro-CT analysis of cemented stems would show that motion along the internal length of the stem-cement interface during bending is influenced by creep of the surrounding bone cement, causing the implant to experience tilting without apparent loosening.

## 1.8 THESIS OVERVIEW

This thesis is written in an integrated article format, with each of the above objectives corresponding to a chapter of the thesis.

Chapter 2 describes the development and validation of the optical tracking system used for measuring stem-cement interface micromotion in subsequent chapters of this thesis. The chapter outlines the resolution, accuracy and reliability of the tracking system to reproduce motion applied by a micrometer gauge.

Chapter 3 investigates the role of clinically relevant surface treatments (*i.e.*, smooth, beaded and plasma spray) on the torsional stability of titanium and cobalt chrome stems. The failure torques and interface stability were analyzed for each of the surface treated stems under simulated joint torsional loads.

Chapter 4 investigates the effect of stem surface treatments and material on the pistoning failure scenario of implant stems. Smooth, beaded and plasma spray surface treatments applied to cobalt chrome and titanium stems were compared for differences in interface strength and interface stability, under cyclic compression loads.

Chapter 5 investigates the effect of a new stem surface design, circumferential grooves, on the stability of cemented stems under compression and torsional loading. Applying the observations and results from Chapters 3 and 4, an alternate surface morphology was investigated to address the failure mechanisms associated with surface treated stems.

Chapter 6 investigates the effect of stem surface treatments and material on implant stability under bending loads. The interface motion for each of the surface treated stems was observed using the optical tracking system described in Chapter 2, and the contribution of the cement mantle in interface stability was addressed.

Chapter 7 uses  $\mu$ -CT imaging to visualize and quantify motion at the stem-cement interface with an applied bending moment. Based on the results from Chapter 6, it was determined that a technique to visualize internal stem- cement motion was needed to understand the contribution of bending moments to interface stability. Micro-CT measurements, made along the length of the stem-cement interface, were used to investigate the contribution of the stem and cement to interface motion during the application of real-time bending loads.

Chapter 8 is the concluding chapter of this thesis, and outlines the main findings of the individual studies detailed within this thesis, along with their strengths and limitations, as well as offers some suggestions for future work in the area of implant interface biomechanics.

## 1.9 REFERENCES

- Amis, A.A., 2012. Biomechanics of the Elbow. In: Stanley, D., Trail, I. (Eds.), *Operative Elbow Surgery*. Churchill Livingstone Elsevier, Edinburgh; New York, pp. 29–44.
- Amis, A.A., Dowson, D., Wright, V., 1980. Elbow joint force predictions for some strenuous isometric actions. *Journal of Biomechanics* 13, 765–775.
- Athwal, G.S., Morrey, B.F., 2006. Revision total elbow arthroplasty for prosthetic fractures. *The Journal of Bone and Joint Surgery; American Volume* 88, 2017–2026.
- Austman, R.L., Beaton, B.J., Quenneville, C.E., King, G.J., Gordon, K.D., Dunning, C.E., 2007. The effect of distal ulnar implant stem material and length on bone strains. *Journal of Hand Surgery* 32, 848–854.
- Australian Orthopaedic Association, T., 2010. National Joint Registry, Hip and Knee Arthroplasty Annual Report 2010, [http://www.dmac.adelaide.edu.au/aoanjrr/documents/aoanjrrreport\\_2010.pdf](http://www.dmac.adelaide.edu.au/aoanjrr/documents/aoanjrrreport_2010.pdf).
- Banaszkiewicz, P., 2009a. The basic science oral. In: Banaszkiwicz, P., Kader, D., Maffulli, N. (Eds.), *Graduate Orthopaedics*. Cambridge University Press, New York, pp. 514–516.
- Banaszkiewicz, P., 2009b. Hip oral core topics. In: Banaszkiwicz, P., Kader, D., Maffulli, N. (Eds.), *Postgraduate Orthopaedics*. Cambridge University Press, New York, pp. 155–193.
- Barrack, R.L., 2000. Early failure of modern cemented stems. *The Journal of Arthroplasty* 15, 1036–1050.
- Barrett, J., Keat, N., 2004. Artifacts in CT: Recognition and avoidance. *Radiographics* 1679–1691.
- Bauer, T.W., Schils, J., 1999. The pathology of total joint arthroplasty. I. Mechanisms of implant fixation. *Skeletal Radiology* 28, 423–432.



- Beksac, B., Taveras, N.A., Valle, A.G., Salvati, E.A., 2006. Surface finish mechanics explain different clinical survivorship of cemented femoral stems for total hip arthroplasty. *Journal of Long-term Effects of Medical Implants* 16, 407–422.
- Bergmann, G., 1987. Biomechanics and pathomechanics of the shoulder joint with reference to prosthetic joint replacement. In: Kolbel, R., Helbig, B., Blauth, W. (Eds.), *Shoulder Replacement*. Springer-Verlag, Berlin, pp. 33–43.
- Bergmann, G., Deuretzbacher, G., Heller, M., Graichen, F., Rohlmann, A., Strauss, J., Duda, G.N., 2001. Hip contact forces and gait patterns from routine activities. *Journal of Biomechanics* 34, 859–871.
- Bergmann, G., Graichen, F., Bender, A., Kääh, M., Rohlmann, A., Westerhoff, P., 2007. In vivo glenohumeral contact forces--measurements in the first patient 7 months postoperatively. *Journal of Biomechanics* 40, 2139–2149.
- Bergmann, G., Graichen, F., Rohlmann, A., 1993. Hip joint loading during walking and running, measured in two patients. *Journal of Biomechanics* 26, 969–990.
- Bergmann, G., Graichen, F., Rohlmann, A., 2004. Hip joint contact forces during stumbling. *Langenbecks Archives of Surgery* 389, 53–59.
- Berzins, A., Sumner, D.R., Andriacchi, T.P., Galante, J.O., 1993. Stem curvature and load angle influence the initial relative bone-implant motion of cementless femoral stems. *Journal of Orthopaedic Research* 11, 758–769.
- Boas, F., Fleischmann, D., 2011. Evaluation of two iterative techniques for reducing metal artifacts in computed tomography. *Radiology* 259, 894–902.
- Boas, F.E., Fleischmann, D., 2012. CT artifacts: causes and reduction techniques. *Imaging in Medicine* 4, 229–240.
- Bobyn, J.D., Pilliar, R.M., Cameron, H.U., Weatherly, G.C., 1980. The optimum pore size for the fixation of porous-surfaced metal implants by the ingrowth of bone. *Clinical Orthopaedics and Related Research* 150, 263–270.

- Bowden, a E., Kurtz, S.M., Edidin, a a, 2005. Validation of a micro-CT technique for measuring volumetric wear in retrieved acetabular liners. *Journal of Biomedical Materials Research. Part B, Applied Biomaterials* 75, 205–209.
- Boyer, P., Lazennec, J.Y., Poupon, J., Rousseau, M.A., Ravaud, P., Catonne, Y., 2009. Clinical and biological assessment of cemented titanium femoral stems: an 11-year experience. *International Orthopaedics* 33, 1209–1215.
- Brånemark, R., Brånemark, P.I., Rydevik, B., Myers, R.R., 2001. Osseointegration in skeletal reconstruction and rehabilitation: a review. *Journal of Rehabilitation Research and Development* 38, 175–181.
- Buechel, F.F., Pappas, M.J., SpringerLink, 2012. Properties of Materials in Orthopaedic Implant Systems. In: *Principles of Human Joint Replacement*. Springer Berlin Heidelberg, Berlin, Heidelberg, pp. 1–35.
- Bundy, K.J., Penn, R.W., 1987. The effect of surface preparation on metal/bone cement interfacial strength. *Journal of Biomedical Materials Research* 21, 773–805.
- Callaghan, J.J., Fulghum, C.S., Glisson, R.R., Stranne, S.K., 1992. The effect of femoral stem geometry on interface motion in uncemented porous-coated total hip prostheses. Comparison of straight-stem and curved-stem designs. *The Journal of Bone and Joint Surgery; American Volume* 74, 839–848.
- Canizares, M., MacKay, C., Davis, A.M., Mahomed, N., Badley, E.M., 2009. A population-based study of ambulatory and surgical services provided by orthopaedic surgeons for musculoskeletal conditions. *BMC Health Services Research* 9, 1–9.
- Chambers, I.R., Fender, D., McCaskie, a W., Reeves, B.C., Gregg, P.J., 2001. Radiological features predictive of aseptic loosening in cemented Charnley femoral stems. *The Journal of Bone and Joint Surgery; British Volume* 83, 838–842.
- Cheung, E. V, O’Driscoll, S.W., 2007. Total elbow prosthesis loosening caused by ulnar component pistoning. *The Journal of Bone and Joint Surgery; American Volume* 89, 1269–1274.

- Clohisy, J.C., Calvert, G., Tull, F., McDonald, D., Maloney, W.J., 2004. Reasons for revision hip surgery: a retrospective review. *Clinical Orthopaedics and Related Research* 429, 188–192.
- Crowninshield, R.D., Brand, R.A., Johnston, R.C., Milroy, J.C., 2006. The effect of femoral stem cross-sectional geometry on cement stresses in total hip reconstruction. *Clinical Orthopaedics and Related Research* 146, 71–77.
- Crowninshield, R.D., Jennings, J.D., Laurent, M.L., Maloney, W.J., 1998. Cemented femoral component surface finish mechanics. *Clinical Orthopaedics and Related Research* 355, 90–102.
- Dall, G.F., Simpson, P.M., Mackenzie, S.P., Breusch, S.J., 2007. Inter- and intra-batch variability in the handling characteristics and viscosity of commonly used antibiotic-loaded bone cements. *Acta Orthopaedica* 78, 412–420.
- Daly, C., Carey, G., Beverland, D.E., Orr, J.F., Dunne, N.J., 2004. Mixing of acrylic bone cement - Current theatre practices. In: 7th World Biomaterials Conference. Biomaterials 2004 Congress Managers, Sydney, p. 1465.
- Datir, S.P., Kurta, I.C., Wynn-Jones, C.H., 2006. Ten-year survivorship of rough-surfaced femoral stem with geometry similar to Charnley femoral stem. *The Journal of Arthroplasty* 21, 392–397.
- Davies, J.P., Harris, W.H., 1993. Strength of cement-metal interfaces in fatigue: comparison of smooth, porous and precoated specimens. *Clinical Materials* 12, 121–126.
- Davis, J.R., 2003. Coatings. In: *Handbook of Materials for Medical Devices*. ASM International, Materials Park, OH, pp. 179–194.
- DiSilvestro, M.R., Sherman, J.T., Dietz, T.L., 2004. A new position measurement system for micromasurements in orthopaedics. In: *Engineering in Medicine and Biology Society, 26th Annual Conference of the IEEE*. IEEE, San Francisco, pp. 2438–2441.

- Doehring, T.C., Rubash, H.E., Dore, D.E., 1999. Micromotion measurements with hip center and modular neck length alterations. *Clinical Orthopaedics and Related Research* 362, 230–239.
- Einsiedel, T., Gebhard, F., Bregolato, I., Hiemeier, A., Kinzl, L., Schultheiss, M., 2008. Proximal cement fixation in total hip arthroplasty--first results with a new stem design. *International Orthopaedics* 32, 295–306.
- Engh, C.A., Bobyn, J.D., 1988. The influence of stem size and extent of porous coating on femoral bone resorption after primary cementless hip arthroplasty. *Clinical Orthopaedics and Related Research* 231, 7–28.
- Engh, C.A., O'Connor, D., Jasty, M., McGovern, T.F., Bobyn, J.D., Harris, W.H., 1992. Quantification of implant micromotion, strain shielding, and bone resorption with porous-coated anatomic medullary locking femoral prostheses. *Clinical Orthopaedics and Related Research* 285, 13–29.
- Evans, B.G., Daniels, A.U., Serbousek, J.C., Mann, R.J., 1988. A comparison of the mechanical designs of articulating total elbow prostheses. *Clinical Materials* 3, 235–248.
- Geesink, R.G., De Groot, K., Klein, C.P., 1988. Bonding of bone to apatite-coated implants. *The Journal of Bone and Joint Surgery; British Volume* 70, 17–22.
- Geiger, M.H., Keating, E.M., Ritter, M.A., Ginther, J.A., Faris, P.M., Meding, J.B., 2001. The clinical significance of vacuum mixing bone cement. *Clinical Orthopaedics and Related Research* 382, 258–266.
- Gelber, A.C., Hochberg, M.C., Mead, L.A., Wang, N.Y., Wigley, F.M., Klag, M.J., 1999. Body mass index in young men and the risk of subsequent knee and hip osteoarthritis. *The American Journal of Medicine* 107, 542–548.
- Glass, L., Pierfrancesco, R., 2011. Macromanagement: Surface Manufacturing for Implants *Orthotec* 2, 4–8.

- Greenspan, A., 2011. Imaging Techniques in Orthopedics. In: McAllister, L., Barrett, K., Rampertab, R. (Eds.), *Orthopedic Imaging: A Practical Approach*. Lippincott Williams & Wilkins, Philadelphia, PA, pp. 17–38.
- Guerra, S.M., 2004. Design and development of a total elbow prosthesis to quantify ulnohumeral load transfer. (M.E.Sc Thesis) University of Western Ontario, pp 85-108.
- Hallab, N.J., Urban, R.M., Jacobs, J.J., 2004. Corrosion and Biocompatibility of Orthopedic Implants. In: Yaszemski, M., Trantolo, D., Lewandrowski, K., Hasirci, V., Altobelli, D., Wise, D. (Eds.), *Biomaterials in Orthopedics*. Marcel Dekker, Inc., New York, pp. 63–91.
- Hallam, P., Haddad, F., Cobb, J., 2004. Pain in the well-fixed, aseptic titanium hip replacement. The role of corrosion. *The Journal of Bone and Joint Surgery; British Volume* 86, 27–30.
- Hansen, D., Jensen, J.S., 1990. Prechilling and vacuum mixing not suitable for all bone cements. Handling characteristics and exotherms of bone cements. *The Journal of Arthroplasty* 5, 287–290.
- Harris, L.J., Tarr, R.R., 1979. Implant failures in orthopaedic surgery. *Biomaterials Medical Devices And Artificial Organs* 7, 243–255.
- Hernigou, P., Daltro, G., Lachaniette, C.H., Roussignol, X., Mukasa, M.M., Poignard, A., 2009. Fixation of the cemented stem: clinical relevance of the porosity and thickness of the cement mantle. *Open Orthopaedic Journal* 3, 8–13.
- Hinrichs, F., Kuhl, M., Boudriot, U., Griss, P., 2003. A comparative clinical outcome evaluation of smooth (10-13 year results) versus rough surface finish (5-8 year results) in an otherwise identically designed cemented titanium alloy stem. *Archives of Orthopaedic and Trauma Surgery* 123, 268–72.
- Hosein, Y.K., Clynick, M.P., McLachlin, S.D., King, G.J.W., Dunning, C.E., 2012. The effect of stem curvature on torsional stability of a generalized cemented joint

- replacement system. *Journal of Applied Biomaterials & Functional Materials* doi: 10.5301/JABFM.2012.9266.
- Huiskes, R., Verdonschot, N., Nivbrant, B., 1998. Migration, stem shape, and surface finish in cemented total hip arthroplasty. *Clinical Orthopaedics and Related Research* 355, 103–112.
- Iesaka, K., Jaffe, W., Kummer, F., 2004. Effects of the initial temperature of acrylic bone cement liquid monomer on the properties of the stem–cement interface and cement polymerization. *Journal of Biomedical Materials Research Part B, Applied Biomaterials* 68, 186–190.
- Incavo, S.J., Havener, T., Benson, E., McGrory, B.J., Coughlin, K.M., Beynnon, B.D., 2004. Efforts to improve cementless femoral stems in THR: 2- to 5-year follow-up of a high-offset femoral stem with distal stem modification (Secur-Fit Plus). *The Journal of Arthroplasty* 19, 61–67.
- Jamali, A.A., Lozynsky, A.J., Harris, W.H., 2006. The effect of surface finish and of vertical ribs on the stability of a cemented femoral stem: an in vitro stair climbing test. *The Journal of Arthroplasty* 21, 122–128.
- Janssen, D., Mann, K.A., Verdonschot, N., 2008. Micro-mechanical modeling of the cement-bone interface: the effect of friction, morphology and material properties on the micromechanical response. *Journal of Biomechanics* 41, 3158–3163.
- Jeon, I.H., Morrey, B.F., Sanchez-Sotelo, J., 2012. Ulnar component surface finish influenced the outcome of primary Coonrad-Morrey total elbow arthroplasty. *Journal of Shoulder and Elbow Surgery* 21, 1229–1235.
- Johnson, J.A., King, G.J.W., 2005. *Anatomy and Biomechanics of the Elbow*. In: Williams, G.R. (Ed.), *Shoulder and Elbow Arthroplasty*. Lippincott Williams & Wilkins, Philadelphia, pp. 279–296.
- Kalender, A., 1995. Thin-Section Three dimensional Spiral CT: Is Isotropic Imaging Possible. *Radiology* 197, 578–580.

- Karlson, E.W., Mandl, L.A., Aweh, G.N., Sangha, O., Liang, M.H., Grodstein, F., 2003. Total hip replacement due to osteoarthritis: the importance of age, obesity, and other modifiable risk factors. *The American Journal of Medicine* 114, 93–98.
- Kedgley, A.E., Takaki, S.E., Lang, P., Dunning, C.E., 2007. The effect of cross-sectional stem shape on the torsional stability of cemented implant components. *Journal of Biomechanical Engineering* 129, 310–314.
- Korkusuz, P., Korkusuz, F., 2004. Hard Tissue-Biomaterial Interactions. In: Yaszemski, M.J., Trantolo, D.J., Lewandrowski, K.-U., Hasirci, V., Altobelli, D., Wise, D. (Eds.), *Biomaterials in Orthopaedics*. Marcel Dekker, Inc., New York, pp. 2–6.
- Kuhn, K.-D., 2009. Properties of Bone Cement: What is Bone Cement? In: Breusch, S.J., Malchau, H. (Eds.), *The Well-cemented Total Hip Arthroplasty: Theory and Practice*. Springer Berlin Heidelberg, New York, pp. 52–59.
- Kurtz, S.M., Lau, E., Ong, K., Zhao, K., Kelly, M., Bozic, K.J., 2009. Future Young Patient Demand for Primary and Revision Joint Replacement: National Projections from 2010 to 2030. *Clinical Orthopaedics and Related Research* 467, 2606–2612.
- Kutzner, I., Heinlein, B., Graichen, F., Bender, A., Rohlmann, A., Halder, A., Beier, A., Bergmann, G., 2010. Loading of the knee joint during activities of daily living measured in vivo in five subjects. *Journal of Biomechanics* 43, 2164–2173.
- Lalone, E., 2012. An Image-Based Tool to Examine Joint Congruency at the Elbow. (Ph.D Thesis) The University of Western Ontario, pp. 1-49.
- Lewis, G., 1997. Properties of acrylic bone cement: state of the art review. *Journal of Biomedical Materials Research* 38, 155–182.
- Macaulay, W., DiGiovanni, C.W., Restrepo, A., Saleh, K.J., Walsh, H., Crossett, L.S., Peterson, M.G., Li, S., Salvati, E.A., 2002. Differences in bone-cement porosity by vacuum mixing, centrifugation, and hand mixing. *The Journal of Arthroplasty* 17, 569–575.

- Maher, S.A., Prendergast, P.J., Lyons, C.G., 2001. Measurement of the migration of a cemented hip prosthesis in an in vitro test. *Clinical Biomechanics* 16, 307–314.
- Mann, K. a, Ayers, D.C., Damron, T. a, 1997. Effects of stem length on mechanics of the femoral hip component after cemented revision. *Journal of Orthopaedic Research* 15, 62–8.
- Mann, K.A., Miller, M.A., Verdonschot, N., Izant, T.H., Race, A., 2010. Functional interface micromechanics of 11 en-bloc retrieved cemented femoral hip replacements. *Acta Orthopaedica* 81, 308–317.
- Maurer, T.B., Ochsner, P.E., Schwarzer, G., Schumacher, M., 2001. Increased loosening of cemented straight stem prostheses made from titanium alloys. An analysis and comparison with prostheses made of cobalt-chromium-nickel alloy. *International Orthopaedics* 25, 77–80.
- Mohler, C.G., Callaghan, J.J., Collis, D.K., Johnston, R.C., 1995. Early loosening of the femoral component at the cement-prosthesis interface after total hip replacement. *The Journal of Bone and Joint Surgery; American Volume* 77, 1315–1322.
- Morshed, S., Bozic, K.J., Ries, M.D., Malchau, H., Colford, J.M., 2007. Comparison of cemented and uncemented fixation in total hip replacement: a meta-analysis. *Acta Orthopaedica* 78, 315–26.
- Nakamura, J., 2005. Basics of Image Sensors. In: Nakamura, J. (Ed.), *Image Sensors and Signal Processing for Digital Still Cameras*. Taylor & Francis Group, Boca Raton, FL, pp. 53–93.
- Navarro, M., Michiardi, A., Castano, O., Planell, J.A., Castaño, O., 2008. Biomaterials in orthopaedics. *Journal of the Royal Society, Interface* 5, 1137–1158.
- New Zealand Orthopaedic Association, T.N.Z.J.R., 2010. Eleven Year Report- January 1999 to December 2009., <http://www.cdhb.govt.nz/njr/reports/A2D65CA3.pdf>.



- Ni, G., Lu, W., Chiu, K., Fong, D., 2005. Cemented or uncemented femoral component in primary total hip replacement? A review from a clinical and radiological perspective. *Journal Orthopaedic Surgery (Hong Kong)* 13, 96–105.
- Nilsson, K.G., Karrholm, J., Ekelund, L., Magnusson, P., 1991. Evaluation of micromotion in cemented vs uncemented knee arthroplasty in osteoarthritis and rheumatoid arthritis. Randomized study using roentgen stereophotogrammetric analysis. *The Journal of Arthroplasty* 6, 265–278.
- Olofsson, K., Digas, G., Karrholm, J., 2006. Influence of design variations on early migration of a cemented stem in THA. *Clinical Orthopaedics and Related Research* 448, 67–72.
- Olsen, R., Munk, P., Lee, M., 2000. Metal Artifact Reduction Sequence: Early Clinical Applications. *Radiographics* 20, 699–712.
- Park, J.B., 1992. Orthopedic prosthesis fixation. *Annals of Biomedical Engineering* 20, 583–94.
- Perruccio, A. V., Power, J.D., Badley, E.M., 2006. Revisiting arthritis prevalence projections--it's more than just the aging of the population. *The Journal of Rheumatology* 33, 1856–1862.
- Race, A., Miller, M.A., Mann, K.A., 2010. Novel methods to study functional loading micromechanics at the stem-cement and cement-bone interface in cemented femoral hip replacements. *Journal of Biomechanics* 43, 788–791.
- Relf, C., 2004. Setting Up. In: *Image Acquisition and Processing with LabVIEW*. CRC Press, Boca Raton, FL, pp. 15–45.
- Rodriguez-Gonzalez, F.Á., 2009. Chapter 9: Failure Modes of Implants. In: *Biomaterials in Orthopaedic Surgery*. pp. 177–197.
- Ryan, G., Pandit, A., Apatsidis, D.P., 2006. Fabrication methods of porous metals for use in orthopaedic applications. *Biomaterials* 27, 2651–2670.

- Saha, S., Pal, S., 1984. Mechanical properties of bone cement: a review. *Journal of Biomedical Materials Research* 18, 435–462.
- Scheerlinck, T., Casteleyn, P.P., 2006. The design features of cemented femoral hip implants. *The Journal of Bone and Joint Surgery; British Volume* 88, 1409–1418.
- Schweizer, A., Luem, M., Riede, U., Lindenlaub, P., Ochsner, P.E., 2005. Five-year results of two cemented hip stem models each made of two different alloys. *Archives of Orthopaedic and Trauma Surgery* 125, 80–86.
- Serbetci, K., Hasirci, N., 2004. Recent Developments in Bone Cement. In: Yaszemski, M.J., Trantolo, D.J., Lewandrowski, K.-U., Hasirci, V., Altobelli, D., Wise, D. (Eds.), *Biomaterials in Orthopaedic*. Marcel Dekker, Inc., New York, pp. 241–286.
- Skinner, H.B., 2006. Basic Science in Orthopaedic Surgery. In: H., S., Naglieri, C., R.Y., B. (Eds.), *Current Diagnosis and Treatment in Orthopaedics*. Lange Medical Books/McGraw-Hill Companies, pp. 1–63.
- Skytta, E.T., Eskelinen, A., Paavolainen, P., Ikavalko, M., Remes, V., 2009. Total elbow arthroplasty in rheumatoid arthritis: a population-based study from the Finnish Arthroplasty Register. *Acta Orthopaedica* 80, 472–477.
- Smeds, S., Goertzen, D., Ivarsson, I., 1997. Influence of temperature and vacuum mixing on bone cement properties. *Clinical Orthopaedics and Related Research* 334, 326–334.
- Stock, S.R., 2009. MicroCT Systems and Their Components. In: *Micro Computed Tomography- Methodology and Applications*. Taylor & Francis Group, Boca Raton, FL, pp. 39–84.
- Teeter, M., 2012. Assessment of Wear in Total Knee Arthroplasty Using Advanced Radiographic Techniques. (Ph.D Thesis) The University of Western Ontario, pp. 1-36.

- Thomas, S.R., Shukla, D., Latham, P.D., 2004. Corrosion of cemented titanium femoral stems. *The Journal of Bone and Joint Surgery; British Volume* 86, 974–978.
- Tortora, G., Nielsen, M., 2012. Synovial Joints. In: *Principles of Human Anatomy*. John Wiley & Sons, Inc., Hoboken, NJ, p. 268.
- Van der Lugt, J.C., Rozing, P.M., 2004. Systematic review of primary total elbow prostheses used for the rheumatoid elbow. *Clinical Rheumatology* 23, 291–298.
- Verdonschot, N., 2005. Philosophies of stem designs in cemented total hip replacement. *Orthopedics* 28, s833–840.
- Verdonschot, N., Huiskes, R., 1995. Dynamic creep behavior of acrylic bone cement. *Journal of Biomedical Materials Research* 29, 575–581.
- Waarsing, J.H., Day, J.S., Weinans, H., 2005. Longitudinal micro-CT scans to evaluate bone architecture. *Journal of Musculoskeletal & Neuronal Interactions* 5, 310–312.
- Wang, G., Frei, T., Vannier, M.W., 2000. Fast iterative algorithm for metal artifact reduction in X-ray CT. *Academic Radiology* 7, 607–614.
- Webb, J.C., Spencer, R.F., 2007. The role of polymethylmethacrylate bone cement in modern orthopaedic surgery. *The Journal of Bone and Joint Surgery; British Volume* 89, 851–857.
- Westerhoff, P., Graichen, F., Bender, A., Halder, A., Beier, A., Rohlmann, A., Bergmann, G., 2009. In vivo measurement of shoulder joint loads during activities of daily living. *Journal of Biomechanics* 42, 1840–1849.
- Westphal, F.M., Bishop, N., Honl, M., Hille, E., Puschel, K., Morlock, M.M., 2006. Migration and cyclic motion of a new short-stemmed hip prosthesis--a biomechanical in vitro study. *Clinical Biomechanics* 21, 834–840.

Willert, H.G., Broback, L.G., Buchhorn, G.H., Jensen, P.H., Koster, G., Lang, I., Ochsner, P., Schenk, R., 1996. Crevice corrosion of cemented titanium alloy stems in total hip replacements. *Clinical Orthopaedics and Related Research* 333, 51–75.

Wroblewski, B.M., Siney, P.D., Fleming, P.A., 2008. Hip Replacements. In: Sanjukta Deb (Ed.), *Orthopaedic Bone Cements*. Woodhead Publishing, Boca Raton, FL, pp. 41–47.

## CHAPTER 2: DEVELOPMENT AND VALIDATION OF A CUSTOM OPTICAL TRACKING SYSTEM TO QUANTIFY STEM-CEMENT INTERFACE MICROMOTION IN STEMMED IMPLANT COMPONENTS

*Overview: Implant loosening is the most common mode of implant failure, which can begin as small scale micromotion at the implant-cement interface. Quantifying differences in the magnitude of interface motion is one approach to compare the relative stability offered by varying implant designs, and serves as a measure of their ability to resist the effects of loosening. As such, a suitable tool was needed to quantify micromotion occurring directly at the stem-cement interface. This chapter describes the development and validation of a custom optical tracking system that will be used for reliable detection and measurement of interface motion in subsequent chapters.*

### 2.1 INTRODUCTION

Implant micromotion is one measure of implant stability, and can be used in both clinical and *in-vitro* studies as a predictor of implant loosening. Most *in-vitro* studies have used linear variable differential transducers (LVDT's), extensometers or sensing devices to detect and quantify overall implant motion (Cristofolini *et al.*, 2003; Jamali *et al.*, 2006; Maher *et al.*, 2001). However, the ability to quantify motion occurring directly at the stem-cement interface can offer valuable information on implant stability, eliminating the effects of motion contributed by surrounding fixturing or anatomy. A few studies have described new methods of investigating interface specific motion (Choi *et al.*, 2010; Race *et al.*, 2010; Zhang *et al.*, 2009); however, their application involved invasive methods of accessing the stem-cement interface, in addition to being specific to loading mode type.

Within the field of biomechanics, optical motion capture systems have been used for defining joint kinematics by tracking the relative motion of landmark markers placed across the joint (Anglin and Wyss, 2000; Zhou and Hu, 2008). While this method is non-invasive, optical motion capture systems used for these purposes do not have the system resolution required for detecting micromotion (Maletsky *et al.*, 2007). However, it was hypothesized that using appropriate optical equipment and markers, it would be possible to develop a measurement system capable of non-invasively detecting and measuring stem-cement interface motion during *in-vitro* testing.

Therefore, the purpose of this study was to develop and validate an optical measurement system that incorporated a high resolution camera, appropriately scaled optical markers, and a custom written data collection and analysis program, to measure relative micromotion between two moving landmarks in a two-dimensional image space.

## 2.2 MATERIALS AND METHODS

A pilot GigE Series piA 2400–12gm/gc camera (Basler AG, Ahrensburg, Germany) with telecentric lens (Opto Engineering, Matua, Italy) and axial diffuse illuminator (Advanced Illumination, Rochester, VT, USA) comprised the hardware selected for the optical system (Figure 2.1). These components were carefully chosen to meet the design requirements of the system; high image resolution with minimal image distortion or error (Appendix B).

For calibration of the optical system, a grid pattern with 0.1 mm squared grid intervals (Pyser-SGI Ltd, Kent, UK) was used with a custom written calibration program (National Instruments Corporation, Austin, TX, USA) (Appendix C.1) to determine the pixel to millimeter conversion (Figure 2.2). The program incorporated a pixel counting method, and based on a selected region of the calibration grid chosen by the user, output the resulting horizontal and vertical pixel count within that region. Using an integrated scaling method, the pixel to millimeter conversion for both the horizontal and vertical orientations were determined based on the known intervals of the calibration grid. This

conversion was done over nine regions of the grid pattern, which allowed for calibration over the entire field of view, and an average pixel to mm value was determined and used for calibration of the optical system. Before the start of the each testing trial, the system was recalibrated to ensure the accuracy of the resultant measurements.

A custom written LabVIEW program (National Instruments Corporation, Austin, TX, USA) (Appendix C.2) integrated with the camera capture program (National Instruments Corporation, Austin, TX, USA), was used for image analysis. This program used a color thresholding method to detect markers of a specific red-green-blue (RGB) value in the image capture region, and output a corresponding threshold image (Figure 2.3). The program further incorporated a centroid tracking method to determine the  $(x,y)$  coordinates of the marker centroids in the threshold image window. The data output of the program included these  $(x,y)$  centroid coordinates throughout the video capture duration, as well as the relative displacement between the markers.

For validation of the optical measuring system, a digit counter inch-micrometer screw gauge (Fowler Inc., Newton, MA, USA) was used as the gold standard to apply known displacements. Droplets of fluorescent paint were used as colored markers, and attached to the anvil and spindle of the micrometer (Figure 2.4). The gauge was moved through displacements that started at 0.0002 inch (0.005 mm), and increased in increments of 0.0002 inch (0.005 mm) to a maximum of 0.001 inch (0.025 mm), after which displacements were set at 0.002 inch (0.051 mm), 0.0039 inch (0.099 mm), 0.0098 inch (0.249 mm), and 0.0197 inch (0.500 mm). This range of displacements was applied in both the horizontal and vertical directions, over the nine regions of the image field of view (Figure 2.2). Each displacement was repeated five times, while the optical system tracked and measured the relative displacement of the markers during each trial.

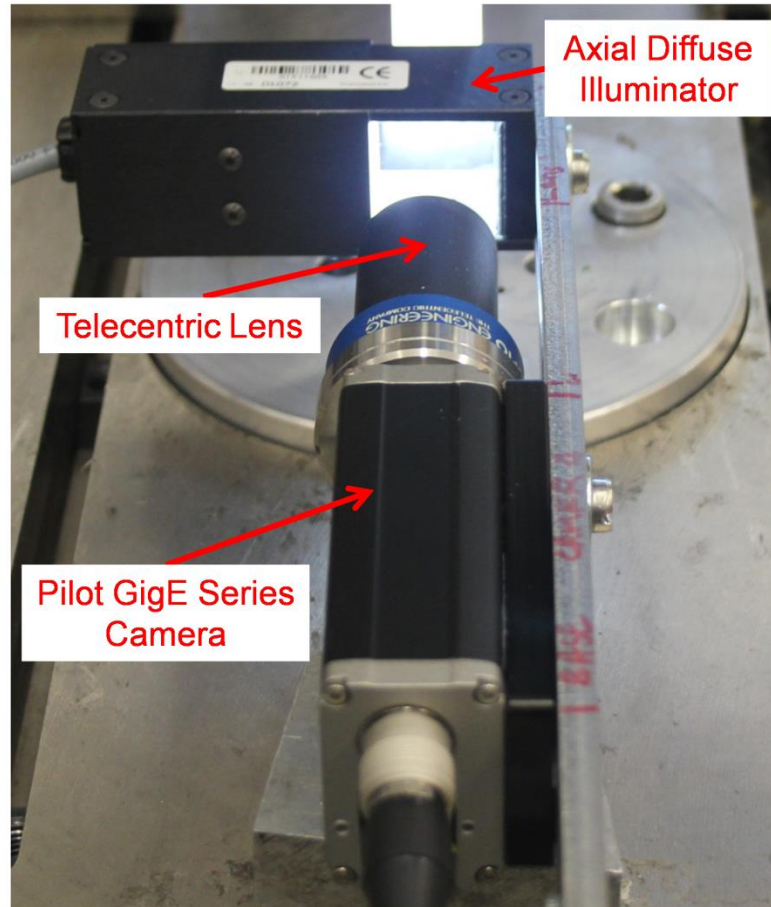


**Figure 2.1: Hardware of the Optical Tracking System**

A high resolution camera with telecentric lens, and axial diffuse illuminator composed the hardware of the optical tracking system.



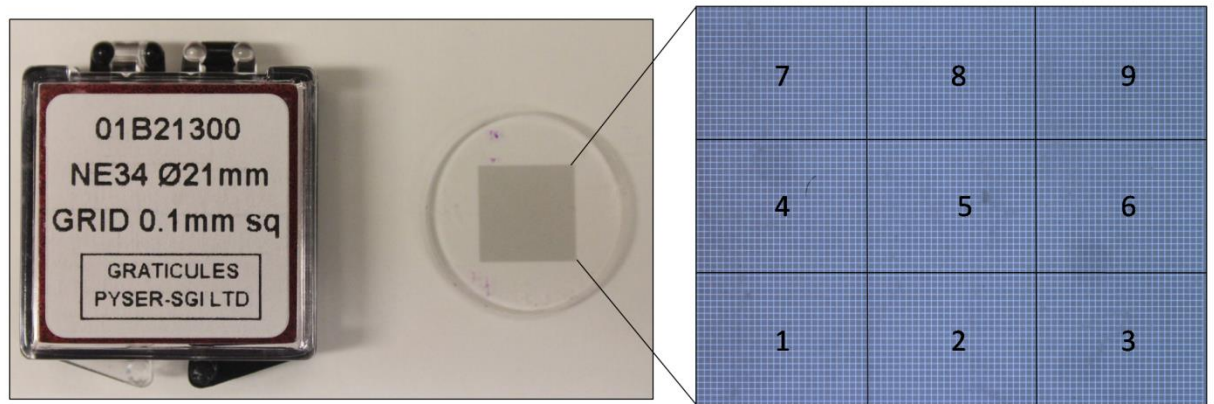


**Figure 2.2: Calibration Grid used for Pixel to mm Conversion**

The calibration grid shown above, with 0.1 mm squared grid spacing, was used for calibration of the optical system. The exploded view displayed on the far right shows the grid as seen in the field of view of the optical system. The grid was divided into nine regions of interest (shown in inset), and pixel to mm conversion was determined for each of the regions. An average conversion value over all nine regions was calculated and used for calibration of the optical system.

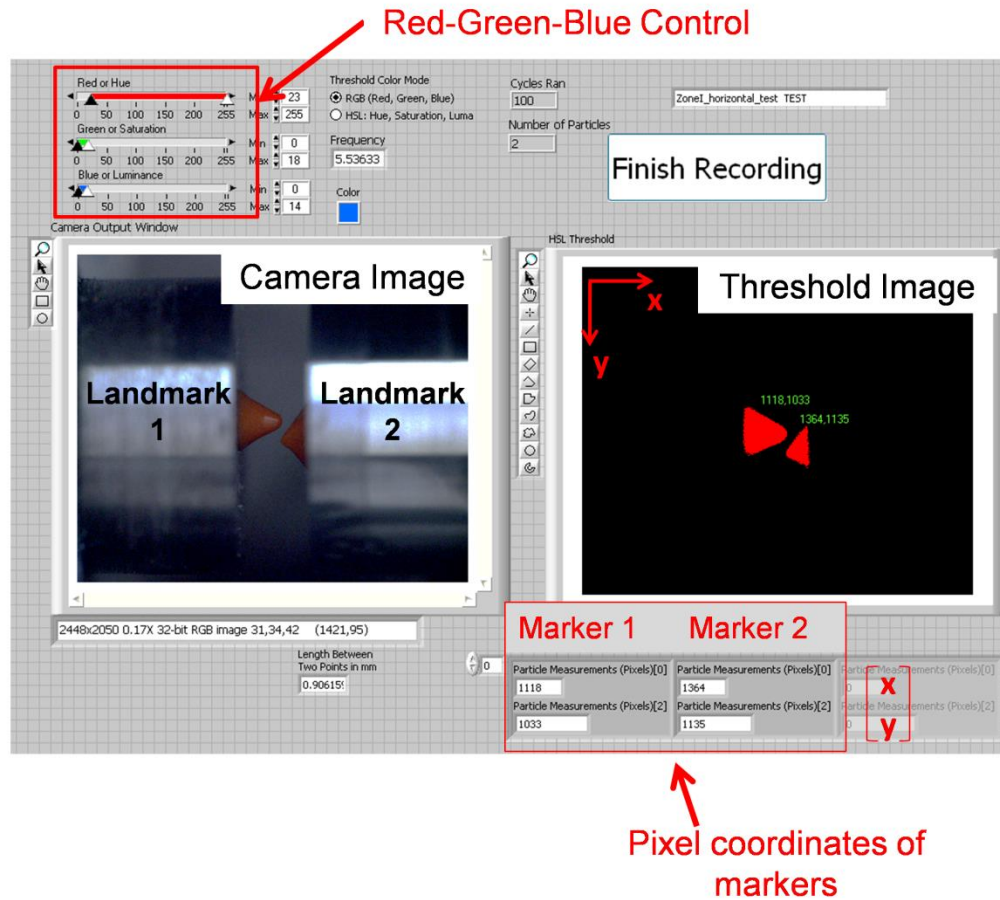


**Figure 2.3: Optical Tracking Software**

The display of the custom written LabVIEW program used for tracking colored markers placed on specific landmarks. Shown in the image are the controls used for setting the color threshold, along with the corresponding camera and threshold image. Also shown are the  $(x,y)$  pixel coordinates of the centroid position of each marker detected in the camera's coordinate system.

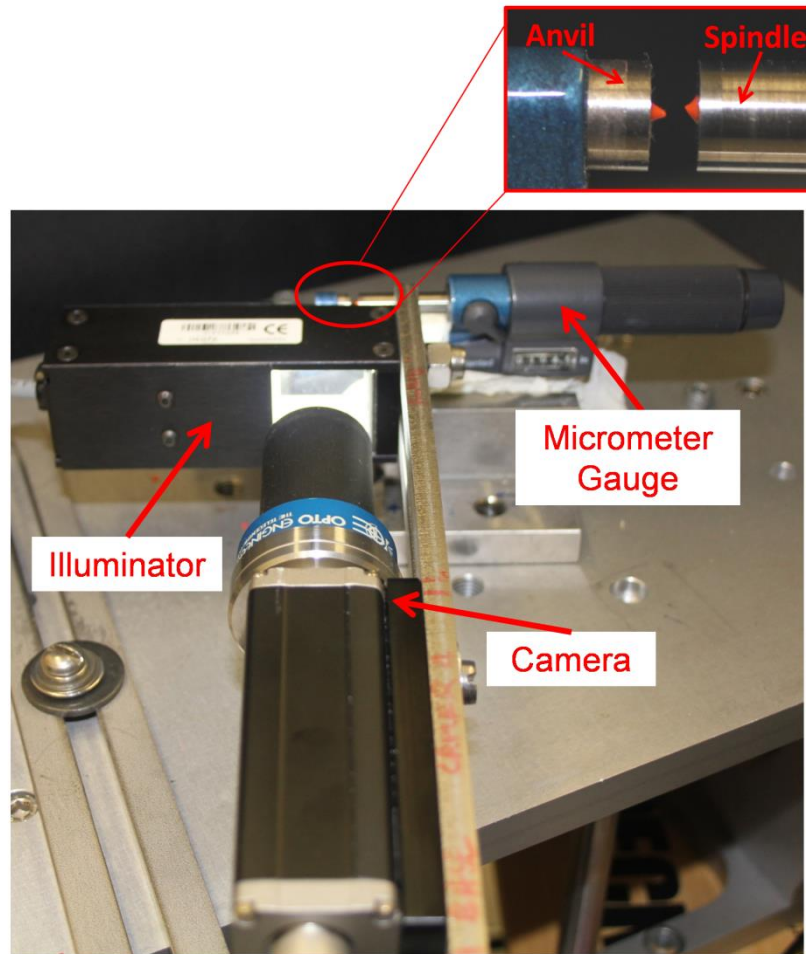


**Figure 2.4: Experimental Set-up for Validation of Optical Tracking System**

A micrometer screw gauge, with colored markers attached to the anvil and spindle (shown in the inset image), was used for validation of the optical system. The micrometer was used as the gold standard to apply known displacements, and the optical system tracked relative motion of the colored markers.

A Bland and Altman plot (Bland and Altman, 1999, 1986; Myles and Cui, 2007) was used to evaluate agreement between the micrometer gauge and optical system, as was the percent error measurement. In addition, the reliability of the optical system was evaluated using the intra-class correlation coefficients (ICC (2,1)) (Shrout and Fleiss, 1979) and Standard Error of Measurements (SEM) of the measured displacements over the nine regions of the image field of view.

## 2.3 RESULTS

The Bland and Altman plot showed good agreement between the optical system and micrometer measurements, based on the scatter of the differences between the measurements from each system, against the average of the measurements (Figure 2.5). The scatter of the points generally fell within 1.96 standard deviations of the mean difference between measurements, with some outliers for measurements greater than 0.1 mm. These outliers were more apparent with 0.5 mm vertical measurements. In addition, as the average measurement increased, the spread of the data also increased. This was observed for both the vertical and horizontal displacements, as represented by the red and black scatter points in Figure 2.5, respectively.

The overall difference based on all of the measured data pooled together between the micrometer and optical system, as measured by the percent error, was found to be +8.8% and -9.3% for the displacement output of 0.005 mm to 0.500 mm (Appendix E).

The ICC's and SEM's of the vertical and horizontal measurements from the optical system, over the nine regions of the image field of view are shown Table 2.1. Excellent reliability was found among the repeated measures from the optical system, where results of the ICC's for the vertical and horizontal displacements were all greater than 0.99, and SEM's ranged from 0.002 mm to 0.007 mm.

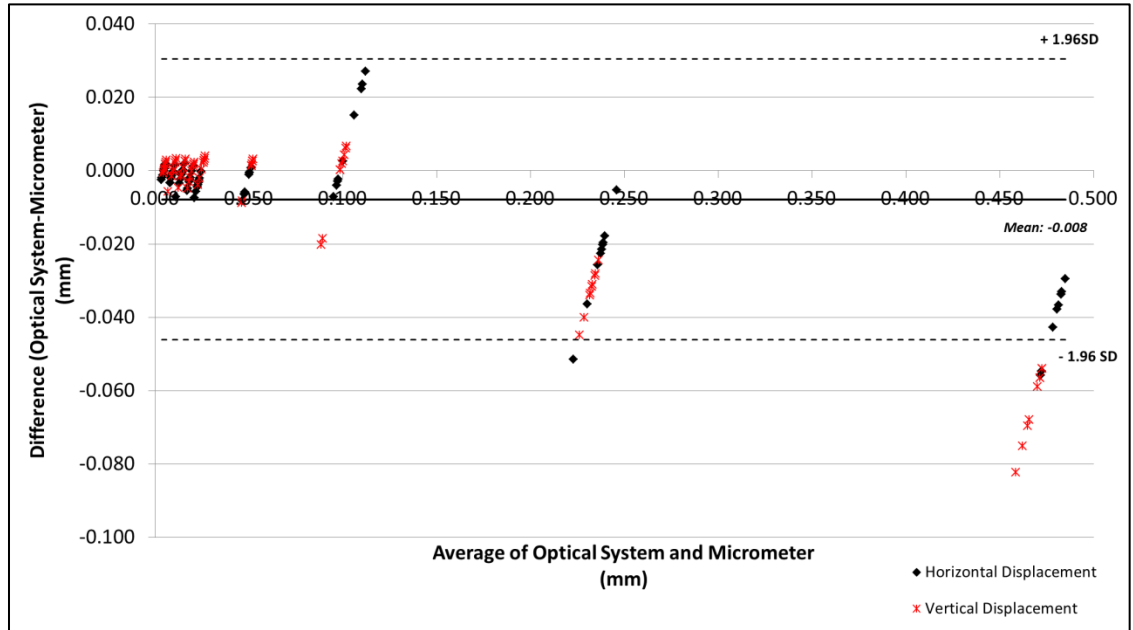


**Figure 2.5: Bland & Altman Plot Comparing Agreement of Measurement Systems**

The Bland and Altman plot showing the difference between the optical system and micrometer measurements against their average measurements for both vertical and horizontal displacements. Each point on the plot represents the difference in measurements (*i.e.*, optical system – micrometer) for the nine applied displacements of the micrometer, over the nine individual regions of the field of view (Note: To see Bland and Altman plots for the individual regions, please refer to Appendix D). The plot shows good agreement between the measurements for all displacements, as most difference values fall within  $\pm 1.96SD$  of the mean difference. For measurements greater than 0.1 mm, however, there were some outliers that fell outside the region of agreement, particularly for vertical measurements of 0.5 mm.

**Table 2.1: Intra-class correlation coefficients (ICC's) and Standard Errors of Measurement (SEM) for the Vertical and Horizontal Displacement Measurements of the Optical System.**

Image Region	Vertical Displacement		Horizontal Displacement	
	ICC	SEM (mm)	ICC	SEM (mm)
1	0.9996	0.003	0.9998	0.002
2	0.9976	0.007	0.9998	0.002
3	0.9997	0.003	0.9994	0.004
4	0.9996	0.003	0.9991	0.005
5	0.9996	0.003	0.9997	0.004
6	0.9996	0.003	0.9994	0.004
7	0.9996	0.003	0.9983	0.006
8	0.9987	0.005	0.9994	0.004
9	0.9995	0.003	0.9996	0.003

## 2.4 DISCUSSION

Implant micromotion is a useful measure for defining implant stability. Many experimental studies involving cemented implants have assessed the survival of implant systems based on their ability to resist implant micromotion (Burke *et al.*, 1991; Cristofolini *et al.*, 2003; Maher *et al.*, 2001). These studies, however, assessed implant motion as a function of stem motion relative to the bone, and not specific to motion occurring at the stem-cement interface. For cemented implants in particular, it has been shown that bone cement is susceptible to ‘creep’, where deformation of the cement occurs under loading conditions (Jeffers *et al.*, 2005; Lewis, 2011; Verdonschot and Huiskes, 1995). As such, measurement of implant motion at the stem-cement interface may be a more reliable measure of implant loosening, eliminating the effect of implant motion from the surrounding cement, as well as the surrounding testing fixtures.

Few studies have reported on stem-cement interface motion as a measure of implant stability (Choi *et al.*, 2010; Mann *et al.*, 2010; Zhang *et al.*, 2009). Mann *et al.*, used a method incorporating digital image correlation to measure displacement along the interface of sectioned regions of cemented implants under torsional loading (Mann *et al.*, 2010). In comparison, Zhang *et al.*, described a method which used a custom made sensor with strain gauges to detect motion occurring between the stem and cement under compression (Zhang *et al.*, 2009). Each measurement tool was successful at measuring interface motion, but involved invasive methods of accessing the stem-cement interface, in addition to being specific to loading mode type. For use in this thesis, however, a non-invasive measuring tool capable of detecting motion under different loading conditions is required, as future studies will be investigating implant micromotion under torsion (Chapter 3 and 5), axial (Chapter 4 and 5), and bending (Chapter 6) loads. As such, the purpose of this study was to develop and validate a measurement system capable of detecting and measuring stem-cement interface micromotion during mechanical testing of implant stems.

Optical measurement systems offer a non-invasive approach to measuring motion in biomechanics studies. The choice of optical system depends on the requirements of

the measurement being made. For interface motion, which is expected to occur on the order of micrometers, an appropriate optical system with high pixel resolution was required. As such, the pilot GigE series camera with sensor size of 2454 x 2056 pixels; 3.45  $\mu\text{m}/\text{pixel}$ , and telecentric lens was incorporated into the optical system. The telecentric lens allowed for consistent image magnification with low distortion and perspective errors. The source of illumination (*i.e.*, axial diffuse illuminator) was also specific to the needs of the measurement system, providing uniform light intensity with low specular deflection. This ensured that there was no light scatter that may compromise the resulting image, and influence the thresholding method used to detect the markers.

From calibration of the optical system, it was determined that the resolution of the system was appropriate for micrometer measurements, with pixel values on the order of  $0.003 \pm 0.002$  mm (Appendix F).

The Bland and Altman plot was chosen to compare the agreement between the optical system and the micrometer measurements, since it allowed comparison of the differences between the measuring systems, based on the expected confidence interval (*i.e.*, limits of agreement) in which 95% of the differences were expected to fall (Bland and Altman, 1999, 1986). Results from the Bland and Altman plot demonstrated good agreement between both measuring tools, since the majority of scatter points fell within 95% confidence interval of the mean difference between the systems' measurements (Figure 2.5). However, for target vertical displacements of 0.5 mm, the optical system consistently underestimated the measurement. This underestimate is believed to be due to systematic error in obtaining large vertical displacements. In addition, as the target displacements increased, the difference in the measurements between the optical system and micrometer also increased as well, suggesting that the optical system was less sensitive to measuring larger displacements from the micrometer. Since interface motion is expected to be small (*i.e.*, less than 200  $\mu\text{m}$ ) this observation was not of concern for the intended application of the measurement system.



When comparing the error in the optical system based on known displacements applied by the micrometer, it was found that for the range of measurements between 0.005 mm and 0.500 mm the percent error was +8.8% and -9.3% (Appendix E). This accuracy measurement seems appropriate for the measuring capabilities required for stem-cement interface motion. While there may be room for improvement, it was determined that the error in the system was acceptable for its intended function of comparing stem-cement interface motions.

With regards to the reliability of the optical system, ICC's were used to compare the correlation among repeated measures of the optical system. This statistic was expected to give information on the precision of the optical system, and its reliability in obtaining repeated measures with little variation. Results of the ICC demonstrated that the correlation values for each of the image regions (*i.e.*, Regions 1–9) were greater than 0.99 (Table 2.1). This agreement among the repeated measures illustrated that the optical system was reliable at reporting 'test-re-test' measurements, which is important for multi-trial testing.

The micrometer screw gauge was used as the gold-standard for assessing the validity of the optical system, since it is a standard measurement tool with system resolution on the order of 0.0001 inch (*i.e.*, 0.0025 mm). However, because the optical system was validated against another measurement tool, it is important to note that errors in the measures obtained by the optical system may also be contributed to by errors inherent in the micrometer screw gauge.

The color thresholding method of the optical system's software detected markers based on a single R-G-B value, which allowed distinction of the colored markers from their surroundings. This was done by hand-tuning the R-G-B scale to a set value, ensuring that only the markers appeared in the resultant thresholded image. While this was a time consuming process to ensure a stable centroid was achieved, no concerns with system performance were noted. However, a range of R-G-B values could have also been used to capture the markers. It is possible that this range may have allowed easier

definition of the marker shapes and boundaries within the thresholded image, to achieve the required stable centroid during static images.

The markers used for validation of the optical system were similar to those expected to be used during mechanical testing in subsequent chapters, with regards to the respective R-G-B values. However, because of the restrictions and difficulty of marker attachment to the micrometer's anvil and spindle, the markers were slightly larger in shape compared to those expected to be used with mechanical testing. In addition, the markers were positioned at the nearest proximity to the center of the anvil and spindle to reduce offset motion during spindle rotation to the target displacement. However, offset motion was still apparent, therefore analysis of relative marker motion in the horizontal and vertical orientations were broken down into individual  $x$  and  $y$  components. Despite meticulous methods to control for appropriate marker size and placement on the micrometer's anvil and spindle faces, the centroid tracking method of the optical system may have been influenced by the non-uniformity of the markers. This may have further contributed to the error detected in the optical measurement system.

## 2.5 CONCLUSION

Overall, this study was able to demonstrate the efficacy of the presented optical system at meeting the system requirements needed for measuring interface motion. Taking into consideration the reliability and accuracy of the system to measure displacements on the order of micrometers, it was concluded that the optical system was satisfactory for the application in this thesis, to compare interface motion of various stem surface designs.

## 2.6 REFERENCES

- Anglin, C., Wyss, U.P., 2000. Review of arm motion analyses. Proceedings of the Institution of Mechanical Engineers, Part H: Journal of Engineering in Medicine 214, 541–555.
- Bland, J., Altman, D., 1999. Measuring agreement in method comparison studies. Statistical Methods in Medical Research 8, 135–160.
- Bland, J.M., Altman, D.G., 1986. Statistical methods for assessing agreement between two methods of clinical measurement. Lancet 1, 307–10.
- Burke, D.W., O'Connor, D.O., Zalenski, E.B., Jasty, M., Harris, W.H., 1991. Micromotion of cemented and uncemented femoral components. The Journal of Bone and Joint Surgery; British Volume 73, 33–37.
- Choi, D., Park, Y., Yoon, Y.-S.S., Masri, B.A., 2010. In vitro measurement of interface micromotion and crack in cemented total hip arthroplasty systems with different surface roughness. Clinical Biomechanics 25, 50–55.
- Cristofolini, L., Teutonico, A.S., Monti, L., Cappello, A., Toni, A., 2003. Comparative in vitro study on the long term performance of cemented hip stems: validation of a protocol to discriminate between “good” and “bad” designs. Journal of Biomechanics 36, 1603–1615.
- Jamali, A.A., Lozynsky, A.J., Harris, W.H., 2006. The effect of surface finish and of vertical ribs on the stability of a cemented femoral stem: an in vitro stair climbing test. The Journal of Arthroplasty 21, 122–128.
- Jeffers, J.R., Browne, M., Taylor, M., 2005. Damage accumulation, fatigue and creep behaviour of vacuum mixed bone cement. Biomaterials 26, 5532–5541.
- Lewis, G., 2011. Viscoelastic properties of injectable bone cements for orthopaedic applications: state-of-the-art review. Journal of Biomedical Materials Research, Part B, Applied Biomaterials 98, 171–191.

- Maher, S.A., Prendergast, P.J., Lyons, C.G., 2001. Measurement of the migration of a cemented hip prosthesis in an in vitro test. *Clinical Biomechanics* 16, 307–314.
- Maletsky, L.P., Sun, J., Morton, N.A., 2007. Accuracy of an optical active-marker system to track the relative motion of rigid bodies. *Journal of Biomechanics* 40, 682–685.
- Mann, K.A., Miller, M.A., Verdonschot, N., Izant, T.H., Race, A., 2010. Functional interface micromechanics of 11 en-bloc retrieved cemented femoral hip replacements. *Acta Orthopaedica* 81, 308–317.
- Myles, P.S., Cui, J., 2007. Using the Bland-Altman method to measure agreement with repeated measures. *British Journal of Anaesthesia* 99, 309–311.
- Race, A., Miller, M.A., Mann, K.A., 2010. Novel methods to study functional loading micromechanics at the stem-cement and cement-bone interface in cemented femoral hip replacements. *Journal of Biomechanics* 43, 788–791.
- Shrout, P.E., Fleiss, J.L., 1979. Intraclass correlations: uses in assessing rater reliability. *Psychological Bulletin* 86, 420–428.
- Verdonschot, N., Huiskes, R., 1995. Dynamic creep behavior of acrylic bone cement. *Journal of Biomedical Materials Research* 29, 575–581.
- Zhang, H.Y., Brown, L., Barrans, S., Blunt, L., Jiang, X.Q., 2009. Investigation of relative micromotion at the stem-cement interface in total hip replacement. *Proceedings of the Institution of Mechanical Engineers. Part H, Journal of Engineering in Medicine* 223, 955–964.
- Zhou, H., Hu, H., 2008. Human motion tracking for rehabilitation—A survey. *Biomedical Signal Processing and Control* 3, 1–18.

## CHAPTER 3: THE EFFECT OF STEM SURFACE TREATMENT ON THE TORSIONAL STABILITY OF TITANIUM AND COBALT CHROME CEMENTED JOINT REPLACEMENT SYSTEMS

*Overview: Stem surface treatment and substrate material are two design factors that can contribute to the stability at the stem-cement interface, in resisting the effects of torsional loads that occur at the upper limb joints. This chapter compared the torsional stability of three stem surface treatments (smooth, beaded and plasma spray), applied to two substrate materials (titanium and cobalt chrome), using the custom optical tracking system described in Chapter 2 to measure interface rotation.*<sup>1</sup>

### 3.1 INTRODUCTION

Implant loosening is a complication that affects the success of joint replacement systems, leading to revision surgery (Australian Orthopaedic Association, 2010; New Zealand Orthopaedic Association, 2010). Loosening can be affected by implant stem design (Verdonschot, 2005) and joint loading (Bergmann *et al.*, 1995). For cemented implants, a successful stem design has the capability of providing secure mechanical fixation and stability at the stem-cement interface, resisting the effects of loosening caused by various loading modes applied to the joint.

Stem surface treatment is one aspect of stem design that plays a role in cemented implant stability. It has been demonstrated that cemented roughened surfaces

---

<sup>1</sup> A version of this work is under review: Y.K. Hosein, G.J.W. King, C.E. Dunning (2013). "The Effect of Stem Material and Surface Treatment on the Torsional Stability at the Metal-Cement Interface of Cemented Upper Limb Joint Replacement Systems" Journal of Biomedical Materials Research: Part B Applied Biomaterials.

experienced greater interface strength when compared to smooth polished surfaces (Chen *et al.*, 1998; Crowninshield, 1998; Walsh *et al.*, 2004). These studies compared surface treatment based on average roughness values ( $R_a$ ), where surfaces used were classified as polished ( $R_a < 1 \mu\text{m}$ ), matte ( $R_a < 2 \mu\text{m}$ ) or rough ( $R_a > 2 \mu\text{m}$ ) (Verdonschot, 2005). While this classification is relevant to micro surface modifications, it does not represent surface treatments that are used clinically with cemented upper extremity stemmed components (*i.e.*, plasma spray and beaded). A study by Jeon *et al.* addressed the clinical success of the Coonrad/Morrey Total Elbow implant which incorporated these treatments (Jeon *et al.*, 2012), however, no known *in-vitro* studies have specifically compared their role in implant stability. Such information may be beneficial to the design of future joint replacement systems.

Stem material is another aspect of stem design that may influence implant stability. Titanium and cobalt chrome alloys are two conventional materials used with implant stems (Buechel *et al.*, 2012). With regards to cemented implants, however, there has been much debate over the use of titanium stems with femoral components, due to increased rates of loosening, as well as high sensitivity to corrosion (Hallam *et al.*, 2004; Schweizer *et al.*, 2005). Despite lack of success with lower limb joint replacements, cemented titanium implants remain extensively used in upper limb applications (Van der Lugt and Rozing, 2004). In such cases, the type of stem material may influence the success of surface treatments applied to the implant stem, by affecting the strength of the bond formed between the stem and coating during the finishing process (Davis, 2003).

Joint loading can also affect implant loosening. Torsional loading that occurs at the joint is one such example that can lead to failure of the prosthesis. This failure mechanism can be initiated during lifting movements with the elbow in a flexed position. During this motion, internal rotational loads are directed at the humerus of the elbow joint (Van der Lugt *et al.*, 2010). Such is the case in lifting with an abducted arm, or the throwing motion of the arm.

Considering the role stem surface roughness plays in implant stability, as well as the lack of literature comparing surface treatments that are clinically relevant to cemented

upper extremity stemmed components, the purpose of this study was to investigate the effect of stem surface treatment on the torsional stability of both titanium and cobalt chrome cemented stems *in-vitro*.

### 3.2 MATERIALS AND METHODS

Thirty generic implant stems of circular cross-section ( $\varnothing = 8$  mm) were custom-machined from cobalt chrome ( $n = 15$ ) and titanium ( $n = 15$ ) by Tornier S.A.S. (Montbonnot Saint Martin, France) (See Appendix G for engineering drawings). Each stem was given a polished smooth surface. The fifteen stems of each material were split into three equal groups. One group of stems retained their smooth surface ( $n = 5$ ), while the remaining groups had two different surface treatments: beaded ( $n = 5$ ) and plasma sprayed ( $n = 5$ ), applied over a 20 mm stem length region by Orchid Bio-Coat (Southfield, MI, USA) (Figure 3.1). The plasma sprayed surfaces were titanium plasma spray (TPS) and had a  $R_a$  value of  $48.5 \pm 3.9$   $\mu\text{m}$ . The beaded surfaces consisted of one layer of beads, with a bead diameter of approximately 500  $\mu\text{m}$ .

All stems were centralized in square aluminum tubes, and potted using vacuum-mixed PMMA bone cement (Simplex P<sup>®</sup>, Stryker<sup>®</sup>, Kalamazoo, MI, USA) to a fixed depth of 20 mm, such that there was full coverage of the surface treated regions (for detailed potting and centralization techniques, refer to Appendix H). The stems were maintained in air at 22 °C for 24 hours during curing. Subsequently, the potted stems were secured in a materials testing machine (Figure 3.2) (Instron<sup>®</sup> 8874, Norwood, MA, USA) and cyclically tested at 1.5 Hz under torsion. Custom machined fixturing ensured that stems were fully centralized during testing (Appendix G.10), allowing the application of pure torsional loads with minimal contribution of off-axis loading, as monitored by the 6 degrees of freedom load cell of the materials testing machine. Loading cycled from a lower limit of 0 Nm to an upper limit that started at 1 Nm, increasing in increments of 1 Nm every 100 cycles to a maximum of 30 Nm, or until a

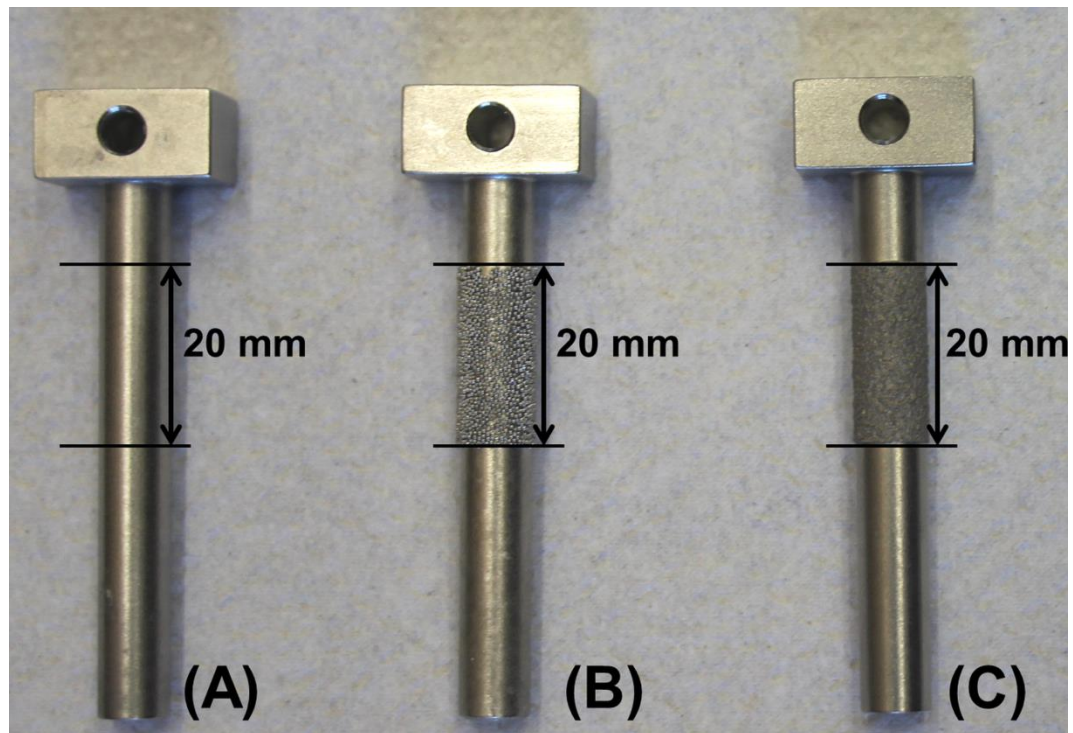


**Figure 3.1: Surface Treated Stems used for Torsional Testing**

(A) Smooth surface, (B) beaded treatment, and (C) plasma spray treatment. All stems were cemented to a fixed depth of 20 mm, to ensure coverage of only the surface treated region of the stem.



rapid increase in rotation of the stem occurred without resistance; the latter being termed catastrophic failure.

Motion at the stem-cement interface was quantified using the custom optical tracking system described in Chapter 2 of this thesis (Basler Pilot GigE Camera [Basler, Ahrensburg, Germany]; Opto Engineering Telecentric Lens [Opto Engineering, Mantua, Italy]; Axial Diffuse Illuminator [Advanced Illumination, Rochester, VT, USA]; and LabVIEW Vision Acquisition System [National Instruments, Austin, TX, USA]). This system incorporated a colour thresholding method to optically track the centroid of markers placed on the stem and cement (Figure 3.2), to determine their relative distances throughout loading.

Stem-cement interface strength and interface stability were both quantified. Interface strength was determined from the values of torque at failure, as obtained from the materials testing machine. Interface stability was determined from the relative rotational displacement between the markers on the stem and cement immediately prior to failure, as obtained from the optical tracking system (*i.e.*, termed “interface toggle”; Figure 3.3).

Two-way analyses of variance with post-hoc Student-Newman-Keuls tests ( $\alpha = 0.05$ ) were used to examine the role of stem surface treatment and stem material on torsional stability, based on the measures of interface strength and stability.

### 3.3 RESULTS

Overall, torsional load targets were achieved with minimal off-axis loads and moments detected. To assess stem-cement interface toggle, graphs of relative stem rotation versus the number of loading cycles were created (Figure 3.3). In addition to interface toggle, which was measured just prior to failure, the presence of offset stem motion was observed in these graphs. This motion, which was representative of the

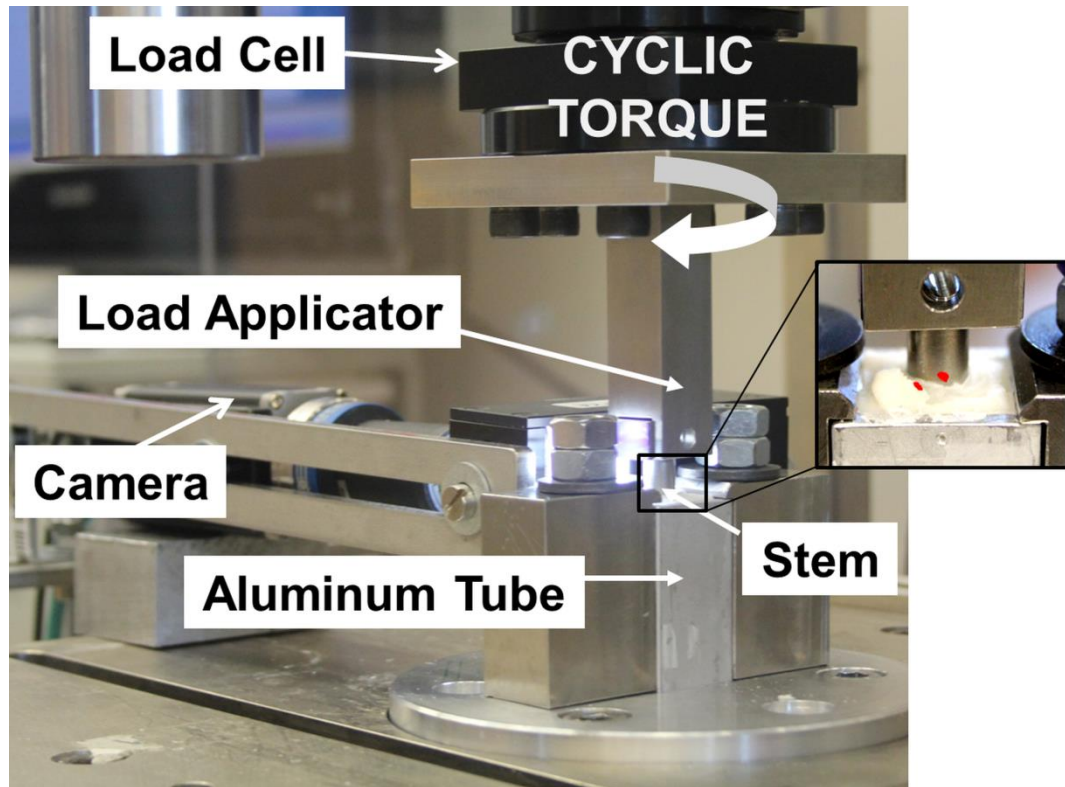


**Figure 3.2: Experimental Set-up for Torsional Testing of Implant Stems**

Cemented stem within the aluminum tube, secured in an Instron<sup>®</sup> Materials Testing Machine. Shown in the inset are optical markers attached to the stem and the cement. The stem was cyclically loaded under torque, and a camera system was used to detect stem-cement interface motion throughout loading.

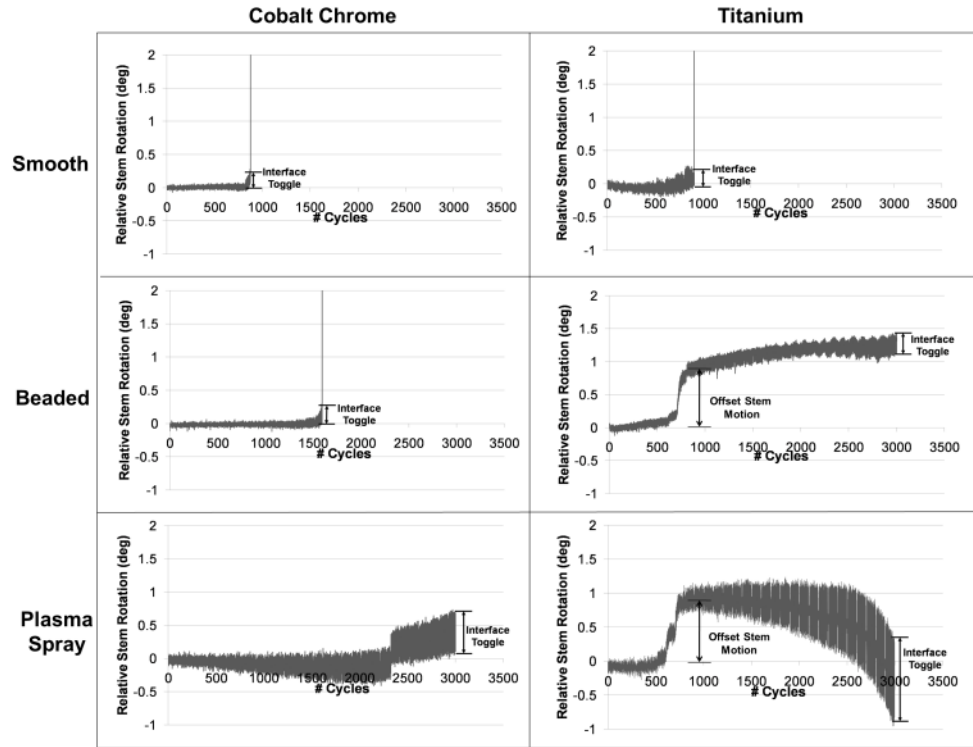


**Figure 3.3: Stem Rotation for Titanium and Cobalt Chrome Surface Treated Stems**

The graphs of relative stem rotation display interface toggle for all stems, which was a measure of the stem-cement interface stability just prior to failure. Offset stem motion, as represented by the deviation of the titanium beaded and titanium plasma spray stems away from their points of origin, is also shown. Stems that did not complete the full 3000 cycles of the loading protocol experienced catastrophic failure, as depicted by the rapid increase in relative stem rotation.

deviation of the stem away from its point of origin, qualitatively appeared to vary with both surface treatment and substrate material, but was not quantitatively analyzed.

From the initial results, it was noted that stem rotation increased with increasing applied torque (Figure 3.3). Therefore, due to the staircase loading protocol employed, the interface toggle was normalized to the value of torque at failure.

Of the three stem surfaces tested, the smooth stem was the only surface that consistently experienced catastrophic failure for both titanium and cobalt chrome stems. The beaded surface experienced catastrophic failure with the cobalt chrome stem material only, and post-testing inspection found that this resulted in mechanical damage to the beaded coating (Figure 3.4). The plasma spray stems, with both the titanium and cobalt chrome stem materials, never experienced catastrophic failure (Figure 3.5).

As such, there was an overall effect of surface treatment on interface strength ( $p < 0.001$ ), where smooth stems required less torque to cause interface failure than either the beaded ( $p < 0.05$ ) or plasma spray stems ( $p < 0.05$ ), and plasma spray was also superior to beaded ( $p < 0.001$ ) (Figure 3.5). Stem material also had an overall effect on strength ( $p = 0.001$ ), where titanium stems experienced higher torques at failure than cobalt chrome stems. In addition, the ANOVA demonstrated a significant interaction between stem surface treatment and stem material ( $p < 0.001$ ). Thus, appropriate one-way ANOVAs were conducted, and differed from the main effect in that there was no difference between material for plasma spray only ( $p = 1.0$ ), and no difference between beaded and plasma spray for titanium stems only ( $p = 1.0$ ).

With regards to interface stability, stem surface treatment had an overall effect ( $p = 0.002$ ) with smooth stems, demonstrating more interface toggle than either beaded ( $p < 0.05$ ) and plasma spray ( $p < 0.05$ ) treatments (Figure 3.6). However, the effect of surface treatment depended on stem material (*i.e.*, significant interaction;  $p = 0.001$ ). One-way ANOVA's showed that all three surfaces were different from one another for titanium stems ( $p < 0.05$ ), with a stability ranking of: beaded > plasma spray > smooth. By comparison, surface treatment did not have an effect on stability for cobalt chrome

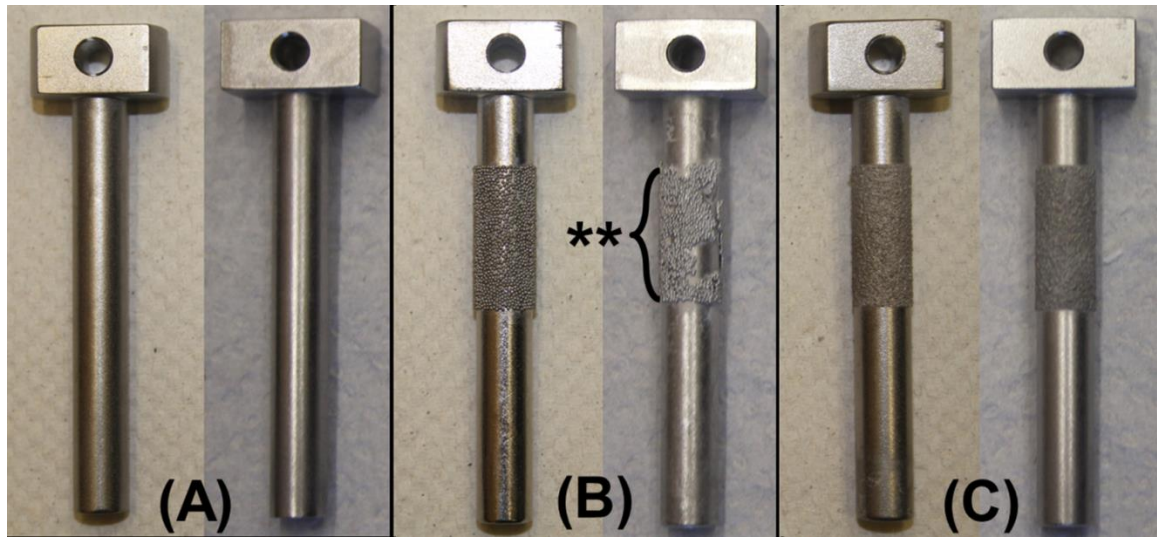


**Figure 3.4: Inspection of Stem Surface Treatments Post-Torsion Tests**

(A) Smooth titanium (left) and smooth cobalt chrome (right), (B) beaded titanium (left) and beaded cobalt chrome (right), and (C) plasma spray titanium (left) and plasma spray cobalt chrome (right). The beaded cobalt chrome was the only stem that experienced mechanical damage to its coating at failure, as depicted by (\*\*) in the figure above.

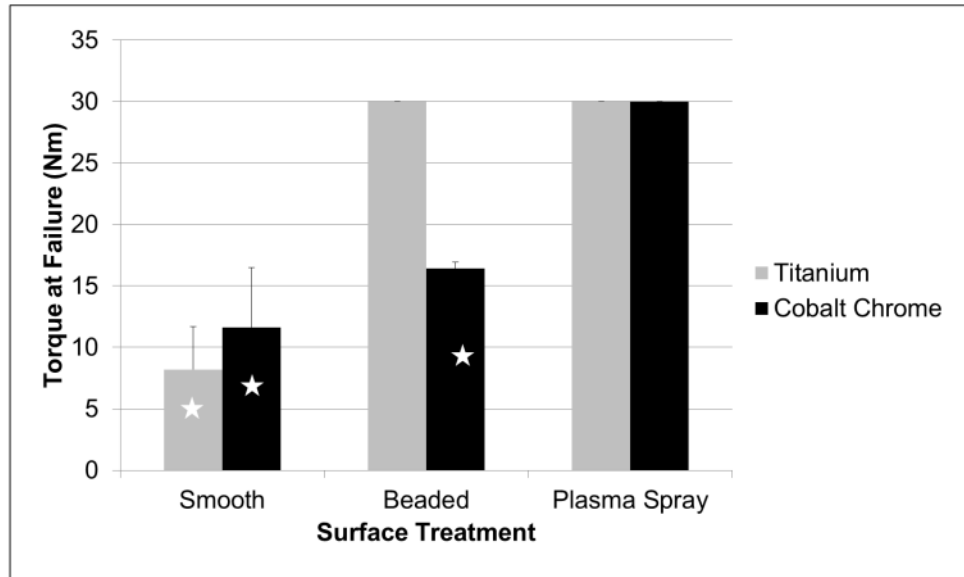


**Figure 3.5: Torque at Failure for Surface Treated Stems**

Graph showing torque at failure (*i.e.*, as a measure of interface strength) for smooth, beaded and plasma sprayed surface treatments, on titanium and cobalt chrome stems. The bars marked with white stars represent those stems that consistently experienced catastrophic failure.

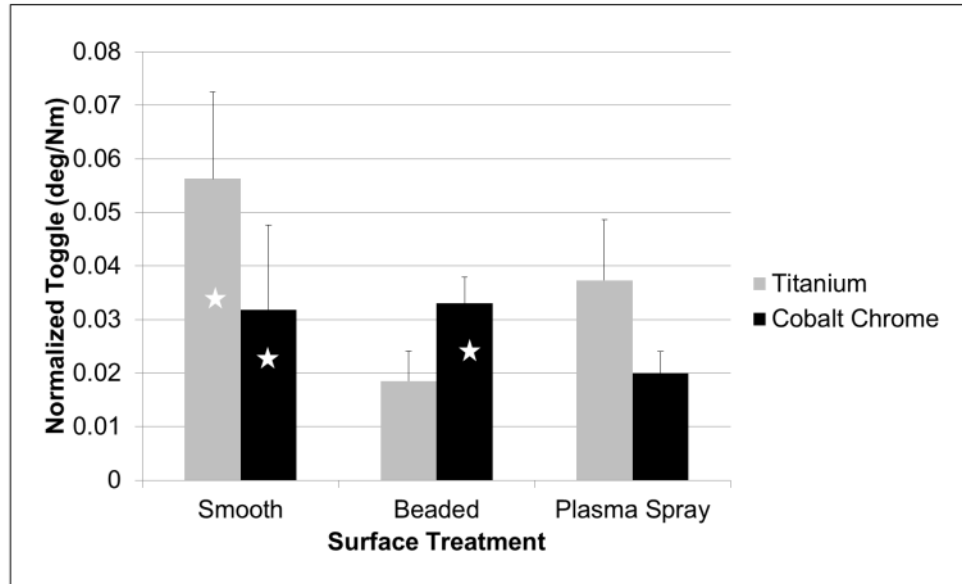


**Figure 3.6: Normalized Interface Toggle for Surface Treated Stems in Torsion**

Graph showing normalized interface toggle prior to failure (*i.e.*, as a measure of interface motion) for smooth, beaded and plasma sprayed surface treatments, on titanium and cobalt chrome stems. The bars marked with white stars represent those stems that consistently experienced catastrophic failure.

stems ( $p > 0.05$ ). Stem material also showed an overall effect on interface stability, where titanium stems experienced more toggle than cobalt chrome stems ( $p = 0.031$ ).

### 3.4 DISCUSSION

Improved implant longevity remain a continuous goal for orthopaedic implant research. Therefore, investigating factors affecting implant loosening is important for understanding possible failure mechanisms. Stem design at the stem-cement interface is one factor that may contribute to the overall stability of the implant system, and subsequent loosening (Barrack, 2000).

Stem surface treatments have been incorporated into implant designs to improve implant fixation. Surface treatments such as sintered beads and plasma spray are typically incorporated into non-cemented implant designs, with the expectation that the porous surface would allow for bony-in-growth onto the implant stem. However, these surface treatments are also utilized with cemented upper limb implant designs, such as the Zimmer<sup>®</sup> Coonrad/Morrey Total Elbow (Zimmer, Warsaw, IN, USA) (titanium plasma spray and beads on titanium stems), Latitude<sup>®</sup> EV Total Elbow Prosthesis (Tornier SAS, Montbonnot Saint Martin, France) (titanium plasma spray on cobalt chrome stems), and Discovery<sup>®</sup> Elbow System (Biomet, Warsaw, IN, USA) (titanium plasma spray on titanium, or cobalt chrome stems). It is expected that the viscous bone cement fills the spaces of the porous stem surface during cement application, and when cured, initiates mechanical interlock of the bulk cement to the stem surface. This mechanical interlock can improve implant fixation by allowing for better anchoring of the implant stem within the cement. In addition, during the lifespan of the implant system, these surface treatments are likely to provide frictional resistance to implant motion that may be caused as a result of loading occurring at the joint.

Cobalt chrome and titanium are two established materials among the orthopaedic community. Within recent years, titanium has been a controversial material for use in femoral cemented stem designs, since it has been reported to experience increased



loosening rates, as well as high sensitivity to corrosion (Jergesen and Karlen, 2002). Despite this, titanium is still commonly used in cemented upper-limb implant applications (Sanchez-Sotelo, 2011; van der Lugt and Rozing, 2004). As such, this study aimed to examine the effect of stem surface treatment on the stability of cemented titanium and cobalt chrome implant stems under torsional loading.

Stem surface treatment affected stem stability, where beaded and plasma sprayed surfaces experienced more resistance to rotation prior to failure when compared to the smooth stems. In addition, the smooth stems consistently experienced catastrophic failure at the lowest torque values for both the titanium and cobalt chrome stems.

Beaded stem surfaces appeared to perform better with a titanium stem material, as observed from their resistance to catastrophic failure, when compared to cobalt chrome stems. Post-testing inspection of the stems showed that catastrophic failure occurred as a result of the beaded coating being completely ripped off the stem surface (Figure 3.4). Thus, it is likely that the torque experienced at failure is more representative of the bonding strength of the beaded coating to the cobalt chrome stem, which is a factor of the coating fabrication process, and not necessarily a representation of the stem-cement interface strength.

For titanium stems examined in our study, the beaded stems experienced less interface toggle than the plasma spray stems, with no difference seen in interface strength (Figure 3.6 and 3.5, respectively). This may be explained based on the mechanism explained previously, involving mechanical interlock of the stem surface with cement. Beaded coatings have greater surface deviation based on the diameter of the sintered beads. This may allow for deeper infiltration of bone cement, subsequently improving the anchoring and stability of the implant system.

Overall results showed that titanium stems experienced more interface toggle throughout loading than cobalt chrome stems (Figure 3.3). This seems reasonable taking into consideration their respective material properties. Titanium is more ductile compared to cobalt chrome, as defined by its lower elastic modulus (Navarro *et al.*,

2008), and therefore likely to result in greater stem twisting with respect to the surface of the cement.

From Figure 3.3 it was observed that in addition to interface toggle, there were also offsets of the relative stem rotation for stems that did not experience catastrophic failure (*i.e.*, plasma sprayed and beaded titanium). The offsets represent deviation of the stem away from the point of origin with increased loading. This deviation may be due to cement creep at the interface as a result of cement exposure to fatigue loading (Jeffers *et al.*, 2005; Lewis, 2011, 1997). One method of defining implant loosening is detection of implant migration within the host bone. As such, it is important to acknowledge bone cement creep when defining interface stability as a measure of implant motion only, since cement creep may cause stem motion without interface loosening.

Plasma spray coatings are applied using a thermal spray in a reduced pressure inert gas chamber at high temperatures, to produce an irregular surface on the stem. In comparison, beaded coatings are applied via a sintering process, where the beads are bonded to the substrate surface of the stem (Ryan *et al.*, 2006). The strength of the bond formed is affected by the carbon content of the base metal substrate, where a lower carbon content reduces the effectiveness of the sintering process, causing an inferior bond at the level of the substrate surface and beads (Davis, 2003). Thus, it is possible that the effect of substrate carbon content on bonding strength may have played a role in our study, where post-testing inspection of the cobalt chrome stems found the beaded coating completely ripped off the stem surfaces during failure, but remained intact for the titanium stems (Figure 3.4).

For this study, only the torsional stability of various surface treatments was investigated. The loading protocol used was chosen based on a review of available literature directly measuring the torque through the use of instrumented implants at various joints (*i.e.*, shoulder, hip, knee) (Bergmann *et al.*, 2007, 2001; Kutzner *et al.*, 2010), as well as incorporation of a cyclic staircase method at a rate of 1.5 Hz to mimic fatigue loading that typically occurs *in-vivo*. This is in keeping with the literature, for example, femoral components have been tested using loading rates between 1–3 Hz (Bell

*et al.*, 2007; Britton *et al.*, 2004; Hernández-Rodríguez *et al.*, 2005; Westphal *et al.*, 2006; Wilson *et al.*, 2009). This protocol ensured comparison of the surface treatments based on clinically relevant joint loads, since upper limb joints experience similar loading patterns to those at the lower limbs (Goldberg *et al.*, 1988). Anatomically, however, the joint is exposed to a variety of loading modes in addition to torque, which typically work in a combined state at the joint. Therefore, future studies will look at investigating stem surface treatment on implant stability under other loading modes.

The optical tracking system used in our study calculated the relative distances between optical markers attached to the exposed surfaces of the stem and cement, to give measurements of interface motion throughout loading. This method is a better representation of interface motion compared to marker attachment to the implant only, since it measures motion solely at the stem-cement interface, regardless of any possible motion in the surrounding fixtures. The measurement, however, does not discern interface motion along the length of the cemented stem. Therefore, future studies will incorporate linear variable differential transducers embedded in the cement mantle, or imaging techniques to detect internal motion of the stem and cement.

Square aluminum tubes were used instead of cadaveric bone for cementing of the implant stems. Although this does not represent a clinically cemented intramedullary component, aluminum tubes were chosen since the study was only interested in the effects at the stem-cement interface. The use of aluminum tubes did have the benefit of providing a controlled cementing and testing environment, reducing any variation in the results that may be caused by varying bone quality.

With regards to the implant stem designs, circular cross-section generic stems, with 20 mm length surface treated regions were used to compare implant stability. This design is not representative of a specific joint implant stem in terms of its geometry and surface treated area, but allowed for comparison of implant stability solely dependent of surface treatment. Circular cross-section implant stems provided the least resistance to torque (Kedgley *et al.*, 2007), and as such, it was intentionally incorporated into the study design to minimize the effects of stem geometry on implant stability. Similarly, a 20 mm

length surface treatment region was used, since pilot testing showed that greater surface coverage did not allow for interface failure in the desired testing period, and reduced surface coverage was not optimal for relative comparison of surface treatments.

The findings from this study suggest that stem surface treatment influences implant stability, offering greater interface strength and resistance to motion than a smooth surface. When comparing surface treatments, the plasma spray finish offered superior interface strength compared to the beaded finish with cobalt chrome stems; however there was no difference in their performance with titanium stems. With regards to interface stability, the beaded finish was more stable than the plasma spray for titanium stems, but showed no difference for cobalt chrome stems. In addition to surface treatment, our study demonstrated that stem material affected implant stability, with titanium stems experiencing greater interface strength but reduced resistance to interface motion than cobalt chrome stems.

### 3.5 CONCLUSION

For surface treated stems tested under cyclic torsional loading, plasma spray performed better than beaded treatments on a cobalt chrome stem substrate, and beaded treatments performed comparable to plasma spray treatments on a titanium stem substrate.

### 3.6 REFERENCES

- Australian Orthopaedic Association, T., 2010. National Joint Registry, Hip and Knee Arthroplasty Annual Report 2010, [http://www.dmac.adelaide.edu.au/aoanjrr/documents/aoanjrrreport\\_2010.pdf](http://www.dmac.adelaide.edu.au/aoanjrr/documents/aoanjrrreport_2010.pdf).
- Barrack, R.L., 2000. Early failure of modern cemented stems. *The Journal of Arthroplasty* 15, 1036–1050.
- Bell, C.G., Weinrauch, P., Pearcy, M., Crawford, R., 2007. In vitro analysis of exeter stem torsional stability. *The Journal of Arthroplasty* 22, 1024–1030.
- Bergmann, G., Deuretzbacher, G., Heller, M., Graichen, F., Rohlmann, A., Strauss, J., Duda, G.N., 2001. Hip contact forces and gait patterns from routine activities. *Journal of Biomechanics* 34, 859–871.
- Bergmann, G., Graichen, F., Bender, A., Kääh, M., Rohlmann, A., Westerhoff, P., 2007. In vivo glenohumeral contact forces--measurements in the first patient 7 months postoperatively. *Journal of Biomechanics* 40, 2139–2149.
- Bergmann, G., Graichen, F., Rohlmann, A., 1995. Is staircase walking a risk for the fixation of hip implants? *Journal of Biomechanics* 28, 535–553.
- Britton, J.R., Lyons, C.G., Prendergast, P.J., 2004. Measurement of the Relative Motion Between an Implant and Bone under Cyclic Loading. *Strain* 40, 193–202.
- Buechel, F.F., Pappas, M.J., SpringerLink, 2012. Properties of Materials in Orthopaedic Implant Systems. In: *Principles of Human Joint Replacement*. Springer Berlin Heidelberg, Berlin, Heidelberg, pp. 1–35.
- Chen, P.C., Pinto, J.G., Mead, E.H., D’Lima, D.D., Colwell Jr., C.W., 1998. Fatigue model to characterize cement-metal interface in dynamic shear. *Clinical Orthopaedics and Related Research* 350, 229–236.

- Crowninshield, R., 1998. Cemented femoral component surface finish mechanics. *Clinical Orthopaedics and Related Research* 90–102.
- Davis, J.R., 2003. Coatings. In: *Handbook of Materials for Medical Devices*. ASM International, Materials Park, OH, pp. 179–194.
- Goldberg, V.M., Figgie 3rd, H.E., Inglis, A.E., Figgie, M.P., 1988. Total elbow arthroplasty. *The Journal of Bone and Joint Surgery; American Volume* 70, 778–783.
- Hallam, P., Haddad, F., Cobb, J., 2004. Pain in the well-fixed, aseptic titanium hip replacement. The role of corrosion. *The Journal of Bone and Joint Surgery; British Volume* 86, 27–30.
- Hernández-Rodríguez, M. a. L., Mercado-Solís, R.D., Pérez-Unzueta, a. J., Martínez-Delgado, D.I., Cantú-Sifuentes, M., 2005. Wear of cast metal–metal pairs for total replacement hip prostheses. *Wear* 259, 958–963.
- Jeffers, J.R., Browne, M., Taylor, M., 2005. Damage accumulation, fatigue and creep behaviour of vacuum mixed bone cement. *Biomaterials* 26, 5532–5541.
- Jeon, I.H., Morrey, B.F., Sanchez-Sotelo, J., 2012. Ulnar component surface finish influenced the outcome of primary Coonrad-Morrey total elbow arthroplasty. *Journal of Shoulder and Elbow Surgery* 21, 1229–1235.
- Jergesen, H.E., Karlen, J.W., 2002. Clinical outcome in total hip arthroplasty using a cemented titanium femoral prosthesis. *The Journal of Arthroplasty* 17, 592–599.
- Kedgley, A.E., Takaki, S.E., Lang, P., Dunning, C.E., 2007. The effect of cross-sectional stem shape on the torsional stability of cemented implant components. *Journal of Biomechanical Engineering* 129, 310–314.
- Kutzner, I., Heinlein, B., Graichen, F., Bender, A., Rohlmann, A., Halder, A., Beier, A., Bergmann, G., 2010. Loading of the knee joint during activities of daily living measured in vivo in five subjects. *Journal of Biomechanics* 43, 2164–2173.

- Lewis, G., 1997. Properties of acrylic bone cement: state of the art review. *Journal of Biomedical Materials Research* 38, 155–182.
- Lewis, G., 2011. Viscoelastic properties of injectable bone cements for orthopaedic applications: state-of-the-art review. *Journal of Biomedical Materials Research Part B, Applied Biomaterials* 98, 171–191.
- Navarro, M., Michiardi, A., Castano, O., Planell, J.A., Castaño, O., 2008. Biomaterials in orthopaedics. *Journal of the Royal Society, Interface* 5, 1137–1158.
- New Zealand Orthopaedic Association, T.N.Z.J.R., 2010. Eleven Year Report- January 1999 to December 2009., <http://www.cdhb.govt.nz/njr/reports/A2D65CA3.pdf>.
- Ryan, G., Pandit, A., Apatsidis, D.P., 2006. Fabrication methods of porous metals for use in orthopaedic applications. *Biomaterials* 27, 2651–2670.
- Sanchez-Sotelo, J., 2011. Total elbow arthroplasty. *The Open Orthopaedics Journal* 5, 115–123.
- Schweizer, A., Luem, M., Riede, U., Lindenlaub, P., Ochsner, P.E., 2005. Five-year results of two cemented hip stem models each made of two different alloys. *Archives of Orthopaedic and Trauma Surgery* 125, 80–86.
- Van der Lugt, J.C., Rozing, P.M., 2004. Systematic review of primary total elbow prostheses used for the rheumatoid elbow. *Clinical Rheumatology* 23, 291–298.
- Van der Lugt, J.C., Suarez, D.R., van der Steenhoven, T.J., Nelissen, R.G., 2010. Minor influence of humeral component size on torsional stiffness of the Souter-Strathclyde total elbow prosthesis. *International Orthopaedics* 34, 1213.
- Verdonschot, N., 2005. Philosophies of stem designs in cemented total hip replacement. *Orthopedics* 28, s833–840.
- Walsh, W.R., Svehla, M.J., Russell, J., Saito, M., Nakashima, T., Gillies, R.M., Bruce, W., Hori, R., 2004. Cemented fixation with PMMA or Bis-GMA resin

hydroxyapatite cement: effect of implant surface roughness. *Biomaterials* 25, 4929–4934.

Westphal, F.M., Bishop, N., Honl, M., Hille, E., Puschel, K., Morlock, M.M., 2006. Migration and cyclic motion of a new short-stemmed hip prosthesis--a biomechanical in vitro study. *Clinical Biomechanics* 21, 834–840.

Wilson, L.J., Bell, C.G.R., Weinrauch, P., Crawford, R., 2009. In vitro cyclic testing of the Exeter stem after cement within cement revision. *The Journal of arthroplasty* 24, 789–94.



## CHAPTER 4: THE EFFECT OF STEM SURFACE TREATMENT AND MATERIAL ON PISTONING OF ULNAR COMPONENTS IN LINKED CEMENTED ELBOW PROSTHESES

**Overview:** *The ulnar component of a total elbow replacement can fail via stem “pistonning”, which occurs as a result of axial loads generated at the ulnohumeral joint in routine daily activities. The application of stem surface treatments to titanium and cobalt chrome elbow systems has resulted in improved clinical success, but with varied responses. This chapter compares the stability response of smooth, beaded and plasma spray surface treatments, applied to titanium and cobalt chrome stems, in resisting axial forces at the stem-cement interface. Results of this study explain the relationship between stem surface treatments and substrate material in overall implant stability, as well as suggest various failure mechanisms associated with each of the surface treatments.*<sup>2</sup>

### 4.1 INTRODUCTION

Ulnar component pistonning has been described as one of the main failure mechanisms of total elbow prostheses (Cheung and O’Driscoll, 2007), leading to loosening of the implant system. Joint reaction forces that result in tension/compression loads acting across the ulnohumeral joint occur when the elbow is in the flexed position and can lead to this pistonning effect (Amis, 2012; Goldberg *et al.*, 1988; Johnson and King, 2005). Stem design factors, including the application of surface treatments, are expected to resist the effects of mechanical loosening caused by these forces (Evans *et*

---

<sup>2</sup> A version of this work has been published: Y.K. Hosein, G.J.W. King, C.E. Dunning (2013). “The Effect of Stem Surface Treatment and Material on Pistoning observed in Ulnar Components of Linked Cemented Elbow Prostheses” *Journal of Shoulder and Elbow Surgery*. [E-pub ahead of print; PMID: 23668920] (See Appendix I for the letter of permission)

*al.*, 1988). With surface treatments, improved cement fixation can be hypothesized based on the premise of a mechanical interlock formed between the bulk cement and treated stem surface. For ulnar components specifically, a clinical study by Jeon *et al.*, showed that various surface treated stems experienced different rates of loosening (Jeon *et al.*, 2012); however, no known *in-vitro* studies have compared the success of these surface treatments relative to one another.

Sintered beads and thermal plasma sprays are two common surface treatments used in ulnar stem designs. The Coonrad/Morrey Total Elbow (Zimmer Inc.), in particular, has modified its titanium prosthesis design over the years based in part on varying these two surface treatments (Jeon *et al.*, 2012). In addition, the Latitude EV (Tornier Inc.) (cobalt chrome stem) and Discovery Elbow System (Biomet Inc.) (titanium stem) incorporate a plasma spray surface treatment in their ulnar component designs. When taking into consideration the varying surface topographies of the respective surface treatments (*i.e.*, beaded and plasma spray), it can be hypothesized that the type of stem surface treatment may affect the strength of the mechanical interlock formed between the stem and cement. Comparisons of this mechanical interlock can offer insight into failure mechanisms associated with these surface treated implants.

Titanium and cobalt chrome alloys are both used as the substrate material in elbow prosthesis stem designs. Stem substrate material may play a role in the success of the applied surface treatment, since the composition of the substrate can influence the strength of stem-treatment bond formed during treatment process (Davis, 2003). As such, it is important to consider stem material when investigating the role of surface treatments in prosthesis loosening.

Therefore, the purpose of this *in-vitro* study was to investigate the role of stem surface treatment and substrate material on the stability of a simulated ulnar implant stem subjected to cyclic compression loading.

## 4.2 MATERIALS AND METHODS

Sixty smooth, circular, implant stems ( $\varnothing = 8$  mm) were custom machined from both titanium ( $n = 30$ ), and cobalt chrome ( $n = 30$ ) by Tornier S.A.S. (Grenoble, France). For each material, the stems were sub-divided into five equal groups. The first group retained their full length smooth surface ( $n = 6$ ), while the remaining four groups had standard commercially employed stem surface treatments applied by Orchid Bio-Coat (Southfield, MI, USA). Two groups received a beaded surface treatment with coverage lengths of 20 mm ( $n = 6$ ) and 10 mm ( $n = 6$ ), while two groups received a plasma spray surface treatment with coverage lengths of 20 mm ( $n = 6$ ) and 10 mm ( $n = 6$ ) (Figure 4.1) (Appendix G). The beaded surfaces consisted of one layer of beads, with a bead diameter of approximately 500  $\mu\text{m}$ . The plasma sprayed surfaces were titanium plasma spray (TPS) and had a  $R_a$  value of  $48.5 \pm 3.9$   $\mu\text{m}$ .

All stems were potted to a fixed depth of 20 mm in square aluminum tubes using vacuum-mixed PMMA bone cement (Simplex P<sup>®</sup>, Stryker<sup>®</sup>, Kalamazoo, MI, USA), such that there was full coverage of the surface treated regions. For the 10 mm surface treated stems, this potting method allowed for cement coverage of the 10 mm treated region, as well as an additional 10 mm of proximal smooth stem surface (Figure 4.1). The potted stems were maintained in air at 22 °C for 24 hours during curing. Subsequently, they were secured in a materials testing machine (Figure 4.2) (Instron<sup>®</sup> 8874, Norwood, MA, USA). Custom machined fixturing ensured that stems were fully centralized during testing (Appendix G.10), accommodating stem push-out under compression, with minimal contribution of off-axis loading, as monitored by the 6 degrees of freedom load cell of the materials testing machine. A Delrin<sup>®</sup> stopper was placed inside the aluminum tube at the base of the cement mantle to ensure push-out of the stem only, without slipping of the cement mantle within the aluminum tube.

Loading cycled at 1.5 Hz under compression, keeping loads between 500 N and an upper limit. The upper limit started at 1000 N and increased in increments of 1000 N every 100 cycles to a maximum 10000 N, after which it cycled for a further 25000 cycles

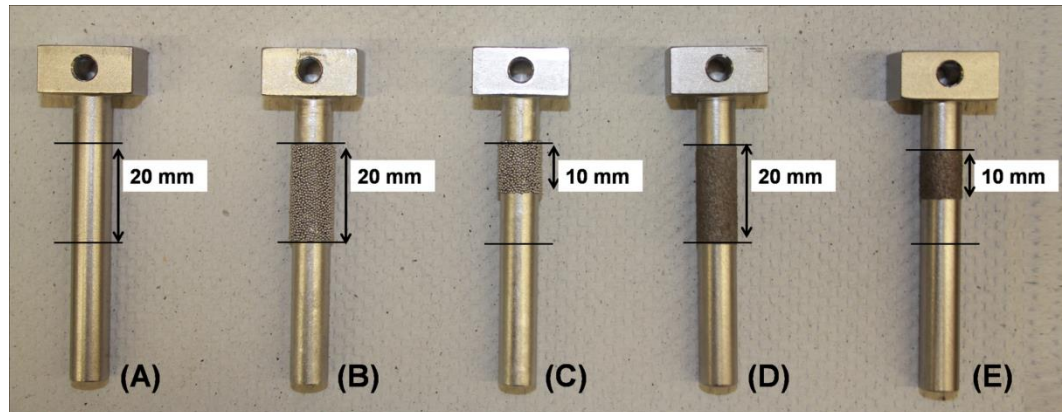


**Figure 4.1: Surface Treated Implant Stems used for Compression Testing**

Implant stems with various surface treatments: (A) smooth, (B) 20 mm length beaded treatment, (C) 10 mm length beaded treatment, (D) 20 mm length plasma spray treatment, and (E) 10 mm length plasma spray treatment. Stems were cemented to a fixed 20 mm depth, as highlighted by the region between the parallel lines. For the 10 mm length surface treated stems, this allowed full cement coverage of the surface treated region, as well as an additional 10 mm length of proximal smooth stem surface.

to complete the testing protocol (*i.e.*, total 25900 cycles). Failure of the stem-cement interface was defined as 2 mm push-out of the stem relative to the cement, termed ‘catastrophic failure’, or until completion of the loading protocol.

Motion at the stem-cement interface was quantified using the custom optical tracking system described in Chapter 2 (Basler Pilot GigE Camera, Ahrensburg, Germany; Opto Engineering Telecentric Lens, Mantova, Italy; and LabVIEW Vision Acquisition System, National Instruments, Austin, TX, USA). This system incorporated a colour thresholding method to optically track the centroid of markers placed on the stem and cement (Figure 4.2), to determine their relative distances throughout loading.

Immediately following testing, the cemented stems were placed into Acetone (Caledon Laboratories Ltd., Georgetown, ON, Canada) for 24 hours to allow dissolution of the surrounding bone cement. The stems were subsequently cleaned and visually inspected to determine the presence of any surface treatment damage associated with testing.

Stem-cement interface strength and stem motion were both quantified. Interface strength was determined from the number of cycles required to cause failure for each of the stems, as obtained from the materials testing machine. Stem motion was determined from the relative distances between the markers on the stem and cement prior to failure (*i.e.*, termed “interface toggle”) (Figure 4.2). For those stems that reached 10000 N in the loading protocol, and survived beyond the first 100 cycles, an additional measure of stem motion (*i.e.*, termed “global motion”) was used. Global motion measured the displacement of the stem within the camera’s coordinate system (*i.e.*, not relative to the cement) from 901 cycles (*i.e.*, start of the 10000 N load step) until failure, and allowed relative comparison of surface treatments at the constant 10000 N load level (Figure 4.2).

Two-way analyses of variance with post-hoc Student-Newman-Keuls tests ( $\alpha = 0.05$ ) were used to examine the role of stem surface treatment and substrate material on cemented stem stability, based on the measures of interface strength and stem motion.

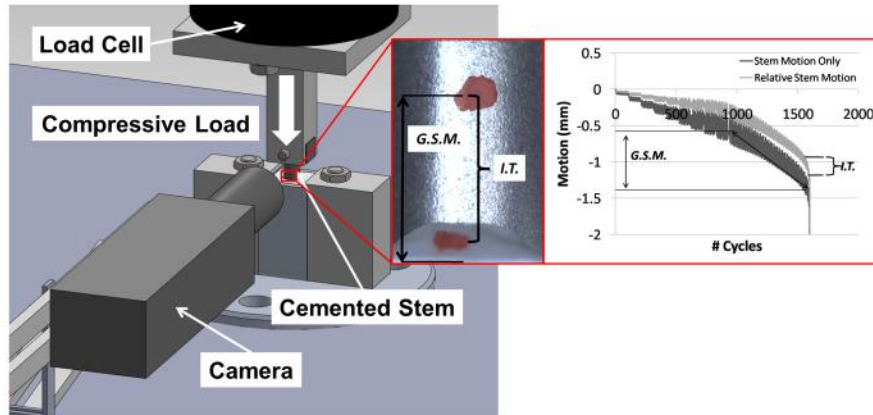


**Figure 4.2: Experimental Set-up for Compression Testing of Implant Stems**

Schematic of the cemented stem in the materials testing machine, showing application of a compressive load. The camera was used to track markers placed on the stem and cement throughout loading as shown in the inset image. The relative distance between the stem and cement was used to determine interface toggle (*I.T.*) just prior to failure. The change in global motion of stems from 901 cycles (*i.e.*, start of 10000 N load step) until failure (*G.S.M.*) was used to compare axial motion of surface treated stems at a constant load level.

### 4.3 RESULTS

Post-testing visual inspection of the stems found that the 10 mm beaded titanium and 10 mm beaded cobalt chrome stems were the only surfaces to experience mechanical damage at failure (Figure 4.3). This was observed as debonding of the beaded treatments from the stem surfaces. All other stem surfaces remained intact, with no visual damage evident.

Survival curves illustrated that stem surface treatment did affect stem stability under compression loading, where the 20 mm length, beaded stems outlasted the other stem surfaces (Figure 4.4). Data obtained from the optical tracking system showed that stem motion increased simultaneously with the cyclic staircase loading protocol (Figure 4.5), and as such, all motion data (*i.e.*, interface toggle and global stem motion) was normalized to their respective loads and cycles, to allow for relative comparison of stem surfaces.

With regards to cycles to failure, the two-way ANOVA found an overall effect of surface treatment ( $p < 0.05$ ) and no overall effect of substrate material ( $p = 0.25$ ), but there was a significant interaction between these factors ( $p = 0.02$ ) (Figure 4.6A). Therefore, one-way ANOVAs were performed, and showed that for titanium, the 20 mm beaded stems outlasted all other treatments ( $p < 0.05$ ). For cobalt chrome, the 20 mm beaded stems outlasted all other treatments ( $p < 0.05$ ), but the 20 mm plasma spray stem also performed better than the 10 mm beaded, 10 mm plasma spray, and smooth stems ( $p < 0.05$ ).

With regards to interface toggle, the two-way ANOVA again found an overall effect of surface treatment ( $p < 0.05$ ), no overall effect of substrate material ( $p = 0.78$ ), and a significant interaction between these factors ( $p = 0.01$ ) (Figure 4.6B). One-way ANOVAs showed that for titanium, the 20 mm beaded, 10 mm beaded, and 20 mm plasma spray stems experienced less toggle than the 10 mm plasma spray and smooth ( $p < 0.05$ ), with the 10 mm plasma spray stem exhibiting less toggle than the smooth ( $p < 0.05$ ).

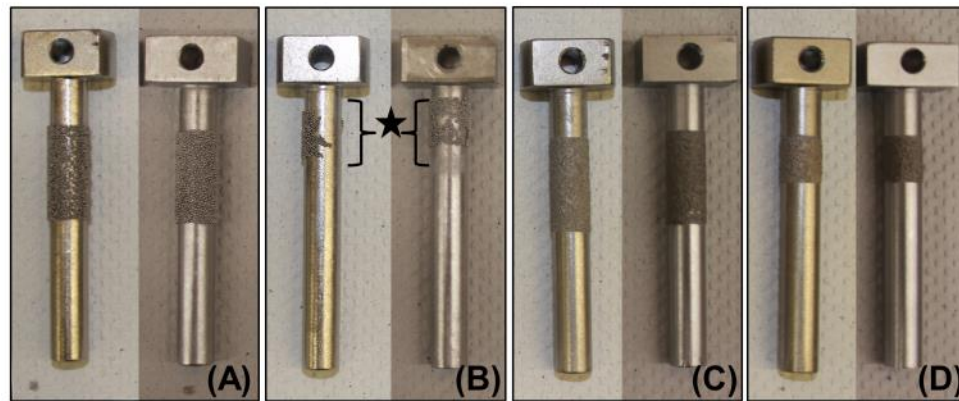


**Figure 4.3: Inspection of Stem Surface Treatments Post-Compression Tests**

(A) Titanium (left) and cobalt chrome (right) 20 mm length beaded stems, (B) titanium (left) and chrome (right) 10 mm length beaded stems, (C) titanium (left) and cobalt chrome (right) 20 mm length plasma spray stems, and (D) titanium (left) and cobalt chrome (right) 10 mm length plasma spray stems. The 10 mm length beaded titanium and cobalt chrome stems were the only stems to experience debonding of the treatment from the stem surface at failure, as highlighted by the starred region.



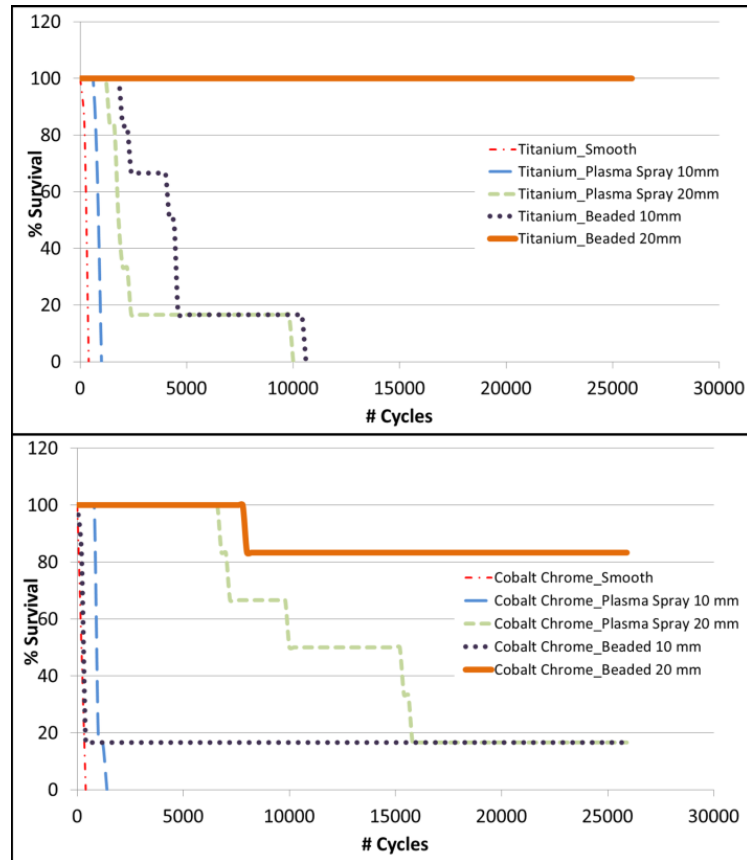


**Figure 4.4: Survival Curves for Titanium and Cobalt Chrome Stems**

Survival curves for titanium (top), and cobalt chrome (bottom) stems. The 20 mm length beaded stem experienced longest survival, while smooth stem surface experienced shortest survival, as defined by the number of cycles required to cause failure.

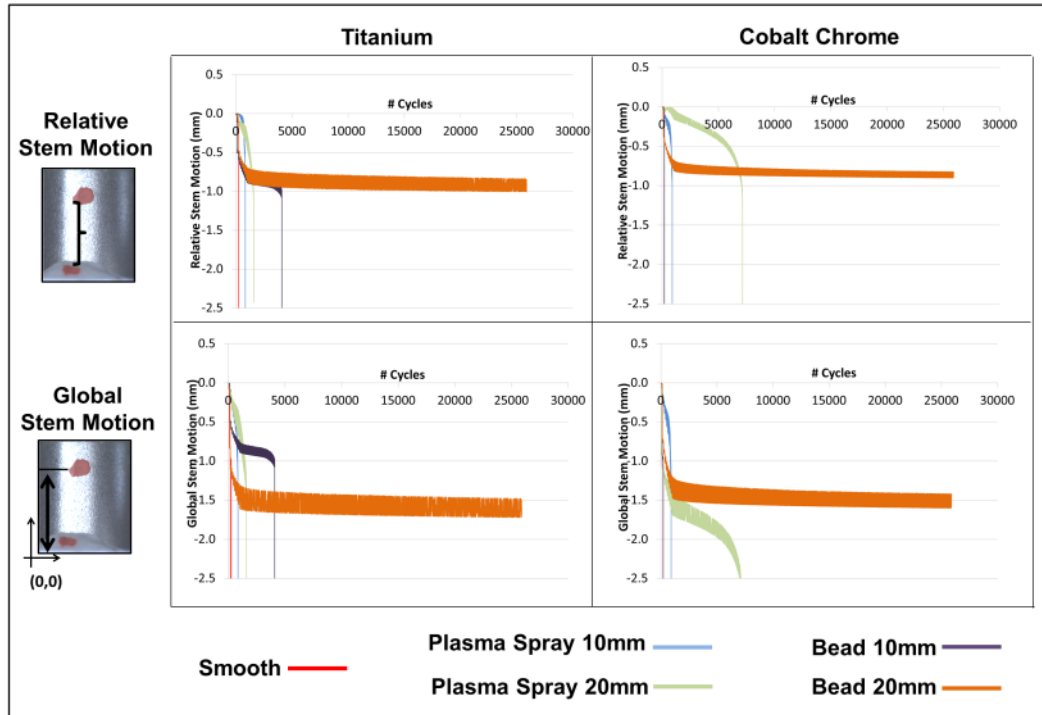


**Figure 4.5: Stem Motion for Titanium and Cobalt Chrome Stems under Compression**

Representative graphs of stem motion relative to cement (top row), and global stem motion (bottom row) for titanium and cobalt chrome stems. The 20 mm length beaded stem did not experience catastrophic failure, as defined by 2 mm of stem push-out, for eleven of the twelve stems tested.

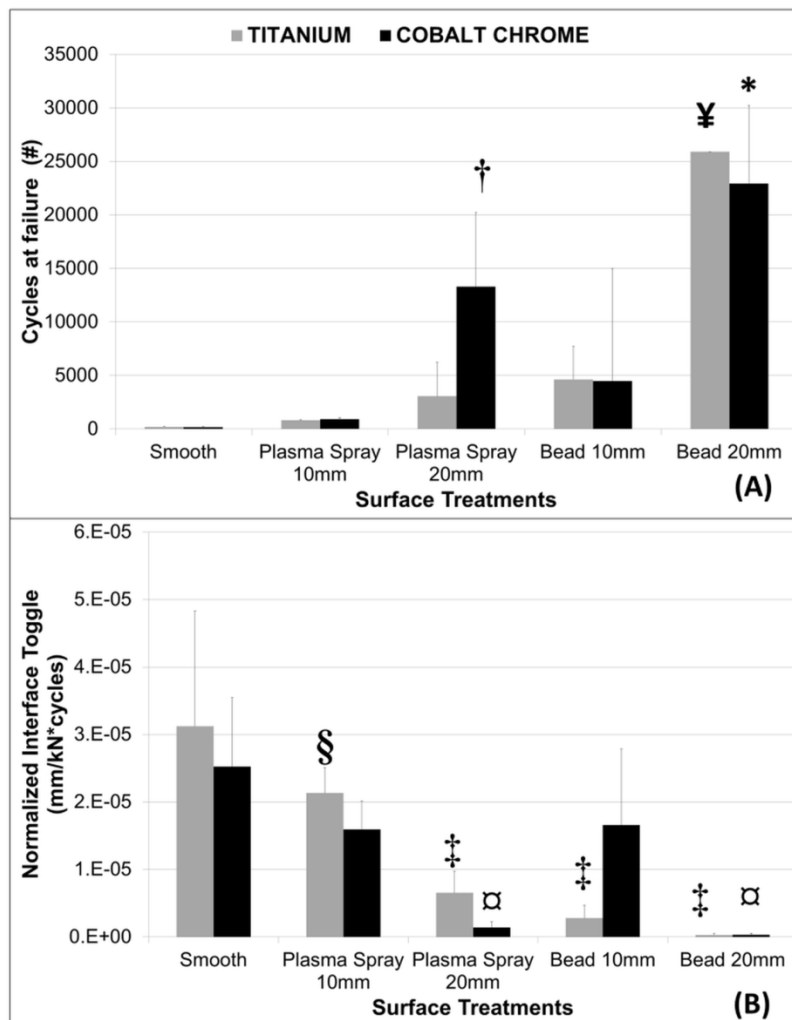


**Figure 4.6: Interface Stability Offered by the Surface Treated Stems in Compression**

**(A) Cycles at failure:** For titanium, the 20 mm beaded treatment experienced the most cycles compared to all stem surfaces ( $p < 0.05^{\ddagger}$ ). For cobalt chrome, the 20 mm beaded stem outlasted the other treatments ( $p < 0.05^*$ ), with 20 mm length plasma spray treatment also showing greater cycles to failure than the other stem surfaces ( $p < 0.05^{\dagger}$ ).

**(B) Interface Toggle prior to failure:** For titanium, the 20 mm beaded, 10 mm beaded, and 20 mm plasma spray stems showed the smallest magnitudes of interface toggle ( $p < 0.05^{\ddagger}$ ), with the 10 mm plasma spray stem experiencing less toggle than the smooth ( $p < 0.05^{\S}$ ). For cobalt chrome, the 20 mm beaded, and 20 mm plasma spray treatments showed reduced interface toggle compared to all other stems ( $p < 0.05^{\text{rt}}$ ).

For cobalt chrome, the 20 mm beaded and 20 mm plasma spray stems experienced less toggle than the 10 mm length surface treatments and smooth stems ( $p < 0.05$ ).

When comparing the global motion of surface treated stems at a constant 10000 N load level, it was found that surface treated stems demonstrated various magnitudes of stem motion (Figure 4.7). Overall, the 20 mm and 10 mm beaded treatments experienced the least stem motion ( $p < 0.05$ ), with the 20 mm plasma spray treatment also showing less stem motion than the 10 mm plasma spray treatment ( $p < 0.05$ ). Cobalt chrome stems showed less motion than titanium ( $p = 0.02$ ).

#### 4.4 DISCUSSION

Surface treatments have been added to cemented ulnar components of total elbow arthroplasties with the aim of improving stem fixation and long term stability (Jeon *et al.*, 2012). Bone cement is considered a connecting agent, much like a grout material. When used with a surface treated component, it is expected to fill the spaces of the treated surface, initiating a mechanical interlock between the stem and cement. The strength of the interlock formed may subsequently improve immediate and long term stem fixation.

The evolution of ulnar component designs over the last decade has incorporated different stem surface treatments, specifically sintered beads and plasma spray, with the goal of improving the strength of the stem-cement interlock formed, while preserving the mechanical integrity (*i.e.*, fracture properties) of the substrate stem material (Jeon *et al.*, 2012). While clinical studies have assessed the success of various commercially available elbow prosthesis designs incorporating these surface treatments (Fevang *et al.*, 2009; Skytta *et al.*, 2009; van der Lugt and Rozing, 2004), there are no known *in-vitro* studies that have compared their role in component stability, or provided information on the failure mechanisms associated with these stem surface treatments.

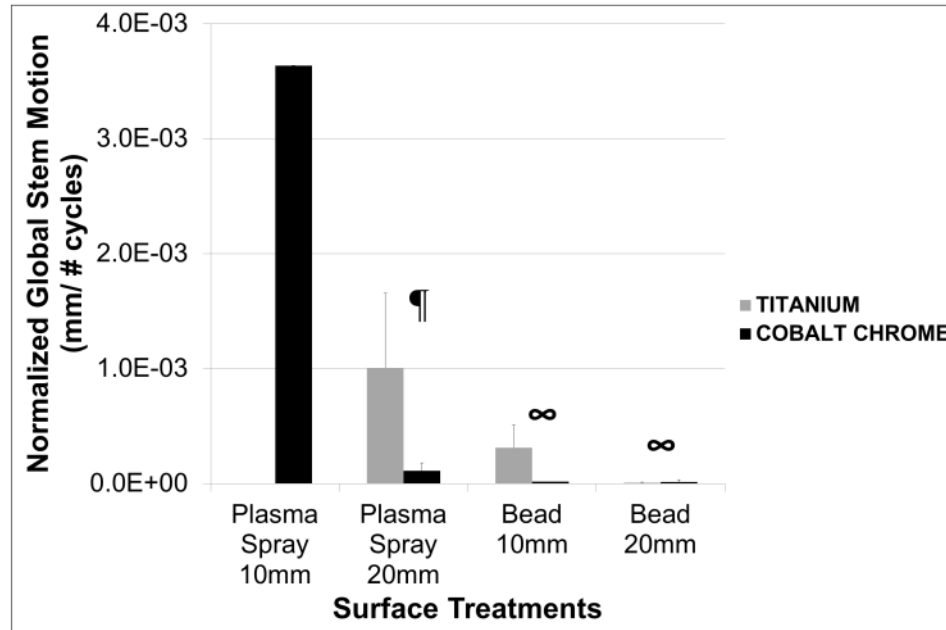


**Figure 4.7: Global Stem Motion of Surface Treated Stems in Compression**

Global motion of the surface treated stems from 901 cycles (*i.e.*, start of the 10000 N load step) until failure. The 20 mm and 10 mm beaded stems demonstrated the smallest magnitudes of stem motion ( $p < 0.05^{**}$ ), with the 20 mm plasma spray treatment also showing less stem motion than the 10 mm plasma spray treatment ( $p < 0.05^{**}$ ). Overall, cobalt chrome stems showed less motion than titanium ( $p = 0.02$ ).

Pistoning of the ulnar component of linked total elbow replacements is one source of implant loosening, and can occur from axial forces acting at the implant-cement interface. These axial forces result from dynamic loading of the ulnohumeral joint in routine daily activities (Amis, 2012; Goldberg *et al.*, 1988; Johnson and King, 2005), or from impingement of coronoid processes or protruding cement during elbow hyperflexion, causing distraction forces to occur on the ulnar component (Cheung and O'Driscoll, 2007). Therefore, in order to compare the effects of different surface treatments on component stability, axial forces that may contribute to stem pistoning should be considered. Pistoning forces that occur *in-vivo* typically act in tension at the proximal end of the ulnar component; however, the shear forces produced at the stem-cement interface are the same as those expected if the stems were exposed to similar compression loads. As such, the purpose of this study was to investigate the role of stem surface treatment on the stability of titanium and cobalt chrome implant stems, using a study design incorporating cyclic compression loading to mimic ulnar pistoning at failure.

Stem surface treatment had a major effect on overall stem stability. When looking at interface strength and stem motion, the 20 mm beaded treatment showed greatest survival and least toggle when compared to the other stem surfaces for both titanium and cobalt chrome stems (Figure 4.6). Beaded treatments have greater surface deviations with regards to its surface topography, when compared to other stem surfaces. Based on the diameter of the sintered beads applied to the stem surface, this may allow for greater infiltration of bone cement onto the stem surface. Failure of the stem-cement interface would therefore be dependent on the amount of shearing force needed to overcome each interlock along the stem's surface. Greater cement infiltration, in terms of depth and number of interlocking sites, would therefore require greater cyclic loads to cause stem instability, resulting in interface failure and stem push-out.

For stems that failed catastrophically (*i.e.*, experienced 2 mm push-out), significant interaction was observed between stem surface treatment and substrate material for measures of interface strength and toggle. The 20 mm plasma spray cobalt chrome stem performed better than both of the 10 mm length, surface treatments and

smooth cobalt chrome stems (Figure 4.6). For titanium stems, however, the 20 mm plasma spray treatment performed similar to the 10 mm length, surface treatments and smooth surfaces. Therefore, although stem surface treatment contributed to improved interface stability prior to catastrophic failure, this was dependent on the stem substrate material.

When comparing the interface mechanics for the individual stem-cement interfaces at catastrophic failure, the smooth stem surfaces appeared to offer no resistance to the shearing force at the interface, and as such, once the stem-cement bond was broken, the stem failed rapidly. In comparison, for cobalt chrome stems, the roughened surface of the 20 mm plasma spray stem provided frictional resistance to the shearing force at the stem-cement interface, which was greater than that provided by the 10 mm length, plasma spray and 10 mm length, beaded treatments. Once the shearing force at the interface became larger than the frictional force, the stems experienced push-out.

Post-testing inspection of the stem surfaces found that the 10 mm beaded stem was the only surface to experience mechanical damage at failure (Figure 4.3). This suggests that the number of cycles to failure for the 10 mm beaded treatment may not be representative of the stem-cement interface strength, but more likely a measure of the strength of the bond between the beads and stem surface. The strength of this bond is directly related to the carbon content of the base substrate material, where a lower carbon content can affect the success of the sintering process, causing a weaker bond between the stem substrate material and attached beads (Davis, 2003). Although beaded treatments are likely to contribute to satisfactory interface strengths, as observed from the 20 mm beaded treatments, there may be variability in its performance based on the success of the sintering treatment during the fabrication process. As such, stringent standards should be placed on the fabrication process of beaded stem designs, ensuring adequate material composition of the base substrate metals before application of the beaded treatments.

For stems that surpassed the staircase region of the loading protocol, and reached 1000 cycles without failure, global stem motion was used to compare the contribution of

stem surface treatments to stem motion at the constant 10000 N level. Global stem motion included motion of the stem with cement, and offered information on the failure patterns associated with the different stem surface treatments. Overall, beaded stems experienced less stem motion compared to the plasma spray surfaces. As mentioned previously, the roughened surface of the plasma spray treatment provided frictional resistance to the shearing force at the stem-cement interface, and this resistance was represented by the gradual increase in stem motion prior to catastrophic failure (*i.e.*, gradual interface failure). In comparison, catastrophic failure of 10 mm length, beaded stems was influenced by the bond broken between the beads and the stem surface, resulting in a stable interface with little stem motion before stem push-out (*i.e.*, rapid interface failure). When analyzing stem motion for the 20 mm length beaded stems that did not experience catastrophic failure, it was seen that these values were comparable to the 10 mm length beaded surfaces, even at the end of the loading protocol (*i.e.*, 10000 N; 25900 cycles). This suggests that the 20 mm length beaded treatment contributed to a stable stem-cement interface.

Titanium and cobalt chrome are two common stem metals used in ulnar component designs (Van der Lugt and Rozing, 2004). Each offers its own advantages to implant systems in terms of biocompatibility, wear resistance and mechanical properties (Hallab *et al.*, 2004; Navarro *et al.*, 2008). However, application of surface treatments to the substrate metal can influence the success of the implant system. Clinical studies have reported that beaded treatments on titanium stems can cause increased rates of component fracture, believed to be caused by weakening of the metal during the bead sintering process (Athwal and Morrey, 2006; Jeon *et al.*, 2012). Our study did not evaluate the strength of the metal stemmed components, but found that the success of the surface treatments was directly related to stem material type. As mentioned before, variations in the metal composition, specifically the carbon content of the substrate metal, can directly affect the strength of the bond formed between the beads and stem during the sintering process. Therefore, future studies should look into investigating the effect of stem substrate material composition on the bonding strength of beaded treatments, as well as the effect of the bead sintering process on the fracture properties of different stem substrate materials commonly used with elbow prostheses.



During elbow flexion, the ulnohumeral joint is under compression/tension, where resultant forces act upwards onto the distal end of the humerus (Amis, 2012), and varies depending on the angle of elbow flexion. These joint forces can act on linked total elbow prostheses in a similar manner, where resultant forces act upwards onto the humeral component causing pull-out of the connected ulnar component. It is postulated that pull-out of the ulnar component may also occur from distraction forces produced when the elbow is hyperflexed past a limit set by an impinging structure (*i.e.*, flange, cement, bone), creating a fulcrum loading scenario (Jeon *et al.*, 2012), or from carrying a heavy object during elbow extension, causing forces at the trochlea of up to twenty times the external load at the hand (Amis *et al.*, 1980). Both axial loading examples create shear forces along the length of the stem-cement interface, which can cause interface debonding and resultant pistoning of the ulnar component. Our study incorporated a cyclic compressive load to mimic dynamic shear forces that may cause pistoning of the implant stem under axial loading, similar to that experienced by the ulnar component. As such, the loads used for compression testing (*i.e.*, 500–10000 N) were intentionally chosen to compare the effect of the different surface treatments in a cyclic pistoning scenario, similar to that caused by resultant joint forces or distraction forces at the ulnohumeral joint.

From the measures of stem motion as detected from the optical tracking system, it was observed that the cement directly surrounding the stem contributed to overall stem motion. This was seen in measures of relative and global stem motion, where the stem experienced greater motion in the global frame when compared relative to the cement (Figure 4.5). This may be explained by the creep properties exhibited by bone cement under dynamic loading (Lewis, 2011). This contribution of cement creep may also explain the variability seen in our motion results for smooth stems. The stability of smooth stems was influenced by the stem-cement bond formed at the interface, and as such, any motion detected prior to failure may have been solely dependent on the visco-elastic nature of the cement on individual testing days. Bone cement properties could have also affected the minimal stem motion observed for the 20 mm beaded stems that completed the testing protocol (*i.e.*, 25900 cycles), since previous work showed that bone cement becomes stiffer with increasing loading cycles (Verdonschot and Huiskes, 1995).

This *in-vitro* study, to the authors' knowledge, is the first to compare the effects of stem surface treatment and substrate material on pistoning of an implant stem under axial load. The study was successful at showing the contribution of beaded and plasma spray surface treatments to stem-cement interface stability, as well as able to provide information on the failure mechanisms associated with these surface treated stems. Overall, the 20 mm beaded stems offered the greatest stability among all stem surfaces, and for cobalt chrome stems only, the 20 mm plasma spray stems contributed to improved stability as well. When comparing mechanisms of catastrophic failure, smooth stems failed via debonding at the stem-cement interface, beaded stems failed via debonding of the beaded surface treatment from the stem surface, and plasma spray stems failed via loss of frictional force between the plasma spray treatment and bone cement. It is expected that the results from this biomechanical analysis will help to understand the contribution of surface treatments in component pistoning, and provide information about the failure mechanisms associated with similar clinical stem designs.

#### 4.5 CONCLUSION

For surface treated stems tested in cyclic compression loading, beaded performed better than plasma spray treatments on titanium and cobalt chrome stem substrates. However, plasma spray treatments performed better on cobalt chrome than titanium stem substrate. Overall, for both beaded and plasma spray treatments stem stability was improved with a greater surface treatment coverage length.

## 4.6 REFERENCES

- Amis, A.A., 2012. Biomechanics of the Elbow. In: Stanley, D., Trail, I. (Eds.), *Operative Elbow Surgery*. Churchill Livingstone Elsevier, Edinburgh; New York, pp. 29–44.
- Amis, A.A., Dowson, D., Wright, V., 1980. Elbow joint force predictions for some strenuous isometric actions. *Journal of Biomechanics* 13, 765–775.
- Athwal, G.S., Morrey, B.F., 2006. Revision total elbow arthroplasty for prosthetic fractures. *The Journal of Bone and Joint Surgery; American Volume* 88, 2017–2026.
- Cheung, E. V, O’Driscoll, S.W., 2007. Total elbow prosthesis loosening caused by ulnar component pistoning. *The Journal of Bone and Joint Surgery; American Volume* 89, 1269–1274.
- Davis, J.R., 2003. Coatings. In: *Handbook of Materials for Medical Devices*. ASM International, Materials Park, OH, pp. 179–194.
- Evans, B.G., Daniels, A.U., Serbousek, J.C., Mann, R.J., 1988. A comparison of the mechanical designs of articulating total elbow prostheses. *Clinical Materials* 3, 235–248.
- Fevang, B.-T.S., Lie, S.A., Havelin, L.I., Skredderstuen, A., Furnes, O., 2009. Results after 562 total elbow replacements: A report from the Norwegian Arthroplasty Register. *Journal of Shoulder and Elbow Surgery* 18, 449–456.
- Goldberg, V.M., Figgie 3rd, H.E., Inglis, A.E., Figgie, M.P., 1988. Total elbow arthroplasty. *The Journal of Bone and Joint Surgery; American Volume* 70, 778–783.
- Hallab, N.J., Urban, R.M., Jacobs, J.J., 2004. Corrosion and Biocompatibility of Orthopedic Implants. In: Yaszemski, M., Trantolo, D., Lewandrowski, K., Hasirci, V., Altobelli, D., Wise, D. (Eds.), *Biomaterials in Orthopedics*. Marcel Dekker, Inc., New York, pp. 63–91.

- Jeon, I.H., Morrey, B.F., Sanchez-Sotelo, J., 2012. Ulnar component surface finish influenced the outcome of primary Coonrad-Morrey total elbow arthroplasty. *Journal of Shoulder and Elbow Surgery* 21, 1229–1235.
- Johnson, J.A., King, G.J.W., 2005. Anatomy and Biomechanics of the Elbow. In: Williams, G.R. (Ed.), *Shoulder and Elbow Arthroplasty*. Lippincott Williams & Wilkins, Philadelphia, pp. 279–296.
- Lewis, G., 2011. Viscoelastic properties of injectable bone cements for orthopaedic applications: state-of-the-art review. *Journal of Biomedical Materials Research, Part B, Applied Biomaterials* 98, 171–191.
- Navarro, M., Michiardi, A., Castano, O., Planell, J.A., Castaño, O., 2008. Biomaterials in orthopaedics. *Journal of the Royal Society, Interface* 5, 1137–1158.
- Skytta, E.T., Eskelinen, A., Paavolainen, P., Ikavalko, M., Remes, V., 2009. Total elbow arthroplasty in rheumatoid arthritis: a population-based study from the Finnish Arthroplasty Register. *Acta Orthopaedica* 80, 472–477.
- Van der Lugt, J.C., Rozing, P.M., 2004. Systematic review of primary total elbow prostheses used for the rheumatoid elbow. *Clinical Rheumatology* 23, 291–298.
- Verdonschot, N., Huiskes, R., 1995. Dynamic creep behavior of acrylic bone cement. *Journal of Biomedical Materials Research* 29, 575–581.

## CHAPTER 5: THE EFFECT OF STEM CIRCUMFERENTIAL GROOVES ON THE STABILITY AT THE IMPLANT-CEMENT INTERFACE

*Overview:* Previous chapters of this thesis discussed the application of beaded and plasma sprayed treatments for improving stem-cement interface stability in joint replacement systems; however, results showed variable success of these surfaces. As opposed to the addition of a treatment or finish to the base stem material, altering stem design through changing the surface topography by removal of a portion of the base stem material may offer some advantages. This study compared the effect stem circumferential grooving, with varying grooved dimensions, on the torsional and axial stability of cemented stems. Findings from this study show the difference in stability response between the two grooved designs, and allowed relative comparison of the circumferential grooves with surface treatments tested in previous chapters of this thesis.<sup>3</sup>

### 5.1 INTRODUCTION

Implant stem design plays an important role in the mechanical stability of implant systems (Barrack, 2000; Evans *et al.*, 1988). Stem surface modifications, such as the application of a surface treatment or surface finish, is one such design factor that can have an influential effect on implant stability (Crowninshield *et al.*, 1998; Jeon *et al.*, 2012; Scheerlinck and Casteleyn, 2006; van der Lugt and Rozing, 2004). Thus far, Chapters 3 and 4 of this thesis have explored the effect of stem surface treatment on the

---

<sup>3</sup> A version of this work is in the revision stage of publication: Y.K. Hosein, G.J.W. King, C.E. Dunning (2013). "The Effect of Circumferential Grooves on the Stability of Cemented Joint Replacement Systems" Journal of Medical Devices.

torsional and axial stability of cemented implant systems. These studies were interested in the overall effect of stem surface treatments on the mechanical response at the stem-cement interface, since it was reported that surface treated implants contributed to reduced rates of loosening in ulnar component systems (Jeon *et al.*, 2012). This clinical finding seemed reasonable considering the expectation of the altered stem surfaces at the fixation interface, which would facilitate infiltration of bone cement during the cement application and curing process. The resulting mechanical connect formed would therefore provide improved implant anchorage, and resistance to implant loosening.

From the results reported in Chapters 3 and 4, it was confirmed that plasma spray and sintered bead treatments improved the overall stability of implant systems under torsional and axial loading; however, their individual contribution to implant stability was quite variable. Beaded coatings appeared to be more stable than plasma spray coatings, but depended on the stem substrate material (*i.e.*, cobalt chrome versus titanium). In addition to this variable stability response, other authors have reported higher fracture rates associated with beaded implant stems, compared to plasma spray stems, which may result from the weakening of the stem substrate metal during the bead sintering process (Athwal and Morrey, 2006; Jeon *et al.*, 2012). As such, the choice between surface treatment types for improving fixation is not a straightforward decision.

Similarly, there have also been mixed reviews over the use of stem surface finishes in cemented lower limb implant designs. It is believed that surface finished stems produce increased cement and/or metal wear at the fixation interface, as a result of the inevitable micromovement of the stem after implantation (Scheerlinck and Casteleyn, 2006). As such, although the surface finish designs initially provide improved implant fixation, they may potentially limit the success of the implant system over time.

An alteration in the surface topography of the base stem material, such as the machining of grooves onto the stem, would eliminate the contribution of an additional interface (*i.e.*, surface treatment onto the stem) to the stability of the cemented stem construct, as well as reduce wear caused by surface finishes at the stem-cement interface, while still allowing for improved mechanical connect and stem fixation during the

cementing process. However, the effect on implant stability is unknown. As such, the purpose of this study was to investigate the effect of circumferential grooves on the stability of cemented stems under compression and torsional loading. It was hypothesized that the application of circumferential grooves would not affect torsional stability, but would have a stabilizing influence in compression, which is of particular interest to upper limb replacement systems that often fail due to tension-compression forces at the joint (Cheung and O'Driscoll, 2007).

## 5.2 MATERIALS AND METHODS

Fifteen metal stems with circular cross-sections ( $\varnothing = 8$  mm) were custom machined from cobalt chrome, and made with smooth ( $n = 5$ ) or circumferentially-grooved ( $n = 10$ ) surfaces (Tornier S.A.S., Grenoble, France) (Figure 5.1) (Appendix G). Individual grooves (*i.e.*, not threaded) were machined along a fixed 20 mm length region of the stem surface. Groove spacing and depths were either 0.6 mm ( $n = 5$ ) or 1.1 mm ( $n = 5$ ), at a spacing to depth ratio of one.

All stems were potted into square aluminum tubes, to a fixed depth of 20 mm, using vacuum-mixed polymethylmethacrylate (PMMA) bone cement (Simplex P<sup>®</sup>, Stryker<sup>®</sup>, Kalamazoo, MI, USA). The potted stems were maintained at 22 °C, and left 24 hours to cure until testing. Subsequently, stems were placed in a materials testing machine (Instron<sup>®</sup> 8874, Norwood, MA, USA) for application of loads at room temperature. Compression and torsional tests were done on separate testing days, using the same implant stems, cleaned with acetone (Caledon Laboratories Ltd., ON, Canada), and re-potted with new cement.

Compression tests were done using a cyclic staircase loading protocol, similar to that described in Section 4.2. Cyclic loads fitted a sine wave function, at a frequency of 1.5 Hz. Load targets oscillated between 500 N and an upper limit, which started at 1000 N and increased in increments of 1000 N every 100 cycles to a maximum 10000 N.

At 10000 N, cycling continued for a further 25000 cycles, totaling 25900 cycles at the end of the protocol. Failure was defined as 2 mm of stem push-out, termed catastrophic failure, or until completion of the loading protocol. For torsional loading of the stems, a similar protocol to that described in Section 3.2 was incorporated, using a sine wave pattern to apply cyclic loads at a frequency of 1.5 Hz. Torque values cycled between 0 Nm and an upper limit, which started at 1 Nm and increased in 1Nm increments every 100 cycles to a maximum of 30 Nm. Failure of the implant stem was defined as a rapid increase in rotation of the stem without resistance, termed catastrophic failure, or until completion of the protocol.

The custom optical tracking system (Basler Pilot GigE Camera, Ahrensburg, Germany; Opto Engineering Telecentric Lens, Mantova, Italy; and LabVIEW Vision Acquisition System, Austin, TX, USA) previously described in Sections 2.2, 3.2 and 4.2 of this thesis, was used to detect motion at the stem-cement interface during compression and torsional loading. The measure of interface toggle was assessed by the width of the relative stem motion and rotation graphs (Figure 5.2A and 5.2B). For stems that did not fail catastrophically before reaching the maximum load/torque (*i.e.*, 10000 N or 30 Nm), global stem motion was quantified (Figure 5.2C). Global stem motion represented the displacement of the stem within the camera's coordinate system (*i.e.*, not relative to the cement), which occurred during the loading cycles at the maximum load only (indicated by the starred region in Figure 5.2C).

One-way ANOVAs ( $\alpha = 0.05$ ) were used to compare the effect of stem surface condition on interface strength (*i.e.*, load to failure), and stem motion (*i.e.*, both interface toggle and global stem motion).

### 5.3 RESULTS

The failures observed were dependent upon the loading mode. In compression, only the smooth stem experienced catastrophic failure prior to the maximum load, with



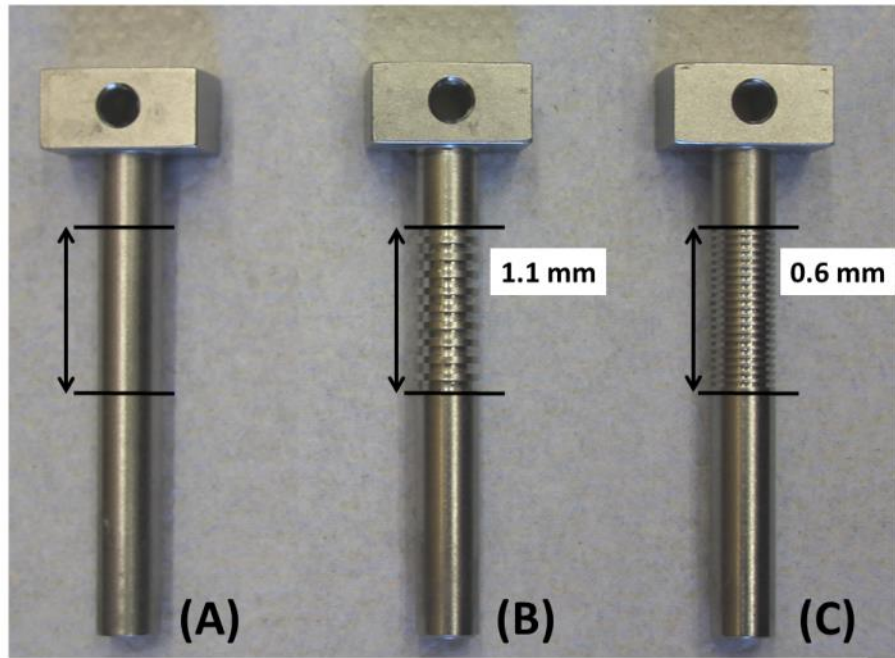


**Figure 5.1: Smooth and Circumferential Grooved Surface Designs Tested in Both Compression and Torsion**

(A) Smooth, (B) 1.1 mm Grooved, and (C) 0.6 mm Grooved. All stems were cemented to fixed 20 mm depth, as indicated by the region highlighted by the double arrows.

both grooved surfaces completing the loading protocol without stem push-out (Figure 5.2A). When subjected to an applied torque, all stem surfaces experienced catastrophic failure prior to reaching the maximum torque (Figure 5.2B). In both loading modes, stem motion increased with increasing cycles of the staircase loading protocols, and as such, stem motion data were normalized to their respective load/torque data for statistical comparisons.

Overall, the presence of grooves increased the number of compressive loading cycles achieved prior to failure ( $p < 0.001$ ) (Figure 5.3A), but had no effect on loading cycles for torsion (Figure 5.4A).

Under compression, grooved stems experienced less interface toggle prior to failure compared to smooth surfaces ( $p < 0.01$ ), with no differences between the two grooved designs ( $p = 0.97$ ) (Figure 5.3B). For torsion tests, motion data showed that grooved 1.1 mm stems experienced the greatest interface toggle prior to catastrophic failure ( $p < 0.01$ ), with no differences between the smooth and grooved 0.6 mm surfaces ( $p = 0.76$ ) (Figure 5.4B).

When comparing stems that reached the maximum load under compression without catastrophic failure, grooved 1.1 mm stems showed greater stem motion with increased cycling, compared to grooved 0.6 mm stems ( $p = 0.03$ ) (Figure 5.5).

## 5.4 DISCUSSION

Implant stem designs are constantly evolving in an effort to reduce the incidence of loosening. Stem surface modification (*i.e.*, application of surface treatment or surface finish) is one factor of implant design that may reduce the effects of loosening. By incorporating a roughened stem surface onto cemented implant designs, the bone cement is allowed to infiltrate the stem surface, providing mechanical fixation between the stem and cement. For femoral components, surface finished stems are described based on their roughness value ( $R_a$  value) (Verdonschot, 2005), and studies have shown that an

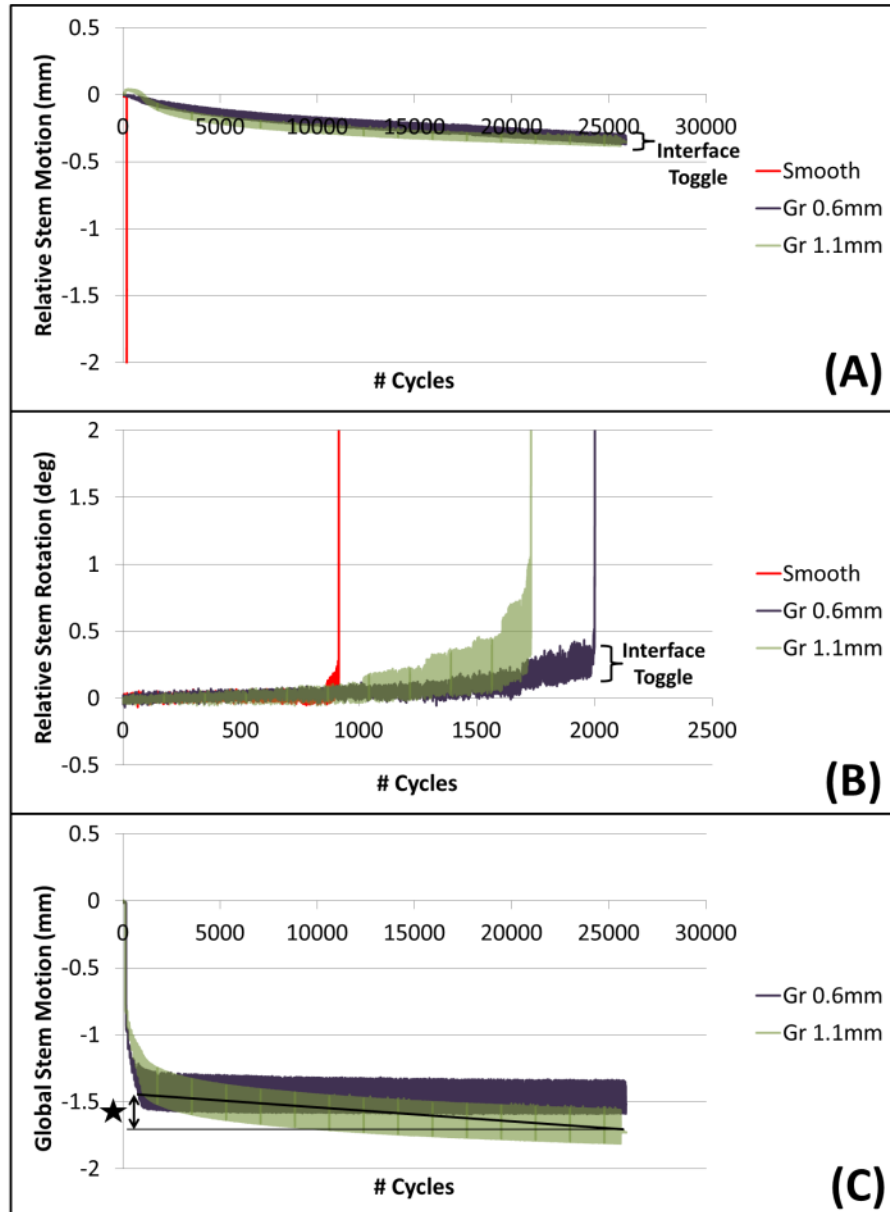


**Figure 5.2: Stem Motion for Smooth and Circumferential Grooved Stems**

Representative graphs of stem motion for smooth, grooved 0.6 mm and grooved 1.1 mm. (A) Relative stem motion under compression, and (B) relative stem rotation in torsion, was used to determine interface toggle prior to failure. (C) Global stem motion was used to determine the change in stem motion with increased number of cycles at the maximum load, as indicated by the starred region.

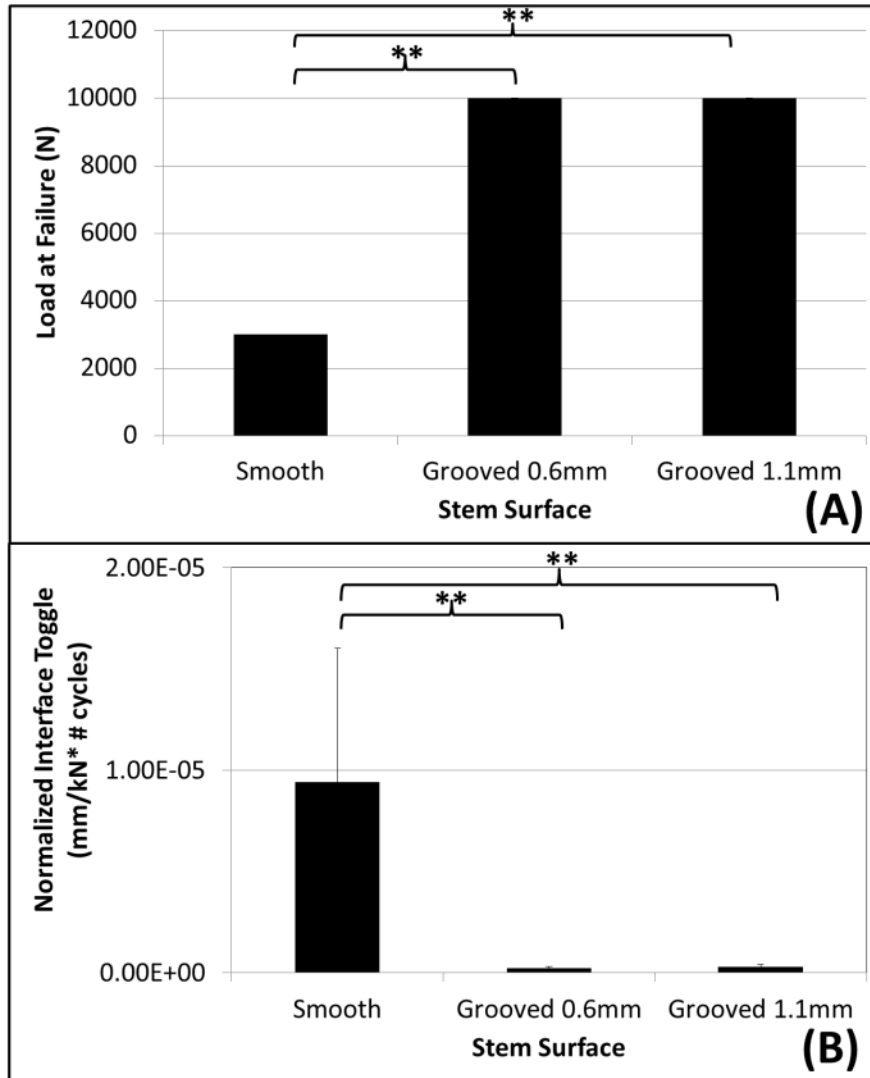


**Figure 5.3: Interface Stability for Smooth and Circumferential Grooved Surfaces in Compression**

(A) Loads required to cause failure and, (B) interface toggle prior to failure. All stems failed at consistent loads, resulting in zero standard deviation for the measures of load at failure, as seen in part (A). Smooth stems showed the least stability ( $p < 0.001^{**}$ ) compared to the grooved surfaces.

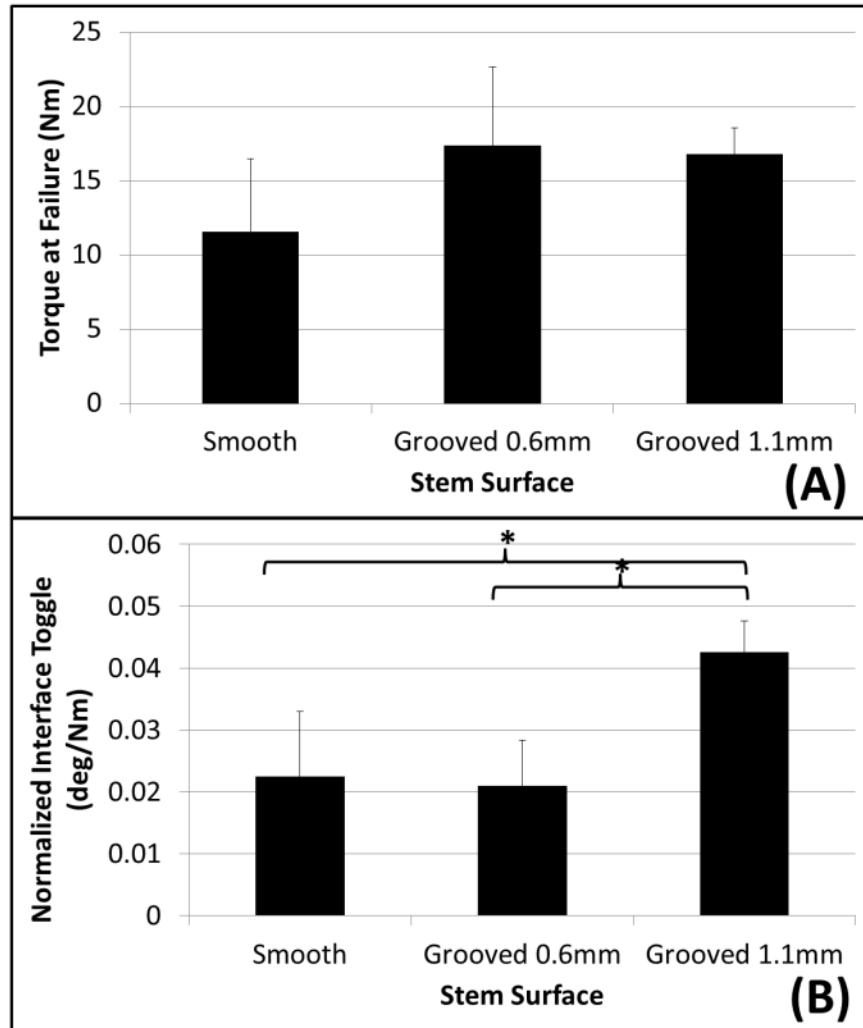


**Figure 5.4: Interface Stability for Smooth and Circumferential Grooved Surfaces in Torsion**

(A) Torque at failure and, (B) interface toggle prior to failure. No differences were found in the torque to failure among all stems ( $p = 0.1$ ), however, grooved 1.1 mm stems showed greatest interface toggle prior to failure ( $p < 0.01^*$ ).

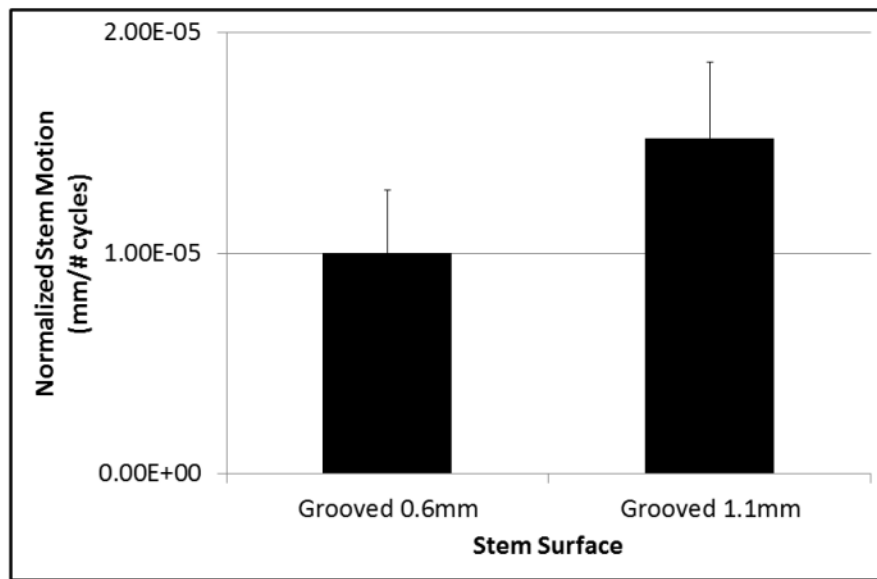


**Figure 5.5: Stem Motion with Increased Number of Cycles**

Stem motion during the loading cycles at maximum compression load, for grooved 0.6 mm and grooved 1.1 mm stems. Grooved 1.1 mm stems showed increased stem motion compared to the grooved 0.6 mm ( $p = 0.3$ ).

increased roughness value contributed to increased interface strength; however, there were implications of interface wear and abrasion once debonding had occurred (Crowninshield *et al.*, 1998; Scheerlinck and Casteleyn, 2006). Similarly for ulnar components, stem surface treatments such as sintered beads and plasma spray incorporated onto cemented stem designs have shown improved clinical success (Jeon *et al.*, 2012; van der Lugt and Rozing, 2004); however, *in-vitro* testing of these surfaces in previous chapters of this thesis has demonstrated variable outcomes dependent on stem substrate material. As such, this chapter examines a different design concept for the stem surface, with the aim of improving implant fixation without the contradictory effects contributed by roughened stem surfaces. Therefore, the purpose of this study was to investigate the effect of circumferential grooves on the stability of implant stems under compression and torsional loads.

The hypotheses for this study were accepted. Under compression, both grooved surfaces significantly improved the interfacial strength compared to the smooth surface. When comparing interface strength for torsional loading, no statistical differences were found among the grooved and smooth surfaces, as expected, given the direction of the grooves relative to the applied torque. Despite this, there was a trend towards increased interface strength with the application of grooves (Figure 5.4A). Thus, with regards to interface strength, it appears that the circumferential design of the grooves created mechanical interlocks along the length of the stem-cement interface and increased the stem surface contact with cement, offering superior resistance to shear forces at the interface. This interfacial resistance would be dictated by the mechanical properties, and in particular, the shear strength of the integrated bone cement. In comparison, smooth stems created an adhesive-type bond with the cement at the interface, and provided some frictional resistance to interface forces. Once these bonding and frictional forces were overcome by the interface shear forces, the smooth stems experienced failure.

Toggle results for compression loading showed that both grooved surfaces experienced little interface toggle compared to the smooth surface, suggesting superior interface stability and resistance in compression. When comparing the grooved stems at the constant 10000 N load with increasing load cycles, the grooved 1.1 mm stem

experienced increased stem motion prior to failure. Similarly, results of interface toggle under torsional loading showed that the grooved 1.1 mm surfaces experienced the largest magnitudes of toggle compared to the other stem surfaces. This may be explained by the size and number of grooves associated with the grooved 1.1 mm stem, which would accommodate a larger volume of cement integration onto the stem surface. As such, the mechanical properties of bone cement would have a greater influence on the interface motion of the grooved 1.1 mm stem surface compared to grooved 0.6 mm, and smooth surfaces. Although bone cement is used as a connector, it is a viscoelastic material (Lewis, 2011), and can cause increased motion of the stem without leading to interface failure.

When comparing the results of this study to those previously reported for surface treated implants in Sections 3.3 and 4.3 of this thesis, circumferential grooves performed comparable to, or better than, surface treated stems in compression. Although they did not improve torsional stability, other stem design factors such as stem cross-sectional shape (Kedgley *et al.*, 2007) and curvature (Berzins *et al.*, 1993; Evans *et al.*, 1988), may work in combination with the circumferential grooves to provide increased torsional stability when incorporated into implant stem designs. In addition, applying longitudinal grooves in combination with the circumferential design may work in synergy to improve both axial and torsional stability; however, further studies are needed to confirm this hypothesis.

Cobalt chrome was the stem material chosen for testing stem circumferential grooves within this study, since results from Sections 3.3 and 4.3 of this thesis showed that this stem substrate material contributed to the variable mechanical response of the beaded treatments in compression and torsional loading. Therefore, the present study aimed to determine the stability response of stem circumferential grooves on cobalt chrome stems, to consider its possible use as an alternative surface design to the beaded treatment on cobalt chrome stems. In addition, it was not expected that stem material would influence the mechanical response of the respective circumferential grooved surfaces; therefore, only one stem material was utilized in the study design.



Cementing technique plays an important role in the fixation mechanics of joint replacements (Faber *et al.*, 1997; Iesaka *et al.*, 2003). Likewise, the properties of the bone cement during preparation (*i.e.*, viscosity, temperature) can affect the mechanical connect formed at the stem-cement interface. This study used low viscosity bone cement for fixation of the implant stems, allowing for better infiltration of cement into the grooved surfaces and improving the mechanical interlock formed once the cement was cured. For the grooved 0.6 mm stems, in particular, low viscosity bone cement would likely ensure sufficient infiltration into the smaller groove spacing. As such, it is important to consider cement consistency during implantation, to allow for proper interdigitation of cement with the grooved stem surface.

Cement shrinkage is another property of bone cement that can affect the success of cemented interfaces (Bishop *et al.*, 1996; Eveleigh, 2001; Kwong and Power, 2006; Lennon and Prendergast, 2001; Lewis, 1997; Orr *et al.*, 2003). In particular, the cement used in this study (*i.e.*, Simplex P) has been shown to have approximately 6 percent decrease in its initial volume during curing (Kwong and Power, 2006). Shrinkage of the cement is initiated by polymerization and temperature effects of the cemented construct (Draenert and Draenert, 2005). However, reports on the effect of cement shrinkage at the stem-cement interface have been variable, ranging from the formation of gaps (Bishop *et al.*, 1996), to shrinkage and compression of the cement onto the stem (Draenert and Draenert, 2005). While this study did not investigate the effects of cement shrinkage on the interface formed with the grooved surfaces, it is important to consider, since the overall stability of the grooved stems were shown to be influenced by the properties of the integrated bone cement. Therefore, future studies should look into methods for quantifying cement shrinkage at the stem-cement interface.

Although the grooved surface improved implant stability, the effect of the grooved edges within the cement should be acknowledged. Sharp edges at the stem-cement interface can act as stress risers (Crowninshield *et al.*, 1980; Evans *et al.*, 1988), initiating cement fracture. Incorporating a rounded edge on the grooved corners may prevent stress fractures in the cement. While this study did not investigate the effects of

the grooved stem surface on fractures within the bone cement, this should be addressed in future finite element studies.

Another limitation of adding grooves to the stem surface is their potential effect on stem strength. The presence of the grooves reduces the minimum cross sectional area of the stem. In addition, the notches created by the grooves on the stem surface may act as stress risers, reducing the overall strength of the stem. However, by controlling the groove dimensions and adding fillets (*i.e.*, rounded internal corners) these effects may be mitigated.

Stem circumferential grooves improved implant stability under compression, with no significant effects in torsion. Overall, grooved 0.6 mm stems experienced less stem motion compared to the grooved 1.1 mm stems. Therefore, introducing circumferential grooves onto implant stem surface designs may reduce the effects of implant loosening caused by compressive forces.

## 5.5 CONCLUSION

When comparing grooved stems, the grooved 0.6 mm stems showed improved stem stability compared to grooved 1.1mm stems in compression, with a trend towards improved stability in torsion as well. This alternative surface topography may address the concerns associated with surface treated and surface finished stems, and potentially reduce the cost of the stem fabrication process.

## 5.6 REFERENCES

- Athwal, G.S., Morrey, B.F., 2006. Revision total elbow arthroplasty for prosthetic fractures. *The Journal of Bone and Joint Surgery; American Volume* 88, 2017–2026.
- Barrack, R.L., 2000. Early failure of modern cemented stems. *The Journal of Arthroplasty* 15, 1036–1050.
- Berzins, A., Sumner, D.R., Andriacchi, T.P., Galante, J.O., 1993. Stem curvature and load angle influence the initial relative bone-implant motion of cementless femoral stems. *Journal of Orthopaedic Research* 11, 758–769.
- Bishop, N.E., Ferguson, S., Tepic, S., 1996. Porosity reduction in bone cement at the cement-stem interface. *The Journal of Bone and Joint surgery; British volume* 78, 349–356.
- Cheung, E. V, O’Driscoll, S.W., 2007. Total elbow prosthesis loosening caused by ulnar component pistoning. *The Journal of Bone and Joint Surgery; American Volume* 89, 1269–1274.
- Crowninshield, R.D., Brand, R.A., Johnston, R.C., Milroy, J.C., 1980. An analysis of femoral component stem design in total hip arthroplasty. *The Journal of Bone and Joint Surgery; American Volume* 62, 68–78.
- Crowninshield, R.D., Jennings, J.D., Laurent, M.L., Maloney, W.J., 1998. Cemented femoral component surface finish mechanics. *Clinical Orthopaedics and Related Research* 355, 90–102.
- Draenert, K., Draenert, Y., 2005. The Three Interfaces. In: Breusch, S.J., Malchau, H. (Eds.), *The Well-Cemented Total Hip Arthroplasty*. Springer Berlin Heidelberg, New York, pp. 93–102.

- Evans, B.G., Daniels, A.U., Serbousek, J.C., Mann, R.J., 1988. A comparison of the mechanical designs of articulating total elbow prostheses. *Clinical Materials* 3, 235–248.
- Eveleigh, R., 2001. Mixing systems and the effects of vacuum mixing on bone cement. *British Journal of Perioperative Nursing* 11, 132–140.
- Faber, K.J., Cordy, M.E., Milne, A.D., Chess, D.G., King, G.J., Johnson, J.A., 1997. Advanced cement technique improves fixation in elbow arthroplasty. *Clinical Orthopaedics and Related Research* 334, 150–156.
- Iesaka, K., Jaffe, W.L., Kummer, F.J., 2003. Effects of preheating of hip prostheses on the stem-cement interface. *The Journal of Bone and Joint Surgery; American Volume* 85, 421–427.
- Jeon, I.H., Morrey, B.F., Sanchez-Sotelo, J., 2012. Ulnar component surface finish influenced the outcome of primary Coonrad-Morrey total elbow arthroplasty. *Journal of Shoulder and Elbow Surgery* 21, 1229–1235.
- Kedgley, A.E., Takaki, S.E., Lang, P., Dunning, C.E., 2007. The effect of cross-sectional stem shape on the torsional stability of cemented implant components. *Journal of Biomechanical Engineering* 129, 310–314.
- Kwong, F.N.K., Power, R. a, 2006. A comparison of the shrinkage of commercial bone cements when mixed under vacuum. *The Journal of Bone and Joint Surgery; British Volume* 88, 120–122.
- Lennon, A.B., Prendergast, P.J., 2001. Evaluation of cement stresses in finite element analyses of cemented orthopaedic implants. *Journal of Biomechanical Engineering* 123, 623–628.
- Lewis, G., 1997. Properties of acrylic bone cement: state of the art review. *Journal of Biomedical Materials Research* 38, 155–182.

- Lewis, G., 2011. Viscoelastic properties of injectable bone cements for orthopaedic applications: state-of-the-art review. *Journal of Biomedical Materials Research, Part B, Applied Biomaterials* 98, 171–191.
- Orr, J.F., Dunne, N.J., Quinn, J.C., 2003. Shrinkage stresses in bone cement. *Biomaterials* 24, 2933–2940.
- Scheerlinck, T., Casteleyn, P.P., 2006. The design features of cemented femoral hip implants. *The Journal of Bone and Joint Surgery; British Volume* 88, 1409–1418.
- Van der Lugt, J.C., Rozing, P.M., 2004. Systematic review of primary total elbow prostheses used for the rheumatoid elbow. *Clinical Rheumatology* 23, 291–298.
- Verdonschot, N., 2005. Philosophies of stem designs in cemented total hip replacement. *Orthopedics* 28, s833–s840.

## CHAPTER 6: THE EFFECT OF STEM SURFACE TREATMENT AND MATERIAL ON THE STABILITY OF JOINT REPLACEMENT SYSTEMS SUBJECTED TO BENDING LOADS

*Overview: Joint loading and resultant interface stresses play a key role in the stability of cemented implants. Previous chapters of this thesis have focused on the effect of torsional and axial loads on implant stability, and discussed the role of stem surface treatments in resisting the resultant shear stresses at the stem-cement interface. Bending loads at the joint, however, result in both normal and shear stresses at the stem-cement interface, which can have a varied effect on the interface's mechanics. As such, this chapter investigates the effect of stem surface treatment on the interface stability of cemented implants subjected to bending loads.*

### 6.1 INTRODUCTION

The influence of stem surface treatments on the stability of cemented implant systems is dependent on their ability to resist interface stresses caused by joint loading. However, depending on the loading mode type, resultant stresses at the stem-cement interface can vary. These variable interface stresses can lead to different mechanisms of stem debonding, and resultant implant loosening.

Chapters 3 and 4 of this thesis have already explored the role of surface treated implant stems on the axial and torsional stability of implant systems. In particular, these studies showed similar results with regards to the performance of sintered beads and plasma spray treatments, on titanium and cobalt chrome stems, in both loading conditions (Sections 3.3 and 4.3). The results seem reasonable considering the resultant stresses that occur at the stem-cement interface due to these loading modes. Shear stresses act

concentric to stem-cement interface in torsional loading, and parallel to the interface under axial loading.

In addition to torsional and axial loads occurring at the replaced joint, bending loads are also apparent, as a result of joint forces acting perpendicular to the longitudinal axis of the implant (Bergmann and Graichen, 2010; Bergmann *et al.*, 2007, 2004, 1993; Guerra, 2004; Kutzner *et al.*, 2010; Westerhoff *et al.*, 2009). These forces result in normal interface stresses that act perpendicular to the stem-cement interface, in addition to shear interface stresses that act parallel to the stem surface.

Normal interface stresses that occur during bending of the stem can be tensile or compressive in nature, depending on the location of the interface relative to the applied perpendicular load. These interface stresses can lead to gradual stem debonding, which is more likely to occur at the region of the stem-cement interface that experiences tensile stresses (Huiskes and Schouten, 1980; Huiskes, 1985). Debonding at the interface can subsequently lead to instability of the stem within the cement. As such, implant systems subjected to bending loads should also be considered when investigating the overall effect of surface designs on implant stability.

Therefore, the purpose of this study was to investigate the effect of stem surface treatment on the stability of titanium and cobalt chrome implant stems under bending loads. It was hypothesized that smooth stems would offer inferior stem fixation compared to the surface treated stems, forming a weak bond at the stem-cement interface that would be susceptible to debonding and stem instability under bending loads. In comparison, it was expected that the surface treated stems would show minimal motion at the stem-cement interface, due to the mechanical resistance to interface tensile and shear stresses. In addition, it was expected that titanium stems may experience greater stem motion as a result of its lower modulus of elasticity than cobalt chrome.

## 6.2 MATERIAL AND METHODS

Fifty implant stems ( $\varnothing = 8$  mm) were custom machined from titanium ( $n = 25$ ) and cobalt chrome ( $n = 25$ ) by Tornier S.A.S. (Montbonnot Saint Martin, France). For each stem substrate material, five stems retained their smooth stem surface, and twenty stems had standard commercially employed stem surface treatments applied by Orchid Bio-Coat (Southfield, MI, USA); 20 mm length beaded treatment ( $n = 5$ ), 10 mm length beaded treatment ( $n = 5$ ), 20 mm length plasma spray treatment ( $n = 5$ ), and 10 mm length plasma spray treatment ( $n = 5$ ), as previously described in Chapter 4.

The fixation method used in this study was similar to that in previous chapters, where all stems were centralized, and potted to a fixed cement depth of 20 mm using vacuum-mixed PMMA bone cement (Simplex P<sup>®</sup>, Stryker<sup>®</sup>, Kalamazoo, MI, USA). The stems were cured for 24 hours in a temperature controlled environment, and subsequently tested in a materials testing machine (Instron<sup>®</sup> 8874, Norwood, MA, USA). Custom fixturing was used to secure the stem at the base of the materials testing machine. The cemented stem in the aluminum tube was positioned on its side, so that the longitudinal axis of the stem was parallel to the base of the materials testing machine. A ball bearing attached to the end of the load applicator was used to apply compressive forces to the centre of the stem head, creating a bending moment about the stem head (Figure 6.1). A cyclic compressive staircase loading protocol was used for testing of the stems; they were pre-loaded to 10 N in compression, and cycled between 10 N and upper load limit value, which started at 50 N and increased in 50 N increments every 100 cycles, to a maximum of 1000 N in compression (limited to ensure there was no permanent deformation to the stem external to the cement).

Stem-cement interface motion was observed using the optical tracking system (Basler Pilot GigE Camera, Ahrensburg, Germany; Opto Engineering Telecentric Lens, Mantova, Italy; and LabVIEW Vision Acquisition System, National Instruments, Austin, TX, USA) described in previous chapters of this thesis (Section 2.2. 3.2, 4.2, and 5.2). The displacement between markers placed on the stem and cement (Figure 6.1) was used



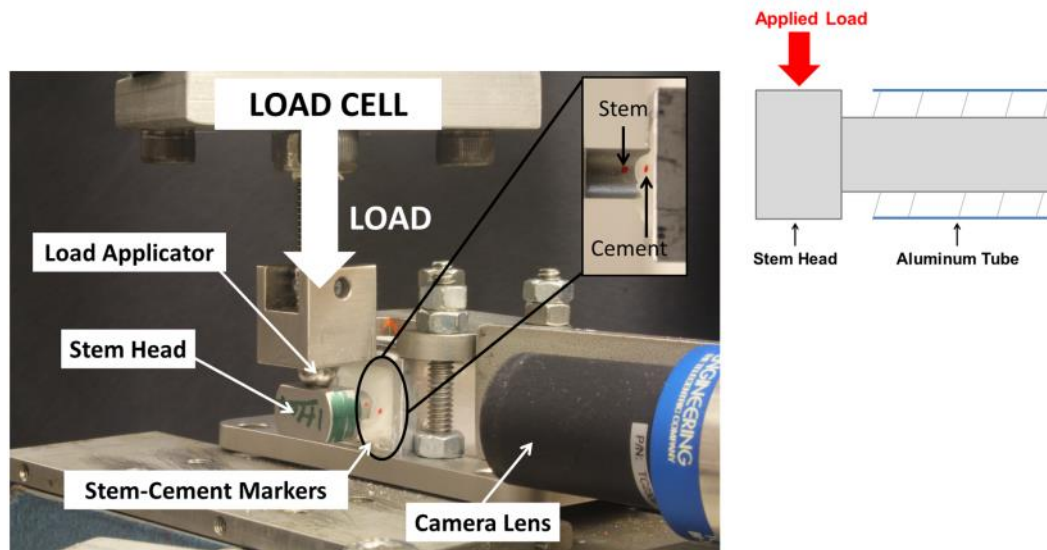


**Figure 6.1: Experimental Set-up used for Bending Tests of Implant Stems**

Cyclic compressive loads were applied to the stem head, inducing bending of the stem within the cement construct (side view shown in schematic at top right). The camera was used to track markers placed on the stem and cement (shown in inset image), and the distance between the markers was defined as relative stem motion.

to determine the relative stem motion during loading. From the graphs of relative stem motion over time, interface stability was quantified by “maximum interface toggle”, which represented the maximum width of the relative stem motion graphs during loading. An additional measure of stem stability was the “offset stem motion”, which was a measure of the average deviation of the stem from its original position at the start of loading (Figure 6.2).

Visual analysis of the cemented stem construct was done post-testing, to determine whether the stem was loose within the cement mantle, or if the cement mantle appeared to be compromised, during mechanical testing.

Two-way analyses of variance with post-hoc Student-Newman-Keuls tests ( $\alpha = 0.05$ ) were used to examine the role of stem surface treatment and stem material on implant stability under bending loads, using measures of interface toggle and offset stem motion.

### 6.3 RESULTS

Post-testing visual inspection of the cemented stem construct found that all stems remained wedged within the cement mantle, without indications of stem loosening. In addition, there were no signs of damage or fracture to the exposed regions of bone cement. However, it was observed that stems appeared displaced within the cement, where analysis of the stem from the proximal and distal ends of the construct showed the stem tilted from its central axis, which was originally in a horizontal configuration (Figure 6.3). This tilt was quantified by the measure of offset stem motion (Figure 6.2).

Statistical analysis of maximum interface toggle found an overall effect of stem surface treatments ( $p = 0.033$ ), where the smooth stems ( $0.074 \pm 0.023$  mm) experienced greater interface toggle compared to the 20 mm beaded treatment ( $0.047 \pm 0.012$  mm) ( $p = 0.018$ ). However, there were no differences found among the other surface

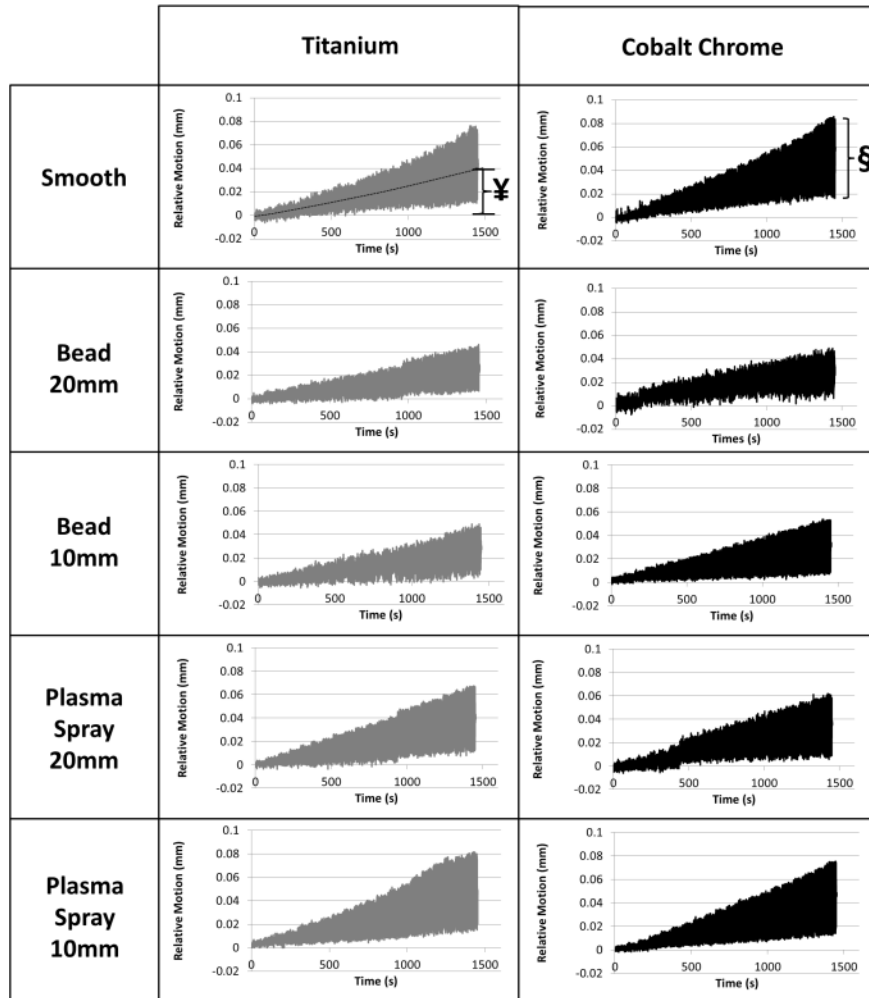


**Figure 6.2: Stem Motion of Surface Treated Stems under Bending Loads**

Representative graphs of relative stem motion for surface treated stems with titanium and cobalt chrome substrate materials. Maximum interface toggle was defined as the maximum width of the relative motion graphs (§), and offset stem motion was defined as the average deviation of stem motion from the starting position, shown by dashed line and (¥).

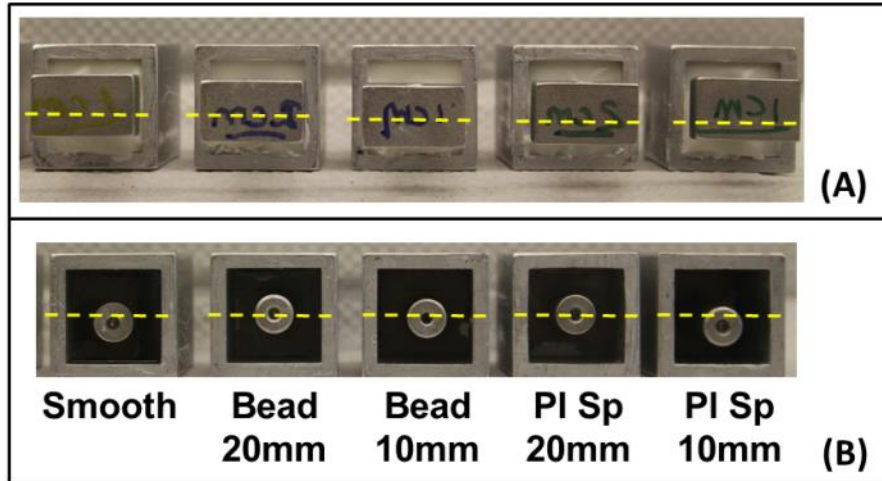


**Figure 6.3: Proximal and Distal Views of Stems Post- Bending Tests**

Post-testing inspection of the (A) proximal, and (B) distal views of the cemented implant stems found that the stems deviated from their central axes (yellow dotted line), and appeared offset within their cement mantles.

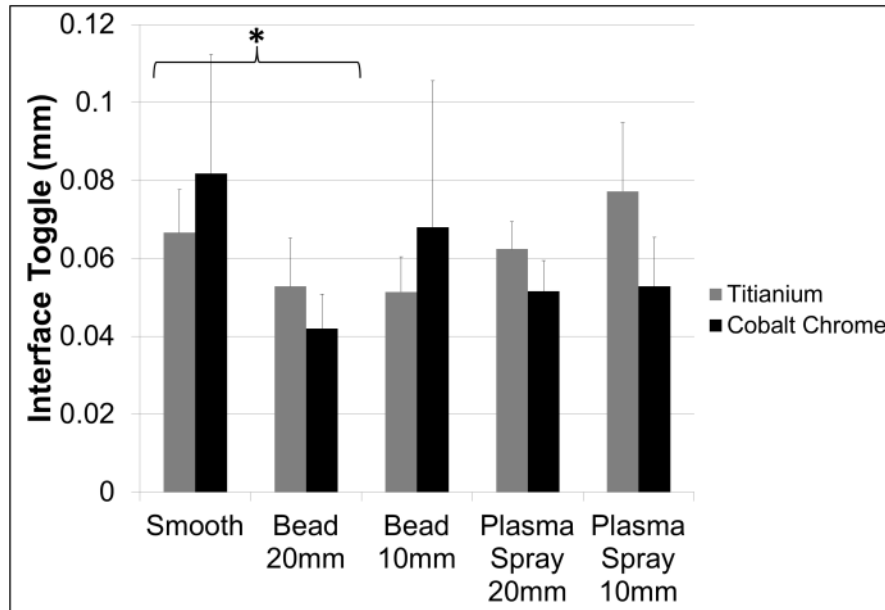


**Figure 6.4: Maximum Interface Toggle for Surface Treated Stems in Bending**

The 20 mm length beaded treatments experienced less toggle than the smooth stems ( $p = 0.018$ ) (as indicated by \*), with no differences found between stem materials ( $p = 0.587$ ).

treatments ( $p > 0.05$ ), as well as no difference in interface toggle between stem materials ( $p = 0.587$ ) (Figure 6.4).

For offset stem motion, differences among the surface treatments were found ( $p = 0.041$ ), where smooth stems ( $0.051 \pm 0.023$  mm) experienced greater stem deviation within the cement mantle than the 20 mm beaded treatment ( $0.031 \pm 0.008$  mm). In addition, there was no effect of stem material on offset stem motion ( $p = 0.577$ ) (Figure 6.5).

## 6.4 DISCUSSION

Joint loads acting perpendicular to the implant stem can induce bending of the cemented stem construct. Throughout various joints of the body, these loads have been shown to range between 0.05 to 5 times body weight during routine daily activities (Bergmann and Graichen, 2010; Bergmann *et al.*, 2007, 2004, 1993; Guerra, 2004; Kutzner *et al.*, 2010; Westerhoff *et al.*, 2009), resulting in varied bending moments acting about the stem head. During bending of the cemented stem, loads are transferred across the stem-cement interface creating regions of tensile, compressive and shear stresses along the interface. These stresses can initiate debonding of the stem from the cement, leading to implant micromotion and subsequent implant loosening.

Chapters 3 and 4 of this thesis discussed the role stem surface treatments played in interface stability under torsional and axial loads, and in particular their contribution to resisting shear stresses at the stem-cement interface. With bending loads, however, the response of surface treatments to resist normal stresses (*i.e.*, tensile and compressive) at the interface may vary. As such, the purpose of this study was to investigate the effect of stem surface treatment on the stability of titanium and cobalt chrome stems under bending loads.

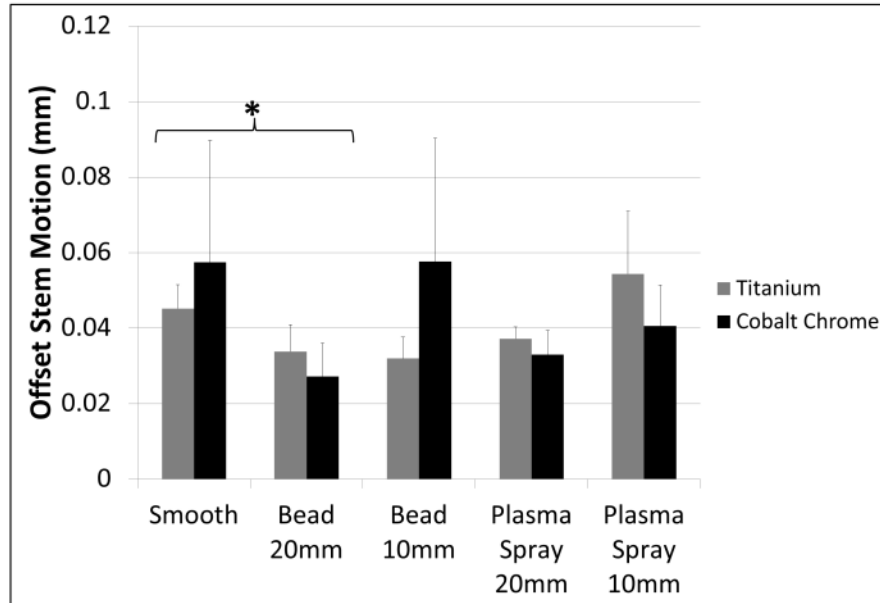


**Figure 6.5: Offset Motion for Surface Treated Stems in Bending**

The 20 mm length beaded stems demonstrated less offset stem motion than the smooth stems (as indicated by \*), with no differences found between stem materials ( $p = 0.577$ ).

Analysis of interface stability found that stem surface treatment had an overall effect on interface stability under bending loads, where smooth stems showed greater interface toggle compared to the 20 mm beaded treatment (Figure 6.4). As discussed previously within this thesis, smooth stems create a chemical bond with the cement at the interface, which is more susceptible to interface stresses compared to the mechanical interlock created by the 20 mm beaded treatment. As such, it is likely the smooth stems may have experienced debonding resulting in greater interface instability compared to the 20 mm beaded treatment.

The results of interface toggle observed among the surface treatments (*i.e.*, 20 mm beaded, 20 mm plasma spray, 10 mm beaded, and 10 mm plasma spray treatment) could be explained by the mechanism of stability expected for the surface treatments under bending loads. Surface treated stems promote interdigitation of bone cement onto the stem surface, which reduces the chances of stem debonding due to normal and shear stresses acting at the stem-cement interface during stem bending. However, the improved interface fixation offered by the surface treated stems may result in the contribution of bone cement to interface toggle measurements. As such, similar interface toggle observed among the surface treated stems may likely be influenced by the mechanical properties of the interlocked bone cement. Despite the non-difference in the results, the overall trend of interface toggle for each of the surface treatments may be indicative of the contribution of the individual surface treatments to interface stability.

This contribution of the mechanical properties of bone cement was also observed in the measure of offset stem motion, where results found that all stems deviated from their original position within the cement mantle during loading, and smooth stems appeared to show greater deviations compared to the 20 mm beaded treatment (Figure 6.5). Depending on the stem-cement interface condition (*i.e.*, fixed or debonded), the load transfer across the interface can vary (Huiskes and Schouten, 1980; Huiskes, 1985). For smooth stems that experience stem debonding, tensile interface stresses are no longer able to be transmitted, and as such, compressive stresses at stem-cement interface are likely to increase. This increase in compressive interface stresses can cause increased loading of the surrounding bone cement. The bone cement consequently exhibits its own



mechanical response to loading, which has been shown to be viscoelastic in nature (Lewis, 2011, 1997; Saha and Pal, 1984), and results in creep of the cement and subsequent drift of the stem within the cement mantle.

Although post-testing inspection of the cemented stem construct found that the stems were offset from their original position, all stems appeared to be securely wedged within the cement mantle. This is important to note since surgical analysis of the cemented stem constructs may assume that a secure stem is indicative of a stable stem construct; however, our results have shown that although stems were not physically loose within the cement mantle, all stems appeared to experience some interface toggle and stem deviation under bending. While these values may appear small in magnitude, they are likely to increase with continuous exposure to interface stresses, as expected in the case of *in-vivo* joint loading.

The loading protocol used in this study was chosen to represent typical bending moments expected at the shoulder, elbow, hip and knee joints (Bergmann *et al.*, 2007, 1993; Guerra, 2004; Kutzner *et al.*, 2010), taking into consideration the dimensions of the cemented stem construct. As such, a cyclic staircase protocol was used with bending loads between 50–1000 N, which created bending moments of 1–20 Nm about the stem head. This protocol also allowed direct comparison of the various surface treatments within the time-frame required for 24 hours testing of the cemented stem samples.

The optical system used for measuring interface stability proved useful for determining stem-cement motion based on analysis of the exposed regions of the stem and cement. However, considering the influential role that bone cement plays in stem stability under bending stresses, analysis of the full length of the cemented stem construct may be needed to fully understand the interface mechanics involved in implant bending. As such, future studies should look into experimental or computational methods that allow analysis of the entire cemented stem construct.

The findings from this study demonstrated that smooth stems experienced greater instability compared to the 20 mm beaded treatments under bending loads, with no differences found among the other surface treatments. Overall, stem substrate material

had no effect on stem stability. Additionally, results from this study suggest that bone cement plays a significant role in the mechanical response of cemented implant stems exposed to bending loads; however, future studies will be needed to confirm this.

## 6.5 CONCLUSION

Stem surface treatments did not improve implant stability under cyclic bending loads; however, overall stem motion appeared to be influenced by creep or motion of the surrounding bone cement.

## 6.6 REFERENCES

- Bergmann, G., Graichen, F., 2010. Realistic loads for testing hip implants. *Bio-medical Materials and Engineering* 20, 65–75.
- Bergmann, G., Graichen, F., Bender, A., Käab, M., Rohlmann, A., Westerhoff, P., 2007. In vivo glenohumeral contact forces--measurements in the first patient 7 months postoperatively. *Journal of Biomechanics* 40, 2139–2149.
- Bergmann, G., Graichen, F., Rohlmann, A., 1993. Hip joint loading during walking and running, measured in two patients. *Journal of Biomechanics* 26, 969–990.
- Bergmann, G., Graichen, F., Rohlmann, A., 2004. Hip joint contact forces during stumbling. *Langenbecks Archives of Surgery* 389, 53–59.
- Guerra, S.M., 2004. Design and development of a total elbow prosthesis to quantify ulnohumeral load transfer. (M.E.Sc Thesis) University of Western Ontario, pp 85-108.
- Huiskes, H., Schouten, R., 1980. Effect of interface loosening on the stress distribution in intramedullary fixated artificial joints. In: *American Society of Mechanical Engineers (Ed.), Advances in Bioengineering*. New York, pp. 213–216.
- Huiskes, R., 1985. Properties of the stem-cement interface and artificial hip-joint failure. In: *The Bone-Implant Interface*. p. 86.

- Kutzner, I., Heinlein, B., Graichen, F., Bender, A., Rohlmann, A., Halder, A., Beier, A., Bergmann, G., 2010. Loading of the knee joint during activities of daily living measured in vivo in five subjects. *Journal of Biomechanics* 43, 2164–2173.
- Lewis, G., 1997. Properties of acrylic bone cement: state of the art review. *Journal of Biomedical Materials Research* 38, 155–182.
- Lewis, G., 2011. Viscoelastic properties of injectable bone cements for orthopaedic applications: state-of-the-art review. *Journal of Biomedical Materials Research, Part B, Applied Biomaterials* 98, 171–191.
- Saha, S., Pal, S., 1984. Mechanical properties of bone cement: a review. *Journal of Biomedical Materials Research* 18, 435–462.
- Westerhoff, P., Graichen, F., Bender, A., Halder, A., Beier, A., Rohlmann, A., Bergmann, G., 2009. In vivo measurement of shoulder joint loads during activities of daily living. *Journal of Biomechanics* 42, 1840–1849.

## CHAPTER 7: THE USE OF MICRO-COMPUTED TOMOGRAPHY ( $\mu$ -CT) IMAGING TO VISUALIZE AND QUANTIFY MOTION AT THE STEM-CEMENT INTERFACE WITH AN APPLIED BENDING MOMENT

### 7.1 INTRODUCTION

Stem-cement interface motion is a useful measure for investigating the stability response of cemented implant systems exposed to joint loading. It provides information regarding the localised motion of the stem relative to the adjacent cement, but can be influenced by the mechanical properties (*i.e.*, creep) of the connecting/interface cement. Bone cement is viscoelastic in nature, and as such, exhibits displacement under loads (Lewis, 2011, 1997; Saha and Pal, 1984). The extent of this response depends on several factors, including the type of loading that occurs at the joint (*i.e.*, compression/tension, torsion, bending) (Lewis, 2011, 1997; Saha and Pal, 1984; Verdonschot and Huiskes, 1995), and can affect the overall stability at the stem-cement interface. Therefore, investigation into the effects of loading on the response at the internal stem-cement interface can offer insight into the interface mechanics that dictate implant stability.

Bending loads, in particular, offer a unique loading response at the stem cement interface, which has been discussed in previous sections of this thesis (*i.e.*, Section 6.1 and 6.4). Depending on the direction of the load, the interface experiences regions of tensile and compressive stresses (Huiskes and Schouten, 1980; Huiskes, 1985). However, the effect of these bending stresses on the displacement response at the interface is not intuitive. Based on the results from Section 6.3, it was found that all implant stems experienced stem motion under bending loads; however, post-testing inspection found that the stems remained securely held within their cement mantles. As such, it was hypothesized that bone cement creep contributed to the observed stem motion, rather than motion resulting from interface loosening. This inference could not

be validated, however, since the optical tracking system was only capable of measuring motion of the exposed regions of the stem and cement (*i.e.*, where the stem exited the cement), with no direct indication of the motion occurring along the length of the stem within the cement mantle. Therefore, an appropriate tool was needed to access the internal stem-cement interface during bending, to determine motion along the entire length of the cemented stem.

Micro-computed tomography ( $\mu$ -CT) imaging is a useful visualization tool that has been used in orthopaedic research to investigate the internal properties of bone and implanted systems (Bernhardt *et al.*, 2006; Blok *et al.*, 2013; Stock, 2009a; Teeter, 2012; Waarsing *et al.*, 2005). The high resolution of the acquired images (*i.e.*, 50–100  $\mu$ m) (Stock, 2009b), allows detection of microstructure details within the object. This has proven useful for studies, including the investigation of bone morphology (Bernhardt *et al.*, 2006; Blok *et al.*, 2013; Waarsing *et al.*, 2005), and wear characteristics of joint replacement components (Teeter, 2012). It was hypothesized that the detailed images provided by the  $\mu$ -CT technology may also be suitable for detecting micromotion at the interfaces of an implanted system.

As such, this study aimed to use  $\mu$ -CT imaging to observe changes at the internal stem-cement interface during loading. Taking into account the observations from Chapter 6 of this thesis, where ambiguity remained regarding the influence of bending loads on the mechanical response at the internal stem-cement interface, this chapter also intended to address those uncertainties. Therefore, the purpose of this study was to investigate the influence of bending loads on internal stem-cement interface motion, using micro-computed tomography ( $\mu$ -CT) imaging to visualize the interface.

## 7.2 MATERIALS AND METHODS

### 7.2.1 TESTING SPECIMENS

Nine implant stems were tested, each machined from titanium by Tornier (France) to consist of a circular cross-section body ( $\text{Ø} = 8 \text{ mm}$ ), with full length smooth surface. All stems were potted to a fixed depth of 10 mm in aluminum tubes using an orthopaedic bone cement (Simplex P, Stryker, Kalamazoo, MI) mixture incorporating miniature steel beads (Metaltec Steel Abrasive Co., Canton, MI) ( $\text{Ø} = 500\text{microns}$ ) (please see Appendix K for details on mixing method). The beads were used as cement markers in subsequent CT images of the stem-cement construct. The appropriate bead to cement ratio was determined to ensure the original flexural modulus of the bone cement was best maintained, while still allowing a reasonable dispersion of beads within the cement mantles (see Appendix K for details concerning the selection of this ratio).

Once the stems were potted, they were left to cure at a constant  $22^\circ\text{C}$  temperature. All stems were allowed 24hrs of curing time before subsequently being placed into a custom built loading device for application of bending loads.

### 7.2.2 CUSTOM-BUILT LOADING DEVICE

The custom built loading device, previously designed for application of bending loads to ulna bone specimens, was modified to incorporate the cemented stem constructs (Figure 7.1) (see Appendix M for details of the loading device). Using the initial design concept and the major components of the device, minor modifications were made to accommodate the application of bending loads to the cemented stem constructs. The design specifications ensured that the device was made of CT-compatible materials, and able to fit within the bore of the CT scanner. In addition, the final prototype was evaluated to ensure its durability during the application of bending loads.

The mechanical components of loading device incorporated a stepper motor (Robbins and Myers, Electrocraft, Willis, TX) connected to an offset bearing cam, which was further attached to a pivoted carbon fibre beam (Figures M.1 and M.2). During one revolution of the motor, the cam connection actuated the pivoted carbon fibre beam in a see-saw motion, with approximately 1 mm of vertical displacement. An aluminum high accuracy S-beam load cell (LCR Series, Omega, Stamford, CT) was mounted at the top of the carbon fibre beam, above which a ball bearing was placed for the application of load to the head of the cemented stem construct. An aluminum jig secured onto the device's platform was used to hold the cemented stem construct in a horizontal orientation above the carbon fibre beam (Figure 7.1). This configuration allowed forces to be applied perpendicular to the cemented stem construct, resulting in a bending moment applied to the implant stem.

### 7.2.3 LOADING AND IMAGING PROTOCOL

Stems were loaded in a combination of static and dynamic conditions, from a minimum load of 50 N to a maximum load of 960 N, in the following sequences: 1) monotonic increase, 2) cyclically loaded at a rate of 0.9 Hz for 1000 cycles (to initiate a fatigue type response within cemented stem construct), and 3) monotonic increase (Figure 7.2).

For each of the static load levels (*i.e.*, pre- and post-dynamic testing), CT scans of the cemented stem were obtained at the unloaded and loaded condition (Figure 7.2), using a micro-CT scanner with voxel spacing of 154  $\mu\text{m}$  (eXplore Ultra, GE Healthcare, London, Canada). The scans were acquired at an x-ray potential of 120 kVp, with 40 mA tube current, over the duration of 8 seconds. The resultant image volume was 1024 mm x 1024 mm x 360 mm.



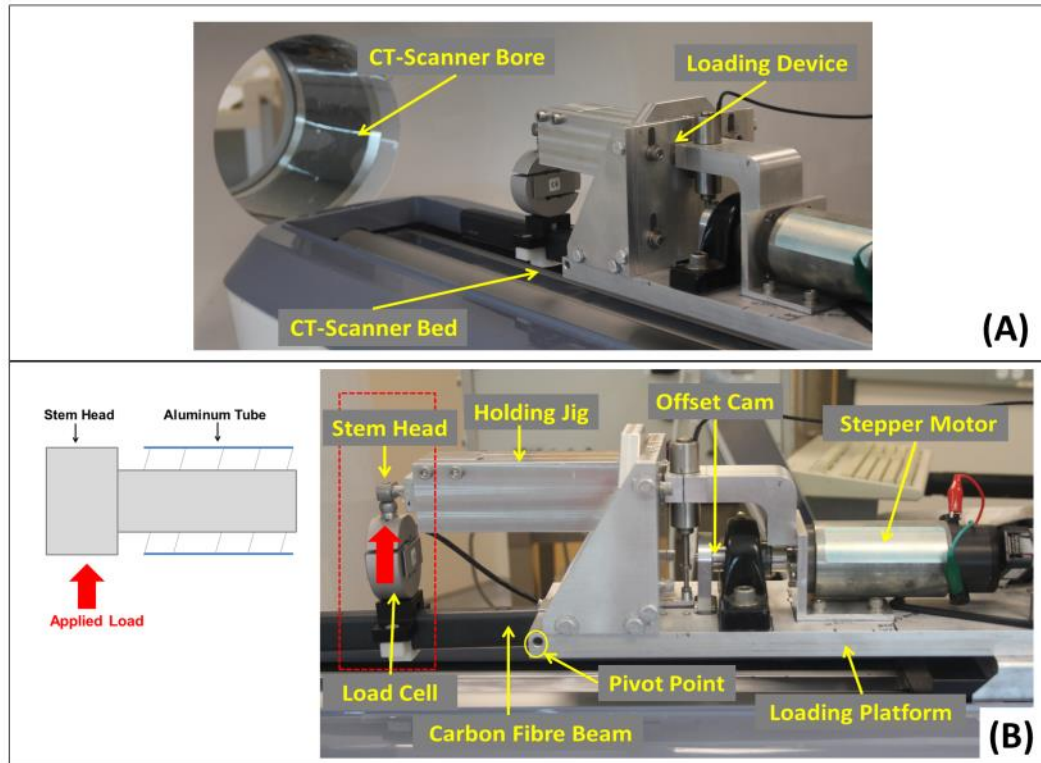


**Figure 7.1: Custom-Built Loading Device used for Application of Bending Loads**

(A) The loading device was designed to be secured onto the CT bed, and fit within the bore of the scanner. For application of bending loads, (B) the cemented stem was secured in a horizontal orientation into an aluminum holding jig, which was fixed to the base of the loading platform. The platform housed a stepper motor connected to an offset cam, which was attached to a pivoted carbon fibre beam. During one revolution of the motor, the beam translated vertically in a sinusoidal displacement pattern. A load cell attached to the top of the beam recorded the load applied to the stem head during vertical translation of carbon fibre beam. The applied load induced bending within the cemented stem construct, as shown in the inset schematic. The region highlighted by the dashed red box indicates the volume of the bending device which was included in scanner's field of view.

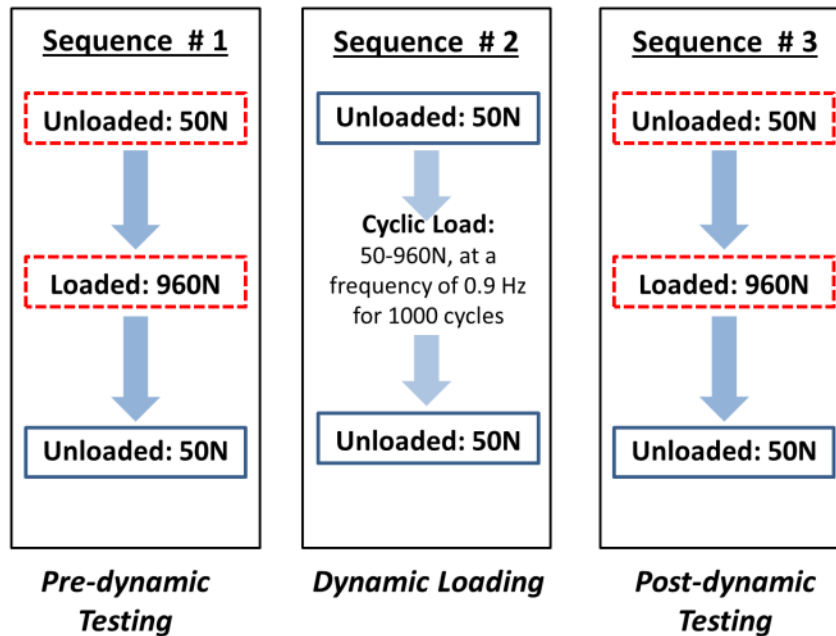


**Figure 7.2: Schematic of Loading and Imaging Protocol used for Static and Dynamic Tests**

All stems were loaded in a combination of static and dynamic conditions from a minimum load of 50 N to a maximum load of 960 N, in the following sequences: 1) monotonic increase, 2) cyclically loaded at a rate of 0.9 Hz for 1000 cycles, and 3) monotonic increase. CT scans were acquired for the unloaded and loaded condition of the pre- and post- dynamic sequences, as highlighted by the red dashed boxes, and used for comparison of stem-cement motion during loading. A cyclic sequence was incorporated between the two monotonic sequences to initiate a fatigue type loading response within the cement mantle.

#### 7.2.4 DATA ANALYSIS

Scans of the cemented stems were reconstructed, and converted from .vff's (*i.e.*, image files) to .stl's (*i.e.*, surface geometry files) using MicroView 3D Image Viewer and Analysis Tool (Parallax Innovations, Ilderton, ON). The surface files were subsequently imported into Geomagic Qualify (Geomagic, Morrisville, NC) for analysis of stem-cement interface motion (see Appendix N for details of analysis). For each stem, the unloaded and loaded surfaces of the pre dynamic scans were compared to determine the response of the stem and the surrounding beads embedded within the cement to the applied static loads. The same analysis was done using the post-dynamic scans. In addition, the unloaded surfaces of the pre- and post-dynamic scans were compared to one another, to determine offsets in stem position as a result of dynamic loading.

This comparison involved registering the surfaces from the two scans, using the square aluminum tube containing the stem as the fixed point of reference, and determining the deviations between the two surface profiles (Figure 7.3A). 2D sections along the length of the implant (Figure 7.3B) were used to analyse changes in the stem and bead surfaces. Measurements of stem surface deviation were obtained from the central 2D profile, while measurements of bead motion were obtained from 2D profiles located within a 2 mm range of this central 2D profile (such that the nearest bead was identified). The vertical change in the stem surface between the unloaded and loaded conditions was quantified (Figure 7.3 C), and the vertical and horizontal changes in bead surfaces were analyzed. However, due to inconsistent deformations in a few of the bead surfaces (see Appendix O), a stringent criteria was applied to analyze bead surface deviation. That was, bead deviation was only recorded if contralateral edges on the bead surface experienced similar quantities of deviations.

Measurements of stem motion were taken at four specific locations along the stem: at the point of load application (*i.e.*, stem head), the beginning of the stem shaft (*i.e.*, uncemented shaft), the beginning of the cement mantle (*i.e.*, cemented shaft #1), and the end of the cement mantle (*i.e.*, cemented shaft #2) (Figure 7.4). The beads embedded within the cement were analyzed based on their location relative to two specific regions

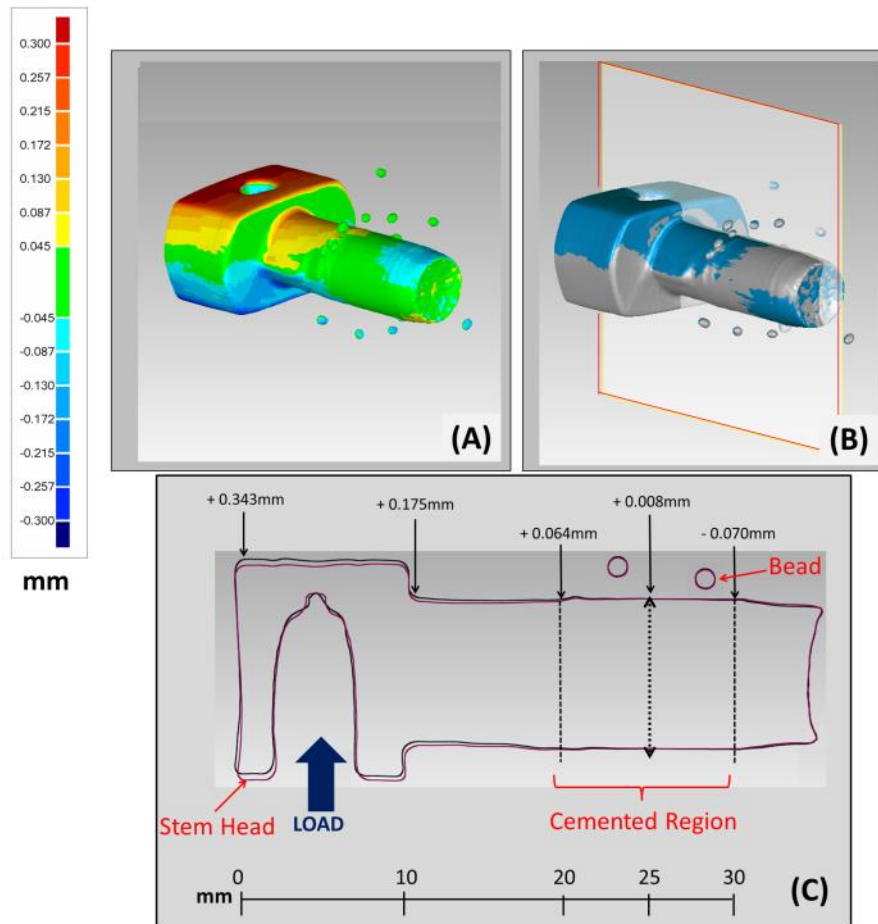


**Figure 7.3: Surface Deviation Analysis with Geomagic®**

Motion of the stem and cemented beads was measured from deviation of their respective surfaces between unloaded and loaded scans. Shown above is the loaded stem with beads embedded within the cement. **(A)** The 3D color plot shows the change in stem position from the unloaded to loaded scan, with red (+ve) and blue (-ve) regions showing greatest stem surface deviation. **(B)** A 2D section along the length (highlighted by the plane) of the cemented implant was used to analyze changes in the stem and bead surfaces. **(C)** From the sectioned profiles, the vertical change in the stem surface between the unloaded (red profile) and loaded (black profile) conditions was measured both before and after the cyclic loading phase. The load was applied to the head of the stem using a ball bearing, as seen in Figure 7.1. (Note: The aluminum tube containing the cemented stem was removed from the image for better visualization of the stem-cement interface).

within the cement (Tables 7.1–7.3). Region 1 of the cement represented the length between cemented shaft #1 and the midpoint along the length of the cement mantle. Region 2 represented the cement length between cemented shaft #2 and the same midpoint of the cement mantle.

A one-way repeated measures ANOVA, with Student-Newman-Keuls post-hoc tests ( $\alpha = 0.05$ ), was used to compare the magnitudes of stem motion from the pre- and post-dynamic scans, thereby determining the effect of cyclic bending loads on the internal mechanical response of the cemented stem constructs. Bead deviations, however, were inconsistent among stems, and as such, provided only a qualitative measure of cement motion (*i.e.*, no statistical analyses were performed).

### 7.3 RESULTS

Inspection of the stems post-testing (*i.e.*, after completion of the three loading sequences) found that all stems remained securely wedged within their cement mantles, with no signs of stem loosening. Statistical analysis comparing the change in stem motion between the pre- and post- dynamic CT images, found no difference in the motion of the stem head ( $p = 0.373$ ), or either of the uncemented ( $p = 0.162$ ) and cemented regions of the stem shaft ( $p > 0.05$ ) (Figure 7.4). However, the average motion observed for each of stem regions showed a trend towards reduced stem motion following the application of dynamic loads (Figure 7.4).

When observing motion along the entire length of the stem during loading, it was found that stems experienced tilting about a pivot point within the cement mantle. This pivot point varied in position among the stems, shifting from the center to the proximal and distal regions (*i.e.*, regions 1 and 2, respectively) of the cement (Tables 7.1 and 7.2).

Analysis of bead motion within the cement found that some beads experienced vertical and horizontal translation, while others remained fixed (Tables 7.1 and 7.2).

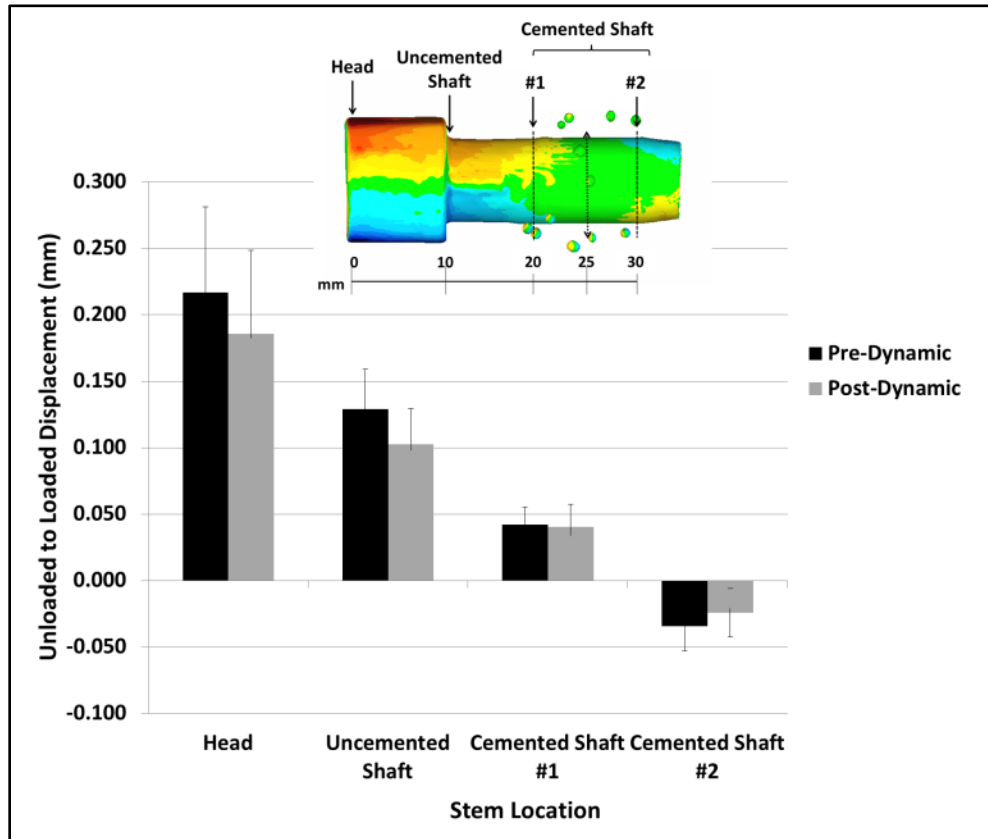


**Figure 7.4: Average Stem Motion during Loading for the Pre- and Post-dynamic Scans**

Comparison of stem motion (*i.e.*, head, uncemented shaft and cemented shaft) between the unloaded and loaded scans, for the pre- and post-dynamic sequences, found that there was no difference in stem motion ( $p > 0.05$ ) as a result of dynamic loading. However, there was a trend towards decreased stem motion after exposure to cyclic loads, as observed from the reduced displacement in the post-dynamic sequence.

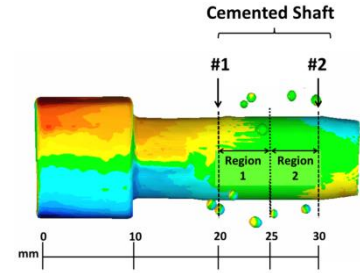


**Table 7.1: Pre-dynamic Cemented Stem and Bead Motion**

Displacement along the length of the cemented mantle for the cemented stem shaft and beads embedded within the cement prior to the cyclic loading sequence. The arrows ( $\uparrow$ ,  $\downarrow$ ) indicate the direction of stem and bead motion. The presence of beads was not consistent between regions, or among the stem samples tested, therefore, dashes (-) represent the absence of a bead within the region, while zero (0) represents an identifiable bead that did not displace.

Stem #	Cemented Shaft (mm)		Bead Motion (Above Stem) (mm)		Bead Motion (Below Stem) (mm)	
	# 1	# 2	Region 1	Region 2	Region 1	Region 2
1	0.040 $\uparrow$	0.059 $\downarrow$	-	0.039 $\downarrow$	0	0.045 $\leftarrow$
2	0.021 $\uparrow$	0.010 $\downarrow$	0.036 $\rightarrow$	-	0.050 $\uparrow$	-
3	0.034 $\uparrow$	0.025 $\downarrow$	-	0.041 $\rightarrow$	-	0
4	0.067 $\uparrow$	0.063 $\downarrow$	0.031 $\uparrow$	0	-	0.134 $\leftarrow$ ; 0.078 $\downarrow$
5	0.033 $\uparrow$	0.026 $\downarrow$	0	-	0	-
6	0.055 $\uparrow$	0.012 $\downarrow$	0	0.025 $\downarrow$	0	-
7	0.050 $\uparrow$	0.044 $\downarrow$	-	0.032 $\rightarrow$ , 0.062 $\downarrow$	0	0.036 $\leftarrow$ ; 0.047 $\downarrow$
8	0.042 $\uparrow$	0.035 $\downarrow$	-	-	0	0
9	0.040 $\uparrow$	0.039 $\downarrow$	-	-	0	0

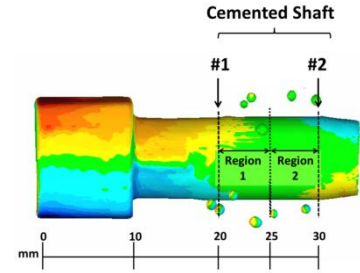


**Table 7.2: Post-dynamic Stem and Bead Motion**

Displacement along the length of the cemented mantle for the cemented stem shaft and beads embedded within the cement following the cyclic loading sequence. The arrows ( $\uparrow$ ,  $\downarrow$ ) indicate the direction of stem and bead motion. The presence of beads was not consistent between regions, or among the stem samples tested, therefore, dashes (-) represent the absence of a bead within the region, while zero (0) represents an identifiable bead that did not displace.

Stem #	Cemented Shaft (mm)		Bead Motion (Above Stem) (mm)		Bead Motion (Below Stem) (mm)	
	# 1	# 2	Region 1	Region 2	Region 1	Region 2
1	0.029 $\uparrow$	0.050 $\downarrow$	-	0.040 $\downarrow$ ; 0.037 $\rightarrow$	0	0
2	0.059 $\uparrow$	0.002 $\downarrow$	0	-	0	-
3	0.049 $\uparrow$	0.045 $\downarrow$	-	0.020 $\rightarrow$	-	0.049 $\leftarrow$
4	0.037 $\uparrow$	0.005 $\downarrow$	0	0	-	0.031 $\downarrow$
5	0.052 $\uparrow$	0.026 $\downarrow$	0	-	0	-
6	0.058 $\uparrow$	0.011 $\downarrow$	0	0	0	-
7	0.038 $\uparrow$	0.012 $\downarrow$	-	0	0.027 $\uparrow$	0
8	0.039 $\uparrow$	0.027 $\downarrow$	-	-	0	0
9	0.004 $\uparrow$	0.042 $\downarrow$	-	-	0	0.028 $\downarrow$



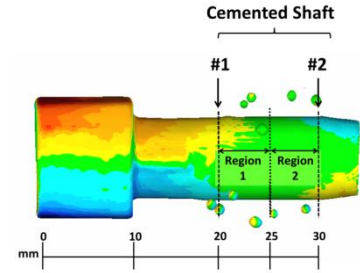


**Table 7.3: Offset Stem and Bead Motion**

Displacement along the length of the cemented mantle for the cemented stem shaft and beads embedded within the cement obtained when comparing the unloaded scans from pre- and post-dynamic testing. The arrows ( $\uparrow$ ,  $\downarrow$ ) indicate the direction of stem and bead motion. The presence of beads was not consistent between regions, or among the stem samples tested, therefore, dashes (-) represent the absence of a bead within the region, while zero (0) represents an identifiable bead that did not displace.

Stem #	Cemented Shaft (mm)		Bead Motion (Above Stem) (mm)		Bead Motion (Below Stem) (mm)	
	# 1	# 2	Region 1	Region 2	Region 1	Region 2
1	0.014 $\uparrow$	0.018 $\downarrow$	-	0	0	0.071 $\leftarrow$
2	0.016 $\uparrow$	0.003 $\downarrow$	0	-	0	-
3	0.009 $\uparrow$	0.014 $\downarrow$	-	0	-	0
4	0.040 $\uparrow$	0.042 $\downarrow$	0	0	-	0.119 $\leftarrow$ ; 0.027 $\downarrow$
5	0.010 $\uparrow$	0.010 $\downarrow$	0	-	0	-
6	0.015 $\uparrow$	0.006 $\downarrow$	0	0	0	-
7	0.029 $\uparrow$	0.012 $\downarrow$	-	0	0.080 $\leftarrow$	0.068 $\leftarrow$
8	0.009 $\uparrow$	0.025 $\downarrow$	-	-	0.035 $\rightarrow$	0
9	0.007 $\uparrow$	0.013 $\downarrow$	-	-	0	0

When comparing offset stem and bead motion between the pre- and post-dynamic unloaded scans, it was observed that all cemented constructs experienced offset motion as a result of dynamic testing, with some constructs showing greater motion than others (Table 7.3).

## 7.4 DISCUSSION

The clinical success of implant systems is dependent, in part, on the stability provided by the connection formed at the stem-cement interface (Barrack, 2000; Mohler *et al.*, 1995). However, the ability of this connect to resist forces that occur at the interface, may be influenced by the mechanical properties of the individual interface materials (i.e., bone cement and metal). Bone cement, in particular, is known to exhibit a time-dependent displacement response when loaded (Lewis, 2011, 1997; Saha and Pal, 1984). Therefore, in order to fully understand the interface mechanics that occur during joint loading, the contribution of individual interface components to overall stem stability needs to be explored.

Chapter 6 of this thesis discussed the unique interface stress response initiated by bending loads. From those results, it was hypothesized that bone cement displaced under interface stresses, and thereby affected the overall stability of the stem. This contribution is important to consider since displacement of cement can cause motion of the stem without loosening, eventually leading to implant misalignment. As such, a thorough investigation into the effect of bending loads on the response of the internal stem-cement interface was needed.

Visual inspection of the cemented stem constructs post-testing found that all stems were secured within their cement mantles, with no signs of stem instability or loosening. This would suggest that any motion observed for the loaded stems may have been contributed to by the displacement of the surrounding bone cement. Statistical analysis found no difference in stem motion between the pre- and post-dynamic loaded scans, implying that exposure to short-term dynamic loading did not cause a significant

increase in stem instability. However, from the graphs of stem motion between the pre- and post- dynamic conditions, there was a trend towards reduced stem motion with application of dynamic loads (Figure 7.4). This may be explained by the mechanical response of bone cement to cyclic loads. If stem motion was dictated by displacement of the surrounding cement, it would seem reasonable that the stems experienced less motion as a result of short-term stiffening of bone cement with increased number of loading cycles (Verdonschot and Huiskes, 1995).

When comparing the motion of the stem along the cemented interface, a distinct pattern was observed in the motion path of the stem. During loading the stems appeared to experience tilting about a pivot point within the cement mantle, suggesting that displacement of the surrounding cement facilitated stem motion (Tables 7.1 and 7.2). For some stems this pivot point occurred at the midpoint along the length of the mantle, where a positive displacement of the stem in the proximal region of the cement reciprocated to negative displacement in the distal region. For other stems this pivot point shifted to the proximal or distal region of the cement mantle. The difference in the location of the pivot point may offer an explanation into the fixation condition along the length of the interface during bending. In a fully-fixed stem condition the normal stresses across the interface would be higher at the proximal and distal ends of the cemented construct, with a middle region of minimal stress transfer (Huiskes and Schouten, 1980; Huiskes, 1985). This would result in increased stem motion at the proximal and distal ends of the cemented stem. In a partially-fixed stem condition, however, the stress transfer across the interface would change (Huiskes and Schouten, 1980; Huiskes, 1985), shifting the pivot point to the fixed region of the interface. It is important to note though, that a well-fixed or partially-fixed interface condition in bending may not be indicative of immediate stem loosening, since all stems remained securely wedged within the cement mantle. Over time, however, the partially-fixed condition may result in increased stem motion and complete debonding at the interface. These interface conditions, particularly for the pre-dynamic scans, demonstrate the variability of bond formation created at the stem-cement interface during cement fixation of smooth stem surfaces.

The specific response of cement to bending loads was observed in the motion of beads within the cement. While all beads did not experience displacements, the beads that showed motion under loading did so in accordance with the direction of the applied load. This observation further verified that the cement experienced some displacement under bending loads. It is believed that the observed bead movement within the cement may have been dictated by the bead position along the length of the stem, along with the fixation condition at the interface. Therefore, for a fully fixed stem condition that experiences pivoting about a central position within the cement mantle, the beads at the proximal and distal regions of the cement (*i.e.*, Regions 1 and 2) may likely show displacement as a result of normal stress transfer across the interface. In comparison, for a partially fixed condition where the pivot point shifts within the mantle, bead motion may only occur in the region of the fixed interface. However, due to the inconsistency of bead distribution within the cement, among the various stems, this hypothesis could not be fully validated. As such, future work should look into embedment methods that allow for controlled positioning of markers within the cement mantle.

The beads used in this study were made of steel, with an approximate density of  $8 \text{ g/cm}^3$ , which made them easy to detect within the cement (approximate density of bone cement =  $1.2 \text{ g/cm}^3$  (Saha and Pal, 1984)). However, this difference in density may also result in the beads not being able to move freely with the bone cement. It may be likely that motion of the bulk cement could have occurred around the embedded beads, rather than initiate bead motion. This would explain the variation in bead displacements observed with the cemented constructs. A less dense bead material may have shown greater motion with the cement during loading. In addition, because of the high density of the steel bead, it is possible that metal artifacts could have been introduced into the CT-images. These artifacts would have subsequently affected the surface profiles used for bead motion analysis (Appendix O). Therefore, it is advised that future studies using this technique should incorporate a suitable cement marker made of a less dense material than the surrounding bone cement.

Analysis of the stem and bead motion during loading utilized a method that measured deviations in stem and bead surfaces between the unloaded and loaded scans.

While this method was useful and allowed relative comparison of stem and bead motion, it depended on the quality of the surfaces created during the conversion of image to surface files. Image parameters used for conversion were standardized for all surfaces; however, variability in image quality between scans could have affected the resultant surface quality.

Smooth surface, titanium stems were used for testing within this study. Smooth stems were chosen based on the results from Chapter 6, which showed an overall trend towards increased stem motion compared to the other stems, and significant increase in stem motion compared to the 20 mm beaded treatment. Additionally, smooth surfaces showed large variability in their stability results, and as such, it was believed that investigation of the internal stem-cement interface of smooth stems under bending moments could offer insight into the interface mechanics associated with these stem surfaces. Titanium was chosen as the material for CT-testing because it is a low density metal, and was not expected to significantly contribute to metal artifacts within the image. However, based on pilot testing comparing the surface deviation between two consecutive scans of unloaded stems (Appendix O), it was found that some artifacts may have still occurred, showing small deviations in the stem surface without the application of a load. Despite this, titanium stems were still useful for CT-imaging tests, compared to other high density implant metals, and offered satisfactory image quality and results during testing.

This study was able to interpret the effect of cyclic loads on the mechanical response of the interface by comparing the motion of the stem and beads during static loading, both before and after the application of dynamic loads (Figure 7.4), where load magnitudes (*i.e.*, 50–980 N) and rate (*i.e.*, 0.9 Hz) were chosen in close accordance with the bending protocol used in Chapter 6.<sup>4</sup> While this method was useful for the purposes of this study, it does not give a true representation of the interface's response during

---

<sup>4</sup> The loading rate of 0.9 Hz was selected for use in future studies, aimed at acquiring scans during dynamic testing. This rate would be required to ensure appropriate gating of the loading device with the acquisition of images from the CT scanner (Armitage *et al.*, 2012).

dynamic loading. A better representation would involve the comparison of scans obtained during cyclic loading. This could be done using a unique imaging technique described by Armitage *et al.*, where a gated CT-image acquisition method would be used to acquire scans of the moving stem (Armitage *et al.*, 2012). The technique would involve image acquisitions of the cyclically loaded stems, and retrospective sorting of the projection data, to reconstruct images at appropriate phases of the cyclic protocol. This would result in a series of reconstructed images of the cemented stem construct at different time points of the cyclic waveform, which could be used to determine the motion of the stem and beads within the cement during one complete cycle of the dynamic protocol. The loading fixture, dynamic protocol and analysis methods developed in this study were designed such that they could be readily employed for such a test. Future studies will look at incorporating this technique to measure dynamic motion of the stem and beads within the cemented stem construct.

This is the first known *in-vitro* study to incorporate  $\mu$ -CT imaging to determine real-time interface motion during loading, by incorporating an active loading device within a  $\mu$ -CT scanner, to obtain images of loaded cemented stem constructs. The study showed that stem stability was not significantly altered by exposure to dynamic bending loads, but found that cement displacement contributed to stem motion during bending.

## 7.5 CONCLUSION

From  $\mu$ -CT image analysis along the length of the internal stem-cement interface, all stems experienced tilting motion about a fixed pivot point within the cement mantle during the application of bending loads, and the bone cement adjacent to the stem demonstrated motion as well.

## 7.6 REFERENCES

- Armitage, S.E.J., Pollmann, S., Detombe, S., Drangova, M., 2012. Least-error projection sorting to optimize retrospectively gated cardiac micro-CT of free-breathing mice. *Medical Physics* 39, 1452–1461.
- Barrack, R.L., 2000. Early failure of modern cemented stems. *The Journal of Arthroplasty* 15, 1036–1050.
- Bernhardt, R., Scharnweber, D., Müller, B., Beckmann, F., Goebbels, J., Jansen, J., Schliephake, H., Worch, H., 2006. 3D analysis of bone formation around titanium implants using micro computed tomography ( $\mu$ CT). In: Bonse, U. (Ed.), *Proceedings SPIE 6318, Developments in X-ray Tomography*, 631807. pp. 1–10.
- Blok, Y., Gravesteyn, F. a, van Ruijven, L.J., Koolstra, J.H., 2013. Micro-architecture and mineralization of the human alveolar bone obtained with microCT. *Archives of Oral Biology* 58, 621–627.
- Huiskes, H., Schouten, R., 1980. Effect of interface loosening on the stress distribution in intramedullary fixated artificial joints. In: *American Society of Mechanical Engineers (Ed.), Advances in Bioengineering*. New York, pp. 213–216.
- Huiskes, R., 1985. Properties of the stem-cement interface and artificial hip-joint failure. In: *The Bone-Implant Interface*. p. 86.
- Lewis, G., 1997. Properties of acrylic bone cement: state of the art review. *Journal of Biomedical Materials Research* 38, 155–182.
- Lewis, G., 2011. Viscoelastic properties of injectable bone cements for orthopaedic applications: state-of-the-art review. *Journal of Biomedical Materials Research Part B, Applied Biomaterials* 98, 171–191.
- Mohler, C.G., Callaghan, J.J., Collis, D.K., Johnston, R.C., 1995. Early loosening of the femoral component at the cement-prosthesis interface after total hip replacement. *The Journal of Bone and Joint Surgery; American Volume* 77, 1315–1322.

- Saha, S., Pal, S., 1984. Mechanical properties of bone cement: a review. *Journal of Biomedical Materials Research* 18, 435–462.
- Stock, S.R., 2009a. Cellular or Trabecular Solids. In: *Micro Computed Tomography- Methodology and Applications*. Taylor & Francis Group, Boca Raton, FL, pp. 171–213.
- Stock, S.R., 2009b. Introduction. In: *Micro Computed Tomography- Methodology and Applications*. Taylor & Francis Group, Boca Raton, FL, pp. 1–8.
- Teeter, M., 2012. Assessment of Wear in Total Knee Arthroplasty Using Advanced Radiographic Techniques. (Ph.D Thesis) The University of Western Ontario, pp 1-36
- Verdonschot, N., Huiskes, R., 1995. Dynamic creep behavior of acrylic bone cement. *Journal of Biomedical Materials Research* 29, 575–581.
- Waarsing, J.H., Day, J.S., Weinans, H., 2005. Longitudinal micro-CT scans to evaluate bone architecture. *Journal of Musculoskeletal & Neuronal Interactions* 5, 310–312.



## CHAPTER 8: GENERAL DISCUSSION AND CONCLUSIONS

*Overview: This chapter re-examines the original objectives and hypotheses proposed in Chapter 1 of this thesis to assess whether each of them were successfully accomplished and proven. Overall strengths and limitations of this body of work are discussed, along with potential future directions for similar implant biomechanics studies. Finally, the overall significance of this type of basic science research in the field of orthopaedics is highlighted.*

### 8.1 SUMMARY

Implant loosening remains the most common mode of joint replacement failure (Australian Orthopaedic Association, 2010; New Zealand Orthopaedic Association, 2010), with mechanical loosening resulting from exposure of implant systems to joint loads. Basic implant biomechanics studies, such as those presented within this thesis, can offer an explanation to clinical questions surrounding mechanical loosening. This thesis focused specifically on the implant's stem surface design and its role in the clinical success of implant systems. Within the literature, surface modified, cemented implants have been reported to experience reduced rates of loosening (Jeon *et al.*, 2012); however, the mechanical response associated with these stem surface designs have not been explored. Therefore, the overarching purpose of the series of studies presented within this thesis was to investigate the effect of clinically-relevant stem surface designs on the mechanical stability at the stem-cement interface, under various loading modes, using *in-vitro* biomechanical analysis tools to assess stem micromotion.

Chapter 1 provided the basic concepts and background knowledge that was used to prepare the study designs for subsequent chapters within the thesis. This chapter introduced joint replacement systems, and factors that may contribute to their clinical success. In addition, various tools used in the biomechanical analysis of implant motion

were detailed, with focus on the use of optical systems as a non-invasive method for interface analysis. This chapter concluded with the expected objectives and hypotheses for each study within this thesis.

Initial focus was the development of an appropriate measurement tool to assess interface micromotion (Objective #1). Chapter 2 described the development and validation of a custom optical tracking system that was capable of measuring displacements on the order of micrometers. The hardware components of the optical system were carefully chosen to meet these requirements. The software used for displacement measurements incorporated a color thresholding method that detected the (x,y) coordinates of coloured markers placed on specific landmarks, and calculated the relative distances between them. The system was validated by comparing motion applied by a micrometer screw gauge, with that measured by the optical tracking system. It was determined that the optical system showed agreement with the micrometer screw gauge for measurements between 0.005 mm and 0.250 mm, based on the scatter of the Bland-Altman plots, and these measurements were reliable based on the results of intraclass correlation coefficients (ICC's) greater than 0.99. Therefore, it was concluded that the optical system was satisfactory for its application in measuring interface motion within subsequent chapters of this thesis (Hypothesis #1 accepted).

Using the optical tracking system described in Chapter 2, the stability response of clinically-relevant stem surface treatments was investigated under torsional loads (Objective #2, Chapter 3). Cemented titanium and cobalt chrome implant stems consisting of smooth, plasma spray and beaded surface treatments were mechanically tested using a cyclic staircase torsional loading protocol, and motion between the stem and cement was observed. Overall, it was found that stem surface treatments improved the torsional stability of stems compared to smooth stem surfaces (Hypothesis #2 accepted), but the individual stability responses of plasma spray and beaded treatments were dependent on the stem substrate material. For cobalt chrome stems, the 20 mm length plasma spray treatment showed greater interface strength than the 20 mm length beaded treatments, with no differences in stem rotation prior to failure. However, for titanium stems, no difference in interface strength was found between the 20 mm length

plasma spray and 20 mm length beaded treatment, but the plasma spray stem experienced more stem rotation prior to failure. In addition, titanium stems showed greater torques at failure, but greater stem rotation prior to failure, compared to cobalt chrome stems.

The axial stability of surface treated stems was also considered. This was of particular interest to the upper limb literature, since it has been reported that ulnar components of linked elbow replacement systems commonly experienced failure via stem ‘pistoning’, or pull-out (Cheung and O’Driscoll, 2007). For cemented implants, improvement in the mechanical connect at the stem-cement interface, by incorporation of stem surface treatments, may result in improved resistance to ulnar component pistoning. Therefore, Chapter 4 of this thesis investigated the effect of stem surface treatment and material on the stability of implant stems under compression (Objective # 3). Similar to Chapter 3, it was found that stem surface treatment improved the axial stability of implant stems compared to smooth surfaces, and this effect was dependent on stem material (Hypothesis #3 accepted). It was found that the 20 mm length beaded treatments showed greatest interface strength, with the 20 mm length plasma spray treatment on cobalt chrome stems also showing improved interface strength, compared to the 10 mm beaded and plasma spray treatments. In addition, the 20 mm length beaded and plasma spray treatments showed least interface motion, with the 10 mm length beaded and plasma spray treatments on titanium stems showing reduced interface motion as well. When comparing stem material, titanium and cobalt chrome stems performed similar to one another under compression.

Considering the variable response of stem surface treatments in Chapters 3 and 4 of this thesis, where results found that the success of surface treatments were dependent on the stem substrate material to which they were applied, Chapter 5 aimed to investigate an alternative stem surface design (*i.e.*, circumferential grooves) and its contribution to the axial and torsional stability of cobalt chrome implant stems (Objective #4). It was determined that the application of 0.6 mm and 1.1 mm circumferential grooves to the stem surface (*i.e.*, separation and depth) offered improved axial stability compared to smooth stems, but offered similar stability response in torsion (Hypothesis #4 accepted). When comparing groove dimensions, no differences were found in interface strength and

interface motion between the 0.6 mm and 1.1 mm circumferential grooved surfaces under compression, however, grooved 1.1 mm stems showed greater stem motion than the grooved 0.6 mm stems in torsion. In addition, it was suggested that motion observed for the grooved stems was influenced by the creep properties of the infiltrated bone cement, since the 1.1 mm grooved stems showed greater overall stem motion than the 0.6 mm grooved stems.

Besides torsional and axial loads, joint replacement systems are also exposed to bending loads, which result from joint forces acting perpendicular to the length of the implant stem. Bending loads produce both shear and normal stresses along the length of the stem-cement interface, with regions of interface experiencing both tensile and compressive stresses, dependent on the direction of the applied load. This unique loading profile can result in varied mechanical response from surface treated implant stems. Chapter 6 of this thesis investigated the role of stem material and surface treatment on the stability of implant stems exposed to bending loads (Objective #5). Based on observations of implant stem motion, it was found that titanium and cobalt stems showed similar stability responses under bending loads, with only the 20 mm length beaded treatments experiencing less interface motion than the smooth stem (Hypothesis #5 rejected). In addition, stem motion was thought to be influenced by the displacement, or creep, of the surrounding bone cement, since all stems demonstrated offset stem motion within their cement mantle during loading, without any indication of stem loosening. This was further supported by the observed tilt of the stem away from its central axis, in post-testing analysis.

Taking into consideration the contribution of bone cement creep to the stability response of the stems tested under bending in Chapter 6, it was determined that analysis of the full length of the stem-cement interface was needed to determine the response of both the stem and cement under bending loads. Chapter 7 of this thesis used  $\mu$ -CT imaging to access the internal stem-cement interface, and facilitated motion analysis along the full length of the interface (Objective #6). A custom built loading device was used to apply a static load to a smooth implant stem, while allowing real-time scanning of the loaded stem. Beads embedded within the cement were used as cement markers to

detect motion of the cement during loading. Scans of the loaded implant stem, obtained before and after exposure to cyclic dynamic testing, detected stem and cement embedded bead motion during loading (Hypothesis # 6 accepted). Motion of the stem appeared to occur about a pivot point within the cement, where stem tilting similar to that observed in Chapter 6 was noted. However, the location of this pivot point within the cement mantle was variable among the stems tested, suggesting different fixation conditions at the interface during loading. Although motion of the cement embedded beads were not consistent among stems, this preliminary result was able to prove that cement motion does occur with implant stems during loading.

## 8.2 STRENGTHS AND LIMITATIONS

Specific strengths and limitations for each of the individual studies within this thesis have already been discussed within their respective chapters, but the consolidation of these studies showed overall strengths and limitations as well.

The series of basic science studies presented within this thesis allowed investigation of implant stability, dependent of the effects of stem surface design and material. The studies tested circular cross-section implant stems ( $\text{Ø} = 8 \text{ mm}$ ), with altered surface topography along a 20 mm or 10 mm region of the implant stems. While these stems were not representative of a specific implant design, they allowed relative comparison of stem surface treatment and material. In particular, circular cross-section implant stems were chosen since they were shown to exhibit the least resistance to torsional loads (Kedgley *et al.*, 2007). In addition, since this study was only interested in motion occurring at the stem-cement interface, stems were potted in standard sized aluminum tubes, without incorporation of variable bone specimens. The use of aluminum tubes controlled the cement volume and interfaces, but contributed to thicker cement mantles, approximately twice the size of those used clinically. The increased thickness could have contributed to the bone cement creep observed in the studies; however, larger mantle sizes allowed testing of implant stems without compromise to the

surrounding bone cement. Thinner cement mantles may have resulted in failure of the bone cement, subsequently affecting the stability results of the surface treated implants. Therefore, although this bench top study design may have limited the clinical scope of these studies, it facilitated exclusive testing of the stem design features without contribution from other variables. Furthermore, given that the cement mantle thickness was consistent across all stems tested, the relative differences would still be reasonable given the repeated measures design of the studies.

The *in-vitro* environment used for testing implant stems within this thesis was different from that expected at the joints in the body. In particular, the temperature and physical environment did not represent typical *in-vivo* conditions. All stems were potted and tested at approximately 22 °C; however, temperatures within the human body are higher. Temperature differences can affect the rate of polymerization of bone cement, with higher temperatures increasing the polymerization rate, and may result in a different loading response of bone cement than that observed in this thesis. In addition, the anatomical joint is exposed to joint fluids and blood that are likely to affect the adhesion properties of stem with the cement. Therefore, while the stems tested within this thesis were compared relative to one another in the same testing environment, it is important to note that *in-vivo* conditions could have resulted in different implant stability outcomes.

The overall aim of this thesis was to investigate the effect of stem surface design under various loads, to determine the stability response of these designs for improved resistance to loosening. Therefore, studies within this thesis tested stems under individual loading modes using custom designed fixtures to secure and accurately align the cemented stems within the materials testing machine, minimizing the effects of off-axis loading, as monitored by the six degree of freedom load cell of the materials testing machine. Although loading that occurs at the anatomical joint acts in a combined state, the individual contribution of each of these components are important for a thorough understanding the mechanical response of surface treatments under specific loads. This is especially useful for studies like the one presented in Chapter 4, where its study design was developed based on the specific failure response (*i.e.*, pistoning) exhibited by ulnar components at the elbow joint (Cheung and O'Driscoll, 2007). As such, testing the effect

of surface treatments to resist these dominant axial loads was imperative for providing knowledge regarding failure mechanisms associated with these surface designs at the ulnohumeral joint.

The magnitudes of loads used for testing of implant stems in torsion, compression and bending, were chosen based on a review of the literature reporting joint loads measured by instrumented implants at the hip, knee and shoulder. However, the maximum loads chosen for the individual testing protocols were on the higher end of loads expected at the joints. While this did not simulate typical joint loads in daily activities, it allowed relative comparison of various surface treatments, by initiating a failure response in the majority of stem surfaces. In addition, the loading protocol used for all implants was cyclic, staircase in nature. This protocol was specifically chosen to ensure that all stems were subjected to a range of dynamic loads, which mimicked repetitive loading experienced by the human joint, while still allowing comparison of interface strength based on loads required to cause failure.

*In- vitro* implant biomechanics have used stem motion as an indicator of implant stability. Few studies however, have compared stem motion relative to the surrounding bone cement. This measurement, however, is more representative of interface motion, and allows analysis of implant motion independent of motion occurring within the surrounding fixturing. The optical tracking system (Chapter 2) and CT measurement technique (Chapter 7) used in this thesis facilitated micromotion measurements at the level of the stem-cement interface. This was advantageous to studying localized interface motion, and further provided additional information regarding the contribution of the bone cement to implant stability.

### 8.3 FUTURE DIRECTIONS

The work done within this thesis has provided the framework for investigation of interface mechanics associated with various stem surface designs. Considering the influential role that stem surface designs play in the mechanical connect at the stem-

cement interface, future work should analyze the response of these varying connections on the loading response at the interface. This could be done using finite element analysis, by creating models of the stem-cement interface (Mann *et al.*, 1991), with interface conditions governed by the different mechanical connects associated with the various surface designs. These analyses would offer information about the resultant stresses and strains induced at the interface as a result the varied stem surfaces connects, and more specifically, the response of the interfacial cement to these varied surface designs.

In addition to utilizing modeling techniques to assess the loading response at the stem-cement interface, embedment of strain gauges within the cement could be also used to experimentally analyze the effect of stem surface designs on interface strains (Fetterly, 2012). This would allow stability testing of surface modified implant stems, with simultaneous analysis of the strain response at the interface. The combination of these measurements may prove useful in future implant studies to provide a comprehensive analysis of the interface mechanics that govern the success of cemented stem surface designs.

The alternative stem surface design (*i.e.*, stem circumferential grooves) tested in Chapter 5 of this thesis, showed promising results with regards to its stability response under torsional and axial loads. This concept of machining patterns onto the stems, rather than incorporating an additional material interface, can limit the variable mechanical response associated with stem surface treatments and coatings, while improving the interface connect and overall stem stability. However, this notion of removing material from the stem needs to be further tested, since alteration to the stem design can also affect the mechanical strength of the stem. Therefore, future studies should look into alternative stem surface designs that involve machining patterns onto the stem surface, and compare these stems for improved interface stability, and mechanical response under various loading conditions.

Considering the influential role that bone cement played in the stability response of implant stems throughout this thesis, future studies should also look into the mechanical behavior of bone cement specific to implant stability. Chapter 7 of this thesis



introduced a preliminary method using CT-imaging to observe motion within the cement mantle during loading of implant stems; however, this technique is still in its rudimentary stage and needs to be further developed and explored. In addition to acquiring scans during static loads, the methodology could also be used to analyze stem and cement motion under dynamic loading, by incorporating unique CT-acquisition techniques to obtain scans at specific time points of the dynamic loading cycle. The resultant series of images could then be analyzed to determine interface motion for one full cycle of the dynamic waveform. The ground work for analyzing stem-cement interface motion from CT images has already been developed within Chapter 7, therefore future studies could look at implementing this methodology in the analysis of dynamic interface motion. Additionally, an improved CT-compatible loading device could be designed to facilitate testing of implant stems under various loading modes (*i.e.*, compression, torsion, bending, and combined loading), for analysis of the internal stem-cement interface response to these individual loading conditions.

## 8.4 SIGNIFICANCE

In conclusion, the studies presented within this thesis are the first known *in-vitro* studies to assess the effect of clinically-relevant stem surface treatments on the stem-cement interface stability, under various loading modes. The results support the theory that stem surface designs affect the mechanical connection at the stem-cement interface, with surface treatments generally providing increased resistance to interface loosening. Overall, the findings from this thesis have provided valuable information to the literature regarding the interface mechanics and failure mechanisms associated with stem surface treatments and machined grooved surfaces, as well as demonstrated the influential role of stem material on the success of surface treated implants. Across all loading modes, beaded treatments applied to titanium stems, and plasma spray treatments applied to cobalt chrome stems, improved interface stability and strength when large surface treatment areas were employed. In addition, the machining of circumferential grooves onto the stem surface improved interface strength in compression, with no influence in torsion. However, smaller groove dimensions resulted in improved stem stability. It is

expected that this knowledge can be applied to future cemented implant designs, to improve on the stability of these systems in resisting the onset of loosening, consequently increasing the longevity of joint replacement systems.

## 8.5 REFERENCES

- Australian Orthopaedic Association, T., 2010. National Joint Registry, Hip and Knee Arthroplasty Annual Report 2010, [http://www.dmac.adelaide.edu.au/aoanjrr/documents/aoanjrrreport\\_2010.pdf](http://www.dmac.adelaide.edu.au/aoanjrr/documents/aoanjrrreport_2010.pdf).
- Cheung, E. V, O'Driscoll, S.W., 2007. Total elbow prosthesis loosening caused by ulnar component pistoning. *The Journal of Bone and Joint Surgery; American Volume* 89, 1269–1274.
- Fetterly, S., 2012. Quantification of bone and cement strains surrounding a distal ulnar implant with varying cement-stem interface conditions. (M.E.Sc Thesis) The University of Western Ontario, pp. 1-38.
- Jeon, I.H., Morrey, B.F., Sanchez-Sotelo, J., 2012. Ulnar component surface finish influenced the outcome of primary Coonrad-Morrey total elbow arthroplasty. *Journal of Shoulder and Elbow Surgery* 21, 1229–1235.
- Kedgley, A.E., Takaki, S.E., Lang, P., Dunning, C.E., 2007. The effect of cross-sectional stem shape on the torsional stability of cemented implant components. *Journal of Biomechanical Engineering* 129, 310–314.
- Mann, K.A., Bartel, D.L., Wright, T.M., Inghraffa, a R., 1991. Mechanical characteristics of the stem-cement interface. *Journal of Orthopaedic Research* 9, 798–808.
- New Zealand Orthopaedic Association, T.N.Z.J.R., 2010. Eleven Year Report- January 1999 to December 2009., <http://www.cdhb.govt.nz/njr/reports/A2D65CA3.pdf>.

## APPENDICES

## Appendix A: Thesis Glossary

*This appendix defines the terminology used throughout this thesis, to assist with understanding the technical terms that may not be familiar to the reader.<sup>5</sup>*

**Abduct:** To draw away from a position near the middle axis of the body (as in a limb).

**Alloy:** A substance composed of two or more metals, or of a metal and non-metal fused together when molten.

**Attenuate:** The decrease or lessening of the amount of energy.

**Bioactive:** Having the effect of a living organism.

**Biocompatibility:** The condition of being compatible with living tissue, or not being toxic to living tissue.

**Camera/Image sensor:** A device that responds to the stimulus of light and transmits a resulting impulse.

**Cartilage:** Flexible connective tissue found in many areas in the bodies of humans and other animals

**Cartilaginous joints:** Joints that are connected by cartilaginous material.

**Charged couple device (CCD):** A semiconductor device, used as an optical sensor, which stores charge and subsequently transfers it to an amplifier and detector.

**Diffraction:** A modification that light undergoes, especially in passing by the edges of opaque bodies or through narrow openings.

---

<sup>5</sup> The medical definitions listed here were obtained from the Marriam-Webster, Medline Plus Medical Dictionary, a service of the U.S. National Library of Medicine and National Institutes of Health. The general terminology was modified from the Marriam-Webster online dictionary, and Wikipedia Online Encyclopedia.

**Extension:** The unbending movement of a joint in a limb, that increases the angle between the bones of the limb and the joint.

**Fibrous joints:** Joints that are connected by fibrous, connective tissue such as collagen.

**Field-of-view (FOV):** The maximum observable area (as seen from a camera).

**Flexion:** A bending movement around a joint in a limb that decreases the angle between the bones of the limb and the joint.

**f-number:** Quantitative measure of the lens speed, and is the ratio of the focal length to the diameter of the lens opening.

**Focal length:** Measure of how strongly the system converges or diverges light; the distance (from the lens) over which the light rays are brought into focus.

**Glenohumeral:** The connection between the glenoid cavity and humerus of the shoulder.

**Glenoid cavity:** The shallow cavity of the upper part of the scapula, in which the humerus articulates.

**Hounsfield unit (HU):** Quantitative scale for describing radiodensity of a material, relative to the radiodensity of distilled water and air at standard pressure and temperature.

**Humerus:** The longest bone of the upper arm or forelimb extending from the shoulder to the elbow.

**Image distortion:** Deviation of projected image, in which straight lines of an object do not maintain similar straightness in the image.

**Implant fixation:** Surgical implementation and anchoring of joint replacement systems.

**Intramedullary:** Situated or occurring within the medulla of bone; use of the marrow space of a bone for support.

**In-vitro:** Outside the living body and in an artificial environment.

**In-vivo:** Inside the living body, or within a living organism

**Lens aperture:** The opening or hole of a lens through which light enters.

**Micromotion:** Motion, such as that of an implant, occurring on the order of micrometers.

**Monomer:** A molecule that may bind chemically to other molecules to form polymers.

**Osseointegration:** The firm anchoring of a surgical implant by growth of bone around it, without fibrous tissue formation at the interface

**Osteoarthritis:** Degenerative joint disease that causes changes in the bone and cartilage at the joint, resulting in wearing down of joint surfaces.

**Osteoporosis:** Decrease in bone mass with decreased density and enlargement of bone spaces.

**Perspective error:** Difference in the image magnification as a result of object position/distance from the lens.

**Photons:** The unit intensity of light; smallest physical quantity of electromagnetic radiation.

**Pixels:** Small discrete elements that make up a image; picture elements.

**Plasma spray:** Coating in which melted or heated materials are sprayed onto a surface.

**Polymer:** Chemical compound consisting of repeating structural units or molecules.

**Stereophotogrammetry:** Technique used for the assessment of three-dimensional migration of joint replacement from bone, using an imaging technique to obtain real-time moving images of markers attached to the bone and implant.

**Resolution:** The detail and image holds; quantification of how close lines can be and still visibly resolved.

**Sintered bead:** Coating in which beads are diffused onto a surface at high temperatures.

**Substrate material:** Material on which a process is conducted; surface to which coating is applied.

**Synovial joints:** Most common of the moveable joints characterized by two bony surfaces covered with cartilage, contained in a fibrous capsule containing joint fluid.

**Telecentric lens:** Compound lens for which chief rays are parallel to the optical axis in a object/image space, making the object appear to be the same size independent of its location in space.

**Tibia:** The large, inner bone of the lower leg, located between the knee and ankle.

**Ulna:** One of the two bones located in the forearm, situated on the side of the forearm with the little finger, and articulates with the humerus in the elbow joint.

**Ulnohumeral:** The connection between the ulna and humerus bone of the elbow joint.



## Appendix B: Specifications for Hardware of Optical System

*This appendix details the specifications for the hardware used in the optical system discussed in Chapters 2,3,4,5 and 6.*

Specification	piA2400-12gm/gc	piA2400-17gm/gc
Sensor Size (H x V pixels)	gm: 2456 x 2058 gc: 2454 x 2056	
Sensor Type	Sony ICX625ALA/AQA Progressive scan CCD	
Optical Size	2/3"	
Pixel Size	3.45 $\mu\text{m}$ x 3.45 $\mu\text{m}$	
Max. Frame Rate (at full resolution)	12 fps	17 fps
Mono/Color	All models available in mono or color	
Data Output Type	Fast Ethernet (100 Mbit/s) or Gigabit Ethernet (1000 Mbit/s)	
Pixel Data Formats	Mono Models: Mono 8 (equivalent to DCAM Mono 8) Mono 16 (equivalent to DCAM Mono 16) Mono 12 Packed YUV 4:2:2 Packed (equivalent to DCAM YUV 4:2:2) YUV 4:2:2 (YUYV) Packed Color Models: Mono 8 (equivalent to DCAM Mono 8) Bayer BG 8 (equivalent to DCAM Raw 8) Bayer BG 16 (equivalent to DCAM Raw 16) Bayer BG 12 Packed YUV 4:2:2 Packed (equivalent to DCAM YUV 4:2:2) YUV 4:2:2 (YUYV) Packed	
ADC Bit Depth	12 bits	
Synchronization	Via external trigger signal or via software	
Exposure Control	Programmable via the camera API	
Camera Power Requirements	+12 to +24 VDC, (min. +11.3 VDC, absolute max. +30.0 VDC ), < 1% ripple	
	5.4 W @ 12 VDC	5.9 W @ 12 VDC
I/O Ports	2 opto-isolated input ports and 4 opto-isolated output ports	
Lens Adapter	C-mount	


**Figure B.1: Specifications for the Basler Pilot AG piA 2400- 12gc Camera**

(Adapted from the User Manual for GigE Vision Cameras; Document No.AW000151, Version 16; Basler Vision Technologies)

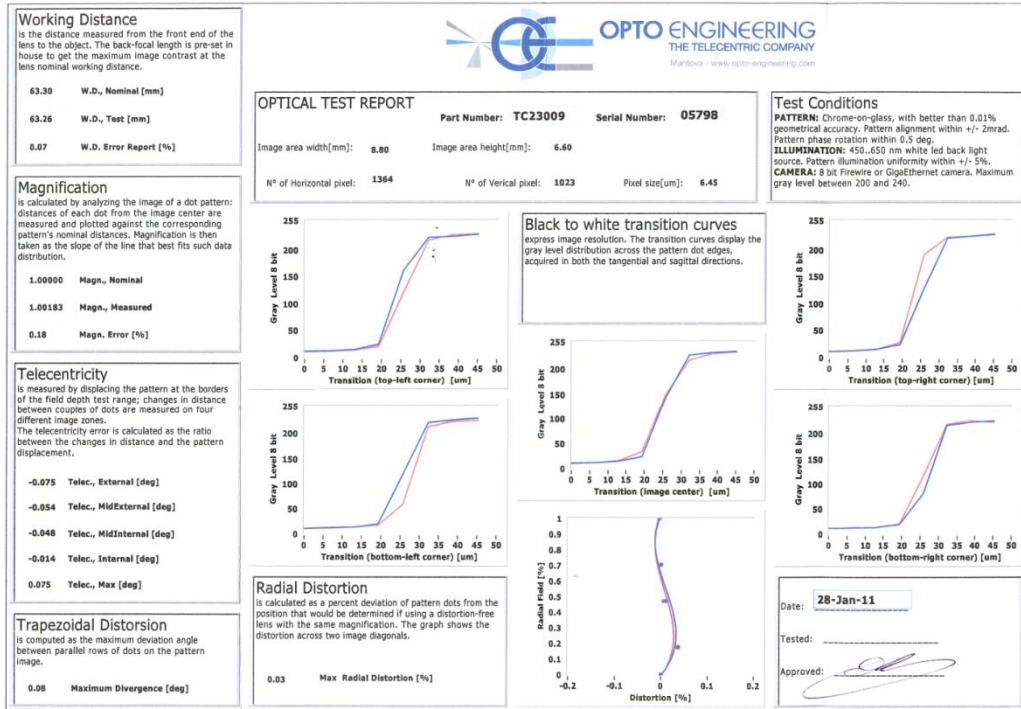


**Figure B.2: Specifications for the Opto Engineering Telecentric Lens**


(Product test report provided with the telecentric lens)



### DL072

1" x 1" Axial Diffuse Illuminator

- 4i) High brightness LED offers long life (50k hours).
- 4i) 25mm x 25mm field-of-view designed for use on small parts, or in environments with space limitations.



---

**Ordering Information**

Standard Product:  
Shipped Next Day

**DL072-WHI24**

Configured for Use with User Supplied 24v Power

Standard Product Variation:  
Shipped Within Two Weeks

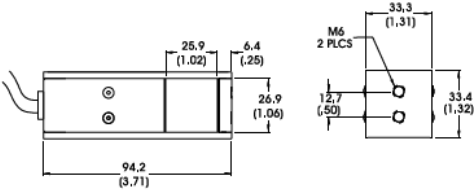
DL072	-	Spectral wavelength	Optional power Compatibility	Alternative Connector
		XXX	XX	XXX
		(blue) 470	IC	M12* (male)
		(green) 530	IS	
		(amber) 590	C2	
		(red) 625	C3	
		(infra-red) 850	C5	
		(white) WHI	24	

ID = IS (requires 24v power supply)  
 IS = ISU (requires 24v power supply)  
 C2 = AI Connector  
 C3 = Pulsar 710 Connector  
 C5 = Pulsar 320 Connector  
 \* Available with IC, IS, and 24v options only  
 † Not available in 12v

Optimal working distance: 25.4mm (1")  
 Effective Working Range: 12.7-50mm (.5"-2")

---

**Dimensional Information**



DIMENSIONS ARE IN MILLIMETERS (INCHES)

Click for Installation Models & Drawings

Cable Length: 1.5 Meter (59")

Standard Variation	Current Specifications														
@24	<table style="display: inline-table; border: none;"> <tr> <td style="padding: 0 5px;">blue</td> <td style="padding: 0 5px;">green</td> <td style="padding: 0 5px;">amber</td> <td style="padding: 0 5px;">red</td> <td style="padding: 0 5px;">infra-red</td> <td style="padding: 0 5px;">white</td> <td style="padding: 0 5px;">mA</td> </tr> <tr> <td style="padding: 0 5px;">350</td> <td style="padding: 0 5px;">350</td> <td style="padding: 0 5px;">350</td> <td style="padding: 0 5px;">350</td> <td style="padding: 0 5px;">350</td> <td style="padding: 0 5px;">350</td> <td style="padding: 0 5px;"></td> </tr> </table>	blue	green	amber	red	infra-red	white	mA	350	350	350	350	350	350	
blue	green	amber	red	infra-red	white	mA									
350	350	350	350	350	350										

**Standard Product Information**

Weight: 226.8 g (8.0 oz)  
 Finish: Black Anodized  
 Operating Temperature: 0-60° C  
 Meets Specifications: CE, RoHS

[advancedillumination.com](http://advancedillumination.com) 06.13.2011

**Figure B.3: Specifications for the Advanced Illumination, Axial Diffuse Illuminator**

(Adapted from sales sheet for Advanced Illumination products;  
<http://www.1stvision.com/lighting/AI/uploads/products/DL072.pdf>)

## Appendix C: LabVIEW® Programs

This appendix shows the LabVIEW® back panels for the custom written programs used for calibration of the optical system and marker tracking data collection. These programs were used for Chapters 2 ,3, 4, 5 and 6.

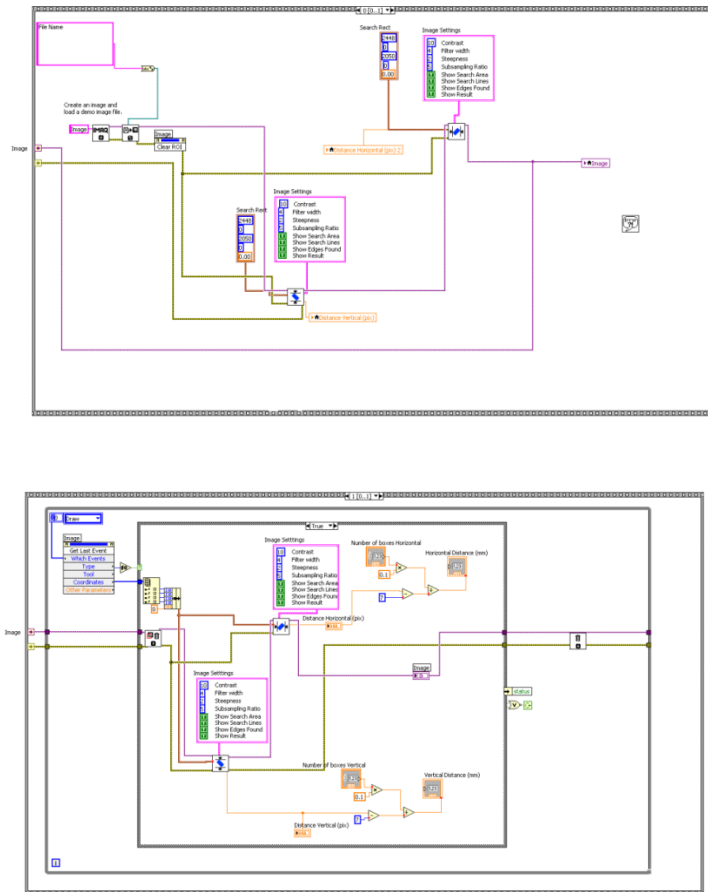


**Figure C.1: Back Panel of Calibration Program**

The calibration program determines the vertical and horizontal pixel count for a rectangular region of interest of the calibration grid, set by the user. Based on the known spacing of the calibration grid (*i.e.*, 0.1 mm), the pixel to millimeter conversion for the region of interest is found.

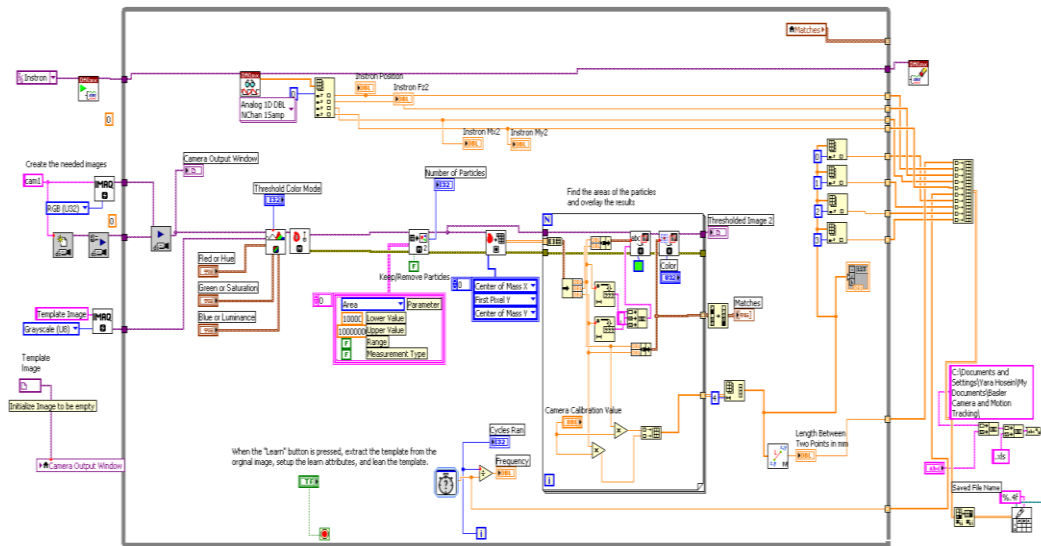


**Figure C.2: Back Panel of the Optical Tracking Program**

The optical tracking program incorporating a thresholding method to detect markers placed on landmarks of interest. The program determines the centroids of the detected markers, and tracks their respective  $(x,y)$  coordinates throughout the duration of the program. The program outputs the individual  $(x,y)$  coordinates of the marker, the length between the two points, and the corresponding load and position data from the materials testing machine.

## Appendix D: Bland-Altman Plots for Optical System Validation

This appendix shows the individual Bland-Altman plots for the various regions of the optical system field of view (Region 1-9), as discussed in Chapter 2.

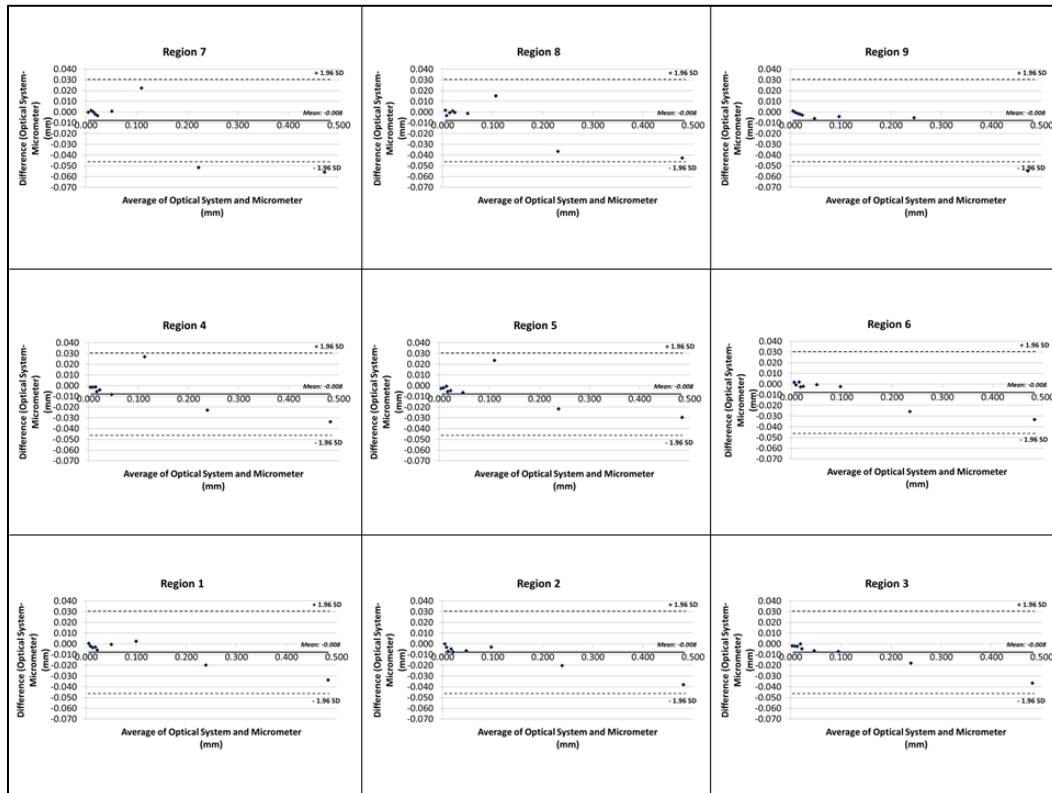


**Figure D.1: Bland Altman plots for Region 1-9 of Horizontal Displacement**

Individual plots for horizontal displacements within the nine regions of the image field of view. Regions 7 and 9 show some scatter points outside 95% limit of agreement (as indicated by dashed lines).

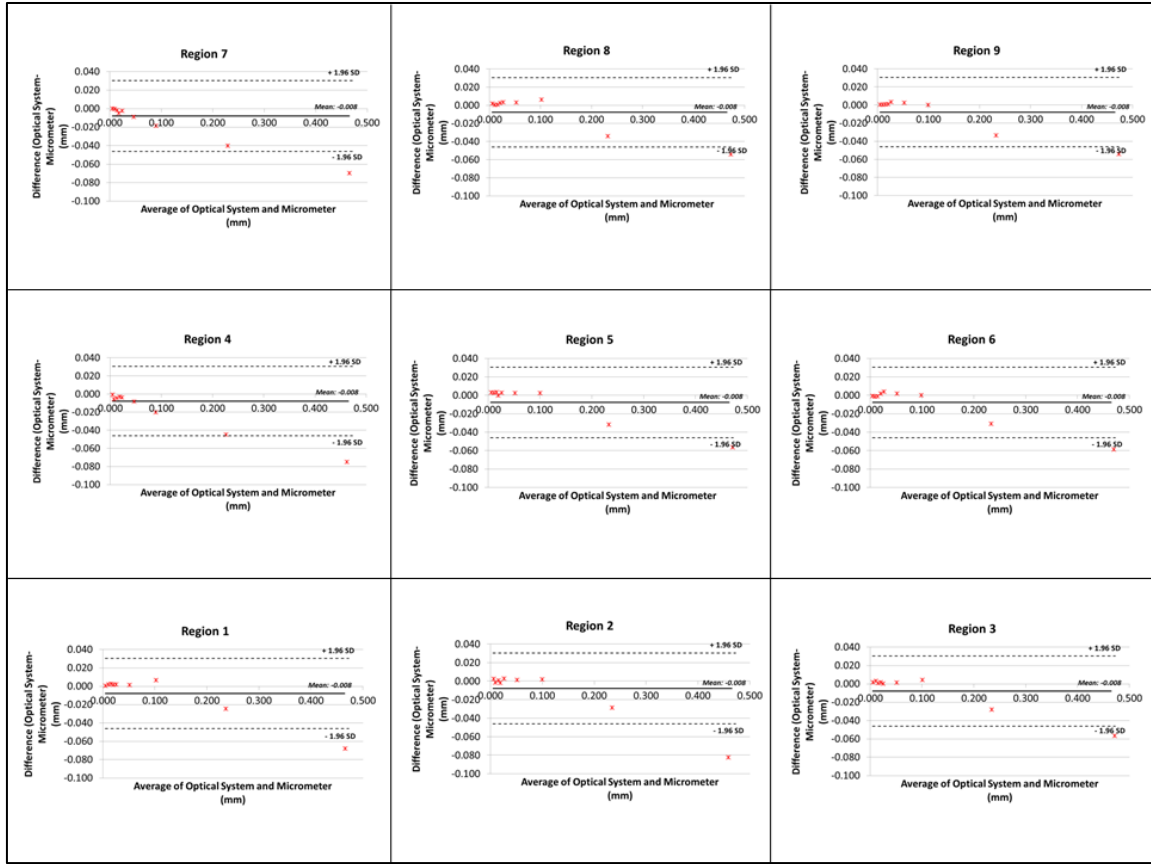


**Figure D.2: Bland Altman plots for Region 1-9 of Vertical Displacement**

Individual plots for vertical displacements within the nine regions of the image field of view. All regions show some scatter points outside 95% limit of agreement (as indicated by dashed line) for measurements of 0.5 mm.

## Appendix E: Calculation of Optical System Accuracy

*This appendix details the calculations used for determining the accuracy of the optical system as described in Chapter 2.*

Accuracy as measured by percent error for the range of applied displacements (0.005-0.500 mm).

### Procedure<sup>6</sup>:

- 1) Determine line of best-fit for data from optical system (*i.e.*, measured) and micrometer (*i.e.*, true) (Figure E.1).

$$\text{Equation of best-fit: } y = 0.8914x + 0.002 \quad (\text{Eq. F.1})$$

- 2) Evaluate errors in the measurements by creating a deviation plot from the data sets (Figure E.2).

*y axis = Measured value (i.e., optical system) – Equation of best fit*

*x axis = True value (i.e., micrometer)*

- 3) Accuracy of the system, presented as % error of the range of output displacements:

- Range of output displacements from equation of best-fit:

$$\circ 0.507 \text{ mm} - 0.007 \text{ mm} = 0.500 \text{ mm}$$

---

<sup>6</sup> As described in: Wheeler AJ, Ganji AR. 2010. Chapter 2: General Characteristics of Measurement Systems. In: Introduction to Engineering Experimentation; Pearson Higher Education, NJ. pp 21-24



- Positive limit:

$$\frac{(+ 0.039mm)}{0.500 mm} \times 100 = + 8.8 \%$$

- Negative limit:

$$\frac{(-0.041mm)}{0.500 mm} \times 100 = - 9.3 \%$$

*Therefore, the accuracy of measurements from the optical system is ( + 8.8 %, – 9.3 % ) of the measured value.*

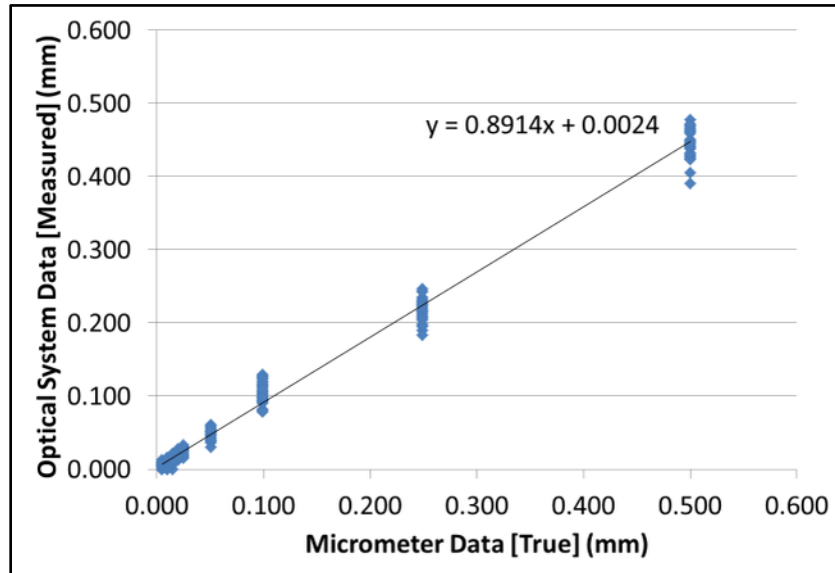


**Figure E.1: Line of Best-Fit for Measured against True Displacements**

The plot shows the scatter of points, along with the line of best fit relating the measured data from the optical system to the true data from the micrometer.

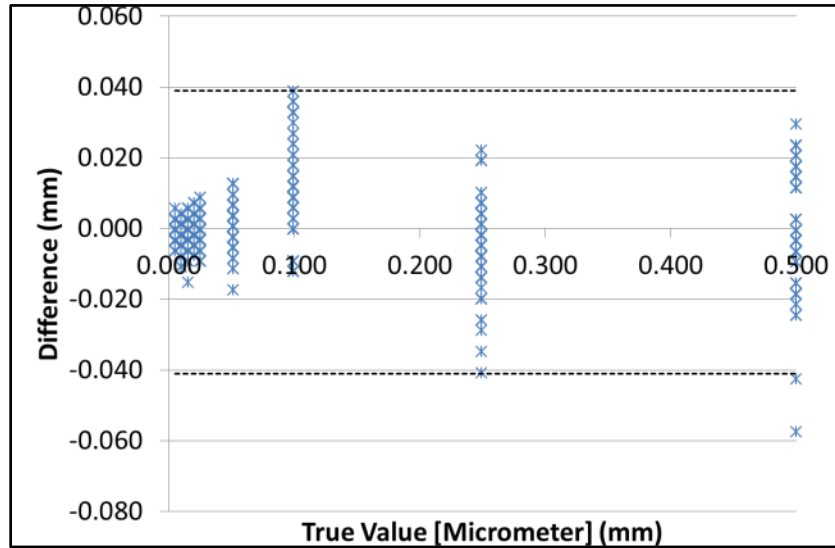


**Figure E.2: Deviation Plot for Optical System Measurements**

This deviation plot shows the difference in measurements from the optical system and micrometer, against true displacements (*i.e.*, micrometer). The dashed lines parallel to the horizontal axis are the accuracy limits of the data (+0.039 mm, -0.041 mm), such that data points not considered to be outliers are contained within them.

## Appendix F: Calculation of Optical System Resolution

*This appendix details the calculations used for determining the resolution of the optical system, based on the calibration method described in Chapter 2.*

### Calibration Method:

- 1) The calibration grid (Figure F.1) (grid spacing  $0.100 \pm 0.002$  mm (Pyser-SGI Ltd, Kent, UK)) was placed in the camera field of view, at the location expected for marker placement.
- 2) Using the LabVIEW calibration program described in Appendix C.1, the horizontal and vertical pixel length (*i.e.*, pixel to millimetre conversion) was determined for the nine regions of the image field of view.
- 3) Two trials were done in each region of the image field of view, and an average pixel size was determined from the measured vertical and horizontal lengths of the pixels.

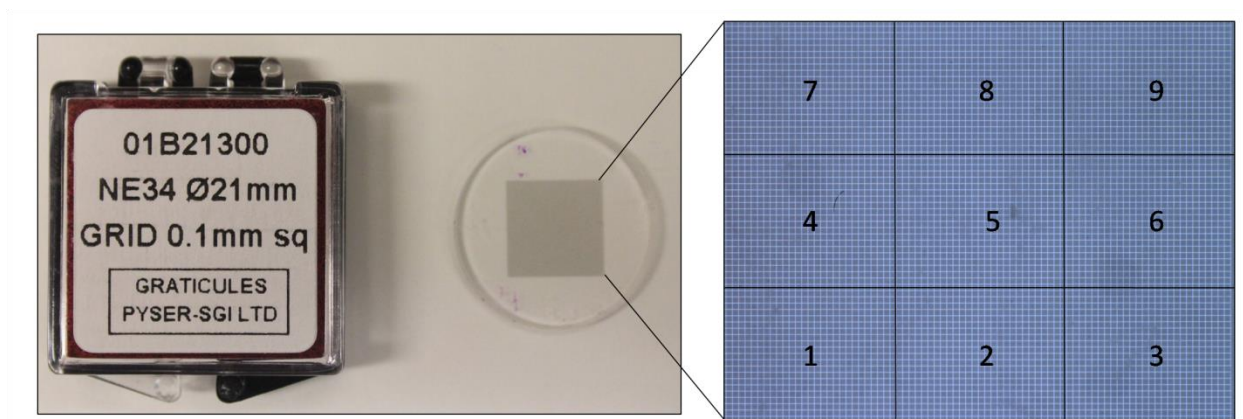


**Figure F.1: Calibration Grid used for Pixel to mm Conversion**

The calibration grid, with grid spacing  $0.100 \pm 0.002$  mm, was divided into 9 regions of the image field of view to determine the pixel to mm conversion for each region.

**Table F.1: Vertical and Horizontal Pixel Lengths**

<b>Trial #</b>	<b>Region FOV</b>	<b>Pixel vertical length (mm)</b>	<b>Pixel horizontal length (mm)</b>
1	1	0.0033	0.0034
1	2	0.0033	0.0035
1	3	0.0033	0.0033
1	4	0.0034	0.0034
1	5	0.0033	0.0033
1	6	0.0033	0.0033
1	7	0.0033	0.0034
1	8	0.0034	0.0034
1	9	0.0033	0.0033
2	1	0.0033	0.0034
2	2	0.0033	0.0034
2	3	0.0033	0.0034
2	4	0.0034	0.0033
2	5	0.0034	0.0033
2	6	0.0034	0.0033
2	7	0.0033	0.0033
2	8	0.0033	0.0033
2	9	0.0033	0.0034
	<b>Average pixel size</b>	<b>0.003</b>	<b>0.003</b>

Uncertainty in calibration measurement <sup>7,8</sup>:

$$U_C = (B_C^2 + P_C^2)^{1/2} \quad (\text{Eq. G.1})$$

Where:

$U_C$  = Total uncertainty

$B_C$  = Systematic error, based on manufacturer specifications of grid

$P_C$  = Random error in repeated measurements of pixel size

Random Error in Repeated Measurements of Pixel Size:

$$P_C = t \times S_{\bar{x}} \quad (\text{Eq. G.2})$$

Where:

$S_{\bar{x}}$  = standard deviation of the mean from repeated pixel to mm conversions  
(n=36)

$t$  = t-statistic with 95% confidence interval for 36 repeated pixel to mm conversions, as obtained from the student's t-distribution table

$$P_C = 1.6896 \times \left( \frac{5.54 \times 10^{-5}}{\sqrt{36}} \right) \quad (\text{Eq. G.3})$$

---

<sup>7</sup> Wheeler AJ, Ganji AR. 2010. Chapter 7: Experimental Uncertainty Analysis. In: Introduction to Engineering Experimentation (3<sup>rd</sup> Ed); Pearson Higher Education, NJ. pp 199-230

<sup>8</sup> Figliola RS, Beasley DE. 2006. Chapter 5: Uncertainty Analysis. In: Theory and Design for Mechanical Measurements (4<sup>th</sup> Ed); John Wiley and Sons, NJ. pp 149-182

Therefore, total uncertainty for pixel to mm conversion from equation G.1:

$$U_C = (B_C^2 + P_C^2)^{1/2}$$

$$U_C = \left( 0.002^2 + \left( 1.6896 \times \left( \frac{5.54 \times 10^{-5}}{\sqrt{36}} \right) \right)^2 \right)^{1/2}$$

$$U_C = 0.002\text{mm}$$

***Optical System Resolution = 0.003 ± 0.002 mm***



**Appendix G: Engineering Drawings and Assemblies**

*This appendix includes the dimensioned drawing of parts and assemblies for the stems and jigs used in Chapters 3,4,5,6 and 7 of this thesis. The models were created in Solidworks (Dessault Systems, Concord, MA).*

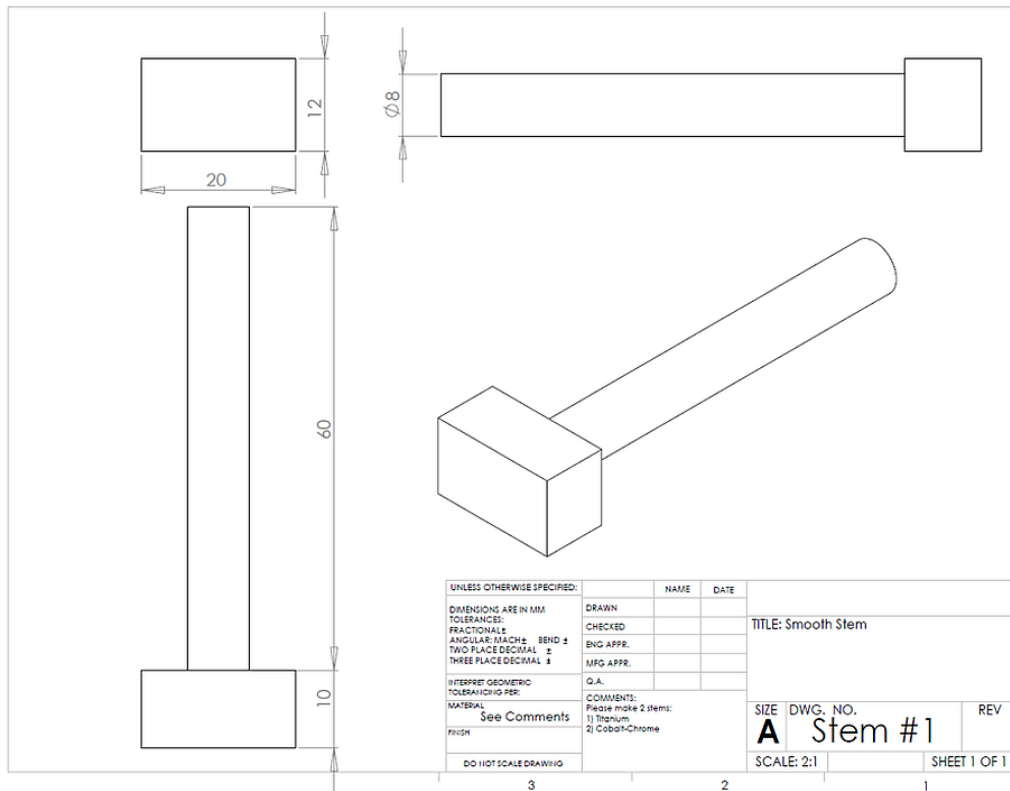


**Figure G.1: Engineering Drawing of Smooth Implant Stem**

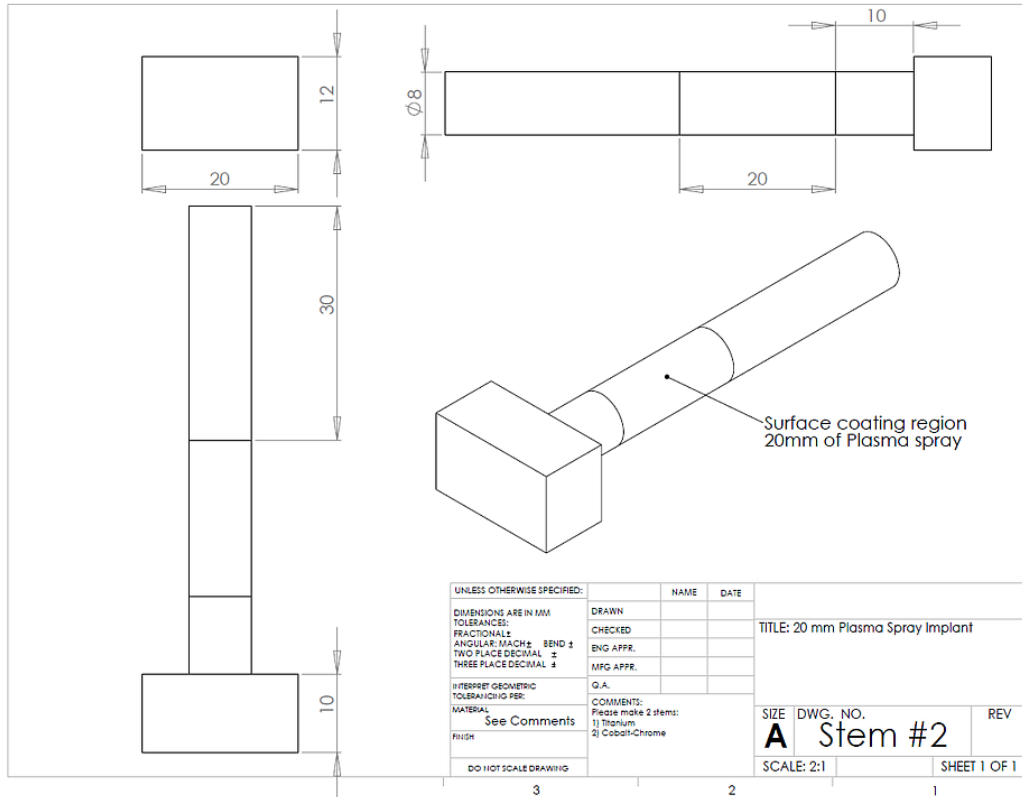
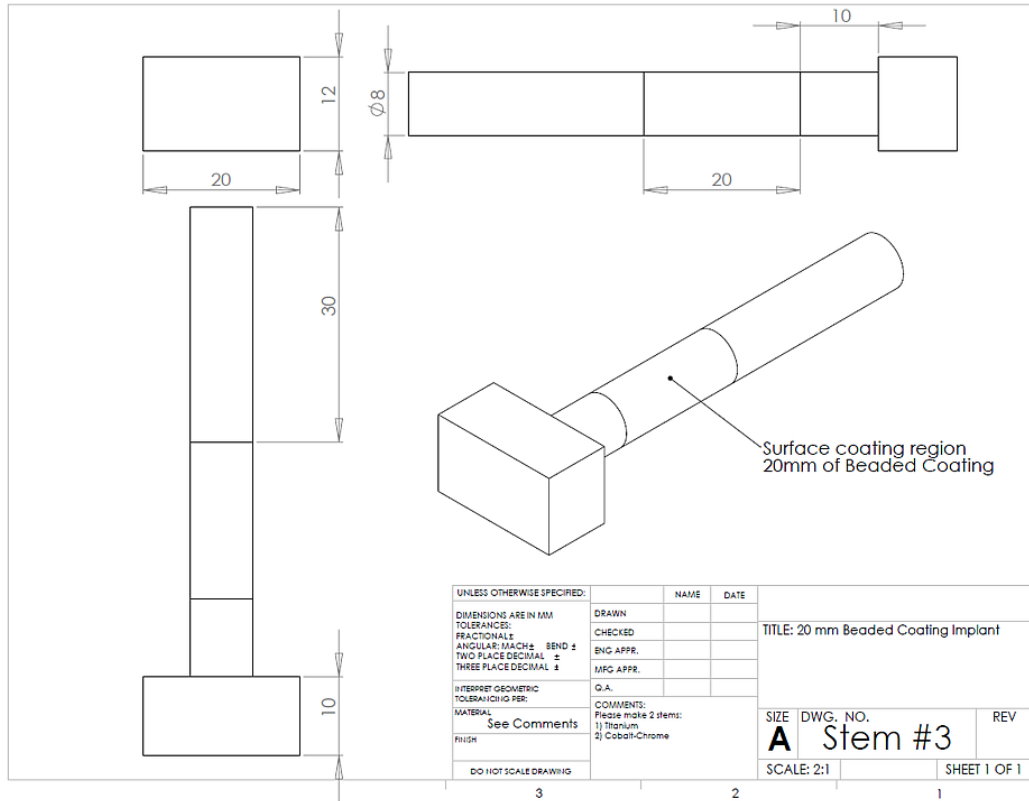


Figure G.2: Engineering Drawing of 20 mm Length Plasma Spray Implant Stem



**Figure G.3: Engineering Drawing of 20 mm Length Beaded Implant Stem**

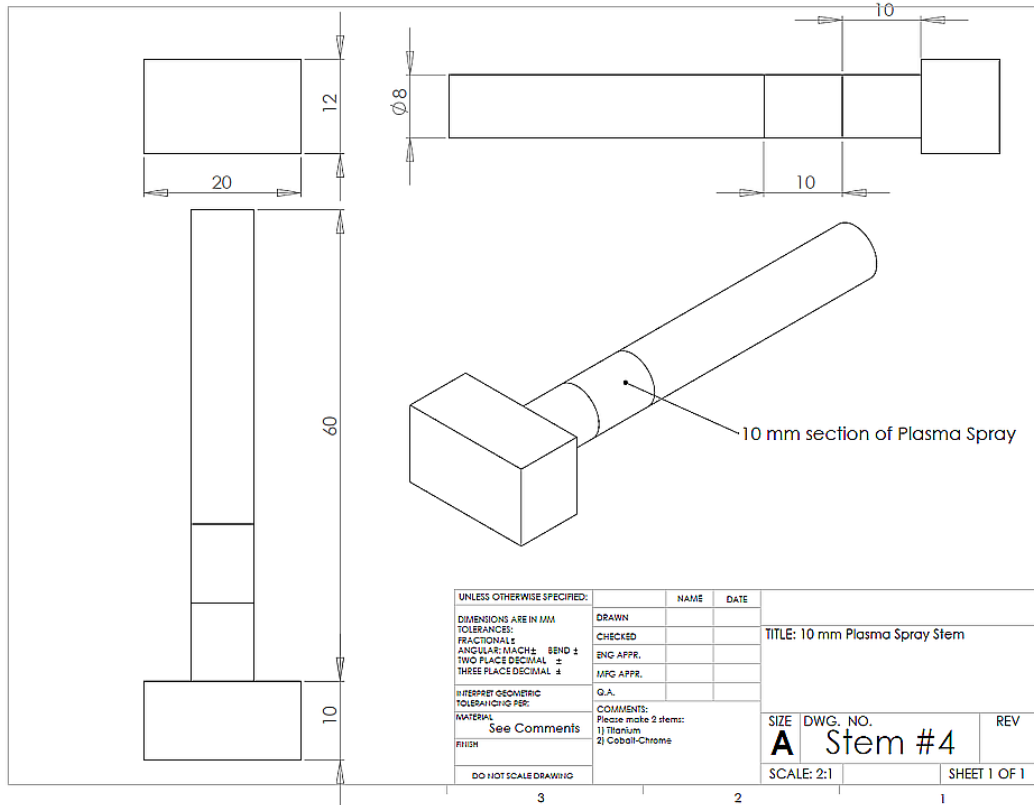
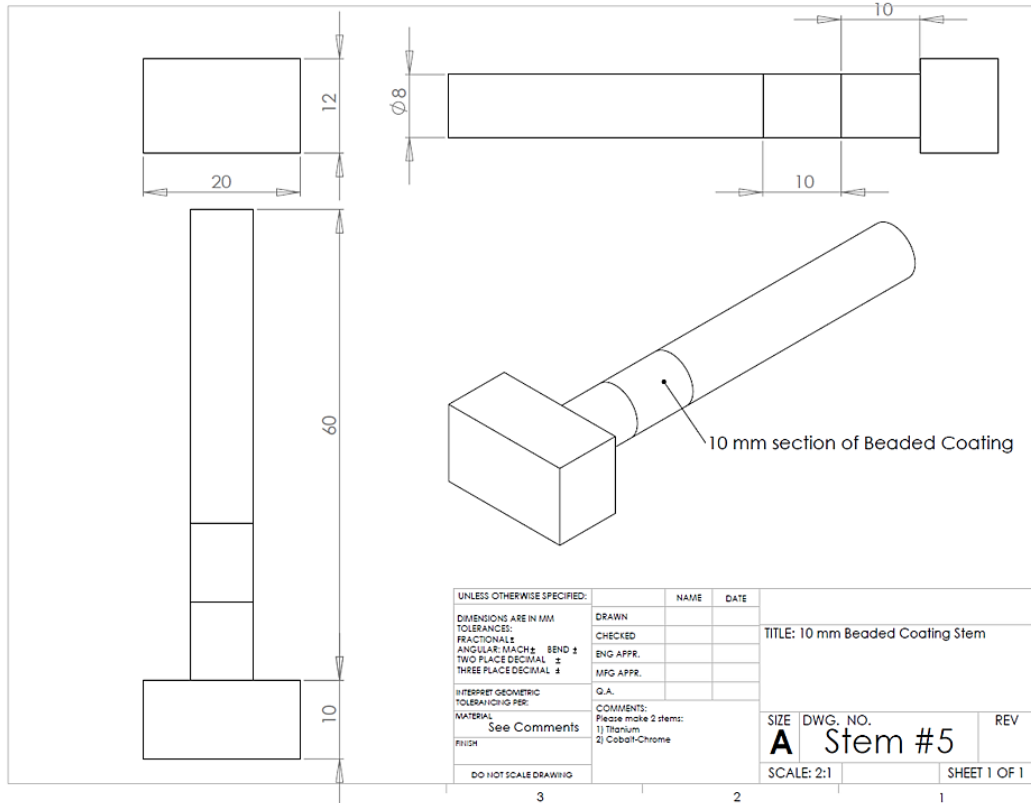


Figure G.4: Engineering Drawing of 10 mm Length Plasma Spray Implant Stem



**Figure G.5: Engineering Drawing of 10 mm length Beaded Implant Stem**

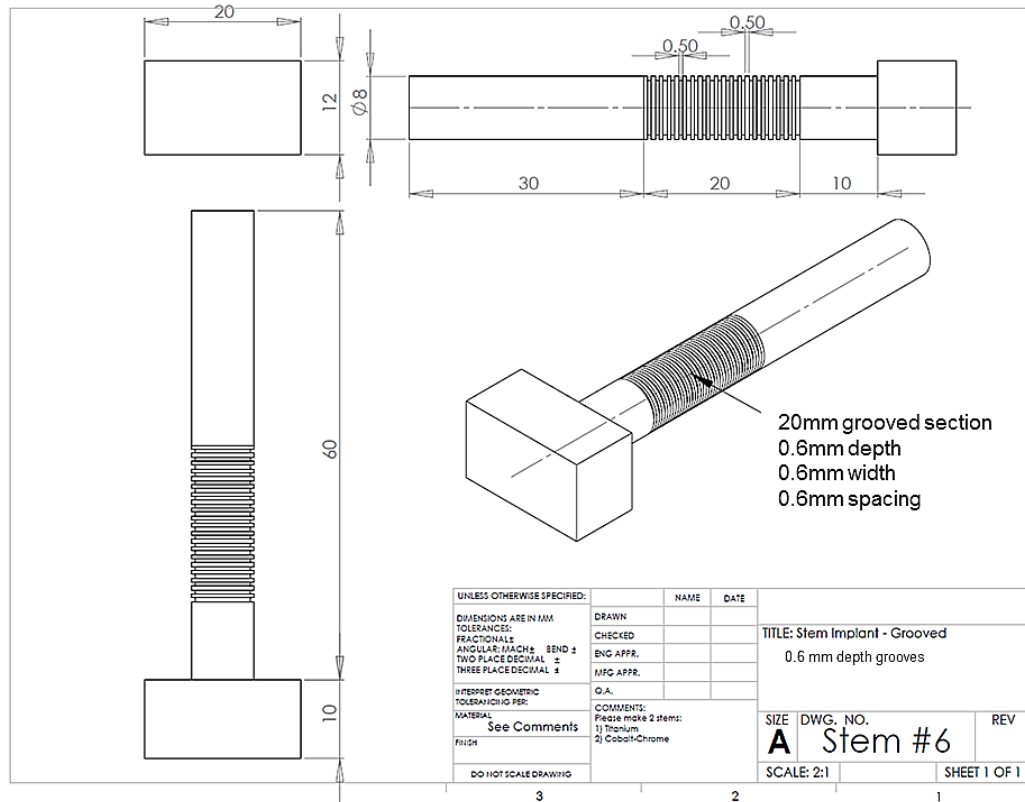


Figure G.6: Engineering Drawing of 0.6 mm Grooved Implant Stem

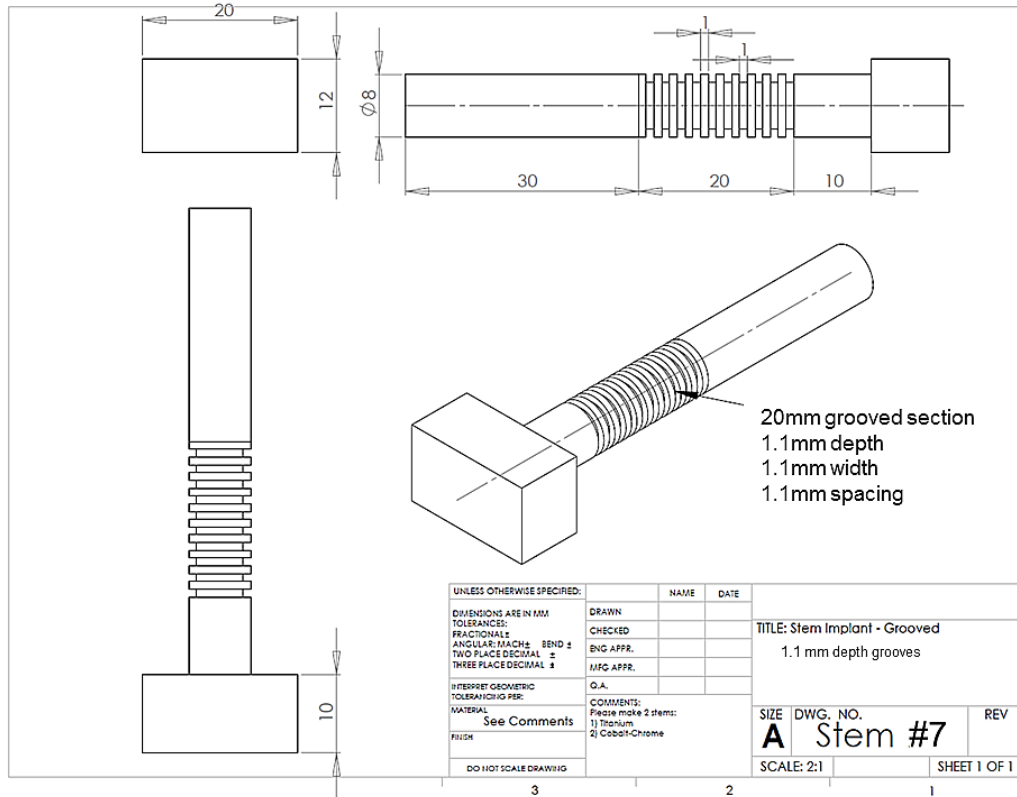


Figure G.7: Engineering Drawing of 1.1 mm Grooved Implant Stem

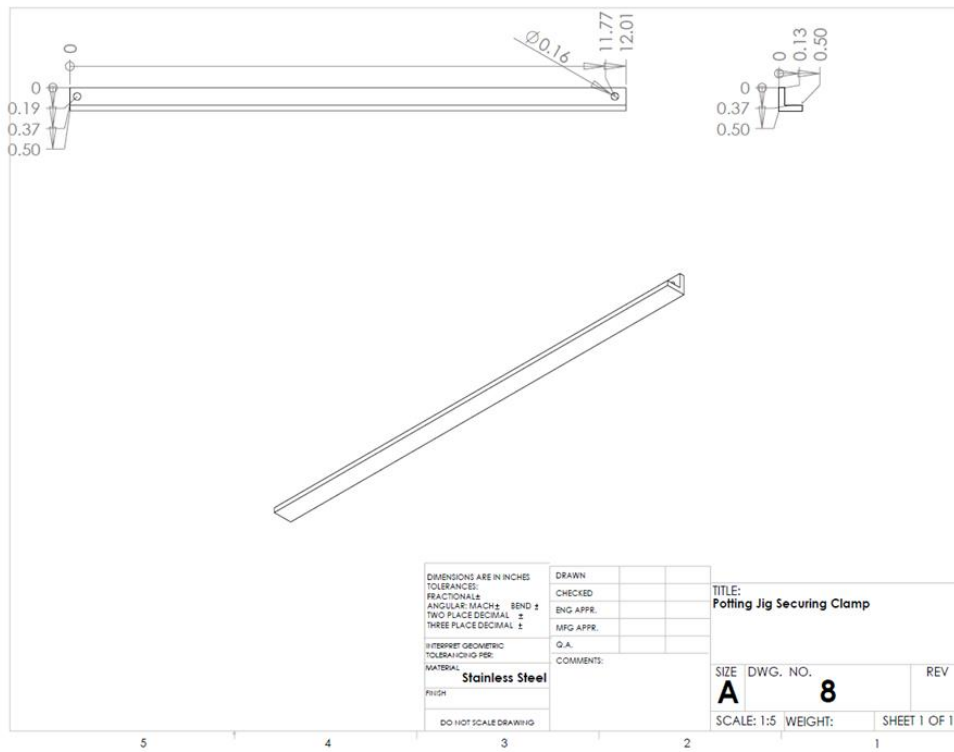
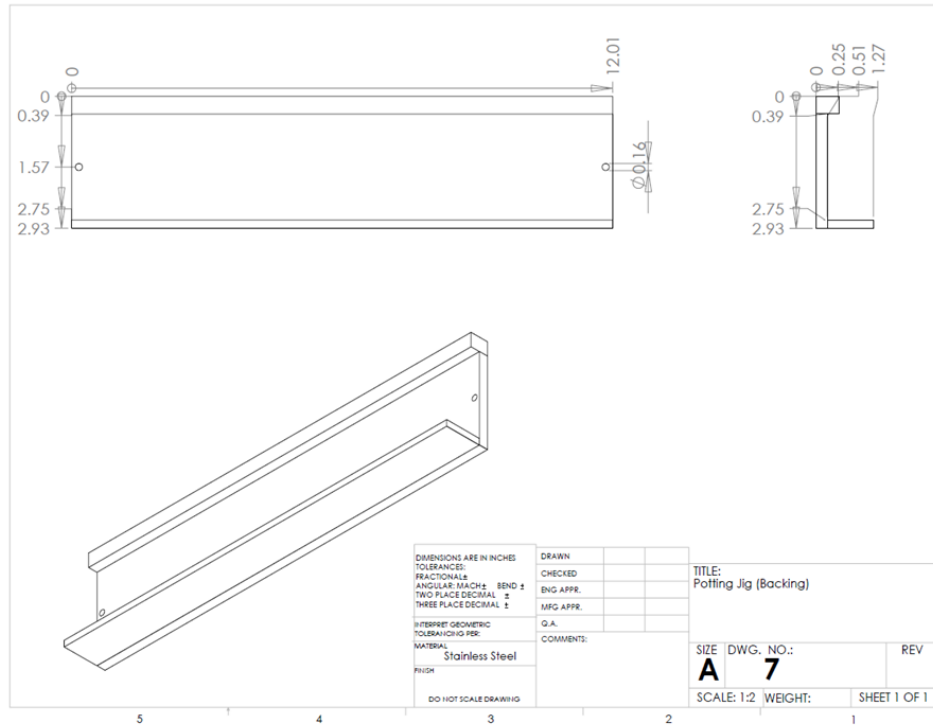
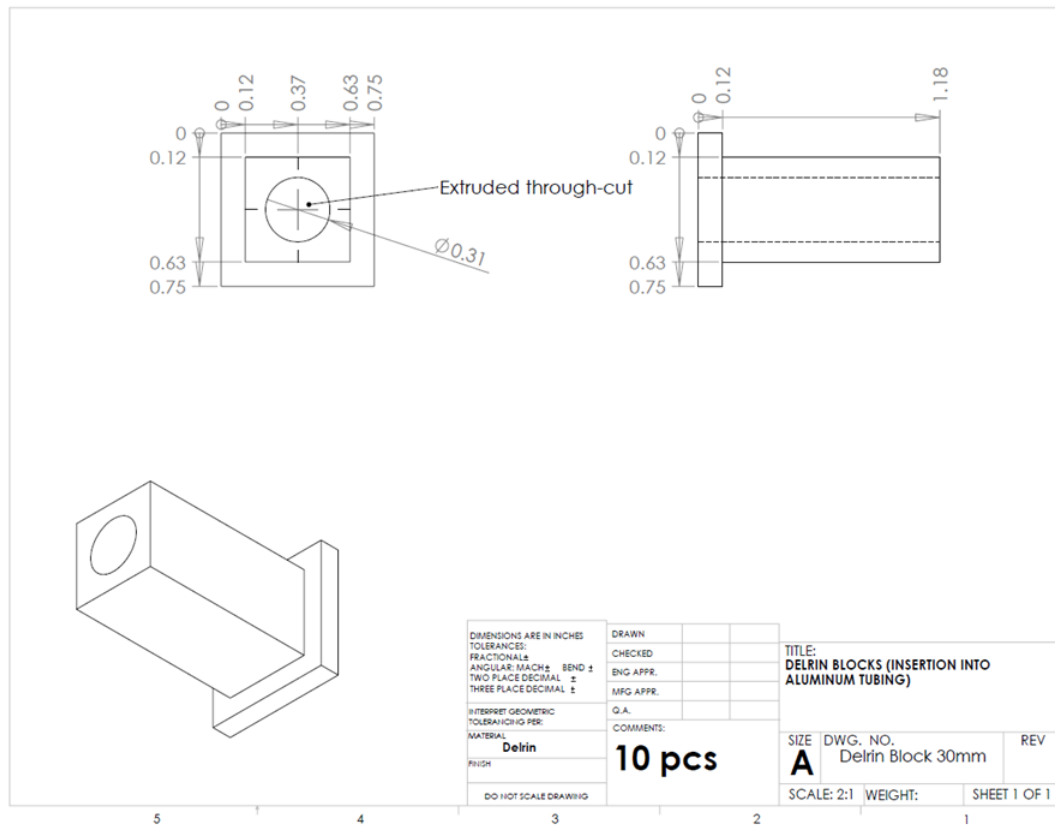
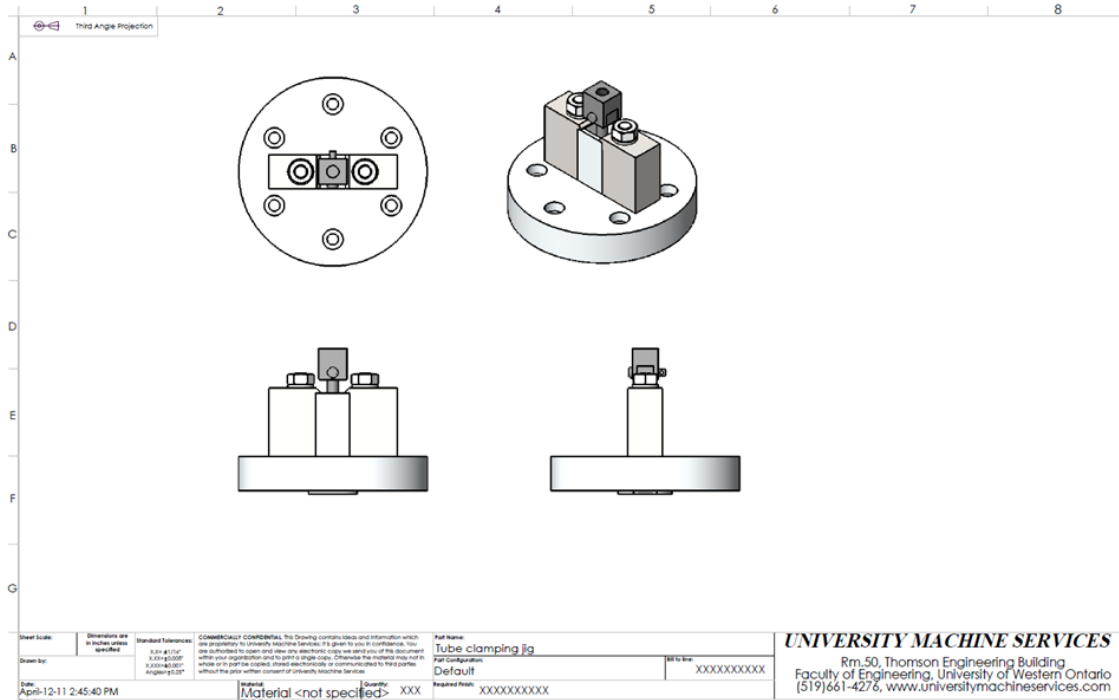


Figure G.8: Engineering Drawing of Parts for Potting Jig Assembly





**Figure G.9: Engineering Drawing of Delrin® Block used to Centralize Stems for Potting**



**Figure G.10: Engineering Assembly of Jig used for securing Stem in Torsion and Compression**

*(Assembly drawing done by University Machine Services)*

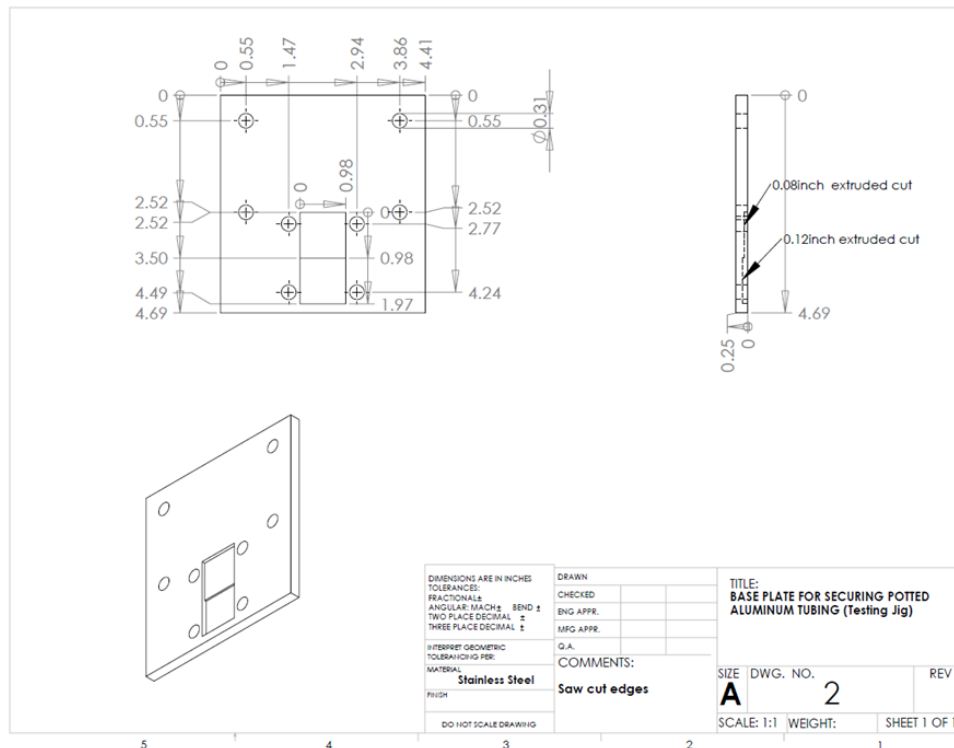
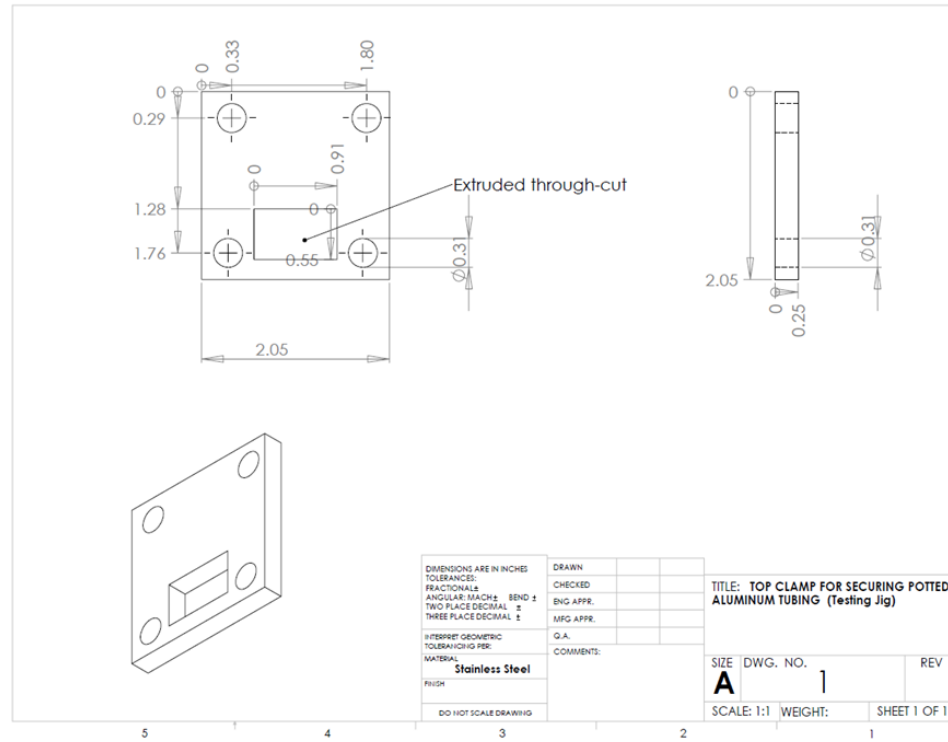


Figure G.11: Engineering Drawing of Securing Plates used for Bending Tests

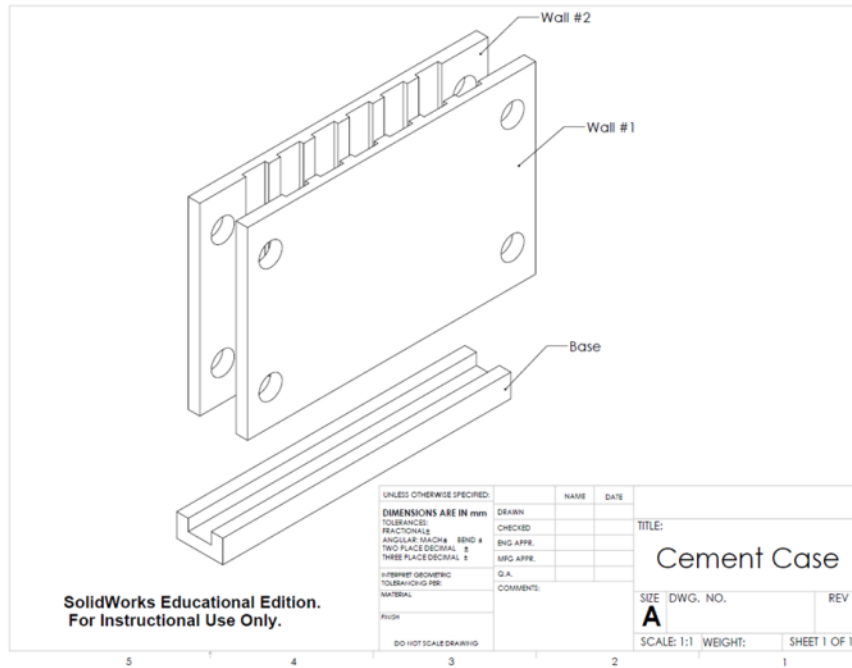


Figure G.12: Engineering Assembly of Cement Sample Template

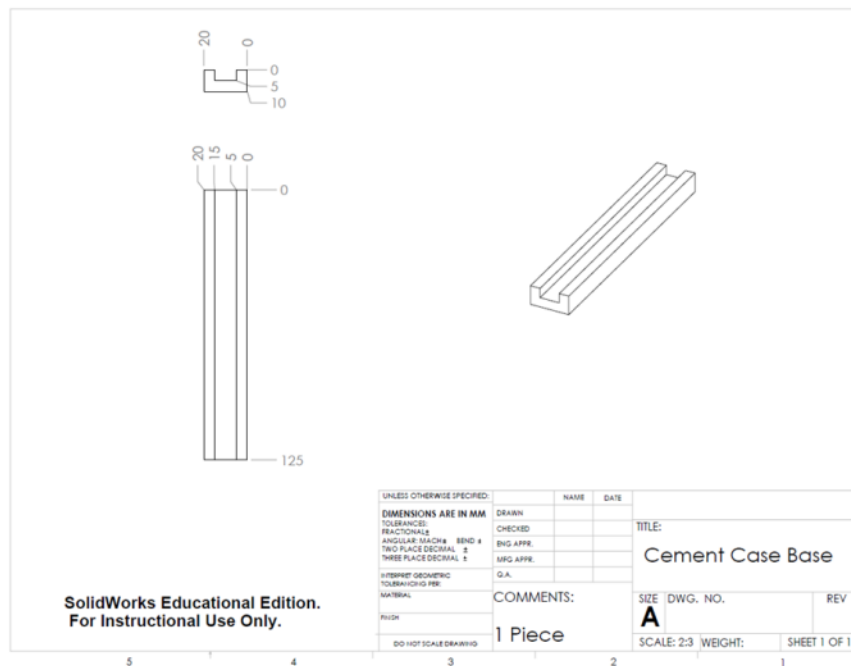
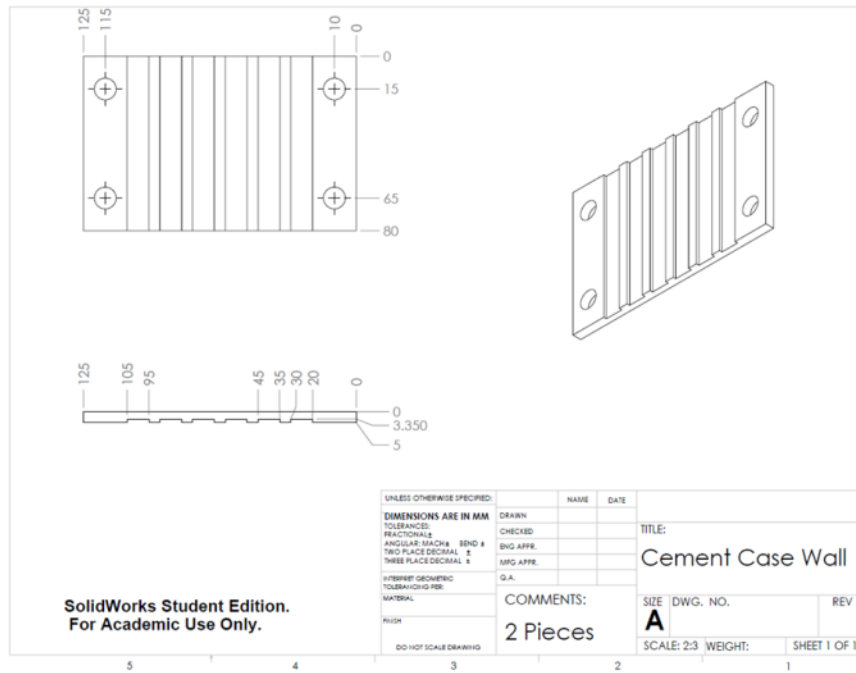
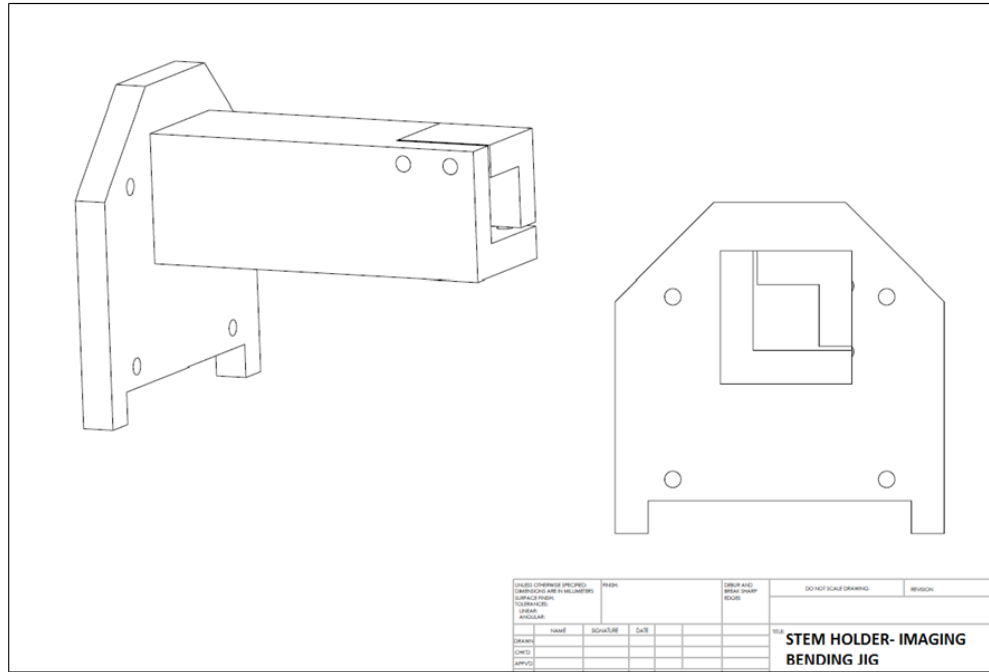
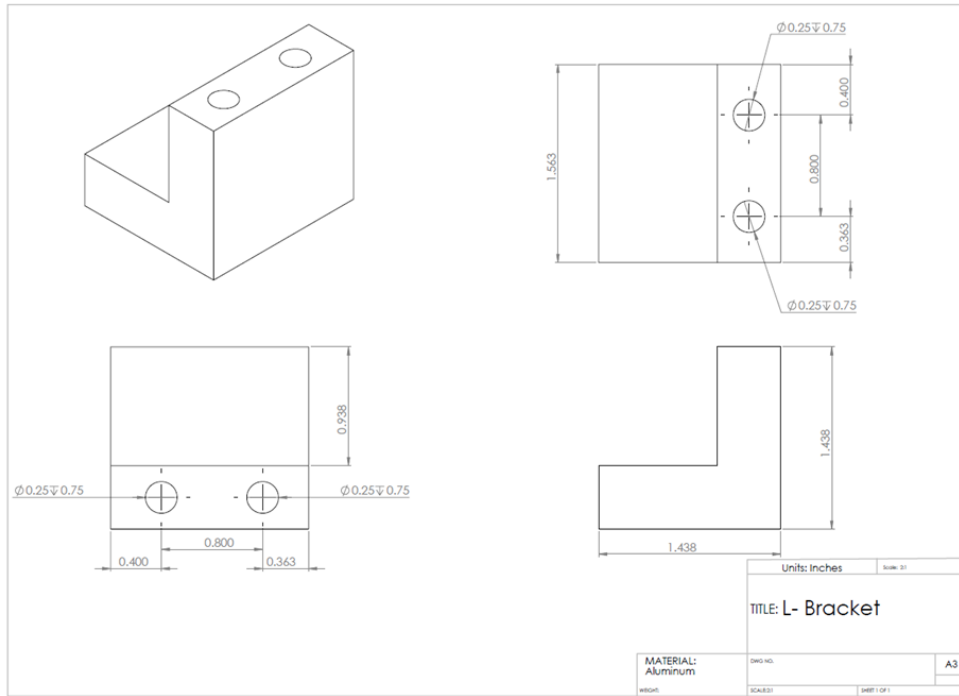
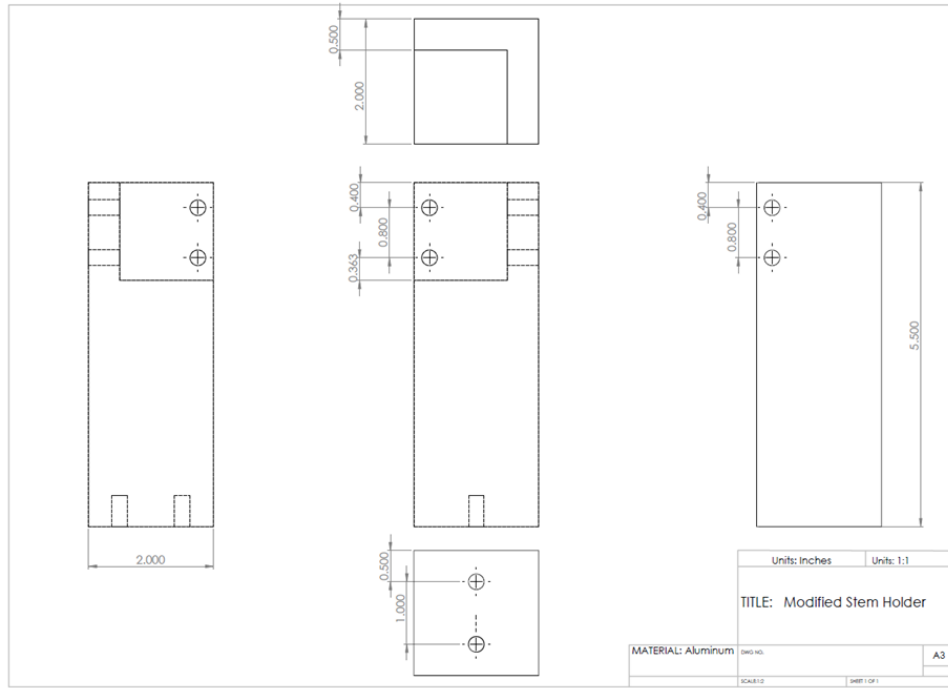


Figure G.13: Engineering Drawing of Parts for the Cement Sample Template



**Figure G.14: Engineering Assembly of Stem Holder used in  $\mu$ CT-imaging Bend Tests**



**Figure G.15: Engineering Drawing of Parts for Stem Holder Assembly used in  $\mu$ CT-imaging Bend Tests**

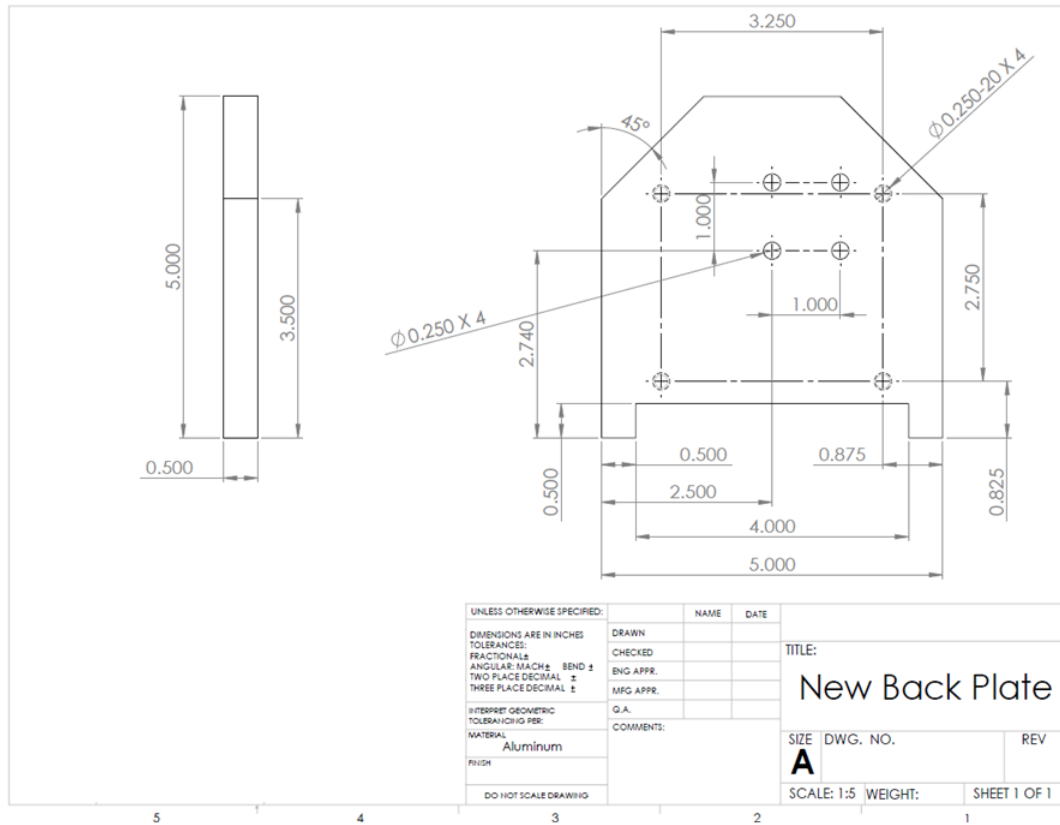


**Figure G.16: Engineering Drawing of Back Plate for Stem Holder Assembly used in  $\mu$ CT-imaging Bend Tests**



## Appendix H: Cement Preparation and Potting Technique

*This appendix describes the cementing procedure used in Chapters 3, 4, 5 and 6 of this thesis, for fixation of the implant stems. The technique details the centralization and positioning of the implant stem (Appendix G) for potting, the mixing of bone cement, and application of cement to the aluminum tubes containing the stems.*

### Preparation of Stem and Cement

In preparation for cementing the following are needed: implant stems, aluminum tubes, delrin blocks, adhesive tape, potting jig.

- 1) Prior to cementing, clean all stems and aluminum tubes with Acetone, and rinse with distilled water.
- 2) Insert Delrin<sup>®</sup> blocks (19 mm x 19 mm x 30 mm) (Appendix G.9) into the base of the aluminum tubes (internal diameter: 19 mm x 19 mm x 50 mm), and secure the tube's base using adhesive tape. These blocks are machined with an extruded through-cut down their center (diameter 8mm), through which stems will be positioned along the central axis of the aluminum tubes.
- 3) Insert stems into the Delrin<sup>®</sup> blocks and carefully position, ensuring all stem are aligned along the central axis of the tubes. These Delrin<sup>®</sup> blocks will also act as stoppers to control the depth to which the stems are potted in subsequent steps of this process (Figure H.1).
- 4) Once the stems are appropriately positioned within the aluminum tubes, secure all tubes within the potting jig for application of bone cement (Figure H.1). This jig will allow the maintenance of stem alignment during the cementing and curing process, as well as eliminate motion of the stem and aluminum tube during the cement application.

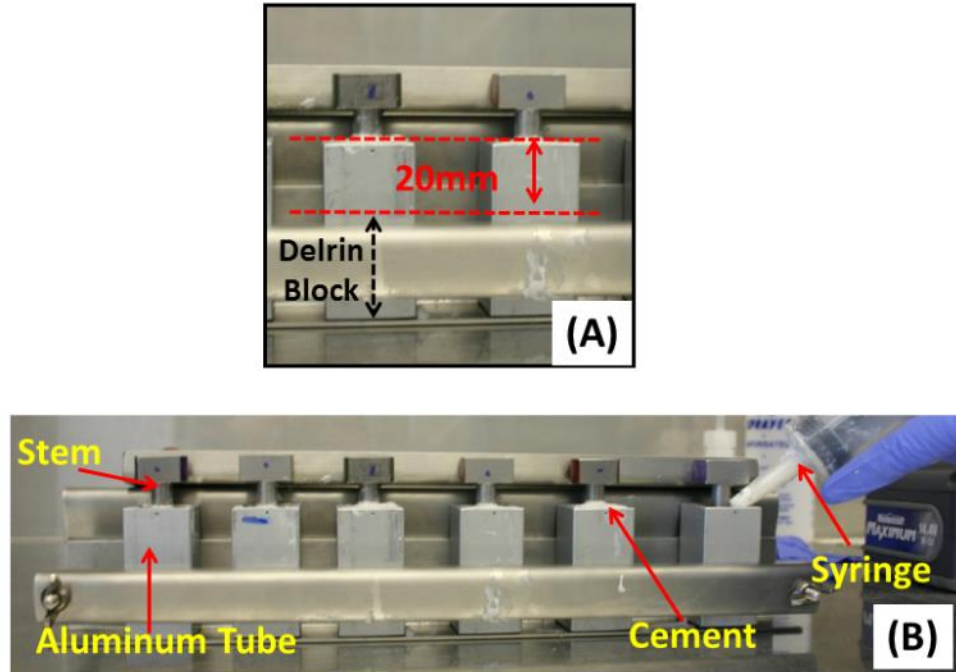


**Figure H.1: Potting Jig used for Securing Stems during Cementing**

(A) All stems are centralized into aluminum tubes using Delrin<sup>®</sup> blocks placed at the base of the tube (indicated by black dashed double arrow). The blocks ensure appropriate positioning of the stem along the central axis of the aluminum tube, as well as control the depth to which the stems are potted (20 mm). (B) Once stems are aligned, the aluminum tubes with stems are placed in the potting jig for cement application and curing.

## Mixing and Application of Bone Cement

- 1) Place the package of Simplex P<sup>®</sup> bone cement in freezer at least 24 hrs prior to cement preparation, to allow for chilling of the monomer liquid and polymer powder.
- 2) Within the fume hood of the laboratory, attach the vacuum mixing system (Optivac<sup>®</sup>, Biomet Inc., Warsaw, Indiana, USA) to a vacuum pump maintaining the pressure at 15-20 mmHg. The temperature within the fume hood should be maintained at 22 °C.
- 3) Place the provided funnel over the larger cartridge (*N.B.*, a small and large cartridge is included in the vacuum mixing system), and empty one packet of the polymer powder into the cartridge.
- 4) Remove the funnel, and empty the monomer liquid into the cartridge already containing the powder.
- 5) Immediately close the vacuum container, and allow 10 seconds for the vacuum pressure to form within the system.
- 6) Begin rapid plunging, rotating the plunger through the cement during each plunging motion. Ensure that the plunger makes contact with both ends of the cartridge to allow the polymer powder to fully integrate with the monomer liquid.
- 7) After 60 seconds of plunging, the cement mixture should have a viscous consistency. Pour the entire mixture into a 60 ml syringe, and immediately insert the syringe's plunger.
- 8) Tilt the syringe upwards and slowly plunge the mixture towards the application tip, to remove the excess air within the syringe.

- 9) Use the syringe to apply the cement mixture to the aluminum tubes containing the implant stems (Figure H.1).
- 10) Leave the cemented construct within the fume hood for 24 hours, at the controlled 22 °C, for curing.

## Appendix I: Tabulated Data

**Table I.1: Tabulated Data for Titanium Surface Treated Implant Stems in Torsion**

TITANIUM				
Surface Treatment	Stem #	Torque (Nm)	Toggle Rotation (deg)	Normalized Toggle (deg/Nm)
Smooth	1	10.00	0.650	0.065
	2	10.00	0.530	0.053
	3	5.00	0.260	0.052
	4	12.00	0.410	0.034
	5	4.00	0.310	0.078
	<i>Average</i>	<b>8.20</b>	<b>0.432</b>	<b>0.056</b>
	<i>SD</i>	<b>3.49</b>	<b>0.160</b>	<b>0.016</b>
Beaded 20mm	1	30.00	0.400	0.013
	2	30.00	0.570	0.019
	3	30.00	0.650	0.022
	4	30.00	0.380	0.013
	5	30.00	0.780	0.026
	<i>Average</i>	<b>30.00</b>	<b>0.556</b>	<b>0.019</b>
	<i>SD</i>	<b>0.00</b>	<b>0.169</b>	<b>0.006</b>
Plasma Spray 20mm	1	30.00	1.070	0.036
	2	30.00	1.610	0.054
	3	30.00	0.840	0.028
	4	30.00	0.790	0.026
	5	30.00	1.290	0.043
	<i>Average</i>	<b>30.00</b>	<b>1.120</b>	<b>0.037</b>
	<i>SD</i>	<b>0.00</b>	<b>0.339</b>	<b>0.011</b>

**Table I.2: Tabulated Data for Cobalt Chrome Surface Treated Implant Stems in Torsion**

<b>COBALT CHROME</b>				
<b>Surface Treatment</b>	<b>Stem #</b>	<b>Torque (Nm)</b>	<b>Toggle Rotation (deg)</b>	<b>Normalized Toggle (deg/Nm)</b>
Smooth	1	9.00	0.320	0.036
	2	18.00	0.200	0.011
	3	13.00	0.450	0.035
	4	13.00	0.310	0.024
	5	5.00	0.270	0.054
	<b>Average</b>	<b>11.60</b>	<b>0.310</b>	<b>0.032</b>
	<b>SD</b>	<b>4.88</b>	<b>0.091</b>	<b>0.016</b>
Beaded 20mm	1	16.00	0.590	0.037
	2	16.00	0.420	0.026
	3	17.00	0.510	0.030
	4	16.00	0.540	0.034
	5	17.00	0.650	0.038
	<b>Average</b>	<b>16.40</b>	<b>0.542</b>	<b>0.033</b>
	<b>SD</b>	<b>0.55</b>	<b>0.086</b>	<b>0.005</b>
Plasma Spray 20m	1	30.00	0.700	0.023
	2	30.00	0.600	0.020
	3	30.00	0.530	0.018
	4	30.00	0.430	0.014
	5	30.00	0.730	0.024
	<b>Average</b>	<b>30.00</b>	<b>0.598</b>	<b>0.020</b>
	<b>SD</b>	<b>0.00</b>	<b>0.123</b>	<b>0.004</b>

**Table I.3: Tabulated Data for Titanium Surface Treated Implant Stems under Compression**

TITANIUM							
Surface Treatment	Stem #	Interface Toggle (mm)	Stem Motion Post-10kN (mm)	Load (kN)	# Cycles	NormalizedToggle (mm/kN*#cycles)	Normalized Stem Motion Post-10kN
Smooth	1	0.025	-	3.00	202	4.13E-05	-
	2	0.009	-	3.00	201	1.49E-05	-
	3	0.006	-	3.00	201	9.95E-06	-
	4	0.031	-	3.00	206	5.02E-05	-
	5	0.005	-	2.00	101	2.48E-05	-
	6	0.028	-	3.00	201	4.64E-05	-
	<b>Average</b>		<b>0.017</b>	<b>-</b>	<b>2.83</b>	<b>185</b>	<b>3.12E-05</b>
<b>SD</b>		<b>0.012</b>	<b>-</b>	<b>0.41</b>	<b>41</b>	<b>1.70E-05</b>	<b>-</b>
Bead 20mm	1	0.160	0.149	10.00	25900	6.18E-07	5.96E-06
	2	0.050	0.207	10.00	25900	1.93E-07	8.28E-06
	3	0.120	0.211	10.00	25900	4.63E-07	8.44E-06
	4	0.040	0.179	10.00	25900	1.54E-07	7.16E-06
	5	0.037	0.194	10.00	25900	1.43E-07	7.76E-06
	6	0.080	0.207	10.00	25900	3.09E-07	8.28E-06
	<b>Average</b>		<b>0.081</b>	<b>0.191</b>	<b>10.00</b>	<b>25900</b>	<b>3.13E-07</b>
<b>SD</b>		<b>0.050</b>	<b>0.024</b>	<b>0.00</b>	<b>0</b>	<b>1.92E-07</b>	<b>9.51E-07</b>
Bead 10mm	1	0.121	0.635	10.00	1889	6.41E-06	6.42E-04
	2	0.080	1.214	10.00	4583	1.75E-06	3.30E-04
	3	0.072	0.339	10.00	2269	3.17E-06	2.48E-04
	4	0.100	0.417	10.00	10435	9.58E-07	4.37E-05
	5	0.090	0.923	10.00	4499	2.00E-06	2.56E-04
	6	0.100	1.156	10.00	4091	2.44E-06	3.62E-04
	<b>Average</b>		<b>0.094</b>	<b>0.781</b>	<b>10.00</b>	<b>4628</b>	<b>2.79E-06</b>
<b>SD</b>		<b>0.017</b>	<b>0.373</b>	<b>0.00</b>	<b>3069</b>	<b>1.92E-06</b>	<b>1.95E-04</b>
Plasma Spray 20mm	1	0.120	0.800	10.00	2349	5.11E-06	5.52E-04
	2	0.163	0.851	10.00	1980	8.23E-06	7.88E-04
	3	0.100	1.120	10.00	9469	1.06E-06	1.31E-04
	4	0.163	0.989	10.00	1601	1.02E-05	1.41E-03
	5	0.108	0.751	10.00	1288	8.39E-06	1.94E-03
	6	0.102	0.872	10.00	1610	6.34E-06	1.23E-03
	<b>Average</b>		<b>0.126</b>	<b>0.897</b>	<b>10.00</b>	<b>3050</b>	<b>6.55E-06</b>
<b>SD</b>		<b>0.029</b>	<b>0.135</b>	<b>0.00</b>	<b>3166</b>	<b>3.22E-06</b>	<b>6.48E-04</b>
Plasma Spray 10mm	1	0.150	-	8.00	722	2.60E-05	-
	2	0.142	-	8.00	791	2.24E-05	-
	3	0.141	-	9.00	871	1.80E-05	-
	4	0.181	-	9.00	842	2.39E-05	-
	5	0.175	-	9.00	887	2.19E-05	-
	6	0.115	-	9.00	805	1.59E-05	-
	<b>Average</b>		<b>0.151</b>	<b>-</b>	<b>8.67</b>	<b>820</b>	<b>2.13E-05</b>
<b>SD</b>		<b>0.024</b>	<b>-</b>	<b>0.52</b>	<b>60</b>	<b>3.76E-06</b>	<b>-</b>

**Table I.4: Tabulated Data for Cobalt Chrome Surface Treated Implant Stems under Compression**

COBALT CHROME							
Surface Treatment	Stem #	Interface Toggle (mm)	Stem Motion post-10kN (mm)	Load (kN)	# Cycles	Normalized Toggle (mm/kN*#cycles)	Normalized Stem Motion Post 10kN
Smooth	1	0.003	-	2.00	101	1.49E-05	-
	2	0.020	-	3.00	201	3.25E-05	-
	3	0.007	-	3.00	232	1.01E-05	-
	4	0.018	-	3.00	201	2.99E-05	-
	5	0.006	-	2.00	101	2.97E-05	-
	6	0.007	-	2.00	101	3.47E-05	-
	<b>Average</b>		<b>0.010</b>	<b>-</b>	<b>2.50</b>	<b>156</b>	<b>2.53E-05</b>
<b>SD</b>		<b>0.007</b>	<b>-</b>	<b>0.55</b>	<b>61</b>	<b>1.02E-05</b>	<b>-</b>
Beaded 20mm	1	0.100	0.195	10.00	25900	3.86E-07	7.80E-06
	2	0.080	0.201	10.00	25900	3.09E-07	8.04E-06
	3	0.045	0.373	10.00	7965	5.65E-07	5.28E-05
	4	0.019	0.201	10.00	25900	7.34E-08	8.04E-06
	5	0.018	0.208	10.00	25900	6.95E-08	8.32E-06
	6	0.150	0.165	10.00	25900	5.79E-07	6.60E-06
	<b>Average</b>		<b>0.069</b>	<b>0.224</b>	<b>10.00</b>	<b>22911</b>	<b>3.30E-07</b>
<b>SD</b>		<b>0.052</b>	<b>0.075</b>	<b>0.00</b>	<b>7322</b>	<b>2.26E-07</b>	<b>1.84E-05</b>
Beaded 10mm	1	0.018	-	3.00	201	2.97E-05	-
	2	0.005	-	3.00	204	8.17E-06	-
	3	0.005	-	3.00	209	7.97E-06	-
	4	0.006	-	2.00	101	2.72E-05	-
	5	0.049	0.415	10.00	25900	1.91E-07	1.66E-05
	6	0.011	-	3.00	201	1.82E-05	-
	<b>Average</b>		<b>0.016</b>	<b>0.415</b>	<b>4.00</b>	<b>4469</b>	<b>1.52E-05</b>
<b>SD</b>		<b>0.017</b>	<b>-</b>	<b>2.97</b>	<b>10499</b>	<b>1.18E-05</b>	<b>-</b>
Plasma Spray 20mm	1	0.160	1.045	10.00	6621	2.42E-06	1.83E-04
	2	0.165	1.175	10.00	7155	2.31E-06	1.88E-04
	3	0.100	0.252	10.00	25900	3.86E-07	1.01E-05
	4	0.129	1.206	10.00	15323	8.41E-07	8.36E-05
	5	0.133	1.124	10.00	15700	8.47E-07	7.59E-05
	6	0.162	1.190	10.00	9990	1.62E-06	1.31E-04
	<b>Average</b>		<b>0.141</b>	<b>0.999</b>	<b>10.00</b>	<b>13448</b>	<b>1.40E-06</b>
<b>SD</b>		<b>0.026</b>	<b>0.370</b>	<b>0.00</b>	<b>7236</b>	<b>8.43E-07</b>	<b>6.87E-05</b>
Plasma Spray 10mm	1	0.100	-	9.00	804	1.38E-05	-
	2	0.193	0.028	10.00	911	2.12E-05	-
	3	0.114	0.869	10.00	1139	1.00E-05	3.64E-03
	4	0.125	0.148	10.00	923	1.35E-05	-
	5	0.159	0.02	10.00	909	1.75E-05	-
	6	0.145	-	9.00	824	1.96E-05	-
	<b>Average</b>		<b>0.139</b>	<b>0.266</b>	<b>9.67</b>	<b>918</b>	<b>1.59E-05</b>
<b>SD</b>		<b>0.034</b>	<b>0.406</b>	<b>0.52</b>	<b>119</b>	<b>4.20E-06</b>	<b>-</b>



**Table I.5: Tabulated Data for Circumferential Grooved Implant Stems under Compression**

<b>COBALT CHROME</b>							
Surface Treatment	Stem #	Load (N)	# cycles	Interface Toggle (mm)	Normalize Toggle (mm/N)	Stem Motion post 10kN	Normalized Stem Motion post 10kN
Smooth	1	3000	201	0.004	6.08E-06	-	-
	2	3000	201	0.006	9.95E-06	-	-
	3	3000	201	0.004	7.19E-06	-	-
	4	3000	201	0.012	2.05E-05	-	-
	5	3000	201	0.002	3.32E-06	-	-
	<b>Average</b>	<b>3000</b>	<b>201</b>	<b>0.006</b>	<b>9.40E-06</b>	-	-
	<b>SD</b>	<b>0</b>	<b>0</b>	<b>0.004</b>	<b>6.62E-06</b>	-	-
Grooved 1.1mm	1	10000	25900	0.054	2.10E-07	0.457	1.83E-05
	2	10000	25900	0.099	3.84E-07	0.449	1.80E-05
	3	10000	25900	0.097	3.76E-07	0.420	1.68E-05
	4	10000	25900	0.084	3.23E-07	0.268	1.07E-05
	5	10000	25900	0.043	1.66E-07	0.308	1.23E-05
	<b>Average</b>	<b>10000</b>	<b>25900</b>	<b>0.076</b>	<b>2.92E-07</b>	<b>0.380</b>	<b>1.52E-05</b>
	<b>SD</b>	<b>0</b>	<b>0</b>	<b>0.026</b>	<b>9.87E-08</b>	<b>0.087</b>	<b>3.47E-06</b>
Grooved 0.6mm	1	10000	25900	0.066	2.54E-07	0.133	5.32E-06
	2	10000	25900	0.085	3.29E-07	0.295	1.18E-05
	3	10000	25900	0.041	1.58E-07	0.320	1.28E-05
	4	10000	25900	0.046	1.79E-07	0.253	1.01E-05
	5	10000	25900	0.025	9.65E-08	0.248	9.92E-06
	<b>Average</b>	<b>10000</b>	<b>25900</b>	<b>0.053</b>	<b>2.03E-07</b>	<b>0.250</b>	<b>9.99E-06</b>
	<b>SD</b>	<b>0</b>	<b>0</b>	<b>0.023</b>	<b>9.01E-08</b>	<b>0.072</b>	<b>2.87E-06</b>

**Table I.6: Tabulated Data for Circumferential Grooved Implant Stems in Torsion**

<b>COBALT CHROME</b>				
<b>Surface Treatment</b>	<b>Stem #</b>	<b>Torque (Nm)</b>	<b>Toggle Rotation (deg)</b>	<b>Normalized Toggle (mm/Nm)</b>
Smooth	1	9	0.200	0.022
	2	18	0.163	0.009
	3	13	0.322	0.025
	4	13	0.240	0.018
	5	5	0.189	0.038
	<b>Average</b>	<b>11.600</b>	<b>0.223</b>	<b>0.022</b>
	<b>SD</b>	<b>4.879</b>	<b>0.062</b>	<b>0.010</b>
Grooved 1.1mm	1	17	0.720	0.042
	2	19	0.719	0.038
	3	15	0.749	0.050
	4	18	0.802	0.045
	5	15	0.569	0.038
	<b>Average</b>	<b>16.800</b>	<b>0.712</b>	<b>0.043</b>
	<b>SD</b>	<b>1.789</b>	<b>0.087</b>	<b>0.005</b>
Grooved 0.6mm	1	20	0.194	0.010
	2	20	0.459	0.023
	3	14	0.422	0.030
	4	10	0.224	0.022
	5	23	0.450	0.020
	<b>Average</b>	<b>17.40</b>	<b>0.350</b>	<b>0.021</b>
	<b>SD</b>	<b>5.27</b>	<b>0.130</b>	<b>0.007</b>

Table I.7: Tabulated Data for Titanium Surface Treated Implant Stems in Bending

TITANIUM			
Surface Treatment	Stem #	Interface Toggle (mm)	Offset Stem Motion (mm)
Smooth	1	0.065	0.045
	2	0.066	0.043
	3	0.052	0.036
	4	0.067	0.050
	5	0.083	0.052
	<i>Average</i>	<b>0.067</b>	<b>0.045</b>
	<i>St Dev</i>	<b>0.011</b>	<b>0.006</b>
Bead 20mm	1	0.050	0.034
	2	0.073	0.045
	3	0.054	0.034
	4	0.040	0.026
	5	0.047	0.030
	<i>Average</i>	<b>0.053</b>	<b>0.034</b>
	<i>St Dev</i>	<b>0.012</b>	<b>0.007</b>
Bead 10mm	1	0.054	0.039
	2	0.066	0.036
	3	0.046	0.026
	4	0.044	0.027
	5	0.047	0.032
	<i>Average</i>	<b>0.051</b>	<b>0.032</b>
	<i>St Dev</i>	<b>0.009</b>	<b>0.006</b>
Plasma Spray 20mm	1	0.064	0.034
	2	0.059	0.038
	3	0.074	0.042
	4	0.058	0.035
	5	0.057	0.037
	<i>Average</i>	<b>0.062</b>	<b>0.037</b>
	<i>St Dev</i>	<b>0.007</b>	<b>0.003</b>
Plasma Spray 10mm	1	0.068	0.048
	2	0.085	0.066
	3	0.087	0.064
	4	0.095	0.066
	5	0.051	0.028
	<i>Average</i>	<b>0.077</b>	<b>0.054</b>
	<i>St Dev</i>	<b>0.018</b>	<b>0.017</b>

**Table I.8: Tabulated Data for Cobalt Chrome Surface Treated Implant Stems in Bending**

COBALT CHROME				
Surface Treatment	Stem #	Interface Toggle (mm)	Offset Stem Motion (mm)	
Smooth	1	0.091	0.071	
	2	0.060	0.049	
	3	0.131	0.102	
	4	0.057	0.014	
	5	0.070	0.051	
	<b>Average</b>		0.082	0.057
	<b>St Dev</b>		0.031	0.032
Bead 20mm	1	0.044	0.027	
	2	0.056	0.039	
	3	0.037	0.024	
	4	0.040	0.031	
	5	0.033	0.015	
	<b>Average</b>		<b>0.042</b>	<b>0.027</b>
	<b>St Dev</b>		<b>0.009</b>	<b>0.009</b>
Bead 10mm	1	0.042	0.039	
	2	0.122	0.099	
	3	0.093	0.087	
	4	0.037	0.033	
	5	0.046	0.030	
	<b>Average</b>		0.068	0.058
	<b>St Dev</b>		0.038	0.033
Plasma Spray 20mm	1	0.061	0.042	
	2	0.051	0.035	
	3	0.056	0.034	
	4	0.050	0.025	
	5	0.040	0.029	
	<b>Average</b>		0.052	0.033
	<b>St Dev</b>		0.008	0.006
Plasma Spray 10mm	1	0.038	0.036	
	2	0.040	0.025	
	3	0.061	0.054	
	4	0.062	0.044	
	5	0.063	0.044	
	<b>Average</b>		0.053	0.041
	<b>St Dev</b>		0.013	0.011

## Appendix J: Letter of Permission

*This appendix includes the letter of permission from the publisher, for the re-print of published material within Chapter 4 of this thesis.*

Journal Publishing Agreement	Page 1 of 2
<a href="#">Authors' Rights</a> <a href="#">Help</a>   <a href="#">Print</a>	
<h3>JOURNAL PUBLISHING AGREEMENT</h3> <hr/> <p style="text-align: center;">Journal of Shoulder and Elbow Surgery Board of Trustees</p>	
<h4>YOUR ARTICLE DETAILS</h4>	
<b>Article:</b>	The Effect of Stem Surface Treatment and Material on Pistoning of Ulnar Components in Linked Cemented Elbow Prostheses
<b>Corresponding author:</b>	Dr. Cynthia E Dunning
<b>E-mail address:</b>	
<b>Journal:</b>	Journal of Shoulder and Elbow Surgery
<b>Our reference</b>	YMSE2548
<b>PII:</b>	S1058-2746(13)00153-5
<b>DOI:</b>	10.1016/j.jse.2013.03.007
<h4>YOUR STATUS</h4>	
<input type="checkbox"/> I am one author signing on behalf of all co-authors of the manuscript	
<h4>DATA PROTECTION &amp; PRIVACY</h4>	
<input type="checkbox"/> I do not wish to receive news, promotions and special offers about products and services from Journal of Shoulder and Elbow Surgery Board of Trustees and Mosby, Inc. and its affiliated companies worldwide.	
<h4>ASSIGNMENT OF PUBLISHING RIGHTS</h4>	
<p>I hereby assign to Journal of Shoulder and Elbow Surgery Board of Trustees the copyright in the manuscript identified above (government authors not electing to transfer agree to assign an exclusive publishing and distribution license) and any supplemental tables, illustrations or other information submitted therewith that are intended for publication as part of the manuscript (the "Article") in all forms and media (whether now known or hereafter developed), throughout the world, in all languages, for the full term of copyright, effective when and if the article is accepted for publication. This transfer includes the right to provide the Article in electronic and online forms and systems. With respect to supplemental data that I wish to make accessible through a link in the Article, I hereby grant a non-exclusive license for such linking. If I have agreed with Journal of Shoulder and Elbow Surgery Board of Trustees to make available such supplemental data on a site or through a service of Journal of Shoulder and Elbow Surgery Board of Trustees, I hereby grant a non-exclusive license for such publication, posting and making available, and further permit indexing and archiving. Articles may sometimes be accepted for publication but later rejected in the publication process, even in some cases after public posting in "Articles in Press" form, in which event all rights will revert to the author (see <a href="http://www.elsevier.com/wps/find/intro.cws_home/article_withdrawal">http://www.elsevier.com/wps/find/intro.cws_home/article_withdrawal</a>).</p>	
<h4>REVISIONS AND ADDENDA</h4>	
<p>I understand that no revisions, additional terms or addenda to this Agreement can be accepted without Journal of Shoulder and Elbow Surgery Board of Trustees's express written consent.  <i>Note:</i> authors at institutions that place restrictions on copyright assignments or that assert an institutional right to distribute or provide access to the works of institutional authors, must obtain an express waiver from those institutions releasing the author from such restrictions to enable the acceptance of this publishing agreement.</p>	
<h4>RETENTION OF RIGHTS FOR SCHOLARLY PURPOSES</h4>	
<p>I understand that I retain or am hereby granted (without the need to obtain further permission) the Retained Rights (see description below), and that no rights in patents, trademarks or other intellectual property rights are transferred to Journal of Shoulder and Elbow Surgery Board of Trustees.          The Retained Rights include:</p>	
<input type="checkbox"/> the right to use the <a href="#">Preprint</a> or <a href="#">Accepted Author Manuscript</a> for <a href="#">Personal Use</a> , <a href="#">Internal Institutional Use</a> and for <a href="#">Permitted Scholarly Posting</a> ;	
<input type="checkbox"/> the right to use the <a href="#">Published Journal Article</a> for <a href="#">Personal Use</a> and <a href="#">Internal Institutional Use</a> .	

but in each case as noted in the Definitions excluding [Commercial Use](#) or [Systematic Distribution](#) (unless expressly agreed in writing by Journal of Shoulder and Elbow Surgery Board of Trustees).

### AUTHOR REPRESENTATIONS / ETHICS AND DISCLOSURE

I affirm the Author Representations noted below, and confirm that I have reviewed and complied with the relevant Instructions to Authors, Ethics in Publishing policy, and Conflicts of Interest disclosure. Please note that some journals may require that all co-authors sign and submit Conflicts of Interest disclosure forms. I am also aware of the publisher's policies with respect to retractions and withdrawal ([http://www.elsevier.com/wps/find/intro.cws\\_home/article\\_withdrawal](http://www.elsevier.com/wps/find/intro.cws_home/article_withdrawal)).

For further information see the publishing ethics page at [http://www.elsevier.com/wps/find/intro.cws\\_home/publishing](http://www.elsevier.com/wps/find/intro.cws_home/publishing) and the journal home page.

#### Author representations

- » The article I have submitted to the journal for review is original, has been written by the stated authors and has not been published elsewhere.
- » The article is not currently being considered for publication by any other journal and will not be submitted for such review while under review by this journal.
- » The article contains no libellous or other unlawful statements and does not contain any materials that violate any personal or proprietary rights of any other person or entity.
- » I have obtained written permission from copyright owners for any excerpts from copyrighted works that are included and have credited the sources in my article.
- » If I am using any personal details or images of patients or research subjects, I have obtained written permission or consent from the patient (or, where applicable, the next of kin). See <http://www.elsevier.com/wps/find/authorsview.authors/rights?tab=1> for further information.
- » If the article was prepared jointly with other authors, I have informed the co-author(s) of the terms of this publishing agreement and that I am signing on their behalf as their agent, and I am authorized to do so.

### FUNDING AGENCY AND SPONSORSHIP OPTIONS

The publisher posts information on funding agencies and arrangements that the publisher has made with such bodies at <http://www.elsevier.com/wps/find/authorsview.authors/fundingbodyagreements>. I understand that documents can be downloaded from this site to help me comply with certain agency requirements. Information can also be found at <http://www.elsevier.com/wps/find/authors.authors/sponsoredarticles> concerning sponsorship options and rights issues concerning publication-fee model journals (information can also be found on the journal home page).

For information on the publisher's copyright and access policies, please see

<http://www.elsevier.com/wps/find/authorsview.authors/rights>.

[For more information about the definitions relating to this agreement click here.](#)

I have read and agree to the terms of the Journal Publishing Agreement.

20th March 2013

T-copyright-v17/2009

## Appendix K: Bead Embedment Procedure

*This appendix describes the procedure used in Chapter 7 for embedding steel bead markers into bone cement during the cementing process. The methodology highlights the cement mixing and application technique used to ensure appropriate suspension of the beads within the cement mantle.*

- 1) Using the cement preparation technique described in Appendix H, vacuum mix the pre-chilled bone cement in the controlled environment of the fumehood.
- 2) After 60 seconds of vacuum-mixing, pour the mixture from the vacuum cartridge into an open bowl, and continue mixing with a spatula for an additional 60 seconds.
- 3) After 60 seconds of hand mixing, the bead-cement mixture should appear doughy in consistency. At this time-point, incorporate the steel beads into the cement and continue mixing. With the doughy consistency of the cement, the beads should remain suspended (as opposed to sinking) within the mixture.

*(N.B. If the cement mixture does not appear doughy after 60 seconds, continue hand mixing until the doughing phase begins. ONLY incorporate the beads into the mixture when this consistency is reached. This is important for appropriate suspension of the beads within the cement)*

- 4) When the beads appear to be fully integrated into the cement, pour the mixture into the 60ml syringe, and immediately insert the syringe's plunger.
- 5) Tilt the syringe upwards and slowly plunge the mixture towards the application tip, to remove excess air within the syringe.
- 6) Use the syringe to apply the bead-cement mixture to aluminum tubes containing the stem, or to the cement template used for moulding cement samples.

## **Appendix L: Mechanical Testing of Beaded Cement Samples**

*This appendix describes the three-point bend tests used to compare cement samples prepared with different bead-cement ratios. The results from this appendix was used to determine the appropriate bead-cement ratio to be used in Chapter 7, ensuring mechanical integrity of the bone cement, while allowing optimum dispersion of beads within the cement mantle.*

### **Introduction:**

The incorporation of steel beads into bone cement can be useful as imaging markers, when studying the internal mechanics of the cemented systems using CT-imaging techniques. The vast difference in density values between the steel beads and the surrounding bone cement make the beads appropriate as high contrast markers within the cement. However, this difference in density values may also affect the mechanical properties of bone cement. As such, this pilot study aimed to determine the change in mechanical properties of bone cement by incorporation of various bead-cement ratios. Therefore, the purpose of this study was to investigate the effect of different bead-cement ratios on the flexural modulus of Simplex P<sup>®</sup> bone cement.

### **Materials and Methods:**

Cement preparation was done using the procedure described in Appendix I, where the beads were incorporated into the bone cement during the doughing phase of cement preparation. Four ratios of cement-bead mixtures were made using four separate packages of pre-chilled Simplex P<sup>®</sup> bone cement; 0%, 0.15%, 0.2%, and 0.25%. Bead ratios represented the volume of beads relative to the volume of bone cement. One package of cement powder mixed with monomer liquid created a cement mixture volume of approximately 40 cm<sup>3</sup>.



Once the beads appeared fully integrated into the cement, the mixture was poured into the syringe for subsequent application to an aluminum cement template. This template created five cement samples of dimensions of 80 mm x 10 mm x 3.3 mm, based on specifications from the ISO 5833 standards<sup>9</sup> (Figure L.1). The cement samples were left to cure for 24 hrs within the template, after which they were removed for mechanical testing.

The remaining bead-cement mixture that was left over from creation of cement samples was incorporated into aluminum tubes containing a stem (Appendix I), and potted to a fixed depth of 10 mm. These cement mantles were used for micro-CT imaging to determine the internal distribution of the beads within the aluminum tubes. Using this bead distribution, along with the results of mechanical testing (see below), the appropriate bead ratio was determined for embedment into the cement mantles.

Mechanical testing was done using a uni-axial materials testing machine (Instron<sup>®</sup> 8872, Canton, MA). The cement samples were positioned on a three-point bending platform placed at the base of the materials testing machine (Figure L.2), and exposed to monotonic loading at a rate of 2 mm/min. The samples were tested to failure, defined by the sudden decrease in load after initial linear increase, accompanied by instantaneous fracture of the cement samples.

The slope of the force-displacement graphs, generated by the data from the materials testing machine, was used to calculate the bending modulus of the 0%, 0.15%, 0.2% and 0.25% cement samples. The respective moduli were compared to determine the effect of bead ratio on the mechanical properties of bone cement.

---

<sup>9</sup> ISO International Standards, ISO 5833/1. Implants for Surgery. Acrylic Resin Cements. Part I: Orthopaedic Applications.

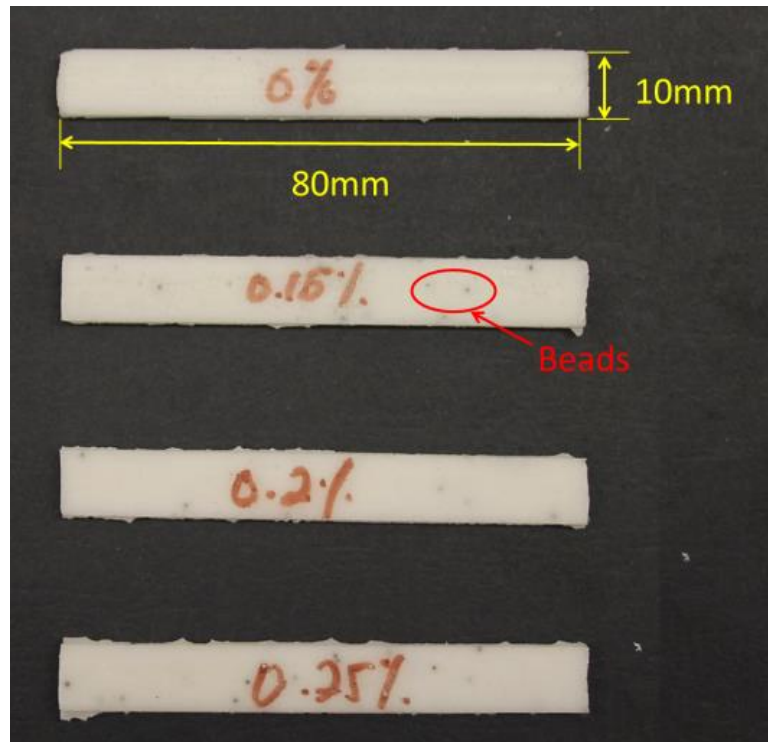


**Figure L.1: Bead Embedded Cement Samples**

Cement samples used to determine the effect of bead ratio on the mechanical properties of bone cement. From top to bottom; 0%, 0.15%, 0.20%, 0.25%.

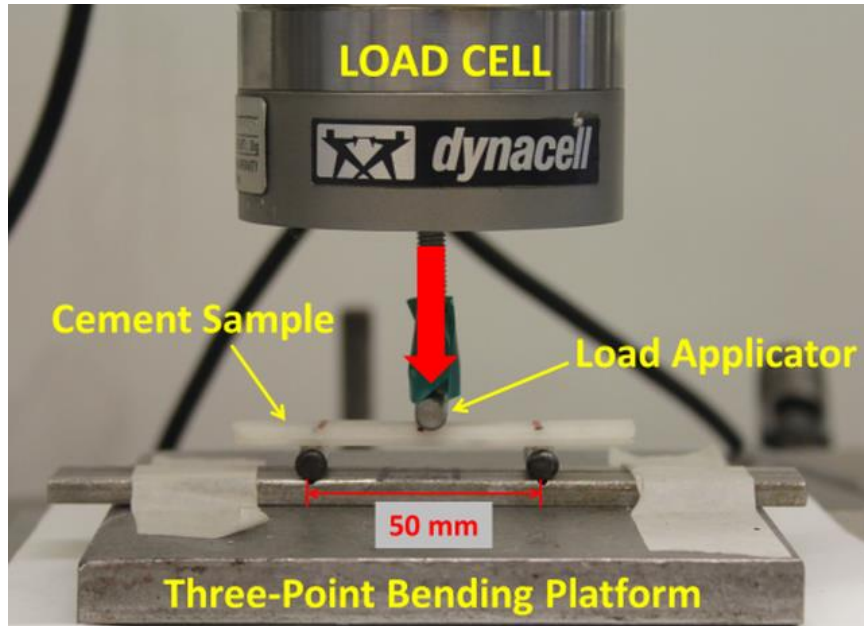


**Figure L.2: Experimental Set-up for Three-point Bending of Cement Samples**

The cement samples were placed on the three-point bending platform for application of loads at a rate of 2 mm/min. Failure was defined as a sudden decrease in load accompanied by instantaneous fracture of the cement sample.

**Table L.1: Bending Modulus of Bone Cement with Various Bead- Cement Ratios**

	<b>Bending Modulus (GPa)</b>			
	<b>0.25%</b>	<b>0.20%</b>	<b>0.15%</b>	<b>0%</b>
Sample 1	3.55	3.56	3.38	2.83
Sample 2	4.22	3.53	3.04	2.93
Sample 3	3.52	3.70	2.77	2.80
Sample 4	3.96	3.09	3.00	3.01
Sample 5	3.66	3.38	2.03	2.74
Average	3.78	3.47	3.05	2.89
S.D.	0.30	0.23	0.51	0.11

## Results:

From visual analysis of the five samples created for each bead ratio, it was observed that the 0.25% samples showed the greatest bead distribution compared to the other bead ratios. In comparison, the 0.15% beaded sample showed the least bead distribution.

Results of mechanical testing showed that the addition of beads caused an overall increase in the bending modulus of bone cement, as seen in Table K.1. In addition, it was found that the 0.15% sample showed the greatest variability in its mechanical response to the three-point bend tests, based on its large standard deviation, compared to the other cement samples.

CT imaging of the various cement mantles found that the 0.20% and 0.25% bead ratios showed suitable dispersion of beads within the samples of cement, with the 0.15% sample showing most inconsistent distribution.

## Discussion:

The cementing technique previously described in Appendix J, proved useful for embedment of steel beads within the bone cement. From the observations of bead distribution within the cement samples, all beads appeared reasonably dispersed throughout the sample volumes, with the 0.25% bead ratio showing greatest dispersion and bead consistency within its samples (Figure L.1).

Mechanical testing showed that the addition of beads to bone cement increased the stiffness of the cement samples. When comparing the bending modulus of bone cement observed in this study, to that found within the literature, it was seen that the

modulus for the 0% bead sample (2.89 GPa) was comparable to that described by Lee<sup>10</sup> (2.55 GPa).

Imaging analysis found that the 0.20% and 0.25% bead ratios showed satisfactory dispersion of beads within the cement mantle surrounding the stem, and it was determined that either of the ratios would be optimal for bead visualization in Chapter 7.

When considering the appropriate bead ratio for inclusion in CT analysis of the cemented construct, it was determined that although 0.25% sample showed the greatest bead dispersion, it caused the largest change in the mechanical properties of bone cement. In comparison, the 0.15% sample showed the least change in the mechanical response of bone cement, but the variability among its measurements was quite high. In addition, CT analysis of its cement mantle showed minimal appearance and distribution of beads. As such, it was decided that the 0.2% bead ratio would be optimum for the use as cement markers in subsequent CT imaging studies.

---

<sup>10</sup> Lee, C. 2005, "Properties of Bone Cement: The Mechanical Properties of PMMA Bone Cement" In: Breusch, S.J., Malchau, H (eds), *The Well-Cemented Total Hip Arthroplasty*, Springer Verlag, Germany, pp 61.

## Appendix M: Custom-built Loading Device

*This appendix details the custom built loading device used for testing implant stems in Chapter 7 of this thesis. The device was initially developed by a fourth year design group (Goutam Datta, Micheal Dottor, Emily Harvey, Geoffrey McLellan)<sup>11</sup> in the Department of Mechanical and Materials Engineering at Western University, under the supervision of Dr. Cynthia Dunning and Dr. Jeffrey Wood, and modified slightly for use in this thesis.*

The initial design of the loading device was developed based on the requirements for a CT-compatible, displacement controlled, loading system, which could apply static and cyclic loads to the human ulna, while simultaneously collecting real-time image data. Based on the specific environment required for the loading device (*i.e.*, within the bore of a micro-CT scanner, while x-ray images are acquired), the design constraints were focused on the CT compatibility, physical size requirements and load requirements.

### CT Compatibility

The device was intended to be place within the CT scanner to acquire real-time images of the loaded specimen. As a result, the material specifications were limited to polymers and low density metals, which would limit artifacts in the resultant CT images. Therefore, the final design incorporated aluminum metal for the fixtures and loading platform, with Delrin<sup>®</sup> and carbon fibre for the load applicator and actuating parts of the device.

### Size Requirement

In addition to the material constraints imposed by the CT environment, the dimensions of the device were limited to the size of the micro-CT scanner's bore. The scanner's bore is 15 cm in diameter, which restricted the design and configuration of the device to this height and width. As such, all parts were machined to these constraints,

---

<sup>11</sup> Datta, G., Dottor M., Harvey E., McLellan G., 2007 Cyclic Loading Device for Micro CT Scanner, Department of Mechanical and Materials Engineering, The University of Western Ontario.

and the mechanical parts of the device were chosen to function within the restricted volume.

### **Load Requirements**

The loading requirements for the initial design were based on the load expected to test the material properties of human ulna. As such, the device was designed to apply maximum loads of 100 N, as well as maintain rigidity under these loads. For the purposes of the implant stem testing within this thesis, however, the loading requirements were increased to 1000 N. Therefore minor modifications were made by replacing the load cell, and motor used for actuation.

### **Final Design of Loading Device**

The mechanical parts of the loading device consist of a stepper motor connected to an offset cam, which is further attached to a carbon fibre beam (Figure M.1). The motor provides rotational motion, which is converted to vertical translation of the carbon fibre beam through the offset bearing cam. Translation is recorded by a linear variable differential transducer (LVDT) located near cam. Vertical translation of the pivoted carbon fibre beam produces a see-saw motion along the length of the beam.

The entire mechanical set-up is housed on an aluminum platform, which is designed to be attached the bed of the CT-scanner. An aluminum holding jig further attached to this platform secures the specimen in a horizontal orientation above the carbon fibre beam (Figure M.2). Therefore, during one rotation of the motor, the see-saw motion of the carbon fibre beam applies a perpendicular load to the head of the specimen. This load is measured by a load cell positioned just below the specimen.



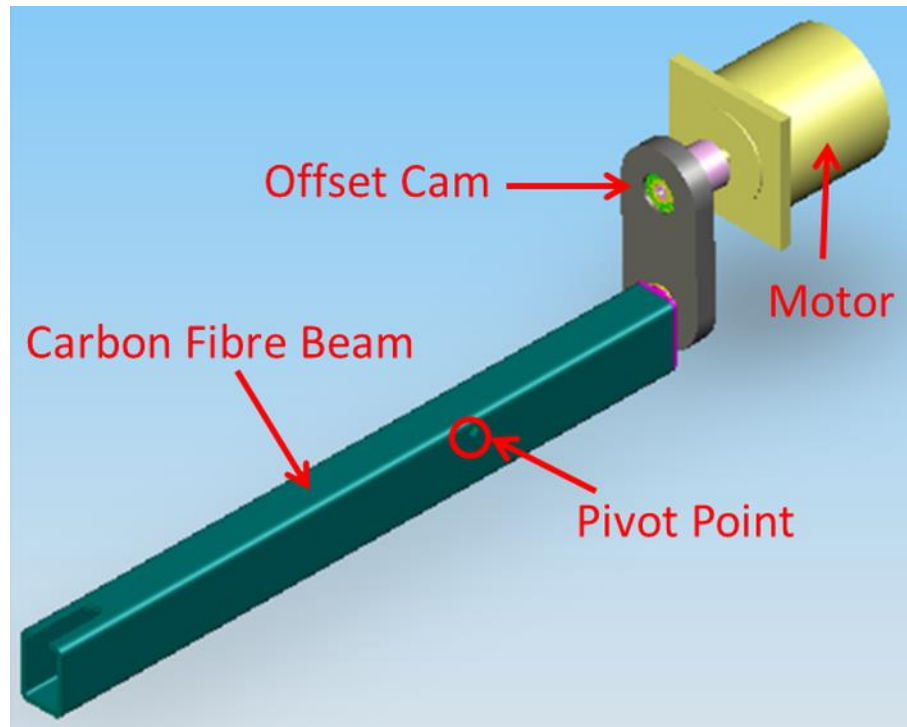


**Figure M.1: Mechanical Parts of Loading Device**

The motor connected to the offset cam, which was further connected to a pivoted carbon fibre beam. During one rotation of the motor, the offset cam facilitated vertical translation of the pivoted carbon fibre beam, resulting in a see-saw motion along the length of the beam

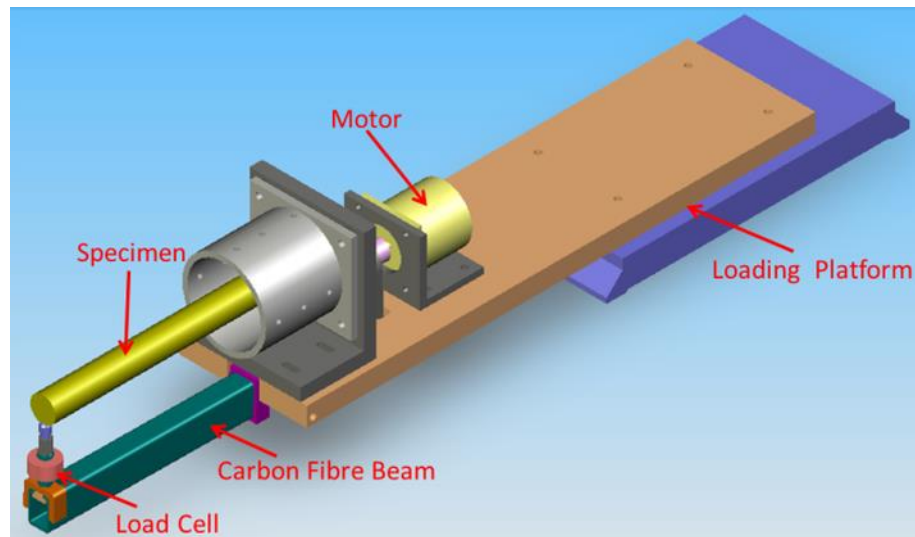


**Figure M.2: Custom-Built Loading Device**

The mechanical parts were attached to the loading platform, which was fixated to the bed of the CT scanner. A holding jig secured the specimen in a horizontal orientation above the carbon fibre beam, allowing cantilever bending of specimen during one rotation of the motor.

## Appendix N: Surface Deviation Analysis

*This appendix describes the process used to analyze stem surface deviations between the unloaded and loaded condition in Chapter 7 of this thesis. This process allowed comparison of stem-cement motion during the application of bending loads.*

Immediately after the scanning protocol is complete, the image data from CT-scanner is reconstructed into .vff files to be viewed as a 3-D volume made up individual image slices. This reconstruction is done within MicroView 3D Image Viewer and Analysis Tool (Parallax Innovations, Ilderton, ON). Once the files are reconstructed, they are further converted to surface files (.stl) within MicroView, to be exported to, and analyzed with Geomagic<sup>®</sup> Qualify (Geomagic, Morrisville, NC). The process below describes the series of steps used for analysis of the CT data files; from the conversion of the reconstructed images (.vff) into surfaces (.stl), to the analysis tools used within Geomagic<sup>®</sup> Qualify.

### STEP 1: Conversion of .vff's to .stl's in MicroView

- 1) Open the .vff image file within MicroView, **File → Open → Select file**. The file should contain a series of image slices which make up the volume of the imaged object. By placing the mouse cursor over the image volume and left clicking while dragging the mouse, the orientation of the image volume can be manipulated.
- 2) Within the MicroView program, the '**Tools & Applications**' tab should be located on the left side of the window. Click on the '**Standard ROI**' icon under the Tools & Applications tab. This will introduce a yellow region of interest (ROI) box in the image volume on the right.

- 3) Within the Standard ROI tab, the **'Box'** tool and **'Millimeter'** unit is set as the default options. These defaults may remain as is.
- 4) To select the region of interest from which the surface files will be created, place the mouse cursor over each of the four walls of the yellow ROI box, and click on the mouse's wheel to extend these walls in the horizontal and vertical directions over the desired region. This will cause a change in the ROI size and ROI center ( $x,y,z$ ) coordinates shown on the tab located to the left of the program window. The **'ROI size'** and **'ROI center'** coordinates can be altered to make fine adjustments to the region of interest.
- 5) Once the desired ROI is shown within the yellow ROI box, select the **'Visualize'** tab on the toolbar located at the top of the program window, and choose the **'Isosurface'** option.

*(Within the Isosurface tab, various isosurfaces can be created dependent on the image threshold chosen for the ROI. For analysis of the cemented implant stems, two different isosurfaces are created; one of the cemented stem contained in the aluminum tube (Figure N.1A), and the second of the stem and embedded cement beads without the aluminum tube (Figure N.1B). An image threshold value of 2000 is typically chosen for the isosurface with the aluminum tube, while the isosurface of the implant stem with beads is set to an image threshold of 3000)*

- 6) Under the **'Isosurface Properties'** of the **'Isosurface tab'**, insert the desired image threshold value (see above) required for creation of the isosurface. Adjust the surface quality factor to 0.75, and click the **'Update'** icon. This will create the desired surface from the image ROI on the right. Once the surface is deemed suitable, select the **'Save Surface'** option, and save the resultant isosurface as a **.stl** file to the desired location (Figure N.1).

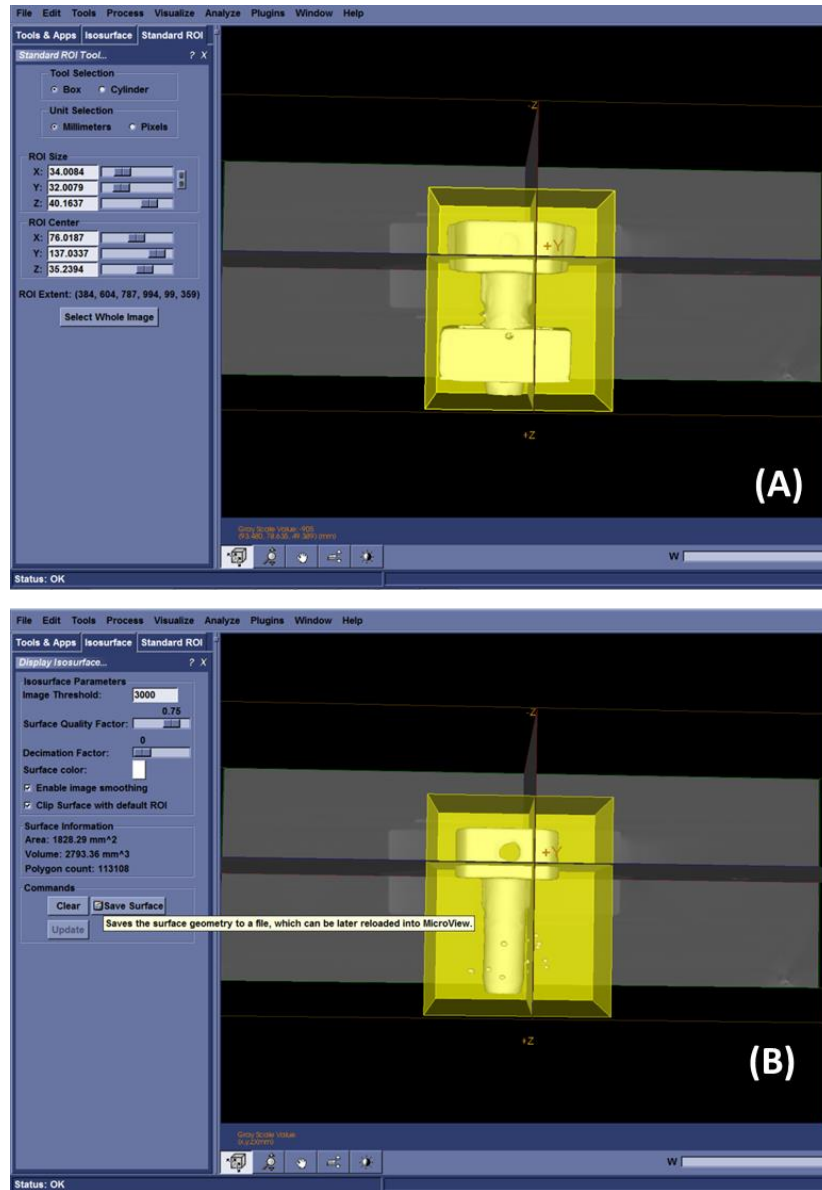


**Figure N.1: Region of Interest (ROI) used to Create Isosurfaces**

(A) The region of interest used to create isosurface for the stem with aluminum tube, and  
 (B) the same region of interest updated with a new image threshold value, to create isosurface of the stem and beads only.

## STEP 2: Analysis using Geomagic Qualify®

Within Geomagic, a single study compares the loaded and unloaded condition for each of the implant stems. This is done by first opening the isosurface of *unloaded stem*, and setting this as the reference surface. Subsequently, the isosurface of the *loaded stem* can be imported and set as the test surface. Analysis tools within Geomagic can then be used to compare the deviation of the test surface (loaded) relative to the reference surface (unloaded) (Figure N.2).

In order compare the isosurfaces, however, the images must be registered to ensure that stem motion is evaluated within the same coordinate system. As such, the isosurfaces of the cemented stem within aluminum tubes are used for registration, by matching the faces of the reference and test aluminum tubes to one another. This allows comparison of stem motion within the reference frame of the aluminum tubes.

### Step 2a: Registration of Aluminum Tubes in Geomagic

- 1) **Open** the .stl containing the isosurface of the unloaded stem contained within the aluminum tube: *File → Open → Select file*
- 2) The file should appear within the '*Model Manager*' tab to the left of the program window. Right click on the file, and select the option "Set as Reference". This will result in the abbreviation 'REF-' appearing adjacent to the file name in the *Model Manager* window.
- 3) **Import** the .stl containing the isosurface of the loaded stem contained within the aluminum tube: *File → Import → Select file*
- 4) Right click the imported file in the *Model Manager tab*, and select the option "Set as Test". This will result in the abbreviation 'TEST-' appearing adjacent to the file name in the *Model Manager* window.

- 5) Select the **rectangular icon** (6<sup>th</sup> icon from the top) located on the vertical toolbar at the right of the program window. Use this option to highlight the rectangular faces of the aluminum tubes by outlining the edges of the faces with the rectangular cursor.
- 6) Once all faces of the aluminum tubes are highlighted for the 'REF-' and 'TEST-' surfaces, click on the '**Home**' tab located at the top of the program window, and select the '**Best Fit**' option. By applying the best fit alignment tool, all surfaces of the aluminum tubes will be registered.
- 7) To save the transformation matrix used to align the aluminum tubes, click on the '**Tools**' tab located at the top of the program window, and select the '**Transform**' option. This will display the individual translation and rotation matrices that make up the transformation matrix. Choose the '**Save Matrix**' option below these coordinates, and save the matrix to the desired folder.

The transformation matrix saved from the registration of the aluminum tube surfaces will be used to align the isosurfaces of the implant stem and beads without the aluminum tube.

## Step 2b: Analysis of Surface Deviation Between the Unloaded and Loaded Stem

- 1) **Open** the .stl containing the isosurface of the unloaded implant stem and beads without the aluminum tube: *File → Open → Select file*
- 2) The file should appear within the '*Model Manager*' tab to the left of the program window. Right click on the file, and select the option "Set as Reference". This will result in the abbreviation 'REF-' appearing adjacent to the file name in the *Model Manager* window.
- 3) **Import** the .stl containing the isosurface of the loaded implant stem and beads without the aluminum tube: *File → Import → Select file*
- 4) Right click the imported file in the *Model Manager tab*, and select the option "Set as Test". This will result in the abbreviation 'TEST-' appearing adjacent to the file name in the *Model Manager* window.
- 5) Click on the '*Alignment*' tab located at the top of the program window. Select the '*Load Matrix*' option. Choose the transformation file saved in (7) of Step 2a. This will align the unloaded and loaded surfaces of stem and beads relative to one another, based on the transformation matrix used to register the aluminum tubes.
- 6) To compare the surface deviation between the the loaded to unloaded isosurfaces, click the '*Home*' tab at the top of the program window, and select the '*3D Compare*'. This will create a 3D- color plot comparing the deviation in the stem surfaces between the loaded and unloaded surfaces (Figure N.2A).
- 7) The cross sections through the isosurfaces along the x, y, z planes could also be compared, to determine the change in surface deviation through each section. On the '*Home*' tab, click '*Section Through Object*' to select the plane along which analysis is desired. For comparison of stem deviation along the length of the stem-cement interface, the Y-Z plane is chosen.



- 8) To analyze the sections through the object, select '**2D Dimensions**' from the '**Home**' tab at the top of the program window. This tool allows the user to select various locations along the reference (unloaded) and test (loaded) profiles, to determine the vertical and horizontal deviations of the test (loaded) surface relative to the reference (unloaded) surface (Figure N.2 B).

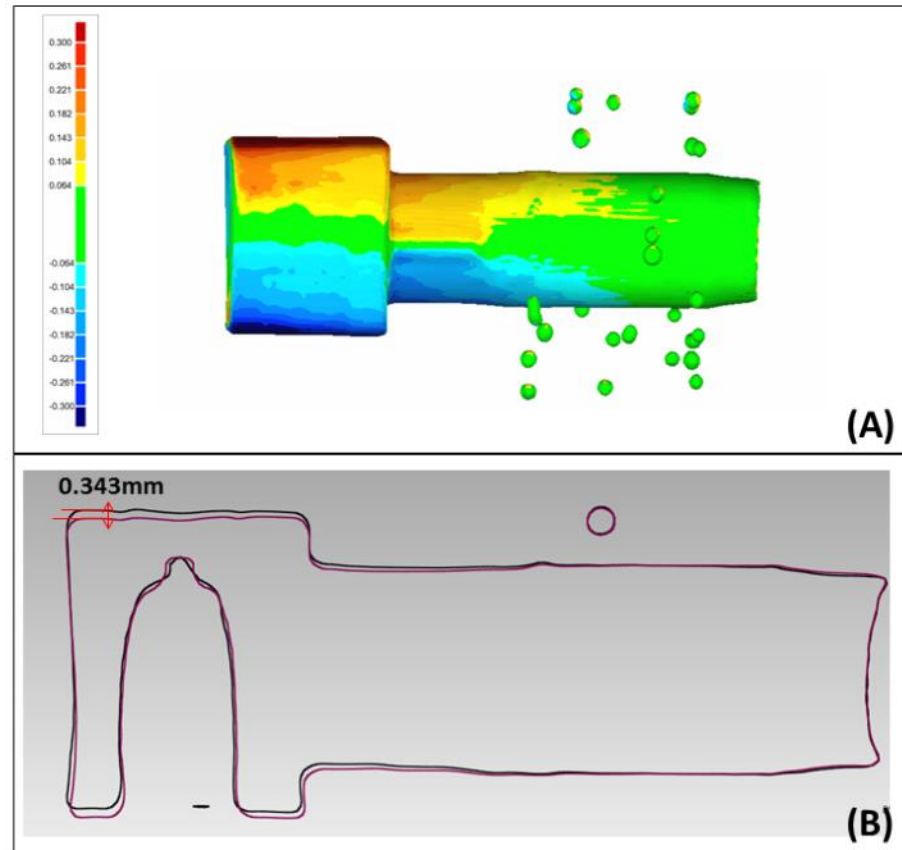


**Figure N.2: Geomagic® Surface Deviation Analysis**

(A) The 3D Compare color plot shows the deviation in the stem and bead surfaces between the unloaded and loaded condition, and (B) the 2D Dimensions from the section through the  $Y$ - $Z$  plane of the cemented stem and beads measure the vertical and horizontal translation of the surfaces. The red profile represents the reference (unloaded) surface, and the black profile represents the test (loaded) surface.

## **Appendix O: Uncertainty of Stem and Bead Displacements**

*This appendix describes the scan-rescan technique used to determine the uncertainty in the measured displacement of the cemented stems and beads embedded within the cement, described in Chapter 7.*

### **Introduction:**

The CT imaging methodology described in Chapter 7 of this thesis provided a useful technique for analysing motion along the stem-cement interface. However, the apparatus used for testing (*i.e.*, holding jig, aluminum tube, titanium stem, steel beads, aluminum load cell) incorporated metal components, which were carefully chosen to meet CT-compatible requirements, but may have resulted in some error from inherent metal artifact. In particular, the embedment of high density steel beads used for analysis of cement motion in Chapter 7 (Appendix J) could have imposed artifact errors in the CT generated surface profiles, which would result in uncertainty in the cement motion measurements. As such, it was necessary to determine the amount of error imposed on the stem and bead displacement measurements as a result of metal artifact contribution.

### **Materials and Methods:**

Three smooth implant stems, similar to those used in Chapter 7, were potted into square aluminum tubes using a 0.2% mixture of orthopaedic bone cement and steel beads (Appendix J). The stems were left 24 hours to cure, and subsequently used for scan-rescan testing.

The stems were secured within the custom built loading device (in the same configuration expected for testing, without the application of a load) and two consecutive scans similar to those described in Chapter 7 (x-ray potential of 120kVp; 40mA tube current; duration of 8 seconds; image volume was 1024 mm x 1024 mm x 360 mm) were acquired. No changes were made to the set up between scans.

The two scans for each of the stems were analyzed using the methodology described in Appendix M. For Geomagic<sup>®</sup> analysis, the first scan was set as the reference, with the second scan (*i.e.*, re-scan) was set as the test. Scan and re-scan surfaces for the three stems were compared to determine the average deviations of the stem and bead surface between the scan and re-scan surface profiles.

### **Results:**

Comparison of surface deviation among the three cemented construct showed that on average, the stems (*i.e.*, head, uncemented shaft and cemented shaft) showed an average surface deviation of  $0.014 \pm 0.010$  mm, and beads (Region 1 and 2, above and below stem) showed an average surface deviation of  $0.018 \pm 0.011$  mm (Table N.1).

### **Discussion and Conclusion:**

Based on results from this pilot test, it was determined that uncertainty in the stem and bead displacement measurements using CT-scanning and Geomagic analysis was on the order of tens of microns. However, from this pilot study, stringent criteria for analysing surface deviation of the stem and bead surfaces were developed, to exclude any inconsistencies in surface morphology from the motion measurements. This included analyzing contralateral edges of the stem and bead surfaces (*i.e.*, top and bottom of stem 2D surface profile, top and bottom/ left and right of bead 2D surface profile), and finding the average surface deviation value to represent motion. If contralateral deviations were not similar, the measurement was excluded from the analysis.

**Table O.1: Deviation in Stem and Bead Surfaces between Scan- Re-scan Tests**

Stem #	Stem Head (mm)	Un-cemented Shaft	Cemented Shaft (mm)	Cemented Shaft (mm)	Bead Motion (Above Stem) (mm)		Bead Motion (Below Stem) (mm)	
			# 1	# 2	Region 1	Region 2	Region 1	Region 2
1	0.013	0.008	0.006	0.010	0.010	-	0.008	0.008
2	0.009	0.008	0.008	0.027	-	0.019	0.025	0.021
3	0.019	0.011	0.008	0.040	-	0.029	0.025	-
<b>Average</b>	<b>0.013</b>	<b>0.009</b>	<b>0.007</b>	<b>0.025</b>	<b>0.010</b>	<b>0.024</b>	<b>0.019</b>	<b>0.014</b>
<b>SD</b>	<b>0.005</b>	<b>0.002</b>	<b>0.001</b>	<b>0.015</b>	<b>-</b>	<b>0.007</b>	<b>0.010</b>	<b>0.009</b>

## CURRICULUM VITAE

**NAME:** Yara Kareen Hosein, B.Sc.

**EDUCATION:**

2008–2013 Doctor of Philosophy Candidate, Biomedical Engineering Graduate Program, The University of Western Ontario, London, ON

2004–2008 Bachelor of Science, Honours Specialization, Medical Biophysics, The University of Western Ontario, London, ON

**HONOURS AND AWARDS:**

2010–2014 CIHR Graduate Fellow in Musculoskeletal Health Research, Joint Motion Program (JuMP)—A CIHR Training Program in Musculoskeletal Health Research and Leadership

Fall 2010 Graduate Student Teaching Award, Department of Mechanical and Materials Engineering, The University of Western Ontario, London, ON

2008–2012 Graduate Thesis Research Awards Fund, Western Internal Grants Competitions, The University of Western Ontario, London, ON

2008–2012 Western Graduate Research Scholarship (WGRS) for outstanding academic achievement, The University of Western Ontario, London, ON

2008 Gold Medalist (highest academic standing), Honours Specialization in Medical Biophysics (Physical Science Concentration), The University of Western Ontario, London, ON

2007 A.K. Knill Residence Staff Leadership Award, Perth Hall, The University of Western Ontario, London, ON

2006–2008 Dean's Honour List, Faculty of Science, The University of Western Ontario, London, ON

2006 Gold Medal, Excellence in Leadership Award (volunteering and community service), The University of Western Ontario, London, ON

**RESEARCH EXPERIENCE:**

- 2008–2013      PhD Candidate; Graduate Research Assistant, Biomedical Engineering Graduate Program, The University of Western Ontario, London, ON
- 2011–2012      Interdisciplinary Research Collaborator, Graduate Department of Orthodontics, Schulich School of Medicine and Dentistry The University of Western Ontario, London, ON
- 2007–2008      4<sup>th</sup> Year Honours Medical Biophysics Thesis, Imaging Research Laboratories, Robarts Research Institute, The University of Western Ontario, London, ON
- May–Aug 2007      Student Research Assistant, Imaging Research Laboratories, Robarts Research Institute, The University of Western Ontario, London, ON
- Jan–Apr 2007      Student Research Project, Jack McBain Biomechanical Testing Laboratory, The University of Western Ontario, London ON

**TEACHING EXPERIENCE:**

- Winter 2012;  
Winter 2011;  
Winter 2009      Graduate Teaching Assistant, Finite Element Analysis, Department of Mechanical and Materials Engineering The University of Western Ontario, London, ON  
*Supervisor: Dr. Paul Kurowski*
- Fall 2011;  
Fall 2010;  
Fall 2009      Graduate Teaching Assistant, Product Design & Development, Department of Mechanical and Materials Engineering The University of Western Ontario, London, ON  
*Supervisor: Dr. Paul Kurowski*
- Winter 2010      Graduate Teaching Assistant, Introductory Engineering Design & Innovation Studio  
Department of Mechanical and Materials Engineering  
The University of Western Ontario, London, ON  
*Supervisor: Dr. Paul Kurowski*

**SUPERVISORY EXPERIENCE:**

May–Aug 2010      Meghan Clynick: First Year Undergraduate Student,  
The University of Western Ontario (NSERC, USRA)

**PUBLICATIONS IN REFEREED JOURNALS:**

1. **Y.K. Hosein**, G.J.W. King, C.E. Dunning. “The Effect of Stem Surface Treatment and Material on Pistoning observed in Ulnar Components of Linked Cemented Elbow Prostheses” *Journal of Shoulder and Elbow Surgery*. 2013 [E-pub ahead of print; PMID: 23668920]
2. **Y.K. Hosein**, G.J.W. King, C.E. Dunning. “The Effect of Circumferential Grooves on the Stability of Cemented Joint Replacement Systems” *Journal of Medical Devices*. 2013 [In Revision: Paper # MED-13-1022]
3. **Y.K. Hosein**, G.J.W. King, C.E. Dunning. “The Effect of Stem Material and Surface Treatment on the Torsional Stability at the Metal-Cement Interface of Cemented Joint Replacement Systems in the Upper Limb” *Journal of Biomedical Materials Research: Part B Applied Biomaterials*. 2013 [Under Review: Paper # JBMR-B-13-0196]
4. S.R. Fetterly, **Y.K. Hosein**, C.E. Dunning. “Development and Validation of a Strain Gauge Embedment Methodolgy for Use with PMMA Bone Cement” *Journal of Biomechanical Engineering*. 2013 [Under Review: Paper # BIO-13-1207]
5. **Y.K. Hosein**, M.P. Clynick, S.D. McLachlin, G.J.W. King, C.E. Dunning. “The Effect of Stem Curvature on Torsional Stability of a Generalized Cemented Joint Replacement System” *Journal of Applied Biomaterials and Functional Materials*. 2012 [E-pub ahead of print; PMID: 22798236]

**SCIENTIFIC POSTER PRESENTATIONS:**

1. **Y.K. Hosein**, G.J.W King, C.E. Dunning. “The Effect of Intramedullary Stem Surface Finish on the Torsional Stability of Cemented Joint Replacement Systems”. Canadian Orthopedic Research Society Annual Meeting, Ottawa ON, Canada 2012.



2. A.L. Smith, **Y.K. Hosein**, A. Tassi, C.E. Dunning, “An *In-Vitro* Study Evaluating the Fracture Resistance and Insertion Torque of Self-Drilling Mini-Implants upon Insertion into Synthetic High Density Mandibular Bone”. Canadian Association of Orthodontists 64<sup>th</sup> Annual Scientific Session, Ottawa ON, Canada 2012.
3. **Y.K. Hosein**, M.P. Clynick, S.E. Takaki, S.D. McLachlin, C.E. Dunning. “The Effect of Intramedullary Stem Curvature on the Torsional Stability of Cemented Joint Replacement Systems”. The Dr. Sandy Kirkley Centre for Musculoskeletal Research - Poster Competition. London, ON., Canada 2011.
4. **Y.K. Hosein**, M.P. Clynick, S.E. Takaki, S.D. McLachlin, C.E. Dunning. “The Effect of Intramedullary Stem Curvature on the Torsional Stability of Cemented Joint Replacement Systems”. CIHR Joint Motion Training Program in Musculoskeletal Health Research and Leadership: Annual Retreat University of Western Ontario. London, ON., Canada 2011.
5. **Y.K. Hosein**, M.P. Clynick, S.E. Takaki, S.D. McLachlin, C.E. Dunning. “The Effect of Intramedullary Stem Curvature on the Torsional Stability of Cemented Joint Replacement Systems”. Summer Bioengineering Conference, American Society of Mechanical Engineers (ASME), Farmington, PA., USA 2011.
6. **Y.K. Hosein**, M.P. Clynick, S.E. Takaki, S.D. McLachlin, C.E. Dunning. “The Effect of Intramedullary Stem Curvature on the Torsional Stability of Cemented Joint Replacement Systems”. Orthopedic Research Society 2011 Annual Meeting, Long Beach, CA., USA 2011.
7. **Y.K. Hosein**, S.D. McLachlin, G.J.W. King, C.E. Dunning. “Development of Methodology to assess stem surface finish in cemented implant loosening”. Summer Bioengineering Conference, American Society of Mechanical Engineers (ASME), Naples, FL., USA 2010.
8. A. Wheatley, S. McKay, L. Mathew, **Y. Hosein**, G. Santyr, D.G. McCormack, C. Licskai and G. Parraga. ‘Hyperpolarized <sup>3</sup>He Magnetic Resonance Imaging of Asthma: Short-term reproducibility’. London Imaging Discovery, London, ON., Canada 2008.
9. A. Wheatley, S. McKay, L. Mathew, **Y. Hosein**, G. Santyr, C. Licskai, D.G. McCormack and G. Parraga. ‘Hyperpolarized <sup>3</sup>He Magnetic Resonance Imaging of Asthma: Short-term reproducibility’. Robarts Research Day, London, ON., Canada 2008.
10. A. Wheatley, S. McKay, L. Mathew, **Y. Hosein**, G. Santyr, D.G. McCormack, C. Licskai and G. Parraga. ‘Hyperpolarized <sup>3</sup>He Magnetic Resonance Imaging of Asthma: Short-term reproducibility’. Society for Photonics and Instrumentation Engineers (SPIE), San Diego, CA., USA 2008.

**INVITED PODIUM PRESENTATIONS:**

1. **Y.K. Hosein**, G.J.W King, C.E. Dunning. “The Effect of Stem Surface Treatment and Material on Pistoning observed in Ulnar Components of Linked Cemented Elbow Prostheses” Ontario Biomechanics Conference, Barrie, ON, Canada 2013
2. **Y.K. Hosein**, G.J.W King, C.E. Dunning. “The Effect of Intramedullary Stem Surface Finish on the Torsional Stability of Cemented Joint Replacement Systems”. Ontario Biomechanics Conference. Barrie, ON, Canada 2012

**SCIENTIFIC MEMBERSHIPS:**

- |           |  |
|-----------|--|
| 2011–2013 | Biomedical Engineering Society (BMES)<br>Student Member  |
| 2012–2013 | American Society of Mechanical Engineers (ASME)<br>Bioengineering Division (BED)<br>Student Member |

**UNIVERSITY SERVICE AND VOLUNTEER WORK:**

- |           |   |
|-----------|---|
| 2010–2013 | Outreach Coordinator, CIHR Joint Motion Program (JuMP), The University of Western Ontario, London, ON                                 |
| 2008–2013 | Biomedical Engineering (BME) Student Committee Member, The University of Western Ontario, London, ON                                  |
| 2011–2012 | Graduate Student Representative, Biomedical Engineering (BME) Undergraduate Task Force, The University of Western Ontario, London, ON |
| 2009–2011 | President, Biomedical Engineering (BME) Student Committee, The University of Western Ontario, London, ON                              |
| 2008–2009 | Volunteer with Western Serves, The University of Western Ontario, London, ON  |